# Low temperature oxidation of hydrocarbons using an electrochemical reactor

**Ippolito, Davide; Kammer Hansen, Kent; Christensen, Henrik**

*Publication date:*
2013

*Document Version*
Publisher's PDF, also known as Version of record

**PhD Thesis**

**April 2013**

# Low temperature oxidation of hydrocarbons using an electrochemical reactor

Davide Ippolito

Department of Energy Conversion and Storage

**Technical University of Denmark**

The satisfaction to involve the loved ones in all this...

*Titaniocromia(e altre cose)*
*Prof. Pietro Pedeferri*

## Preface

This thesis finalizes the study on *Low Temperature Oxidation of Hydrocarbons using an Electrochemical Reactor* which was funded by the Danish Strategic Research Council under contract no. 09–065186.
The work was carried out between the 1st of May 2010 and the 30th of April 2013 at the Department of Energy Conversion and Storage of the Technical University of Denmark, under the supervision of senior researcher Dr. Kent Kammer Hansen and co-supervision of Dr. Henrik Christensen from Dinex A/S.


### Acknowledgements

I would like to thank my supervisor Kent Kammer Hansen for giving me the opportunity to be a Ph.D. student at the Department of Energy Conversion and Storage DTU and for guiding me during these three years.
Many thanks go to my colleagues of the Flue Gas Purification group, present and past members, for the help, discussion and laughs.
I would like to thank all the technical staff because they never say no to me for last minute analyses or crazy questions.
Special thanks go to: Frederik, Michela, Alberto, Frantz, Irene and Francesco, Jonathan, Marie, Pia and Ane.
I would like to thank my friends in Italy that visited me in CPH and supported me during these three years: Alberto (Frantz), Cairo, Max, Tino, Francesco (Frantz) amd Mattia.
Iper thanks to my family, starting from my mum, Lauri, dad, Maria and Maria, Antonia, Sara and Massi.

And I want to thank my beautiful wife, Ele, the noblest among noble metals, thanks for the patience and comprehension, nothing would had never begun without you.


Davide Ippolito
Roskilde, Denmark, April 2013

## Abstract

This study investigated the use of a ceramic porous electrochemical reactor for the deep oxidation of propene.

Two electrode composites, $La_{0.85}Sr_{0.15}MnO_{3\pm\delta}/Ce_{0.9}Gd_{0.1}O_{1.95}$ (LSM/CGO) and $La_{0.85}Sr_{0.15}FeMnO_3/Ce_{0.9}Gd_{0.1}O_{1.95}$ (LSF/CGO), were produced in a 5 single cells stacked configuration and used as backbone for the infiltration of materials able to modify the electrochemical and catalytic activity of the reactor.

The catalytic activity of the reactor and the effect of polarization on the propene oxidation have been studied by gas analysis with a gas chromatograph (GC), during the reactor polarization at different reaction temperatures. The study of the effect of the infiltration of different electroactive materials on the electrode behavior has been carried on by the use of electrochemical impedance spectroscopy (EIS). Both the methods have been employed to understand the relationship between the catalytic activity of the reactor under polarization and the reactor electrochemical behavior. The impact of the morphology of the infiltrated material on the electrocatalytic activity was assessed by scanning electron microscopy.

This project helped to better understand how the effect of polarization on propene conversion was a complex function of multiple variables: the microstructure of the backbone, the polarization resistance of the electrodes, both at OCV and under polarization, the electrical and morphological properties of the infiltrated material and the specific reaction conditions like the propene conversion.

Although both the LSM/CGO and LSF/CGO backbones have demonstrated the ability to oxidize propene, the LSM/CGO exhibited the best performance both in terms of catalytic activity and faradaic efficiency for the propene oxidation. While LSF/CGO showed instability due to prolonged polarization, the LSM/CGO exhibited a strong electrode activation and increase of catalytic activity after the application of prolonged polarization.

The infiltration of LSM/CGO backbone with $Ce_{0.9}Gd_{0.1}O_{1.95}$, heat treated at low temperature to form a continuous layer on the electrode, was the best compromise to obtain high propene conversion at open circuit voltage together high rate enhancement ratio and faradaic efficiency values at low temperatures (300-350 °C). Although some stability problems affected the performance of multiple infiltrated $Ce_{0.9}Gd_{0.1}O_{1.95}$ on LSM/CGO backbone, the strong activation of LSM upon prolonged polarization was able to partially counteract the instability of the infiltrated $Ce_{0.9}Gd_{0.1}O_{1.95}$.

This project demonstrated the possibility to enhance the oxidation of propene by polarization in a porous ceramic reactor. The infiltration of different active materials helped to

increase the catalytic activity at open circuit voltage and the effect of polarization on propene oxidation rate at low temperature.

The future development of this technology will see the infiltration of an active catalyst towards propene oxidation together with a NOx storage compound for the simultaneous oxidation of propene and the reduction of NOx with high efficiency.

## Dansk Resume´

Dette projekt omhandler fuldstændig oxidation af propen ved brug af en porøs, keramisk, elektrokemisk reaktor.

To elektrode kompositter, $La_{0.85}Sr_{0.15}MnO_{3\pm\delta}/Ce_{0.9}Gd_{0.1}O_{1.95}$ (LSM/CGO og $La_{0.85}Sr_{0.15}FeMnO_3/Ce_{0.9}Gd_{0.1}O_{1.95}$ (LSF/CGO), blev testet i en cellestak-konfiguration bestående af 5 enkelt-celler, som herefter benævnes ”reaktoren”. Reaktoren blev i projektet infiltreret med materialer, som påvirkede dens elektrokemiske og katalytiske aktivitet.

Reaktorens aktivitet og effekten af elektrisk polarisering på propen oxidation blev målt ved hjælp af gas analyse med en gas kromatograf, analysen blev lavet både under polarisering af reaktoren og ved forskellige temperaturer. Elektrokemisk impedans spektroskopi (EIS) blev brugt til at studere, hvordan infiltrering med elektroaktive materialer påvirkede elektroderne. Både gas kromatografi og EIS blev anvendt for at klarlægge forholdet mellem reaktorens katalytiske aktivitet under polarisering og reaktorens elektrokemiske egenskaber. Effekten af de infiltrerede materialers morfologi på den elektrokatalytiske aktivitet blev vurderet ud fra scanning elektron mikroskopi.

Dette projekt har bidraget til forståelsen af, hvordan effekten af polarisation på propen omsætning er en kompleks funktion af en række variable: mikrostrukturen af de ikke-infiltrerede elektroder, elektrodernes polarisations modstand - både under og uden polarisation, de elektriske og morfologiske egenskaber af de infiltrerede materialer og den specifikke reaktion, som selve propen oxidationen er.

Selvom både de ikke-infiltrerede LSM/CGO og LSF/CGO elektroder var i stand til at oxidere propen, var LSM/CGO bedst både i forhold til katalytisk aktivitet og Faradaisk effektivitet under propen oxidationen. Mens LSF/CGO blev ustabil under langvarig polarisation, udviste LSM/CGO en markant elektrode aktivering samt forbedring af den katalytiske aktivitet efter langvarig polarisation.

Infiltrering af LSM/CGO elektroderne med $Ce_{0.9}Gd_{0.1}O_{1.95}$ varmebehandlet ved lav temperatur, var det bedste kompromis i forhold til at opnå en høj propen omsætning uden polarisering kombineret med en stærk forbedring af reaktionshastighed forholdet og Faradaisk effektiviteten ved lave temperaturer (300-350 °C). På trods af, at stabilitetsproblemer påvirkede LSM/CGO elektroder infiltreret flere gange med $Ce_{0.9}Gd_{0.1}O_{1.95}$, var den stærke aktivering under langvarig polarisation i stand til delvist at modvirke den manglende stabilitet af den infiltrede $Ce_{0.9}Gd_{0.1}O_{1.95}$.

Dette projekt demonstrerede muligheden for at øge propen oxidationen ved at polarisere en porøs, keramisk reaktor. Infiltreringen af forskellige aktive materialer medvirkede til at øge den katalytiske aktivitet uden polarisation, samt til at øge effekten af polarisation på propen oxidations hastigheden ved lav temperatur.

Den fremtidige udvikling af denne teknologi vil fokusere på infiltrering af en aktiv propen oxidations katalysator kombineret med infiltrering af en $NO_x$ lagrings forbindelse med det mål at opnå simultan oxidation af propen og reduktion af $NO_x$ med høj effektivitet.

**TABLE OF CONTENTS**

# 1 INTRODUCTION

The reduction of the emissions of volatile organic compounds (VOCs), NOx (NO and $NO_2$), particulate matter (PM) or soot and SOx ($SO_2$, $SO_3$) from stationary sources and road transport has become an international concern for more than 15 years due to the increase of number of vehicles and industrial emissions.

The VOCs are considered any organic compound with vapor pressure exceeding 0.1 mmHg in standard conditions. VOCs are present in fuel combustion, solvents and industrial manufacturing. NOx and VOCs are considered as responsible for the formation of ozone and peroxyacetyl nitrates (PAN), toxic for human health, in urban areas at ground level [1]. NOx gases can also cause respiratory problems and contribute to the formation of acid rains.

To understand the magnitude of the polluting emissions problem, the European Environment Agency [2] reported that, in the summer of 2012, the threshold of 120 micrograms of ozone per cubic meter of air ($\mu g/m^3$) maximum daily eight-hour mean, a value used to assess whether countries meet the target value for protecting human health, was exceeded on more than 25 days across large parts of Europe. The most widespread concentrations occurred in the Mediterranean area.

This project is related to the development of a new technology for the treatment of typical pollutants emitted by Diesel engines. This new technology was named: electrochemical flue gas purification.

The idea is to use an electrochemical porous reactor for the simultaneous reduction of NOx and the oxidation of unburned hydrocarbons and particulate matter without the use of precious metals, a reductant agent like ammonia, multiple catalytic converters in series and on-board diagnostic units.

Particularly, this Ph.D. project studies the possibility to deep oxidize propene, a representative hydrocarbon molecule of Diesel exhausts, using a porous electrochemical reactor. A particular focus was given in the understanding and improving the electrocatalytic activity and selectivity of the reactor towards the oxidation of propene.

## 1.1 Emissions from Diesel Engines

In traditional stoichiometry gasoline engines the combusting mixture always contains sufficient oxygen to just combine with the fuel. In contrast, in a Diesel engine, air and fuel are injected separately into the combustion chamber where the air is compressed and the fuel is subsequently added for ignition. In order to improve the fuel efficiency, the oxygen is always in excess (lean conditions). The consequence of this mode of combustion is that Diesel exhaust contains NOx and particulate matter together with an excess of oxygen, and while this is advantageous for the oxidation of hydrocarbons (HCs) and CO, it makes controlling NOx emissions extremely difficult because, under practical conditions, NOx can only be converted to $N_2$ by reaction with a reductant. The highly active three-way catalyst (TWC), effectively used for exhausts treatment in gasoline engines, cannot be used for Diesel exhausts treatment due to the presence of 10-15% of $O_2$.

Due to the negative impact on human health and environment, stricter limits on Diesel emissions have been imposed worldwide. Figure 1 shows an example of the increase of strictness of European legislation for light-duty vehicles emissions.

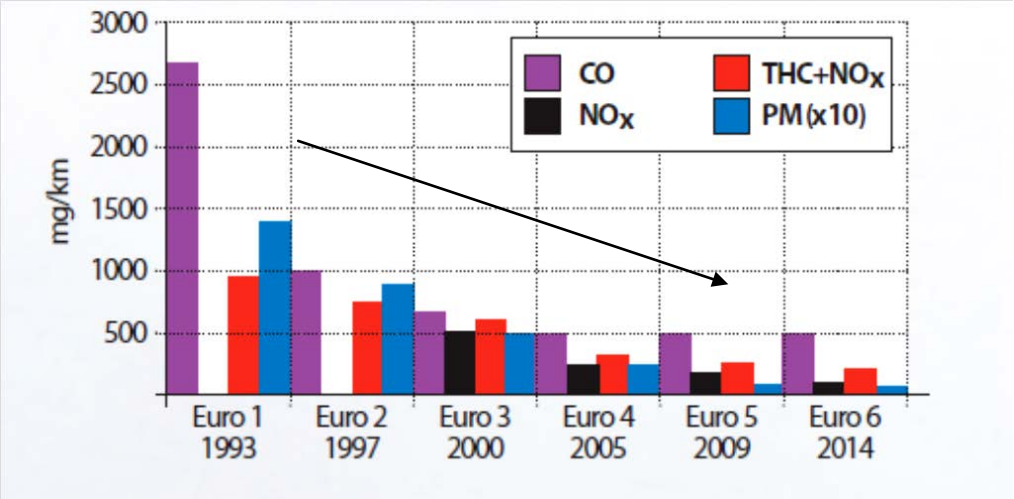


**Figure 1:** European Emissions Guide for light duty vehicles [3]. * THC= total hydrocarbons

### 1.1.1 Methods for the treatment of unburned hydrocarbons and PM emitted from Diesel exhausts

The oxidation of unburned hydrocarbons and CO have been carried on initially by the Diesel Oxidation Catalysts (DOC), becoming mandatory in 1996 in US and in 1998 in Europe for all new Diesel cars [4]. These converters resembled the conventional catalytic converters for gasoline engines with some variation to the catalyst composition based on noble metals in order to optimize the catalyst activity under lean conditions. PM particles were not trapped

by these systems but CO and hydrocarbons (including those of the soluble organic fraction of the PM) were burned from 200 °C. The particulate mass abatement efficiency in the flow-through DOC was however lower than 5%. Zeolites were used to adsorb HCs and CO under cold-start condition, when the Pt-based catalysts were not sufficiently warm to oxidize HCs and CO and to avoid that the active sites could be poisoned by HCs adsorption at low temperature; the use of Zeolites strongly improved the HCs oxidation during cold-start [5]. The noble metal catalysts were sensitive to poisoning from $SO_2$, derived from the sulphur present in the fuel.

The new technologies for HCs and PM treatment are based on the coupling of an oxidation catalyst (pre-oxidizer) and a catalyzed wall-flow filter (DPF) for trapping and oxidation of PM to $CO_2$ and water; in these systems $NO_2$ is used as oxidizing agent for PM.

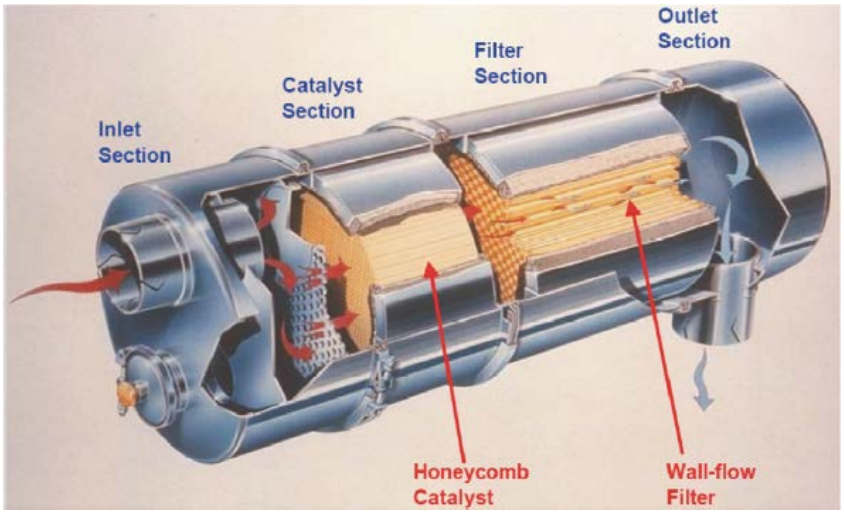


**Figure 2:** Continuously Regenerating Trap (CRT) technology by Johnson Matthey [6].

The oxidation catalyst upstream of the filter oxidizes HCs and CO to $CO_2$ and water, and also converts NO to $NO_2$ that is a very powerful oxidant, and this continually removes PM, according to the reactions 1 and 2 below.

$$2NO + O_2 \rightarrow 2NO_2 \qquad [1]$$

$$5NO_2 + 2CH\ (PM) \rightarrow 5NO + 2CO_2 + H_2O \qquad [2]$$

This technology is called Continuously Regenerating Trap (CRT ®), shown in Figure 2, and it is normally applied to heavy duty diesel vehicles, like trucks or buses, where the engine is normally working at high load and the exhausts temperature is between 250 °C and 400 °C. The application of a catalyst on the wall-flow filter helps to catalyze the further formation of $NO_2$ derived from the reaction 2 and increase the oxidation rate of the PM. In trucks or bus-

es, this system is normally coupled with a downstream selective catalytic reduction (SCR) system for the removal of NO using ammonia as reductant agent.
The exhausts temperature of passenger cars does not exceed 250 °C under normal urban driving, with an average of 150 °C [7], so the use of $NO_2$ to oxidize the PM is not feasible. The PM combustion in passenger cars is normally achieved by fuel post-injection. When too much PM is accumulated on the filter, the backpressure over the filter increases and the filter regeneration is obtained by a rise of the temperature above 450 °C through fuel post-injection. The use of a noble metal catalyst deposited on the DPF walls to enhance the filter regeneration is still under debate: the comparison of the regeneration efficiency between a Pt/Pd coated DPF and uncoated DPF show very close values. The use of so-called direct PM oxidation catalysts with oxygen ion conducting properties (ceria, Zr/Gd/Pr doped ceria) seems to offer increased regeneration efficiency compared to the Pt/Pd coated filter [8].

### 1.1.2 Electrochemical oxidation of hydrocarbons and PM

Numerous studies were conducted in the electrochemical oxidation of different hydrocarbons, especially since the group of Vayenas at MIT first reported that on silver deposited on an $O^{2-}$ conductor the ethylene catalytic oxidation rate and selectivity could be modified in a very pronounced and reversible manner by applying electrical currents or potentials [9]. In the case of use of an $O^{2-}$ conductor the increase in reaction rate was found to be considerably higher than the rate of oxygen ion supply to the electrode; a single ion could activate the reaction of more than one gaseous adsorbed species. This phenomenon was named Non Electrochemical Modification of Catalytic Activity (NEMCA) or more recently Electrochemical Promotion of Catalysis (EPOC).
A metal catalyst in the shape of porous and electronically conducting film is deposited on solid electrolyte ($O^{2-}$, $H^{+}$, $Na^{+}$ or mixed conductors). In the case of $O^{2-}$ conductors, the origin of EPOC was found into the electrochemically induced migration (backspillover) of anionic species $O^{\delta-}$ from the electrolyte to the metal-gas interface. These electrochemically assisted backspillover species, together with their image charge in the metal, create an overall neutral double layer at the metal–gas interface and strongly affect both chemisorption and catalysis.
The effect of electrochemical pumping of oxygen active species can be evaluated by two parameters as suggested by Vayenas [10].
The apparent faradaic efficiency (Λ):

$$\Lambda = \Delta r / (I/nF)$$

and the rate enhancement ratio (ρ) defined by:

$$\rho = r / r_o$$

where Δr is the difference between the catalytic rate at open circuit voltage $r_o$ and r is the catalytic rate (mol O/s) measured under polarization, n is the number of exchanged electrons during the electrode reaction and F is the Faraday constant; the I/(nF) is the ionic flux through the electrolyte current recorded under polarization.
The oxygen ions supplied to the electrode surface can desorb to the gas phase (oxygen evolution) according to the reaction:

$$O^{2-} \rightarrow 1/2O_2\,(g) + 2e^-,$$

or react with co-adsorbed hydrocarbons molecules:

$$C_nH_{2n+2} + (3n+1)\,O^{2-} \rightarrow nCO_2 + (n+1)\,H_2O + (6n+2)e^-$$

or migrate over the entire electrode surface for the formation of a double layer at metal-gas interface and give rise to EPOC.
In the first case, the rate of catalytic reaction under study is not influenced while in the second case the increase of reaction rate ($r-r_o$) will be at maximum equal to the ionic flux with Λ=1.
In the latter case when the migration of oxygen ions occurs over the entire electrode surface, faradaic efficiencies much higher than one have been found for the oxidation reactions of several hydrocarbons, mostly using Pt, Pd and Rh as metal electrode deposited on YSZ [11,12].

Few studies have been published on the electrochemical oxidation of non-methane VOCs with the use of perovskite oxides as electrode. The faradaic efficiencies found using perovskite oxides are much lower compared to faradaic efficiencies observed for the electrochemical oxidation of VOCs using noble metals. For example, Gaillard et al. [13] found a faradadaic efficiency of about 28 for the oxidation of propene at 450 °C on $La_{0.8}Sr_{0.2}Co_{0.8}Fe_{0.2}O_3$ deposited on Yttria Stabilized Zirconia (YSZ). Kaloyannis et al. [14] showed Λ equal to 1930 for the oxidation of propene in similar reaction conditions but using a porous Pt paste deposited on dense YSZ.
Roche et al.[15] studied the effect of polarization on the electrochemical oxidation of propane using $La_{0.7}Sr_{0.3}MnO_3$ deposited on YSZ. Upon application of +4 V at 300 °C, the propane conversion increased from 1.25 % to 1.78% with a Λ of 5. The cause of the low faradaic efficiency values was explained by the high speed of oxygen evolution on the $La_{0.7}Sr_{0.3}MnO_3$

electrode and the corresponding short life time of the $O^{\delta-}$ promoting species pumped on the electrode surface. This was confirmed by the low anodic overpotential of only 100 mV for the oxygen evolution reaction visible in the polarization curve recorded under 10% $O_2$ at 500 °C.
Kambolis et al.[16] studied the effect of Pt nanoparticles (8 nm) infiltration into $La_{0.6}Sr_{0.4}Co_{0.2}Fe_{0.8}O_{3-\delta}$ (LSCF)/$Ce_{0.9}Gd_{0.1}O_{1.95}$ (CGO) composite electrode deposited on $Ce_{0.9}Gd_{0.1}O_{1.95}$ electrolyte for propane deep oxidation. No impact of polarizations between -1V and +1V was visible on the catalytic performance of Pt-free LSF/CGO electrode; when Pt nanoparticles were added to LSCF/GDC electrode, non-Faradaic enhancement of propane conversion were evidenced by applying +200 µA at 338 °C with Λ equal to 12. Although no clear explanation of this behavior was given in the study, it is possible to deduce that the Pt infiltration partially covered the three phase boundary of highly performing LSCF/CGO electrode [17] decreasing the speed of the oxygen evolution reaction and at the same time increasing the lifetime of $O^{\delta-}$ species promoting the EPOC behavior.
The electrocatalytic oxidation of ethanol was studied by Douvarzides et al.[18] on $La_{0.6}Sr_{0.4}Co_{0.2}Fe_{0.8}O_3$ (LSCF) deposited on YSZ. The LSCF electrode behaved as effective catalyst for total oxidation of ethanol at 750 °C mainly producing acetaldehyde. Due to the high reaction temperature used, the homogeneous reactions together with electrocatalysis, instead of EPOC, affected the kinetic behavior, indeed the faradaic efficiencies exhibited values between 2 and 3.

The literature on the application of the simultaneous reduction of NOx and oxidation of HCs and PM for the treatment of Diesel exhaust under real operation conditions is nowadays limited.
Dinex A/S company in Denmark studied a bipolar electrochemical reaction unit for Diesel exhausts purification [19]. Figure 3 shows the monolithic reactor unit.

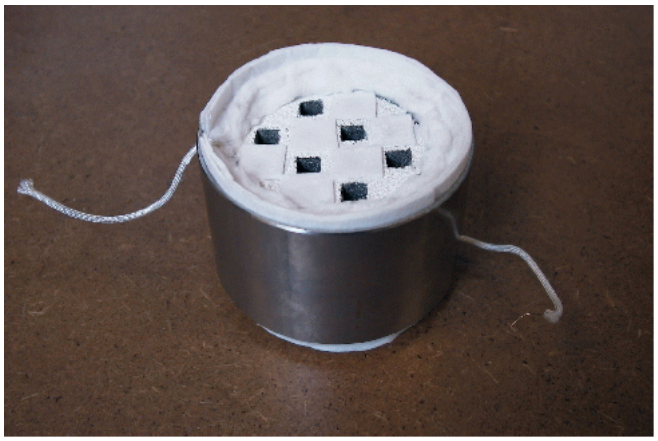

**Figure 3:** Dinex´s electrochemical reactor for PM and soot oxidation [19]

The reactor consists of a porous ionic conductive material like $Ce_{1-x}Gd_xO_{2-x/2}$ as electrolyte and of an electroactive material like $La_{1-x}Sr_xMnO_{3\pm\delta}$ as electrode. Through the application of AC or DC current the reactor was continuously able to oxidize PM, HCs and CO, according to the reaction mechanism shown in Figure 4.

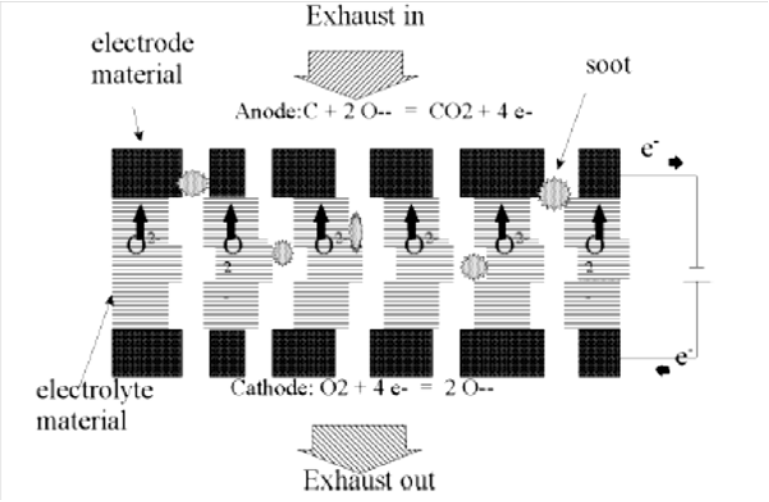


**Figure 4:** Reaction mechanism of DInex´s bipolar reactor [20]

The reactor activity tests were carried on a 1.5 liters Diesel Engine with exhausts temperature of 300 °C; no back pressure increase with time was visible along the reactor showing that the PM removal was continuous without blocking the pores. The removal of PM reached 90% with the application of 30 V while HCs and CO conversion reached 50 %. The conversion of NOx, exhibited values of only 10 %; this behavior was due to the strong competing reaction of oxygen electroreduction that decreased the selectivity towards direct electroreduction of NOx.

More recently Balomenou et al.[21] tested a novel monolithic-type electrochemical promoted reactor (MEPR) for treatment of a 1.9 liter Euro III Diesel engine exhausts. It consists of up to 22 yttria-stabilized zirconia (YSZ) plates coated on both sides with a conducting layer of catalyst (Pt and Rh) and mounted into a ceramic housing. EPOC was observed for the oxidation of HCs and CO while a decrease of NO reduction ($\rho<0$) was observed with polarization of both +4 V and -4 V. A particulate filter was used upstream of the electrochemical reactor to avoid particulate matter deposition and short-circuit of the working and current electrode.

Yoshinobu et al.[22] recently reported studies on the simultaneous reduction of NOx and PM oxidation; the studied were made both in a disk-electrode set-up and in a honeycomb module tested in the treatment of simulated exhausts and 2.2 liter Diesel engine exhausts, respectively.

The material studied were a composite of Pt/YSZ and Ag/CGO. The honeycomb cell was able to remove 97% of the PM and 74% of NOx with a fuel penalty of 9%; further reduction of fuel penalty is needed for market applications.

## 1.2 Electrochemical Porous Reactor for $C_3H_6$ oxidation

In this Ph.D. project, a new concept of highly porous electrochemical reactor for the purification of Diesel exhausts has been studied. The high reactor porosity permits to reduce the pressure drop and increase the conversion of the exhaust gases through the reactor. In order to get higher surface area for the reaction and gain mechanical strength, 5 symmetrical cells are stacked together to obtain a 11-layers structure without interconnects.
An oxygen ions conductor like CGO is used as electrolyte and a composite of LSM/GDC or LSF/GDC is used as electrode. The porous structure (backbone) also allows the infiltration of different catalytic and electroactive materials able to increase the catalytic activity of the reactor for the exhaust gases conversion.
The complexity of the chemical reactions occurring in a Diesel exhaust purification catalytic system is very high due to the coexistence of several reactive species.
This project focuses specifically on the electrochemical oxidation of propene, a representative hydrocarbon component of the Diesel exhaust gases and a model for the oxidation of the VOCs in diluted media [23].
The desired reactions occurring under polarization at the anode and cathode of the porous reactor are:

$$\textit{Cathode}: \quad 4.5O_2 + 18e^- \rightarrow 9O^{2-} \qquad [3],$$

$$\textit{Anode}: \quad C_3H_6 + 9O^{2-} \rightarrow 3CO_2 + 3H_2O + 18e^- \qquad [4]$$

The competing reaction at the anode side is the oxygen evolution reaction (OER); if the OER occurs, the electrochemical reactor is simply working as an oxygen pump, which will cause a waste of energy. The electrode materials and the reaction conditions need to be chosen carefully to increase the selectivity towards the electrochemical oxidation of propene.
It is important to highlight that the conversion of propene to oxidation products like $CO_2$, $H_2O$ or CO, on the contrary of NOx reduction, occurs also at OCV due to the ability of electrode and electrolyte to act as catalyst for the propene oxidation and to the high content of $O_2$ in the Diesel exhausts.

## 1.3 Objectives of the thesis

This PhD work is based on the following objectives:

1) show the possibility to electrochemically oxidize propene using a porous electrochemical reactor without the use of noble metals and at low temperature;
2) identify the best electrode material for the reactor fabrication characterized by good stability of the catalytic activity for propene oxidation and electrode performance under high polarization voltages;
3) study the effect of the reactor microstructure on the electrochemical behavior and catalytic activity;
4) study the effect of prolonged polarization on the reactor catalytic activity;
5) identify the electrochemical and chemical/process affecting the reactor behavior, particularly when propene is present in the reactive system;
6) study the effect of infiltration of catalytic materials on propene conversion and on electrochemical behavior of the reactor;
7) study the effect of the infiltrated material morphology on the electrochemical and catalytic behavior of the reactor.

The catalytic activity of the reactor and the effect of polarization on the propene oxidation have been studied by gas analysis with a gas chromatograph (GC) during the reactor polarization at different reaction temperatures. The study of the effect of the infiltration of different electroactive materials has been carried on by the use of electrochemical impedance spectroscopy (EIS). Both the methods have been employed to understand the relationship between the activity of the reactor under polarization and the reactor electrochemical behavior. Further techniques, like scanning electron microscopy (SEM) and the measurement of the specific surface area using the B.E.T equation have been useful to better comprehend the relation between the morphology of the infiltrated material, the electrochemical behavior of the reactor and the catalytic activity for propene oxidation.

## 1.4 Layout of the thesis

This thesis is divided into 9 chapters:

**Chapter 1:** a brief introduction of emissions formation from Diesel engines and the different methods for emissions abatement is given in this chapter. The objectives of the thesis are also described;

**Chapter 2:** a description of the materials used for the production of the electrochemical reactor is given in this chapter. The electrical and catalytic properties together with the defect chemistry of the materials are discussed;

**Chapter 3:** in this chapter an overview is given of the experimental test set-up and techniques used to measure the catalytic activity for propene oxidation and characterize the electrochemical behavior of the reactor;

**Chapter 4:** the effect of $Ce_{0.9}Gd_{0.1}O_{1.95}$ infiltration on the catalytic activity for propene oxidation and electrochemical behavior of the LSM/CGO reactor is described and discussed in this chapter. Part of these experimental results are part of the published paper: "Electrochemical oxidation of propene by use of LSM $_{15}$/CGO $_{10}$ electrochemical reactor", *Journal of the Electrochemical Society*, **159,** P57-P64 (2012);

**Chapter 5:** the effect of $CeO_2$ and $Ce_{0.8}Pr_{0.2}O_{2-\delta}$ infiltration on the catalytic activity for propene oxidation and electrochemical behavior of the LSM/CGO reactor is described and discussed in this chapter. These experimental results and discussion are part of the published paper: "Effect of infiltration material on a $LSM_{15}/CGO_{10}$ electrochemical reactor in the electrochemical oxidation of propene", *Journal of Solid State Electrochemistry ,***17,** 895-908 (2013);

**Chapter 6:** the effect of $Ce_{0.9}Gd_{0.1}O_{1.95}$ infiltration on the catalytic activity for propene oxidation and electrochemical behavior of the LSF/CGO reactor is described and discussed in this chapter;

**Chapter 7:** in this chapter the catalytic activity for propene oxidation and the electrochemical behavior of a LSM/CGO reactor with improved porosity is described and discussed. A manuscript containing these experimental results and discussion was submitted to the *Electrochimica Acta* with the title: "Impedance Spectroscopy and Catalytic Activity Characterization of a LSM/GDC Electrochemical Reactor for the Oxidation of Propene".

**Chapter 8:** the effect of $Co_3O_4$ and $Co_3O_4/CeO_2$ infiltration on the catalytic activity for propene oxidation and electrochemical behavior of the LSM/CGO reactor with high porosity is described and discussed in this chapter.

**Chapter 9:** this chapter contains the overall discussion, conclusions and outlook.

## References

1. R. Atkinson, *Atmospheric Environment*, **34**, 2063–2101 (2000)

2. European Environment Agency, *Air pollution by ozone across Europe during summer 2012*, (2013).

3. Johnson Matthey A/S, *European Emissions Guide*, (2010) http://ect.jmcatalysts.com/.

4. D. Fino, *Science and Technology of Advanced Materials*, **8**, 93–100 (2007)

5. M. Twigg, *Applied Catalysis B: Environmental*, **70**, 2–15 (2007).

6. D. Fino, *Science and Technology of Advanced Materials*, **8**, 93–100 (2007)

7. F. Klingstedt, K. Eränen, and L. Lindfors, *Topics in catalysis*, **2004**, 27–30 (2004)

8. B. Southward, S. Basso, and M. Pfeifer, *SAE Technical Paper*, **01**, 558 (2010).

9. M. Stoukides and C. Vayenas, *Journal of Catalysis*, **146**, 137–146 (1981)

10. Costas G. Vayenas, S. Bebelis, C. Pliangos, and S. Brosda, *Electrochemical activation of catalysis: promotion, electrochemical promotion, and metal-support interactions*, Kluwer Academic Publishing, (2002).

11. G. Marnellos and M. Stoukides, **175**, 597–603 (2004).

12. A. Katsaounis, *Journal of Applied Electrochemistry*, **40**, 885–902 (2009)

13. F. Gaillard, X. Li, M. Uray, and P. Vernoux, *Catalysis Letters*, **96**, 177–183 (2004).

14. A. Kaloyannis and C. Vayenas, *Journal of Catalysis*, **47**, 37–47 (1999).

15. V. Roche et al., *Ionics*, **14**, 235–241 (2008)

16. A. Kambolis et al., *Electrochemistry Communications*, **19**, 5–8 (2012)

17. W. Wang and M. Mogensen, *Solid State Ionics*, **176**, 457–462 (2005)

18. S. Douvartzides and P. Tsiakaras, *Solid state ionics*, **137**, 849–855 (2000)

19. H. Christensen, J. Dinesen, and H. Engell, *SAE International*, **01**, 1–5 (2000)

20. H. Christensen, J. Dinesen, H. Engell, and K. Hansen, *SAE International*, **01**, 1–5 (1999)

21. S. P. Balomenou et al., *Topics in Catalysis*, **44**, 481–486 (2007).

22. Y. Yoshinobu and Y. Tsuda, *SAE Technical Paper*, **3**, 50–60 (2010)

23. F. Buciuman and F. Patcas, *Applied Catalysis B: Environmental*, **35**, 175–183 (2002).

# 2 MATERIALS

In this chapter an overview of the defect chemistry, electrical properties and catalytic activity of the materials used for the production of the electrochemical reactor is given.
In this work two different electrode composites were studied: $La_{0.85}Sr_{0.15}MnO_3/Ce_{0.9}Gd_{0.1}O_{1.95}$ and $La_{0.85}Sr_{0.15}FeO_3/Ce_{0.9}Gd_{0.1}O_{1.95}$.

## 2.1 Strontium substituted Lanthanum Manganite: $La_{1-x}Sr_xMnO_3$

The $La_{1-x}Sr_xMnO_3$ (LSM), among other materials, has been for many years the most utilized and studied electrode for oxygen reduction reaction in the cathode compartment of solid oxide fuel cells (SOFCs), thanks to the good thermal and chemical compatibility with the electrolyte (YSZ) and the high electronic conductivity shown at SOFC operating temperature (850 °C-1000 °C). LSM belongs to the $ABO_3$ perovskite oxide family, where A and B are large and small cations, respectively. The strontium substitution in the A-site of $LaMnO_3$ enhances the stability, conductivity and catalytic activity of this perovskite. Moreover the LSM shows good catalytic activity for hydrocarbons oxidation and NOx reduction; $La_{0.85}Sr_{0.15}MnO_3$ especially exhibited the highest performance for NOx reduction, between LSM with different Sr doping level (x=0.05-0.5), according to the study of Hansen et al. [1].
These characteristics make the LSM an ideal candidate electrode/catalyst material for the propene electrochemical oxidation coupled with NOx electro-reduction in a porous electrochemical reactor.

### 2.1.1 The unusual nonstoichiometry of $La_{1-x}Sr_xMnO_3$

LSM shows unique features between the perovskite oxides. The most unique feature of the nonstoichiometry of LSM is the existence of an apparent oxygen excess region at high oxygen partial pressures. A simple mixed-valence conductor like $La_{1-x}Sr_xFeO_3$ (LSF) does not exhibit oxygen excess at high $P_{O2}$. Figure 1 shows the nonstoichiometric diagrams as a function of $P_{O2}$ for $La_{1-x}Sr_xFeO_3$ and $La_{1-x}Sr_xMnO_3$. It is possible to observe that, respect to the LSF, the LSM exhibits an apparent oxygen excess (δ) region at high $P_{O2}$.

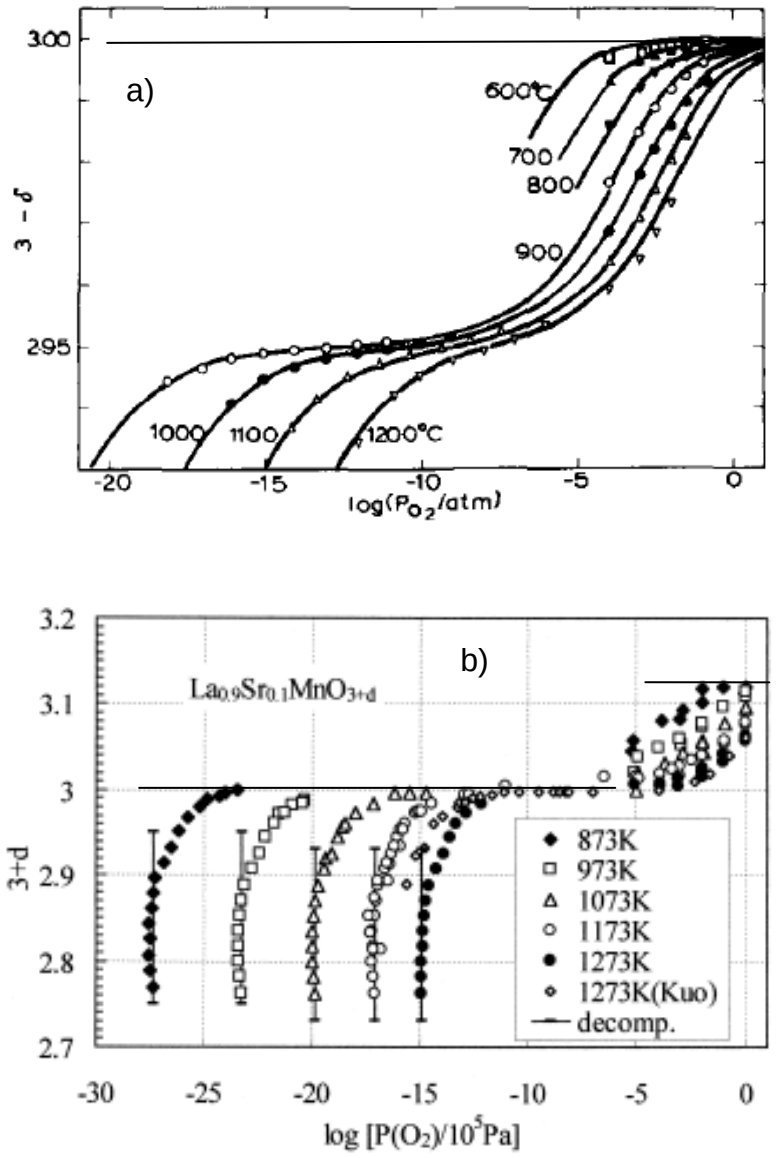


**Figure 1**: oxygen non-stoichiometry diagram as a function of $P_{O2}$ : a) schematic diagram of oxygen non stoichiometry of $La_{0.9}Sr_{0.1}FeO_3$ at different temperatures [2] and b) oxygen non-stoichiometry of $La_{0.9}Sr_{0.1}MnO_3$ as a function of $PO_2$ at different temperatures [3].

In the case of LSM, the oxygen content exhibits two plateaus at stoichiometric oxygen ($\delta$=0) and at oxygen excess (3+$\delta$) corresponding to the $P_{O2}$ of $10^{-10}$-$10^{-5}$ atm and above 1 atm, respectively. This behavior is due to the mixed valence state of the B-site ion of $La_{1-x}Sr_xMnO_3$, At low $P_{O2}$, the oxygen vacancies ($V_o^{\bullet\bullet}$) are created to compensate for the reduction of $Mn^{4+}$ to $Mn^{3+}$ maintaining the charge neutrality; the oxygen deficient nonstoichiometry becomes larger with the increase of Sr content. At high oxygen partial pressure, the oxygen excess is balanced by the formation of metal vacancies, as reported by Mizusaki [3].

### 2.1.2 Electronic and ionic conductivity of $La_{1-x}Sr_xMnO_3$

$La_{1-x}Sr_xMnO_{3+d}$ shows p-type electronic conduction in the entire $P_{O2}$ region in which the solid solution is stable [3].The substitution of $Sr^{2+}$ in the A-site of $La^{3+}$ induced the formation of an electron hole at the B-site in order to maintain the charged neutrality; this behavior induced an increase of electronic conductivity with a maximum at Sr doping of x=0.5, as illustrated in Figure 2.

As described by Poulsen [4], the electron transport in LSM can be formulated as a charge transfer reaction (hopping), where an electron is transferred from a Mn ion, in one oxidation state, to another Mn ion into higher or lower oxidation state. The conductivity is dependent on the concentration products of the Mn ions in the three different oxidation state ($Mn^{4+}$, $Mn^{3+}$ and $Mn^{2+}$). The conductivity is nearly independent from oxygen partial pressure at high $P_{O2}$ where the concentration product between $Mn^{4+}$ and $Mn^{3+}$ is constant, as reported in Figure 2.

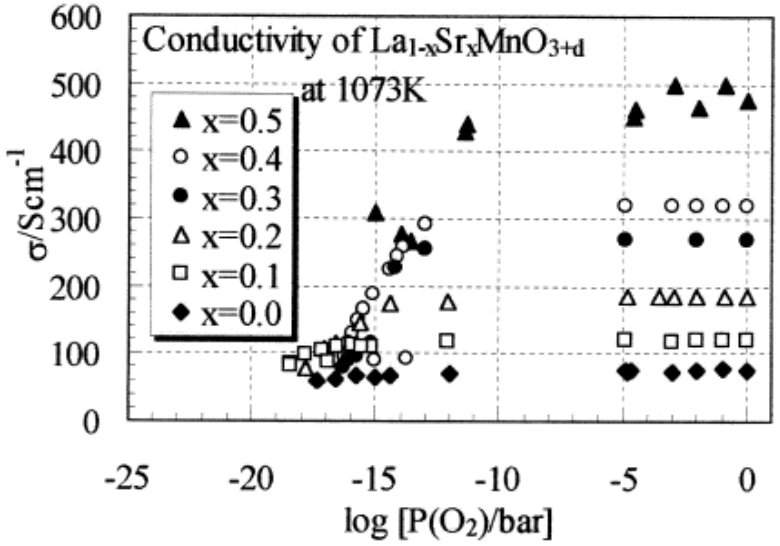


**Figure 2:** $P_{O2}$ dependence of electronic conductivity of $La_{1-x}Sr_xMnO_{3\pm\delta}$ [3]

On the contrary, in the oxygen deficiency range (below $10^{-12}$ atm of $O_2$ at 800 °C), the conductivity is decreasing with decreasing $P_{O2}$ until the instability of LSM structure is reached. Below $10^{-12}$ atm of $O_2$ the product of the concentrations of $Mn^{4+}$ and $Mn^{3+}$ monotonically decreases and never passes through a maximum; this behavior induces a decrease of electronic conductivity.

The LSM exhibits very low ionic conductivity ($5.8\times10^{-8}$ S/cm at 800 °C [5]); this induces high polarization losses in the oxygen reduction reaction and seriously limits the use of

LSM as cathode material for IT-SOFC. The ionic conductivity of $La_{1-x}Sr_xCo_yFe_{1-y}O_3$ (LSCF) for example, is in the order of 0.2 S/cm at 900 °C; this characteristic, together with a similar electronic conductivity if compared to LSM, makes LSCF the most promising cathode material for IT-SOFC. Contrary to the LSM, the LSCF reacts with YSZ already at 800 °C with the formation of a $SrZrO_3$ insulating phase; this behavior forces to the use of a buffer layer of oxygen ion conductor like $Ce_{1-x}Gd_xO_{2-x/2}$ between YSZ and LSCF [6].

### 2.1.3 Activation of $La_{1-x}Sr_xMnO_3$ by cathodic polarization

LSM-based electrodes exhibit activation under cathodic polarization or current passage. The activation is characterized by a strong decrease of electrode polarization resistance or polarization potential after the application of cathodic voltage or current. This behavior is reversible when the LSM electrode is subjected to anodic polarization.

There is no general agreement on the mechanism of LSM activation and its hysteretic behavior. The most common mechanism used to explain this phenomenon is the reduction of Mn species of LSM with cathodic polarization but, why this should result in an increased electrode performance is still unclear.

Chen et al.[7] studied the effect of anodic and cathodic current passage on a $La_{0.85}Sr_{0.15}MnO_3$ electrode deposited on an YSZ electrolyte by using impedance spectroscopy and cyclic voltammetry; the test was carried on at 850 °C in air with 0.3 A/cm$^2$ of anodic current. The impedance resistance of the newly prepared LSM electrode was found to decrease under cathodic current treatment, and subsequently increases when subjected to anodic current treatment. The current treatment only influenced the low frequency part of the spectra while it had negligible effect on the high frequency part. The electrochemical behavior was reversible under anodic current. The authors explained the activation of the freshly prepared electrode by the reduction of Mn species and the formation of oxygen vacancies on the LSM surface, according to the following reactions:

$$O^x_{O,LSM} + 2Mn^{\bullet}_{Mn,LSM} + V^{\bullet\bullet}_{O,YSZ} + 2e^- \leftrightarrow O^x_{O,YSZ} + 2Mn'_{Mn,LSM} + V^{\bullet\bullet}_{O,LSM} \quad [1]$$

$$O^x_{O,LSM} + 2Mn^x_{Mn,LSM} + V^{\bullet\bullet}_{O,YSZ} + 2e^- \leftrightarrow O^x_{O,YSZ} + 2Mn'_{Mn,LSM} + V^{\bullet\bullet}_{O,LSM} \quad [2].$$

where $V^{\bullet\bullet}_{O,YSZ}$ and $V^{\bullet\bullet}_{O,LSM}$ are oxygen vacancies of YSZ and formed on the LSM surface, respectively; $Mn'_{Mn,LSM}$, $Mn^{\bullet}_{Mn,LSM}$, $Mn^{x}_{Mn,LSM}$ are $Mn^{2+}$, $Mn^{4+}$ and $Mn^{3+}$ respectively. $O^{x}_{O,LSM}$ and $O^{x}_{O,YSZ}$ are the $O^{2-}$ in the LSM and YSZ lattice site, respectively.

According to Chen´s study the oxygen vacancies formation would increase the active sites on the LSM surface, enhancing the oxygen dissociative adsorption on the electrode surface and the oxygen species surface diffusion from the LSM to the three phase boundary.

Wang et al.[8] studied the activation mechanism of a A-site substoichiometric $(La_{0.8}Sr_{0.2})_{0.9}MnO_3$ deposited on YSZ, by using impedance spectroscopy. The electrode was tested in air at 800 °C with the application of 200 mA/cm$^2$ of cathodic current. The effect of cathodic current was to strongly reduce the polarization resistance of the electrode; particularly, the low frequency region of the impedance spectra was affected, showing one order of magnitude increase of characteristic time frequency. The application of anodic current brought the polarization resistance to the initial value of the freshly prepared sample. Similar to that observed under cathodic polarization, the effect of anodic polarization was primarily visible on the low frequency resistance in the impedance spectra.

Further tests in the Wang´s work showed that the cathodic current passage on a HCl weak acid-etched LSM electrode induced a decrease of polarization resistance much lower if compared with the LSM electrode without acid-etching. Since the acid-etching would be able to remove the SrOx and MnOx species on the LSM surface, Wang evidenced the critical role of these inhibiting species on LSM electrode performance.

The removal of SrOx and MnOx upon cathodic polarization could be the cause of the strong initial decrease of polarization resistance exhibited by the LSM; the removal of SrOx and MnOx could enhance the oxygen dissociative adsorption/diffusion process on LSM surface and a further cathodic treatment will bring to the generation and propagation of oxygen vacancies.

Ricoult et al. [9] studied the surface chemistry of operating $La_{0.8}Sr_{0.2}MnO_3$/YSZ cathode by *in-situ* photoelectron microscopy at oxygen partial pressure of $10^{-6}$ mbar at 650 °C. Under anodic polarization or at OCV the Mn ions in LSM adopted an oxidation state of +4. On the contrary, at cathodic polarization lower than -1 V the $Mn^{2+}$ specie reached very high concentration value and strongly migrated to the YSZ electrolyte surface; this behavior resulted into an increase of cathodic current density, as normally observed under LSM electrochemical activation.

Ricoult et al. suggested that the strong enrichment of $Mn^{2+}$ on the electrolyte surface could have induced high electronic conductivity on the YSZ surface and provided a

pathway for the direct incorporation of oxygen from the gas phase directly into the electrolyte.

The cathodic treatment also improves the microstructure and morphology of LSM electrodes that could cause enhance the diffusion of oxygen species [10,11].

Huang et al.[12] studied the effect of different calcination temperatures on the electrochemical performance of a $La_{0.8}Sr_{0.2}MnO_3$ infiltrated cathode on YSZ backbone. The LSM-YSZ composite calcined at 850 °C did not show any activation with polarization, while the composite calcined at 1050 °C and forming a dense layer on YSZ, was activated. The formation of a dense layer on YSZ at high calcination temperature limited the electrode performance because the oxygen species were forced to diffuse through the LSM with very low ionic conductivity. Brief reduction of an LSM–YSZ composite in humidified $H_2$ at 700 °C, produced a decrease in electrode impedance similar to that obtained by electrode polarization. Specific area measurements also showed that reduction introduced microporosity, as evidenced by a large increase in the surface area of the composite. Huang et al. concluded that the formation of microporosity could be induced also by polarization; this behavior will allow oxygen to reach the YSZ interface giving rise to an improvement of electrode performance.

## 2.2 Strontium substituted Lanthanum Ferrite: $La_{1-x}Sr_xFeO_3$

The $La_{1-x}Sr_xFeO_3$ (LSF) has been considered as an alternative cathode material in SOFC and it has been widely studied, as infiltrated cathode on YSZ backbone, by the group of Raymond J. Gorte at University of Pennsylvania.

The electronic conductivity of LSF is lower than that of LSM but still above 80 S/cm at SOFC operating conditions [13]. The lack of electronic conductivity in LSF is compensated by the presence of ionic conductivity, estimated to be $5\times10^{-3}$ S/cm at 800 °C and atmospheric pressure for $La_{0.8}Sr_{0.2}FeO_3$ [14]. At the maximum temperature used in this work (500 °C) the ionic conductivity is estimated to be $0.6 \times 10^{-5}$ S/cm [13], many orders of magnitude higher than that of LSM.

Wang et al. studied the electrode performance of 40% wt $La_{0.8}Sr_{0.2}FeO_3$ infiltrated into YSZ backbone as a function of calcination temperature and test time [15]. No solid state reaction was found between LSF and YSZ with a calcination temperature of 1100 °C or after operation for 1000 h at 700 °C and 700 h at 800 °C. No reactivity was found between $La_{0.8}Sr_{0.2}FeO_3$ and $Ce_{0.9}Gd_{0.1}O_{1.95}$ after 1 week at 1200 °C in air [16].

At our knowledge no specific studies were reported on the catalytic activity of LSF for propene oxidation. With respect to NOx reduction, LSF has shown the ability to reduce

nitrous oxide ($N_2O$) and furthermore reactivity between NO and LSF has been demonstrated [17,18].

### 2.2.1 Nonstoichiometry of $La_{1-x}Sr_xFeO_3$

Typical oxygen nonstoichiometry profile of LSF is shown in Figure 1a. Two plateaus are visible: the first one at δ=0, corresponding to the lattice stoichiometry, and the second for δ<0 corresponding to electronic stoichiometry. In the latter case, the average valence of Fe ions is +3.

### 2.2.2 Electronic and ionic conductivity of $La_{1-x}Sr_xFeO_3$

The p-type small polaron hopping conduction mechanism was established for LSF conduction by Mizusaki et al [19].

The introduction of SrO into $LaFeO_3$ results in the formation of unstable $Fe^{4+}$ ($Fe^{\bullet}_{Fe}$) p-type carriers responsible for electronic conductivity and of oxygen vacancies ($V_o^{\bullet\bullet}$) for ionic conductivity.

Figure 3 shows the defect concentration diagram as a function of $P_{O2}$ for $La_{0.6}Sr_{0.1}FeO_3$ and $La_{0.75}Sr_{0.25}FeO_3$, as reported by Mizusaki.

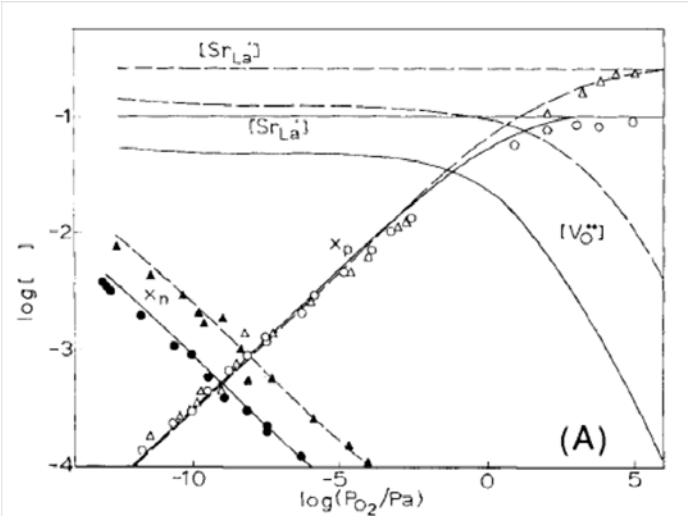


**Figure 3:** Defect concentration diagram as a function of $P_{O2}$ for $La_{0.9}Sr_{0.1}FeO_3$ and $La_{0.8}Sr_{0.2}FeO_3$ at 1000°C[19]

It is possible to observe that the concentration of oxygen vacancies ($V_o^{\bullet\bullet}$) increases with decreasing of oxygen partial pressure up to a plateau that is depending on $Sr^{2+}$ ([$Sr'_{La}$]) doping level. The decrease of oxygen partial pressure also induces a decrease of p-type

carrier concentration ($[Fe^{\bullet}_{Fe}]$ or $x_p$) to a point of a minimum that induces also a minimum of electronic conductivity: this is the point where the stoichiometric composition holds for electronic defects, i.e. $[Fe^{\bullet}_{Fe}]=[Fe'_{Fe}]$. This point corresponds to the plateau of the electronic stoichiometry. The charge carrier concentration is very small and the electroneutrality holds between $V_o^{\bullet\bullet}$ and $Sr'_{La}$. A further decrease of $P_{O2}$ gives rise to an increase of n-type carrier concentration ($[Fe'_{Fe}]$ or $x_n$) with concomitant increase of electronic conductivity. The behavior of electronic conductivity with $P_{O2}$ for $La_{0.9}Sr_{0.1}FeO_3$ is reported in Figure 4.

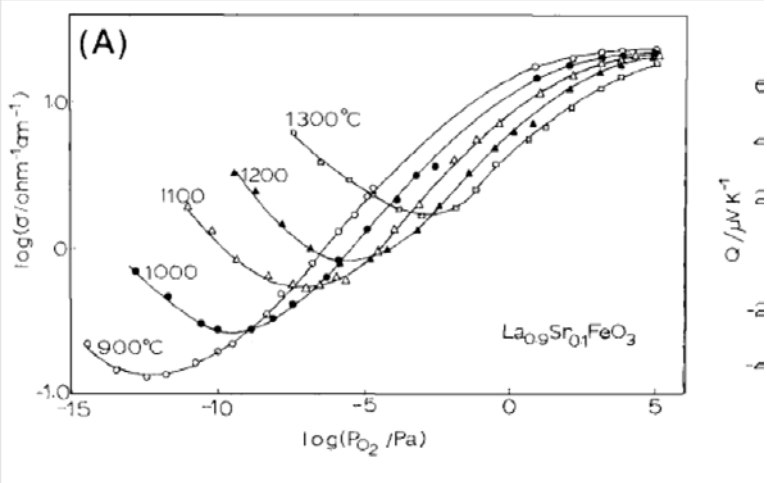


**Figure 4:** Electrical conductivity of $La_{0.9}Sr_{0.1}FeO_3$ as a function of $P_{O2}$ [19]

### 2.2.3 Catalytic activity of perovskite $La_{1-x}Sr_xMnO_3$ and $La_{1-x}Sr_xFeO_3$ in the oxidation of VOCs.

Transition-metal perovskite ($LaMO_3$) (M=Mn,Co,Fe) is a potential alternative to noble metals for catalytic deep oxidation of hydrocarbons [20,21] due to its large amount of non-stoichiometric oxygen, a high concentration of lattice defects and and low cost if compared to noble metals.

Perovskites possess good thermal stability in oxygen and steam rich atmosphere, although preserving a high surface area, while obtaining the perovskite structure is a challenge. Despite many advantages shown in the use of perovskite, their catalytic activity for hydrocarbons oxidation is lower than that of noble metals.

Combustion catalysis on Sr-substituted perovskite oxides involves two oxygen species depending on the reaction temperatures. The suprafacial mechanism prevails at low temperatures (250 °C-300 °C) and involves the reaction of chemisorbed oxygen species (α oxygen) on perovskite oxygen vacancies. In addition, the intrafacial mechanism occurs at higher temperatures (up to 600 °C), when the concentration of adsorbed species

becomes low. The bulk oxygen species in the perovskite lattice (β oxygen) act as oxidizing agents [20].

Spinicci et al.[22] studied the catalytic activity of $LaMnO_3$ and $LaCoO_3$ for the oxidation of acetone, isopropanol and benzene. $LaMnO_3$ showed higher catalytic activity if compared to $LaCoO_3$; the higher catalytic activity was attributed to the high mobility and availability of less anchored oxygen on the surface of $LaMnO_3$ if compared to $LaCoO_3$. The presence of mixed valence state for Mn ($Mn^{4+}$ and $Mn^{3+}$) in $LaMnO_3$ was addressed as the reason for the high mobility of oxygen species on the surface, readily available for VOCs oxidation.

Blasin-Aube´et al.[23] studied the catalytic oxidation of different VOCs on $La_{0.8}Sr_{0.2}MnO_3$. According to their study, in the case of VOCs, the activation and cleavage of the weakest C-H bond is the rate determining step for their oxidation. The presence of chemisorbed oxygen on the neighboring site would be sufficient to carry out the VOCs destruction. Blasin-Aube´ et a.l found a linear correlation between the temperature at which 50% of VOCs conversion was reached ($T_{50\%}$) and the bond strength of the weakest C-H bond. Two different slopes were found for linear hydrocarbons and cyclic and aromatic hydrocarbons. The bond strength of the weakest C-H bond seems to be a key parameter for determining the reactivity of the different VOCs.

Few specific studies have been published for the deep oxidation of propene on Sr-doped $LaMnO_3$.

Buciuman et al.[24] studied the catalytic properties for propene oxidation of $La_{0.8}A_{0.2}MnO_3$ as function of A-site substitution with Sr, Ba, K and Cs in the presence of steam in the reaction atmosphere. The Sr substitution exhibited the highest activity for propene oxidation. This behavior was explained by the ability of Sr doping to reduce the oxygen nonstoichiometry (δ) of $LaMnO_{3\pm\delta}$ keeping the $Mn^{3+}/(Mn^{3+}+ Mn^{4+})$ ratio stable and consequently improve the oxygen adsorption capability of the perovskite; this appeared to enhance the suprafacial oxidation mechanism at temperatures below 250 °C. The concentration of $Mn^{3+}$ seems to play a fundamental role in the oxygen adsorption for the low temperature suprafacial mechanism.

In agreement with the explanation of the high catalytic activity of $La_{1-x}Sr_xMnO_3$ for propene oxidation given by Buciuman , Nitadori et al.[25] found that the amount of reversibly oxygen adsorbed on $La_{1-x}Sr_xMnO_3$ increased with the level of Sr doping in the perovskite up to a maximum of strontium doping of x equal to 0.6; the catalytic activity of $La_{1-x}Sr_xMnO_3$ for CO and propane oxidation increased with the increase of the the amount of adsorbed oxygen calculated from temperature desorption experiments.

Roche et al. [26] studied the effect of Zr doping in the B site of $La_{0.7}Sr_{0.3}MnO_3$ on the catalytic activity for propene deep oxidation. The sample without Zr doping ($La_{0.7}Sr_{0.3}MnO_3$) demonstrated the highest catalyst activity; the authors argued that the decrease of catalytic activity was due to the decrease in $Mn^{3+}$ concentration and oxygen vacancies formation resulting from Zr doping.

The literature on the use of $LaFeO_3$ or $La_{1-x}SrFeO_3$ for VOCs oxidation is really scarce and this is probably due to the lower catalytic activity of these two perovskite oxides if compared to $LaMnO_3$ and $LaCoO_3$.
Kremenic et al.[27] studied the chemisorption of oxygen in the presence of propene and isobutene for $LaMO_3$ (M=Fe,Mn,Co,Ni, Cr). The total adsorption of oxygen showed a minimum for $LaFeO_3$; the minimum corresponds also to a minimum in the catalytic activity for propene oxidation while $LaCoO_3$ and $LaMnO_3$ exhibited higher oxygen total oxygen adsorption together with higher conversion of propene. The close parallelism between oxygen adsorption and catalytic activity in the combustion of propene and isobutene suggested that these reactions occur through a suprafacial mechanism, in which the adsorbed oxygen is the dominant specie participating in the reaction.
A correlation was proposed between the strength of M-O bond in simple oxides, increasing in the sequence $Co_3O_4<MnO_2<Fe_2O_3$, and the catalytic activity towards propene oxidation [28]: the catalytic activity was found to be improved for the oxides with the lowest M-O bond strength like $Co_3O_4$.
Hexane total oxidation on different perovskites and on $PdO/Al_2O_3$ was studied by Spinicci et al.[29] $LaFeO_3$ exhibited lower catalytic activity if compared to $LaMnO_3$ and $LaCoO_3$. Although $LaFeO_3$ and $LaCoO_3$ showed similar oxygen desorption profile during TPD, no insight was given for the difference in catalytic activity.
To best knowledge of the author no literature was reported on the catalytic activity of $La_{1-x}Sr_xFeO_3$ for propene oxidation.

## 2.3 Gadolinium doped ceria: $Ce_{1-x}Gd_yO_{2-x/2}$

SOFCs typically operate at temperatures between 800 °C and 1000 °C and utilize electrolyte consisting of yttria stabilized zirconia (YSZ). The operation at this temperature limits the choice of interconnect materials to be used in the stack due to the high corrosion rates and strongly increases the electrode degradation. A decrease of operating temperature to 650 °C or even lower would be beneficial to decrease the rate of electrode and interconnects materials degradation, together with a more rapid start-up and a simplified

thermal management system. The low ionic conductivity of YSZ at 650 °C will strongly increase the ohmic resistance associated with the transport of oxygen ions through the electrolyte.

The electrolytes based on ceria doped with gadolinium or samarium has been used as alternative electrolyte material for IT-SOFC application. These materials exhibit one order of magnitude higher ionic conductivity if compared to YSZ at 600 °C [30].

The chemical stability of ceria and doped ceria with cathode materials, like LSF and LSM, has been demonstrated to be higher than zirconia based electrolytes. Despite these favorable characteristics for use in IT-SOFC, the ceria based electrolytes become mixed conductors in reducing atmospheres typical of anode compartment, due to formation of electronic charge carriers associated with the partial reduction of ceria. This could lead to the presence of electronic conductivity over a large part of the electrolyte extending from the anode [31].

The $Ce_{0.9}Gd_{0.1}O_{1.95}$ (CGO) has been chosen as electrolyte in the electrochemical reactor used in this work thanks to its good ionic conductivity ($0.95 \times 10^{-2}$ S/cm at 500 °C [32]) at low temperatures. Moreover $CeO_2$ and doped ceria have shown good catalytic activity for hydrocarbons oxidation [33,34].

### 2.3.1 Ionic conductivity in Gadolinium doped ceria

The ionic transport takes place through hopping of oxide ions to vacant site and the ionic conductivity is proportional to the concentration of oxygen vacancies ($V_o^{\bullet\bullet}$) up to a maximum of a concentration of $V_o^{\bullet\bullet}$ of 2-5% The total ionic conductivity of pure reduced ceria is usually very low and accounts only for the 3% of the total conductivity at 1000 °C and at $P_{O2}$ of $10^{-6}$ atm, as reported by Mogensen et al. [35].

The doping of ceria with three valent metal oxides, like $Gd_2O_3$, induces the formation of oxygen vacancies ($V_o^{\bullet\bullet}$) as charge compensating defect.

According to Steele, $Ce_{0.9}Gd_{0.1}O_{1.95}$ exhibits higher ionic conductivity if compared to $Ce_{0.9}Sm_{0.1}O_{1.95}$ or $Ce_{0.887}Y_{0.113}O_{1.943}$ and also $Ce_{0.8}Gd_{0.2}O_{1.05.}$

The total ionic conductivity is the sum of the contributions from the bulk conductivity and the grain boundaries conductivity in series. The grain boundaries conductivity is at least two orders of magnitude lower than the corresponding bulk conductivity. Perez-Coll et al. re-examined the bulk and grain boundary conductivities of $Ce_{1-x}Gd_xO_{2-x/2}$ by using impedance spectroscopy in air and studied the effect of Co addition as sintering agent on the conductivity [36]. Perez-Coll´s study reported a decrease of bulk ionic conductivity with increasing Gd content; this was due to the increase interaction of $V_o^{\bullet\bullet}$ with aliovalent

additive (Gd) limiting the oxygen ion mobility, particularly at the lowest temperatures, where the interaction is stronger.

Figure 5 shows the total and bulk conductivity as function of Gd content at 400 °C, as reported by Perez-Coll.

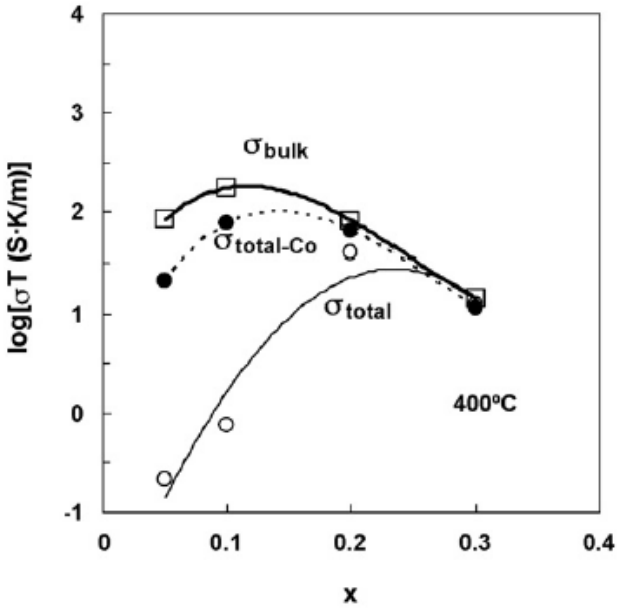


**Figure 5:** Bulk and total conductivity for Ce1-xGdxO1.95 as function of Gd concentration at 400 °C [36]

It is possible to observe in Figure 5 that the maximum in bulk conductivity was reached for doping of Gd close to 10%, but the total ionic conductivity was strongly decreased by the low grain boundary conductivity. The grain boundaries effect became less severe for high concentration of Gd. The addition of Co did not change the bulk conductivity but helped to increase the grain boundaries conductivity making the total conductivity approaching the bulk conductivity.

As verified by Perez-Coll, nanocrystalline (120 nm) $Ce_{0.9}Gd_{0.1}O_{1.95}$ showed higher grain boundaries resistivity if compared to micrometric $Ce_{0.9}Gd_{0.1}O_{1.95}$; the increase of grain boundaries resistance was attributed to the effect of smaller grain size of nanosized CGO [37].

### 2.3.2 Catalytic activity of $CeO_2$ and doped $CeO_2$ for hydrocarbons oxidation

One of the important catalytic properties of $CeO_2$ is its ability to deeply oxidize hydrocarbons along with carbon monoxide. The oxidation properties of ceria are related to the $Ce^{4+}/Ce^{3+}$ electrochemical potential of 1.61 V meaning that $Ce^{4+}$ species are strong oxi-

dizing agents. Both paraffin and unsaturated hydrocarbons are totally oxidized on ceria between 300 °C and 500 °C [38].

Morooka et al. [28,33] evidenced the ability of ceria in the total oxidation of acetylene, ethylene, propene, isobutene and propene. Although ceria was active, the catalytic activity for hydrocarbons deep oxidation was reported to be one or two order lower than that of transition metal oxide [38].

As reported by Trovarelli et al.[39], ceria is seldom used alone as catalyst but preferably in combination with noble metals and thermally stable supports. Ceria functions as electronic/structural promoter or as co-catalyst, like in the catalytic converters for spark and Diesel engines flue gas purification, but not as true catalyst although the load of ceria in certain catalyst formulations can reach 20-30% weight.

In the case of VOCs oxidation, ceria is usually coupled to noble metals like Pt, Pd and Rh [40] showing superior catalytic performance compared to metal like Au on $CeO_2$ [41] or metal oxides like $Co_3O_4$ on $CeO_2$ [42,43]. The ceria or doped ceria compounds are rarely used alone as catalysts also for VOCs oxidation. Zhao et al. [44] studied the catalytic activity of $CeO_2$ and Samaria doped ceria ($Ce_{0.95}Sm_{0.05}O_3$-SDC) for methane, ethane, propane and n-butane oxidation. The rates for methane and ethane oxidation were found to be very close over the two catalysts, while the rates for propane and n-butane oxidation were much higher on ceria compared to Samaria doped ceria. The light-off curves carried on for methane and n-butane oxidation using the two catalysts showed a low temperature process for n-butane oxidation on $CeO_2$ and not observed for methane oxidation; that process was not visible when SDC was used. This suggested that there was an additional mechanism over $CeO_2$ that was not important in the case of methane oxidation and made $CeO_2$ a good catalyst for n-butane oxidation comapred to SDC. The important conclusion drawn by the authors is that the general assumption that doping $CeO_2$ increases its reactivity is not generally correct and that the catalytic activity of $CeO_2$ or doped ceria compounds is strongly dependent on the type of hydrocarbon to be oxidized.

## References

1. K. Hansen, H. Christensen, and E. Skou, *Ionics*, **6**, 340–345 (2000) 2. J. Mizusaki, M. Yoshihiro, S. Yamauchi, and K. Fueki, *Journal of Solid State Chemistry*, **58**, 257–266 (1985).

3. J. Mizusaki, N. Mori, H. Takai, and Y. Yonemura, *Solid State Ionics*, **129**, 163–177 (2000)

4. F. Poulsen, *Solid State Ionics*, **129**, 145–162 (2000)

5. A. Endo, M. Ihara, H. Komiyama, and K. Yamada, *Solid State Ionics*, **86-88**, 1191–1195 (1996)

6. S. Jiang, *Solid State Ionics*, **146**, 1–22 (2002)

7. X. Chen, *Solid State Ionics*, **167**, 379–387 (2004)

8. W. Wang and S. Jiang, *Solid State Ionics*, **177**, 1361–1369 (2006)

9. M. Backhaus-Ricoult et al., *Solid State Ionics*, **179**, 891–895 (2008)

10. S. Jiang and J. Love, *Solid State Ionics*, **158**, 45–53 (2003)

11. X. . Chen, K. . Khor, and S. . Chan, *Journal of Power Sources*, **123**, 17–25 (2003)

12. Y. Huang, J. M. Vohs, and R. J. Gorte, *Journal of The Electrochemical Society*, **152**, A1347

13. Y. Ren, R. Küngas, R. J. Gorte, and C. Deng, *Solid State Ionics*, **212**, 47–54 (2012)

14. J. M. Vohs and R. J. Gorte, *Advanced Materials*, **21**, 943–956 (2009)

15. W. Wang, M. D. Gross, J. M. Vohs, and R. J. Gorte, *Journal of The Electrochemical Society*, **154**, B439 (2007)

16. J. M. Ralph, C. Rossignol, and R. Kumar, *Journal of The Electrochemical Society*, **150**, A1518 (2003)

17. M. L. Traulsen, F. Bræstrup, and K. K. Hansen, *Journal of Solid State Electrochemistry*, **16**, 2651–2660 (2012)

18. K. K. Hansen, *Materials Research Bulletin*, **45**, 1334–1337 (2010)

19. J. Mizusaki, T. Sasamoto, C. Roger, and Bowen Kent, *Journal of the American Ceramic Society*, **66**, 247–252 (1983).

20. T. Seiyama, *Catalysis Reviews*, **34**, 281–300 (1992).

21. N. Yamazoe and Y. Teraoka, *Catalysis Today*, **8**, 175–199 (1990).

22. R. Spinicci, M. Faticanti, P. Marini, S. De Rossi, and P. Porta, *Journal of Molecular Catalysis*, **197**, 147–155 (2003).

23. V. Blasin-Aubé, J. Belkouch, and L. Monceaux, *Applied Catalysis B: Environmental*, **43**, 175–186 (2003).

24. F. Buciuman and F. Patcas, *Applied Catalysis B: Environmental*, **35**, 175–183 (2002).

25. T. Nitadori, S. Kurihara, and M. Misono, *Journal of Catalysis*, **98**, 221–228 (1986)

26. V. Roche et al., *Applied Catalysis A: General*, **385**, 163–169 (2010)

27. G. Kremenic and J. Nieto, *Journal ofChemical. Society., Faraday Transactions…*, **81**, 939–949 (1985)

28. Y. Morooka and a Ozaki, *Journal of Catalysis*, **5**, 116–124 (1966)

29. R. Spinicci, A. Tofanari, and M. Faticanti, *Journal of Molecular Catalysis*, **176**, 247–252 (2001).

30. J. W. Fergus, *Journal of Power Sources*, **162**, 30–40 (2006)

31. G. Christie and F. Van Berkel, *Solid State Ionics*, **83**, 17–27 (1996)

32. B. C. H. Steele, *Solid State Ionics*, **129**, 95–110 (2000).

33. Y. Moro-Oka, Y. Morikawa, and A. Ozaki, *Journal of Catalysis*, **32**, 23–32 (1967)

34. S. Zhao and R. J. Gorte, *Applied Catalysis A: General*, **248**, 9–18 (2003)

35. M. Mogensen, N. M. Sammes, and G. A. Tompsett, *Solid State Ionics*, **129**, 63–94 (2000).

36. D. Pérez-Coll, P. Núñez, J. C. Ruiz-Morales, J. Peña-Martínez, and J. R. Frade, *Electrochimica Acta*, **52**, 2001–2008 (2007)

37. D. Pérez-Coll and G. C. Mather, *Solid State Ionics*, **181**, 20–26 (2010).

38. A. Trovarelli, *Catalysis by Ceria and Related Materials*, Imperial College Press, (2002), p. 408–410.

39. A. Trovarelli, C. de Leitenburg, M. Boaro, and G. Dolcetti, *Catalysis Today*, **50**, 353–367 (1999)

40. L. F. Liotta, *Applied Catalysis B: Environmental*, **100**, 403–412 (2010)

41. S. Scirè, S. Minicò, C. Crisafulli, C. Satriano, and A. Pistone, *Applied Catalysis B: Environmental*, **40**, 43–49 (2003).

42. L. F. Liotta et al., *Applied Catalysis A: General*, **347**, 81–88 (2008)

43. L. F. Liotta et al., *Catalysis Letters*, **127**, 270–276 (2008)

44. S. Zhao and R. J. Gorte, *Applied Catalysis A: General*, **277**, 129–136 (2004)

# 3 INSTRUMENTS

In this chapter an overview is given of the experiments used to characterize the catalytic and electrochemical properties of the electrochemical reactor for propene oxidation. The chapter includes the detailed description of the test set-up, the fabrication of the sample and the techniques used to investigate the catalytic, electrochemical and structural characteristics of the electrochemical reactor.

## 3.1 Fabrication of porous reactor

The reactor used in this study was ceramic and made of 11 alternating layers of electrode and electrolyte to form 5 single cells. The electrolyte tape was made of $Ce_{0.9}Gd_{0.1}O_{1.95}$ (CGO) purchased from Rhodia, while the electrode was made of a 35% weight $Ce_{0.9}Gd_{0.1}O_{1.95}$ and 65% weight of $La_{0.85}Sr_{0.15}FeO_3$ (LSF) purchased from American Elements or $La_{0.85}Sr_{0.15}MnO_3$ (LSM) purchased from Haldor Topsøe. For the fabrication of the electrode, LSF or LSM and CGO were mixed with binder, dispersant and pore former; the slurries were ball milled before tape casting. The CGO electrolyte was produced following the same procedure of the electrode. Six electrodes and five electrolyte green tapes were laminated together alternatively. Round cells were stamped with a diameter of 18 mm. The cells were then sintered at 1250 °C for 2 h.The heat treatment was able to burn the pore former and generate the desired porosity. Before any test was carried on, gold paste with 20% weight graphite was painted on both sides of the porous reactor; the sample was then heat treated at 800 °C for 1 h to remove the graphite and create an adequate porosity to allow reactive gas passage. The deposited gold was used as porous current collector. The gold has been chosen as current collector due to its inactivity towards propene oxidation.

## 3.2 Infiltration

The infiltration of different materials was used in this work to modify the catalytic and the electrochemical properties of the porous electrochemical reactor (backbone). The infiltration (or impregnation) technique has been widely used only in the recent years in the field of solid oxide fuel cells (SOFC) although the infiltration technique of catalyst support like cordierite is well known in the catalyst manufacturing industry.
The objective of the use of this technique in the SOFC field is for example, to increase the electrochemical performance of anode and cathode, protect the anode from sulphur

poisoning and carbon deposition when operated in methane. The effects of active materials infiltration on the electrode performances found in the literature are controversial. They depend simultaneously on different properties like morphology, specific surface area and electrical characteristics; moreover the nanosized particles formed in the electrode structure (backbone) upon infiltration sometime posses completely different and unpredictable catalytic and electrical properties if compared to the bulk material.
The infiltration procedure used in this work involved the following steps:

1. measurement of the sample´s weight;
2. preparation of aqueous solution of nitrate metal salts precursors;
3. addition of surfactant Triton X-100 with 10% weight respect to water;
4. application of the infiltration solution on the sample by using of a pipette until the complete coverage of the sample was obtained;
5. placing the sample in a vacuum chamber followed by application of vacuum to ensure that the precursor solution could reach the inner layers of the porous reactor;
6. removing of the sample from the vacuum chamber and removing excess precursor solution by wipe;
7. heat treatment of the precursor solution to remove nitrates and organics and form the desired material phase and morphology;
8. measurement of the sample´s weight after heat treatment to assess the loading of the infiltrated material.

The infiltration was carried on after the gold current collector was painted and heat treated. This permitted to keep the heat treatment of the impregnated material completely independent from the deposition of the current collector. The high temperature of current collector heat treatment (800 °C) could have induced the sintering of the impregnated particles if carried on after the infiltration.
This technique showed good reproducibility in the loading of the infiltrated material.
Further details of the different precursor solutions and heat treatments used in the material infiltration are reported in the experimental part of the Chapters from 4 to 8.

## 3.3 Test set-up for electrochemical and catalytic activity characterization

Figure 1 illustrates the test set-up configuration. The sample was composed of 11-alternating layers of electrode and electrolyte for a total of 5 single cells stacked to form the porous electrochemical reactor. The cell stack behaves as a symmetric cell.

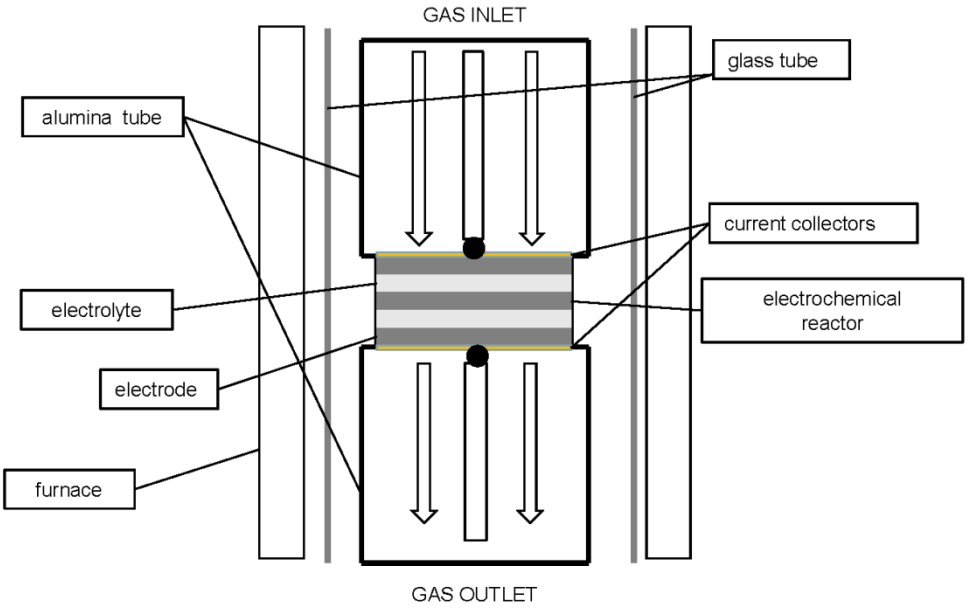


**Figure 1:** Scheme of the reactor configuration

The porous cell stack was mounted in a tubular reactor between two hollow alumina tubes. The alumina tubes contained the measurement probes and allowed the access of the reactive gas to the porous cell. The alumina tubes also permitted the contact between the current collector and the two Pt electrodes which were used as working and reference/counter electrodes under one reactive atmosphere.

The sample and the alumina tubes were placed inside a glass tube surrounded by a furnace. The reactor temperature was monitored by two thermocouples: the Pt measurement probe, directly in contact with the sample, was also used as first thermocouple (T-sample) while the second thermocouple (T-top) was placed 4 mm above the sample. Figure 2 shows the pictures of test set-up together with the detailed image of the place where the cell stack was positioned.

For the catalytic activity and electrochemical evaluation, a mixture of $O_2$ (Air Liquide: 20% $O_2$ ± 2% Ar), $C_3H_6$-propene (Air Liquide: 1% ± 0.02% propene in Ar) and Ar to balance was used with a total flow rate of 2 L $h^{-1}$, unless otherwise specified, controlled by Brooks flow meters.

The reactive gas flow passed through the porous sample where propene was converted to the oxidation products. Reactants and products were analyzed by an on-line gas chromatograph connected to the reactor, as it will be described in 3.4.

This set-up configuration permitted the simultaneous analysis of the outlet gas and the electrochemical properties of the sample.

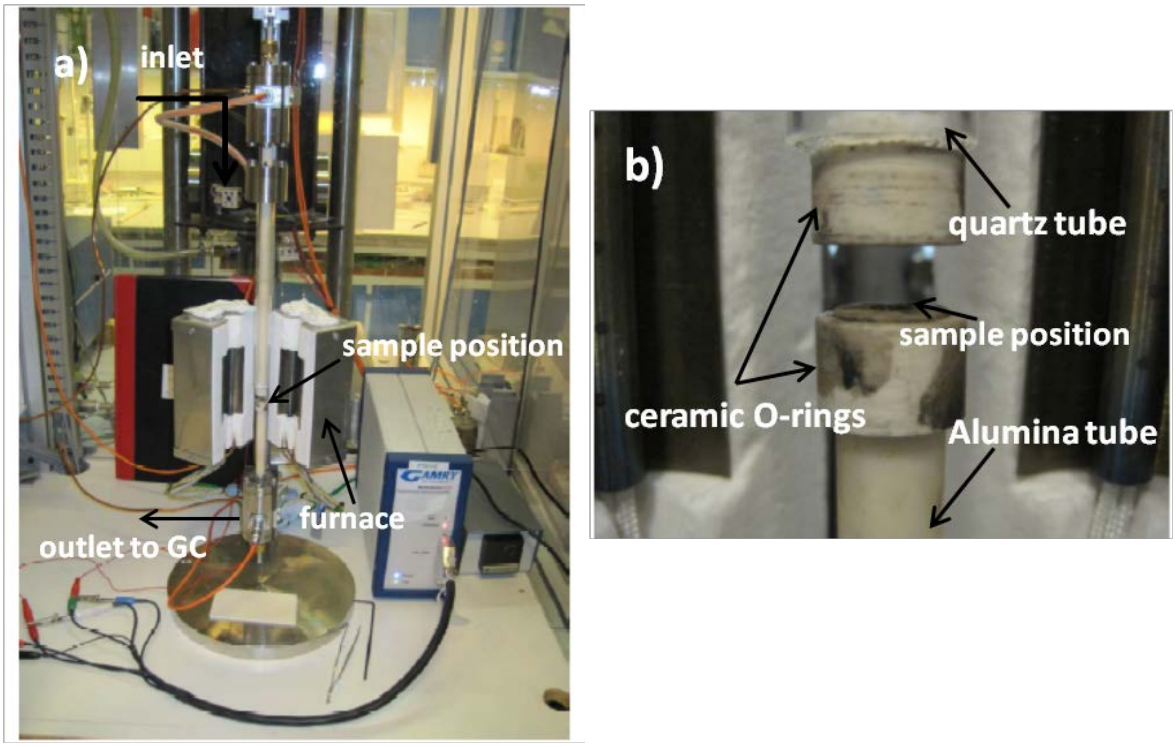


**Figure 2:** a) Image of the whole test set-up and b) zoom on the sample position

Blank gas analysis tests were conducted on the reactor set-up with the presence of 1000 ppm $C_3H_6$ and 10% $O_2$ in the reaction atmosphere at 2 L $h^{-1}$, in order to verify that propene oxidation was not caused by the Pt probes. The blank test showed that the conversion of propene was below 1% at 500 °C without the presence of the sample.

The reaction rate (r) per mol of propene and per gram of catalyst for propene oxidation was calculated using the formula:

$$r = \frac{d}{3600} \times \frac{1}{22.4} \times \frac{273}{298} \times \frac{[C_3H_6]_{inlet}}{10^6} \times \frac{C_3H_6 \text{ conversion}}{100} \times \frac{1}{m_{reactor}}$$

where d is the flow expressed in L/h, $[C_3H_6]$ is the concentration of propene expressed in ppm and $m_{reactor}$ is the total mass of the reactor in grams considered as catalyst.

The propene conversion was calculated using the formula:

$$C_3H_6 \text{ conversion } (\%) = \frac{(P_{CO2} + P_{CO})}{(P_{CO2} + P_{CO} + 3P_{C3H6})} \times 100$$

where $P_{CO2}$, $P_{CO}$ and $P_{C3H6}$ are the partial pressures of carbon dioxide, carbon monoxide and propene in the outlet gas, respectively.

The selectivity to $CO_2$ ($S_{CO2}$) of the propene oxidation was calculated using the formula:

$$S_{CO2}\,(\%) = \frac{(P_{CO2})}{(P_{CO2} + P_{CO})} \times 100$$

The only undesired co-product found for the propene oxidation was carbon monoxide. The carbon mass balance had an error of less than 5%.

## 3.4 Gas Analysis

The composition of the outlet gas from the test set-up was analyzed by on-line gas chromatograph. In this work two different chromatographs have been calibrated and used for gas analysis. The Agilent 6890 N, shown in Figure 3, has been equipped with two packed columns connected in series and a thermal conductivity detector (TCD).

**Figure 3:** Agilent 6890N gas chromatograph

The first column was a Hayesep N for the elution of $CO_2$, $C_3H_6$ and $H_2O$ and the second column was a Molsieve 13X for the elution of CO, $O_2$, Ar.
The Agilent 490 microGC, shown in Figure 4, has been equipped with two capillary columns connected in parallel and two thermal conductivity detectors, one for each column. A Porapak Q capillary column was used for the elution of $CO_2$, $C_3H_6$ and $H_2O$ and a Molsieve 5X was used for the elution of CO, $O_2$, Ar.

**Figure 4:** Agilent 490 micro gas chromatograph

## 3.5 Electrochemical characterization

### 3.5.1 Electrochemical Impedance Spectroscopy (EIS)

A potentiostat (Gamry, reference 600 USA) was used for recording impedance spectra. The open-circuit voltage of the cell was stabilized before every measurement. The impedance spectra were recorded at open-circuit voltage (OCV) and under anodic polarization with root mean square amplitude of 36 mV over the frequency range 0.78 MHz to 5 mHz with 10 or 12 points/decade.

*Impedance Spectra Modeling*

The deconvolution of the impedance spectra was carried on using ZSimpWin [1] or Elchemea [2] Analytical software based on Complex Non-Linear Square (CNLS) fitting. The spectra were validated using the Kramers-Kronig test for causality, linearity and time invariance [3].The inductance coming from the wiring was subtracted for every spectrum to perform the fitting.

### 3.5.2 Analysis of Differences in Impedance Spectra (ADIS)

The ADIS was used to separate the different contributions affecting the impedance spectra upon a change in reaction parameter like propene concentration, oxygen partial pressure and ± 15 °C reaction temperature variation. The application of this technique in this work was based on the Jensen et al. study [4] on solid oxide electrolysis cells.

The method consists in the calculation of the difference between the derivative of the real part of two different spectra ($\Delta\partial Z'(f_n)$) according to the formula:

$$\Delta\partial Z'(f_n)=\{[\Delta Z'(f_{n+1})-\Delta Z'(f_{n-1})]_{\varphi}-[\Delta Z'(f_{n+1})-\Delta Z'(f_{n-1})]_{\varphi^*}\}/[\ln(f_{n+1})-\ln(f_{n-1})]$$

where $\Delta\partial Z'(f_{n+1})$ is the real part of Z at $n$+1 measurement frequency and $[\Delta Z'(f_{n+1})-\Delta Z'(f_{n-1})]$ is the difference between $\Delta\partial Z'(f_{n+1})$ and $\Delta\partial Z'(f_{n-1})$, measured under the specific operating condition φ; φ* represents the reference operating condition.

### 3.5.3 Distribution of Relaxation Times (DRT) Analysis

A polarization process in an electrochemical system can be described by an equivalent circuit made of a parallel connection of an ohmic resistance *R* and a capacitance *C* with a characteristic time frequency of $f = 1/(R\times C)$ and the distribution function of the relaxation times $g(\tau)$ corresponds to a Dirac pulse. More complex systems are characterized by a distribution of relaxation times with a characteristic shape and width and distributed around a main frequency.

The DRT analysis was employed in this work to increase the degree of separation between the processes contained in the impedance spectra and to help in the determination of their number. This method is based on the work of Schichlein et al. [5]. The approach is based on the application of Fourier analysis of the impedance data. In the practical impedance spectrum recording, only a small portion of the spectrum is sampled at certain discrete points. The impedance data frequencies are artificially extended by extrapolation at both high and low frequencies assuming that only one polarization process is still active.

The numerical error amplification caused by the extrapolation is solved by the application of a visual Hanning filter. Adequate extrapolation is crucial to obtain good frequency resolution and to avoid ghost peak, especially at low frequency.

In this work, the DRT analysis was performed using in-house software based on Schichlein et al. work. A visual Hanning filter was used for data filtering, and the filtering values were kept fixed for all analyses.

## 3.6 Reactor and infiltrated material morphology characterization

### 3.6.1 Microscopy

The structure and morphology of the porous reactor and infiltrated materials were examined in a Zeiss Supra 35 electron microscopy equipped with a field emission gun and in a Hitachi TM1000 tabletop microscope. SEM images were recorded in two ways: the sample was simply broken and inserted into the microscope to check the infiltration material morphology while the second way involved the mounting of the porous cell in epoxy resin, polished and carbon coated with the objective to inspect the overall structure of the reactor layers.

### 3.6.2 Specific surface area measurement

Specific surface area (SSA) measurements were performed with Autosorp-1-MP Instrument, by physical adsorption of Kr, using the B.E.T.equation
All the samples were de-gassed for 3 h in vacuum at 300 °C prior to adsorption. The B.E.T. specific surface areas were calculated from the adsorption isotherm keeping the values of the relative Krypton pressure ($p/p_0$) between 0.05 and 0.3 for all the samples.

## References

1. B. Yeum, **ZSimpWin**, Echem Software, 1999-2005.

2. S. Kock, C. Graves, and K. Hansen Vels, **Elchemea Analytica**l ,2012.

3. B. A. Boukamp, **K-K test program**, 1999.

4. S. H. Jensen, A. Hauch, P. V. Hendriksen, and M. Mogensen, *Journal of The Electrochemical Society*, **156**, B757 (2009)

5. M. Voigts, A. Kru, H. Schichlein, and A. C. Mu, *Journal of Applied Electrochemistry*, 875–882 (2002).

# 4 ELECTROCHEMICAL OXIDATION OF PROPENE BY USE OF $LSM_{15}/CGO_{10}$ ELECTROCHEMICAL REACTOR

## 4.1 Abstract

The propene catalytic oxidation was studied over an 11-layers porous electrochemical reactor made by $La_{0.85}Sr_{0.15}MnO_3$ and $Ce_{0.9}Gd_{0.1}O_{1.95}$ with the objective to simulate the abatement of exhaust gases emitted from Diesel engines.

This work shows the possibility to enhance the catalytic activity through infiltration of $Ce_{0.9}Gd_{0.1}O_{1.95}$ using the porous electrochemical reactor as a catalyst support.

The infiltration of an oxygen ion conductor as $Ce_{0.9}Gd_{0.1}O_{1.95}$ showed an increased catalytic activity either at open circuit voltage (OCV) or under polarization with respect to the non infiltrated cell. The use of infiltration permitted to maintain high the effect of polarization also at low temperatures. The electrode was found to be strongly affected by morphology of infiltrated material and long term polarization brought about to an increase of catalytic activity.

Moreover the phenomenon of electrochemical promotion of catalysis (EPOC) was found at low temperature.

## 4.2 Introduction

Electrochemical oxidation of hydrocarbons is a potential method for post-treatment of exhaust gases from Diesel engines and for the improvement of hydrocarbons catalytic combustion. Typical catalysts are supported Pt or Pd and single or mixed metal oxides[1]. Despite their good efficiency, these catalysts suffer from sintering through a process involving migration of oxide species, moreover the cost is so high that recovery and recycling phases have been considered [2]. Transition metal perovskites ($LaMO_3$) (M=Mn,Co) are considered as alternative catalysts to noble metals to perform hydrocarbons combustion reactions due to redox properties of the M cation, the presence of lattice defects and weakly bonded oxygen at the surface. They offer good thermal stability in oxygen and steam-rich atmosphere and low cost, although they nowadays present lower efficiencies [3,4]. The catalytic activity of the perovskites towards light hydrocarbons oxidation can be enhanced by the use of the electrochemical promotion of catalysis (EPOC), also called non-faradaic electrochemical modification of

catalytic activity (NEMCA), as demonstrated by Gaillard, Roche et al. [5,6] and Tsiakaras et al. [7]. In those studies the catalyst is normally interfaced with a dense oxygen ion conductor electrolyte, either YSZ or CGO. In this study a porous composite electrode is interfaced with a porous electrolyte with the objective to use this electrochemical device as catalytic filter for Diesel exhaust aftertreatment.

The present work studies the possibility of using an 11-layers porous single chamber electrochemical reactor for propene oxidation, one of the major Diesel emission exhaust gas components [8]. In this work the whole reactor is thought as a catalytic filter with both porous electrolyte and electrode composite. Moreover this work shows the possibility to infiltrate the cell with an ionic conductor. The objective was to enhance the catalytic activity through ceria´s ability to catalyze oxidation reactions [9] and analyze the effect of an increase of three-phase boundary area for the electrochemical reaction. Moreover the reaction mechanism was investigated using electrochemical impedance spectroscopy (EIS) in the temperature range from 350 °C to 500 °C, over the propene auto-ignition temperature.

## 4.3 Experimental

The 11-layers electrochemical reactor (backbone) was prepared by laminating layers of electrode and electrolyte made by tape casting for a total of 5 single cells. The electrolyte tape is made of $Ce_{0.9}Gd_{0.1}O_{1.95}$ (CGO) which was purchased from Rhodia, while the electrode was made by a composite 35% weight of $Ce_{0.9}Gd_{0.1}O_{1.95}$ and 65% weight of $La_{0.85}Sr_{0.15}MnO_3$ (LSM), (Haldor Topsøe). Slurries for tape casting were made from metal oxide powder, solvent, binder and graphite as pore former. The slurries were ball milled before tape casting. The cell was sintered at 1250 °C for 2 h. The average diameter of the cells was 13 mm. The cells were impregnated using a 1.35 M solution of 10% mol $Gd(NO_3)_3$ + 90% mol of $Ce(NO_3)_3$ with or without Triton X-100 as surfactant in order to obtain $Ce_{0.9}Gd_{0.1}O_{1.95}$ ($CGO_{10}$) as infiltrated active material. Solution was prepared with Millipore water, Triton X-100 (Sigma-Aldrich), Gd nitrate hexahydrate (Alfa Aesar) and Ce nitrate hexahydrate (Alfa Aesar). Infiltration was carried out in one step applying vacuum onto the cell after application of impregnation solution. The cell infiltrated only with water solution ($CGO_{10}$-water) was fired at 850 °C for 2 h; the cell infiltrated with water and Triton X-100 ($CGO_{10}$-Tr) solution was fired at 400 °C for 2 h. The weight of the cell was measured before infiltration and after firing in order to estimate the infiltration loading. The infiltration loading was around 4.5 mg of CGO for each cell, equivalent to 2.7 % weight of the cel without infiltration. The weight of the backbone cell was 0.166 g.

Gold paste with 20% weight of carbon was painted on both sides of the electrochemical reactor and used as current collector. The cells´ weights are measured without current collector and the cell area is approximately 1.32 $cm^2$. The sample was mounted in a tubular reactor between two alumina tubes with contact between the gold paste and the two Pt-electrodes used as working and reference/counter electrode in one atmosphere setup as already reported by Werchmeister et al. [10]. The setup was placed inside a glass tube surrounded by a furnace. For the catalytic activity evaluation a mixture of 10% $O_2$ ( Air Liquide; 20% $O_2$ ± 2% in Ar, 1000 ppm propene (Air Liquide; 1% ± 0.02% propene in Ar) and Ar to balance was used with a total flow rate of 2 L h-1 controlled by Brooks flowmeters. Reactants and products were analyzed by an on-line Agilent 6890 N gas chromatograph connected to the reactor and equipped with Hayesep N, Molsieve columns and a TCD detector. The reaction temperature was monitored by two thermocouples one touching the cell and the other one placed 4 mm over the cell.

A potentiostat (Gamry, reference 600) was used to perform chronoamperometry tests and impedance spectra recording. The open-circuit voltage of the cell was stabilized before every measurement. The impedance spectra were recorded at open-circuit voltage and with an anodic bias of +4 V respect to open circuit voltage with an amplitude of 36 mV RMS over the frequency range 0.78 MHz to 5 mHz with 10 points/decade in a a reaction atmosphere of 1000 ppm propene and 10% $O_2$ at 2 L/h.

The impedance spectra were analysed with ZSimpWin 3.21 software using Complex Non-Linear Square (CNLS) fitting. The inductance coming from the wiring was subtracted for every spectrum to perform the fitting. The spectra were validated using the Kramers-Kronig test for causality and time invariance.

The chronoamperometry tests were carried out for 2 h with anodic potentials from +1 V cell to +5 V respect to open-circuit voltage with 1V step followed by cathodic polarization. The temperature range of the measurements was between 350 °C and 500 °C.

The 11-layers reactor morphology and infiltrated particles morphology were characterized with a Zeiss Supra-35 scanning electron microscopy (SEM).

Adsorption/desorption experiments using Krypton were conducted on the backbone and on the infiltrated samples in order to determine the specific surface area (SSA) using the B.E.T. equation. The samples were measured in an Autosorp-1-MP, where all the samples were de-gassed for 3 h in vacuum at 300 °C prior to adsorption. The BET specific surface areas were calculated from the adsorption isotherm keeping the values of the relative Krypton pressure ($p/p_0$) between 0.05 and 0.3 for all the samples. The porosity of the electrochemical reactor was measured by mercury intrusion porosimetry using Micrometrics Autopore IV.

## 4.4 Results and Discussion

### 4.4.1 Structure characterization and catalytic activity measurements

Figure 1 shows the micrograph of the 11 alternating layers of LSM/CGO electrode composite and CGO electrolyte to form the backbone to be infiltrated. The thickness of the cell was around 300 µm.

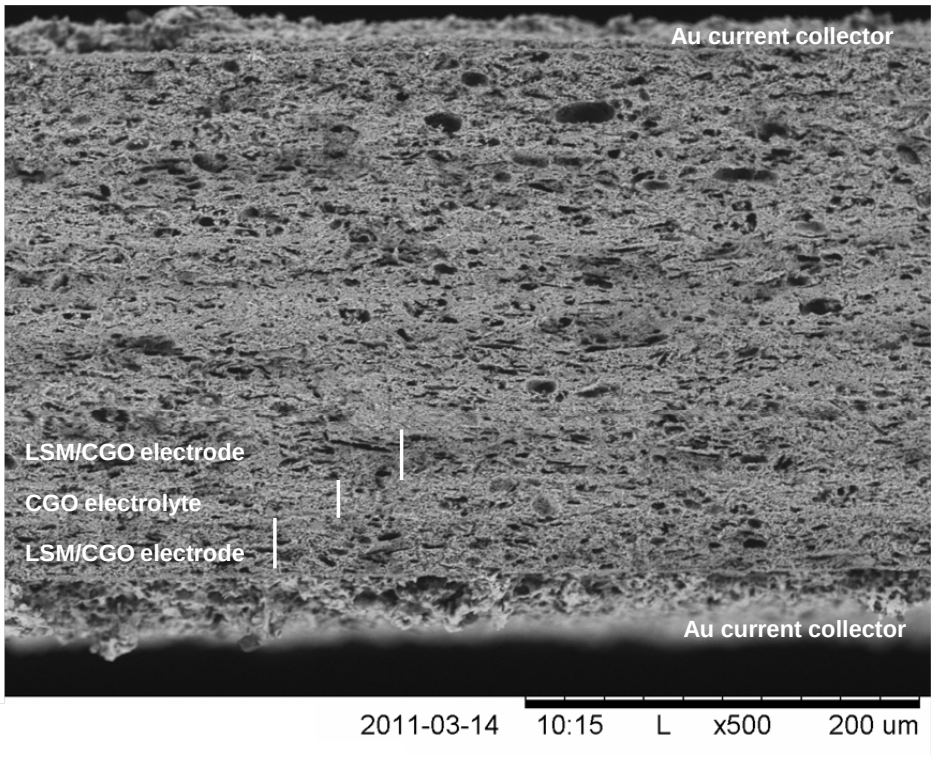


**Figure 1:** SEM micrograph cross section of LSM/CGO 11-layers porous electrochemical reactor.

The electrochemical reactor was porous with a porosity of 39%; more than 90% of the pores size was distributed between 0.1 µm and 1.5 µm with an average pore sizes of 1.12 µm as indicated by mercury porosimetry analysis. The micrograph showed that pores were well distributed in the layers and the adhesion between layers was good without any delamination. The porous gold current collector painted on the top and on the bottom of the cell is also visible in the micro-graph. Figures 2 and 3 show the micrographs of $CGO_{10}$-Tr and $CGO_{10}$-water respectively.

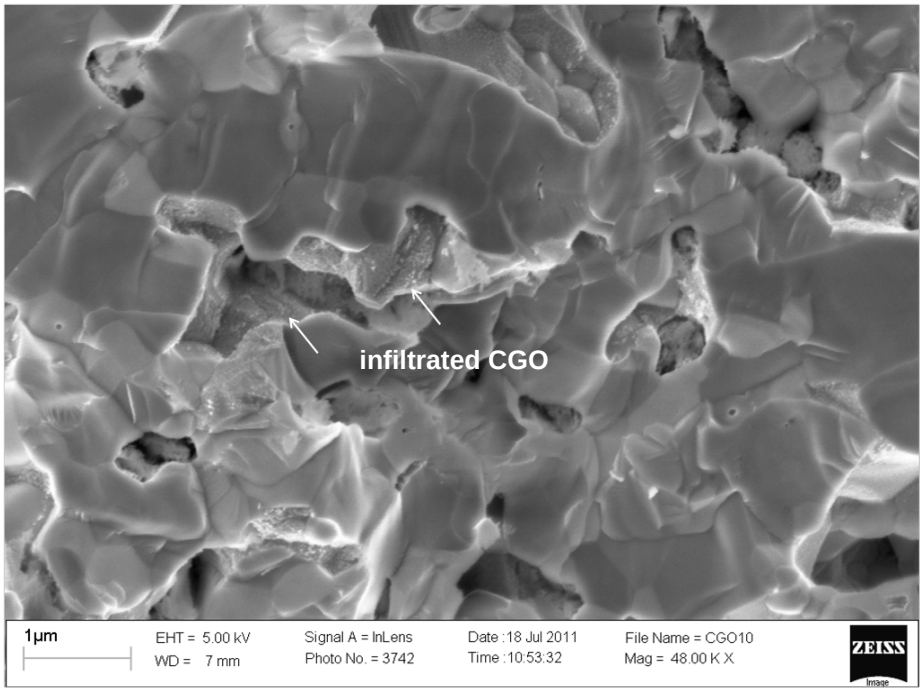


**Figure 2**: Cross sectional SEM micrograph of the backbone cell infiltrated with $CGO_{10}$ precursors solution containing Triton X-100 ($CGO_{10}$-Tr).

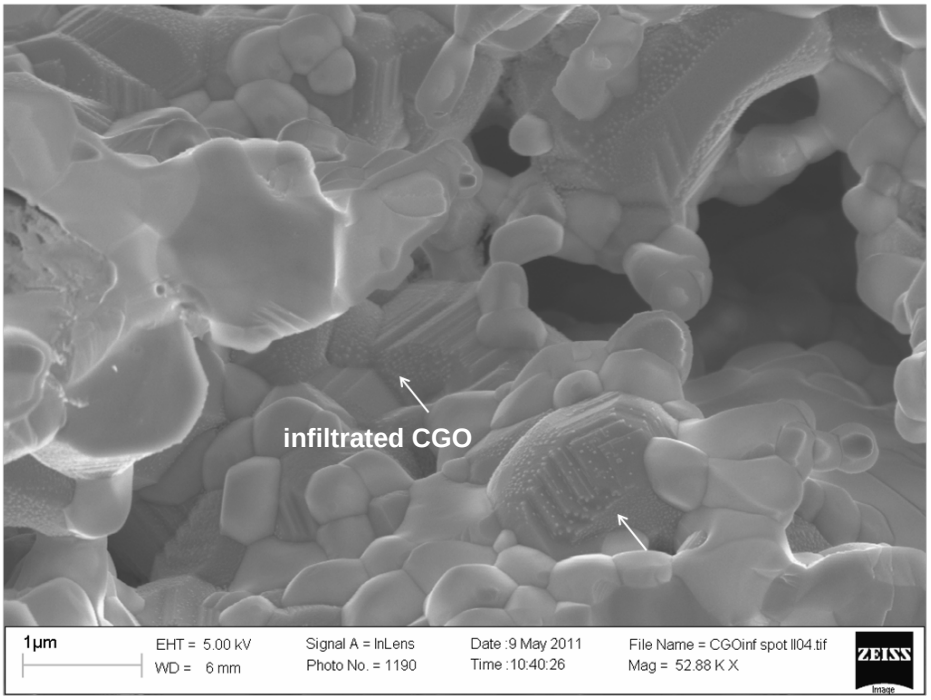


**Figure 3:** Cross sectional SEM micrograph of the backbone cell infiltrated with $CGO_{10}$ precursors ($CGO_{10}$-water)

As it was possible to see from the pictures, in the $CGO_{10}$-Tr cell the distribution of $CGO_{10}$ particles was more uniform. For $CGO_{10}$-Tr cell it was possible to observe the formation of a continuos layer into the pores as indicated by the arrows. Into the $CGO_{10}$-water cell the

infiltrated particles, as indicated by the arrows, appear not to be interconnected and do not show a formation of a continuous layer on both electrode composite and electrolyte.

The $CGO_{10}$ formation is guaranteed by the exhothermicity of surfactant combustion reaction as reported by Blennow et al. [11,12]. The use of Triton X-100 permitted to lower the calcination temperature for CGO formation, to further increase the specific surface area and to create a uniform layer of CGO capable to improve the intrinsic catalytic activity. The specific surface area results are shown in Table 1. Infiltration of $CGO_{10}$ was able to increase the specific surface area of the backbone cell and more catalytic sites were available for propene oxidation.

Figure 4 shows the reaction rates of propene oxidation for the cells as a function of reaction temperatures at open-circuit voltage (OCV).

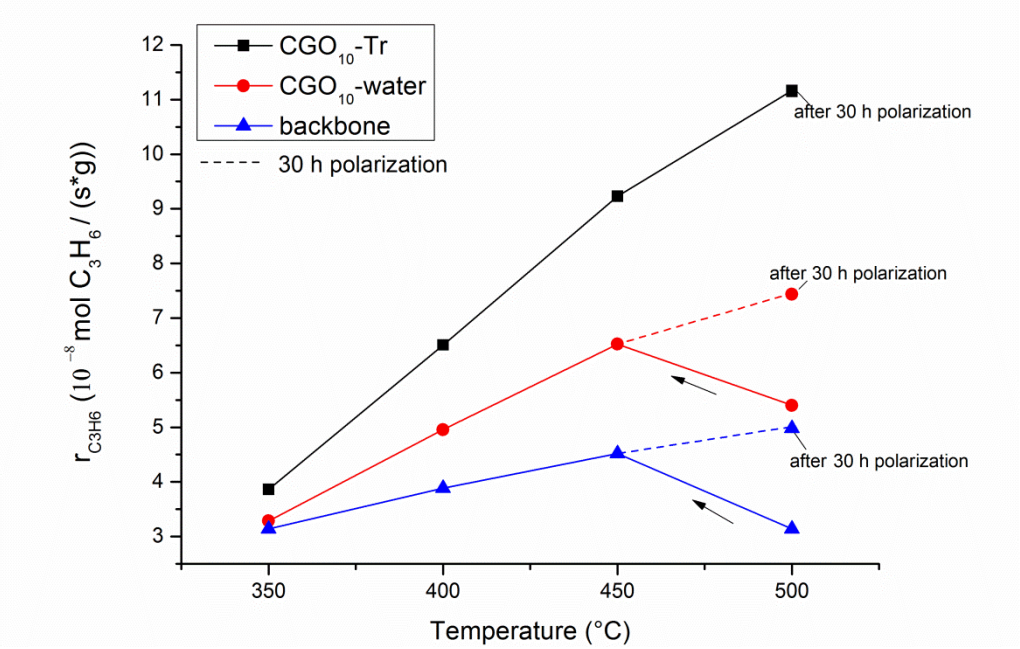


**Figure 4:** Intrinsic catalytic reaction rates for the propene oxidation vs temperature at open circuit voltage. Reaction mixture: 1000 ppm propene, 10% $O_2$, Ar to balance, 2 L/h.

The propene conversion for the backbone cell at 500° C, before the beginning of the chronoamperometry tests, was around 21.3%. The $CGO_{10}$ infiltration increased the conversion up to 40.5% and 83.5% at 500°C for $CGO_{10}$-water and $CGO_{10}$-Tr cell, respectively. The difference between reaction rates decreases with decreasing temperature; the infiltration promoting effect on propene conversion was clearly visible for temperature above 350 °C, where ceria is less susceptible to poisoning by $CO_2$ adsorption [13]. The $CGO_{10}$-Tr cell shows, at 350°C, 29% of propene conversion against 25% and 22% of $CGO_{10}$-water and backbone respectively. The higher reaction rate of $CGO_{10}$-Tr cell respect to $CGO_{10}$-water could be due to the higher uniformity of dispersion

of $CGO_{10}$ infiltrated particles obtained by using lower calcination temperature preventing particles agglomeration, as confirmed by higher specific surface area of $CGO_{10}$-Tr cell shown in Table 1.

| SAMPLE | SPECIFIC SURFACE AREA ($m^2/g$) |
|---|---|
| $CGO_{10}$-Tr | 1.9 |
| $CGO_{10}$-water | 0.45 |
| backbone | 0.17 |

**Table 1**: Specific surface area (SSA) measurements obtained by BET analysis.

As possible to see from the reaction rates profiles in Figure 4, for the backbone and $CGO_{10}$-water cells, the open circuit voltage (OCV) propene oxidation rate is higher at 450 °C than at 500 °C. The experiments started at 500 ºC as first reaction rate characterization test. After one cycle of anodic and cathodic polarization at different voltages, the temperature was lowered to 450ºC in order to carry on the second cycle of polarizations at lower temperature. At this temperature the results of gas chromatographic analysis showed a reaction rate higher with respect to reaction rate measured at 500 ºC. This anomalous behavior was attributed to the effect of the polarization tests that the sample went through at 500 ºC. The activity increase of the catalyst could be due to the oxygen vacancies ($V_o^{\bullet\bullet}$) formation, induced by polarization, according to the mechanism proposed by Wang et al. [14]. The oxygen vacancies formation increases the amount of oxygen from the gas phase adsorbed on the catalyst surface known as α oxygen as described by Ferri et al. for methane combustion over perovskites [15] and responsible for the catalyst oxidation activity. Since the controlling step of propene oxidation reaction is the adsorption of molecular oxygen, the formation of oxygen vacancies by polarization could have improved also the propene oxidation at OCV.

Roche et al. [6] reported that a thin layer of LSM interfaced with YSZ did not recover the intrinsic reaction rate after 7.5 hours of polarization at +4 V resulting in an increased catalyst performance. This effect could be due to the strong modification of the LSM layer upon prolonged polarization. The propene oxidation rate was measured again at 500 °C and OCV, immediately after the end of all chronoamperometry tests carried on at different temperatures with a total duration of about 30 h. This measurement of the reaction rate was carried on to study the effect of prolonged polarization on the reactor OCV catalytic activity. Figure 4 shows clearly an increase of catalytic activity at 500 °C

(OCV) of 58% for the backbone cell and of 38% for $CGO_{10}$-water cell. The $CGO_{10}$-Tr cell infiltrated with Triton X-100 instead did not show any evident activity improvement after 30 h of polarization; this effect could either be hidden by the high activity of the cell or the magnitude of the change could be much smaller, with respect to the other tested cells, given by the stability (covering) effect of uniform $CGO_{10}$ layers as reported by Chen et al. [16]. The specific surface area measured on $CGO_{10}$-Tr cell after the test was around 2 $m^2/g$; the value was very close to the value measured for a fresh cell as reported in Table 1.

It was clear that the catalytic activity of the LSM/CGO porous reactor for the oxidation of propene was strongly influenced by the test hystory and subjected to strong activation due to prolonged polarization; this behavior could be the explanation of the linearity of the reaction rate curves with temperature.

The selectivity to $CO_2$ for the backbone cell was around 90% at 500°C and OCV, CO was formed as a co-product; at the same temperature, $CGO_{10}$-water and $CGO_{10}$-Tr cells exhibited a selectivity to $CO_2$ of 94% and 98%, respectively. The reaction selectivity to $CO_2$ was strongly influenced by the infiltrated material morphology.

Figure 5 shows the $CO_2$/CO concentration ratio for the backbone cell as a function of applied voltage. $CO_2$/CO concentration ratio seems not influenced by polarization at temperatures lower than 500 °C but the $CO_2$/CO ratio together with carbon efficiency are affected by polarization for a temperature equal to 500 °C.

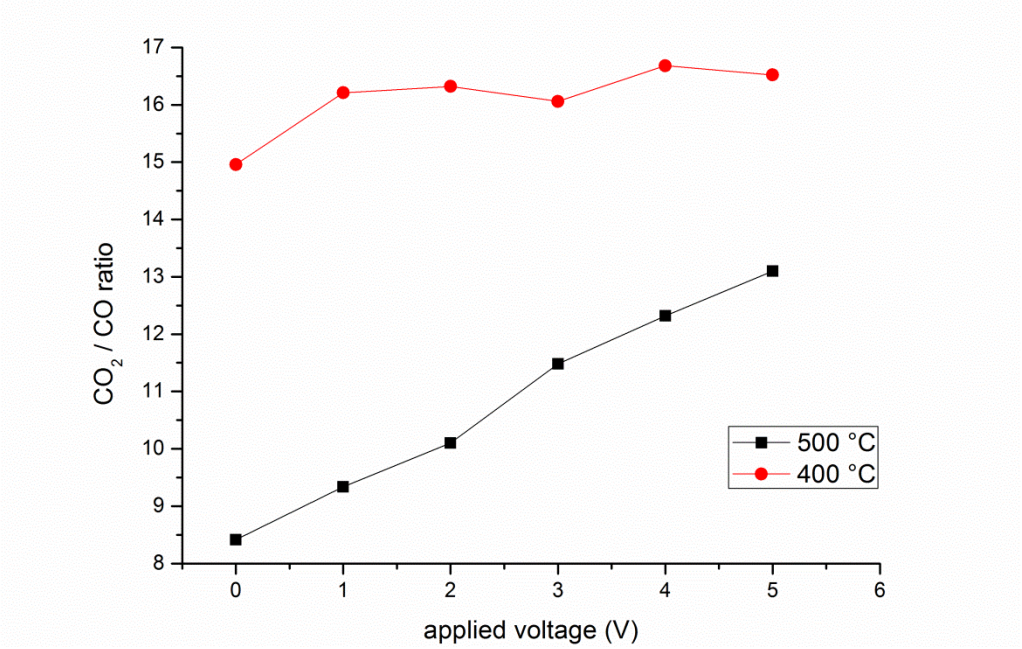


**Figure 5:** $CO_2$/CO concentration ratio as a function of applied voltage for the backbone cell.

This phenomenon could be due to a change in the reaction mechanism as suggested below:

<u>350 °C <T≤ 470 °C</u>

$C_3H_6 + O_{ad,\ gas\ phase} \rightarrow CO+CO_2+H_20$ catalytic reaction on LSM and CGO [1a];

$C_3H_6 + O_{exchanged,TPB} \rightarrow CO+CO_2+H_20$ $O^{-2}$ ions promoted reaction [1b];

<u>470 °C <T≤ 500 °C</u>

$C/CHx + O_{exchanged,TPB} \rightarrow CO+CO_2$ $O^{-2}$ ions promoted front reaction [2a];

At temperatures between 350°C and 470°C and under polarization, it was possible to observe a pure catalytic reaction on LSM and CGO involving both O adsorbed from the gas phase and $O^{2-}$ exchanged at the three-phase boundary (TPB) with anodic polarization, as illustrated by equations 1a and 1b. At this temperature the carbon formation from propene was low and the direct carbon oxidation on the surface by oxygen exchanged and adsorbed at the TPB is not favorable. Instead, at temperatures over the auto-ignition temperature of propene (475 °C) together with the reactions 1a and 1b, the formation of a carbon layer on the catalyst surface was enhanced and this could bring to a direct carbon layers front oxidation reaction carried on by the oxygen ions discharged at the TPB, as illustrated by reaction 2a. This speculation was not confirmed by impedance measurements although some processes could be invisible due to an overlap of different processes characteristic time but it represented an explanation for the dependence of $CO_2$/CO ratio with voltage.

Further reaction tests carried out on the backbone cell with a increased flow rate (3 L/h) show selectivity to $CO_2$ of 100 % at temperature below 500 °C.

Figures 6a and 6b show the effect of polarization on propene reaction rate at 450°C and 350°C, respectively, as a function of the applied voltage. At these temperatures all the three cells were expected to be equally activated by the chronoamperometry tests carried on at 500 °C.

The polarization effect was expressed by using the rate enhancement ratio (ρ) factor defined in the equation 3 as:

$$\rho = r / r_o \qquad [3]$$

where $r$ is the catalytic rate of propene oxidation measured under polarization and $r_0$ is the catalytic rate measured at OCV.

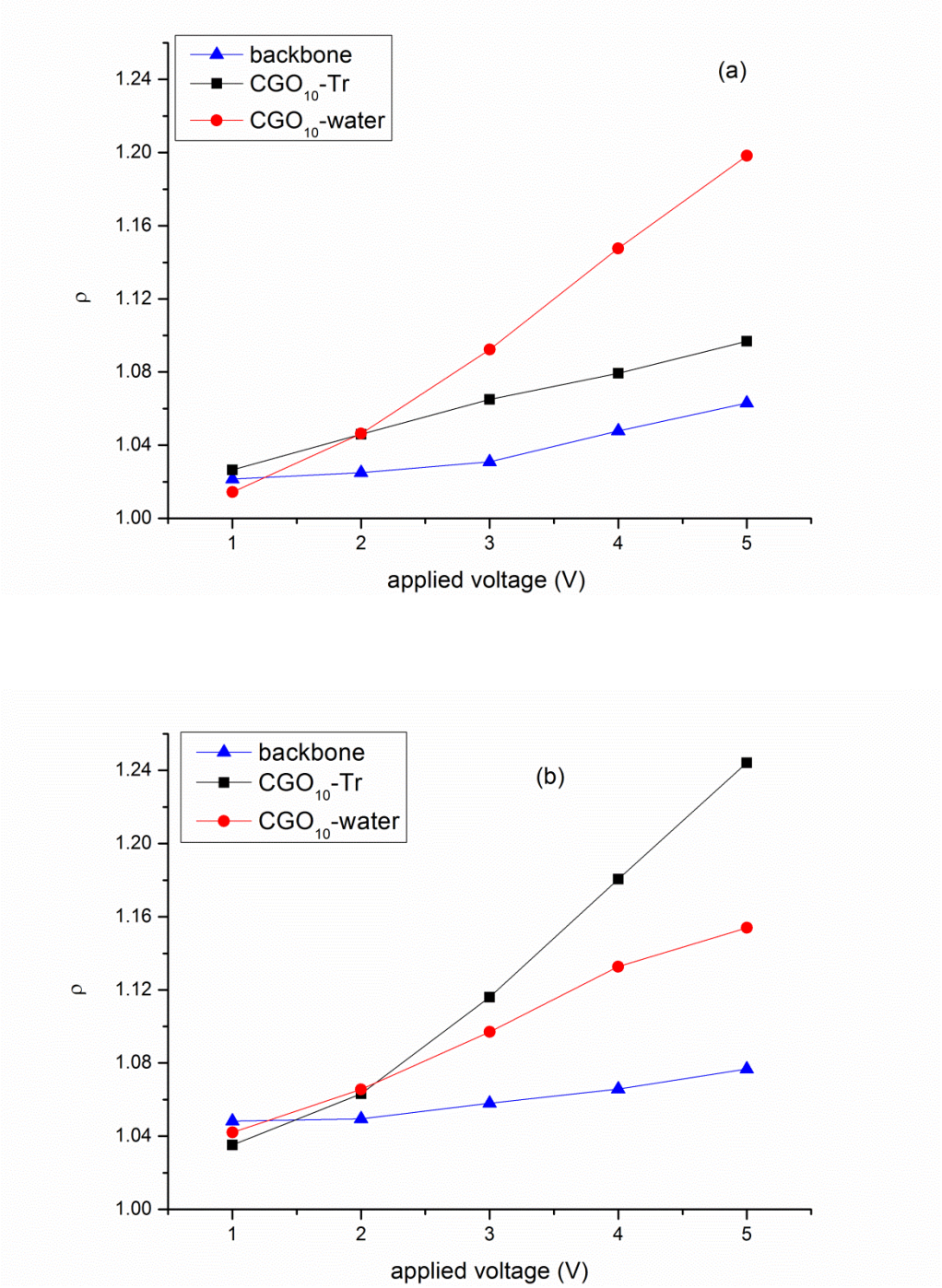


**Figure 6:** Rate enhancement ratio vs applied voltage at different temperatures: a) 450°C , b) 350° C. Reaction mixture: 1000 ppm propene, 10% $O_2$, Ar to balance 2 L/h.

It is possible to observe that the infiltration of $CGO_{10}$ increased the rate enhancement ratio if compared to the backbone cell. While for the backbone cell the effect of polarization flattens decreasing the reaction temperature, the infiltration of $CGO_{10}$ into the backbone is able to maintain high the rate enhancement ratio.

Particularly, the $CGO_{10}$-Tr cell exhibited the highest ρ values at 350 °C; at 450 °C instead, the $CGO_{10}$-Tr showed lower ρ values compared to the $CGO_{10}$-water cell. This

behavior could be due to high conversion of propene shown by the $CGO_{10}$-Tr cell (69%) at 450 °C compared to the the propene conversion exhibited by $CGO_{10}$-water cell (49%). The high conversion of propene could have established a regime of reactants diffusion limitation and inhibited the effect of the polarization on the propene oxidation rate.
Figure 7 reports the faradaic efficiency $\Lambda$ as defined by the in Equation 4 as:

$$\Lambda = \Delta r / I /(nF) \qquad [4]$$

with n=2 is the number of charges carried by the oxygen ion, Δr is the difference between the reaction rate of propene oxidation measured under polarization and the reaction rate measured at OCV expressed as molO $s^{-1}$, I is the current recorded under polarization and F is the Faraday´s constant.
At medium and high temperatures the process was faradaic but the efficiency becomes close to 2.6 for all the samples at 350 °C. The faradaic efficiency values were not high if compared to those observed on precious metals by Vernoux et al. of around -60 [18]. Surprisingly the faradaic efficiency for the backbone cell was 0.95 at 500 °C but decreased to 0.26 when measured again at 500 °C after prolonged polarization for about 30 h. The backbone cell improved its performance both in terms of catalytic activity ($r_0$) and electrode activity (current density) but this was not followed by a concomitant increase of polarization susceptibility of the reaction rate ($r$), giving rise to a decrease of faradaic efficiency. It is worth to highlight that prolonged polarization for 30 hours improved the current density of the backbone cell from 3.2 mA/$cm^2$ to 3.7 mA/$cm^2$.

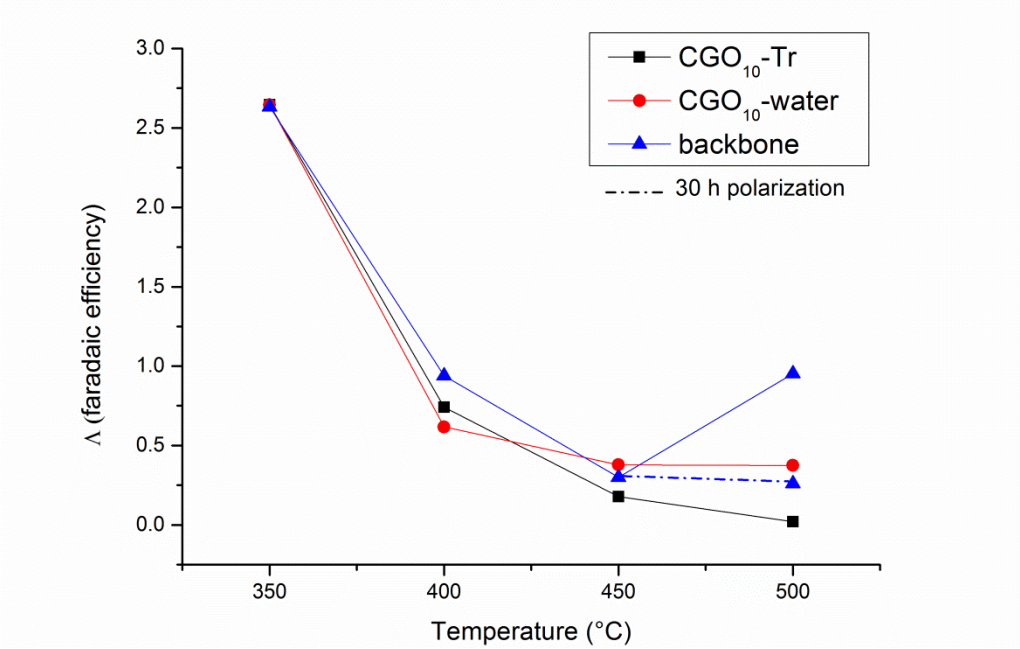


**Figure 7** : Faradaic efficiency values vs temperature under polarization voltage of +4 V. Reaction mixture: 1000 ppm of propene, 10% $O_2$, Ar to balance 2 L/h

### 4.4.2 Electrochemical characterization

Figure 8 displays the Arrhenius plot of the polarization resistance (Rp) of the cells at OCV as extracted by impedance spectra as difference between the intercept value of $Z'$ if $\omega \rightarrow \infty$ and the intercept of $Z'$ if $\omega \rightarrow 0$.The polarization resistance follows the behavior of the intrinsic catalytic activity of the cells. Only one step $CGO_{10}$ infiltration was able to decrease the Rp of one order of magnitude compared to the polarization resistance of the backbone cell.

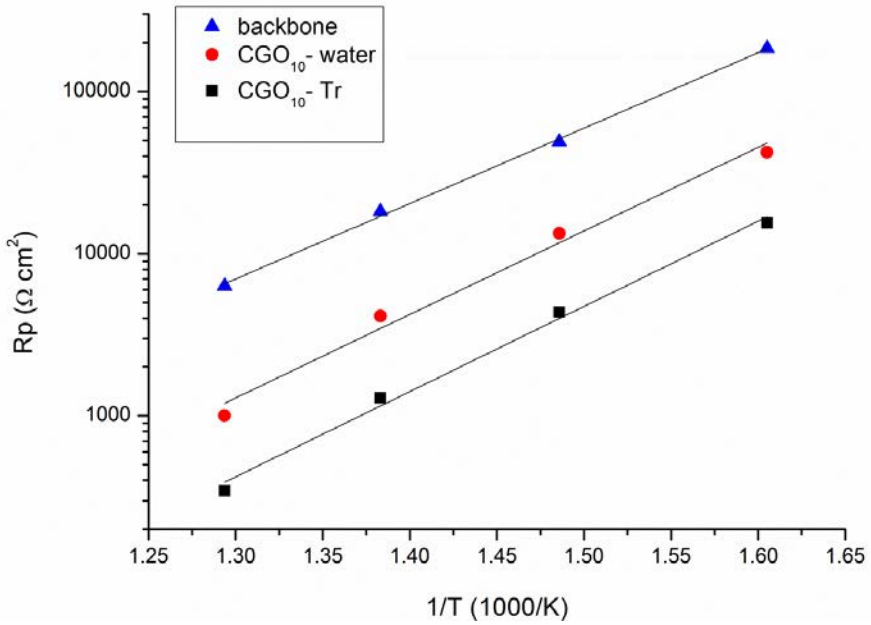


**Figure 8**: Arrhenius plot of polarization resistance (Rp) extracted from impedance spectra measured at open circuit voltage (OCV), 1000 ppm propene + 10% $O_2$, 2L/h.

The Rp activation energy of the backbone cell exhibited a value of 0.92 eV while the $CGO_{10}$ infiltrated cells showed activation energy of 1.04 eV and 1.02 for the $CGO_{10}$-Tr and $CGO_{10}$-water cell, respectively. Due to the close values of the activation energies, it was possible to state that the infiltration of $CGO_{10}$ into LSM/CGO backone did not affect the overall reaction mechanism occuring at OCV.

Figure 9 shows the Arrhenius plot of the Rp under +4 V polarization, as extracted from the impedance spectra. The Rp at +4 V was one order of magnitude lower with respect to the Rp at OCV; the Rp under polarization was similar for $CGO_{10}$-water and $CGO_{10}$-Tr, this could be due to a limiting resistance/current regime reached for the infiltrated cells at +4 V. This behavior agreed well with the Arrhenius plot of the current densities recorded at +4 V for all three samples and shown in Figure 10. Since both infiltrated cells reached similar values of Rp under +4 V polarization, the electrochemical properties of the infiltrated material instead of those of the backbone, could be responsible for polarization behavior under polarization, although an increase of activation of 0.1 eV was detectable for the activation energy of the Rp at +4 V compared to the Rp at OCV.

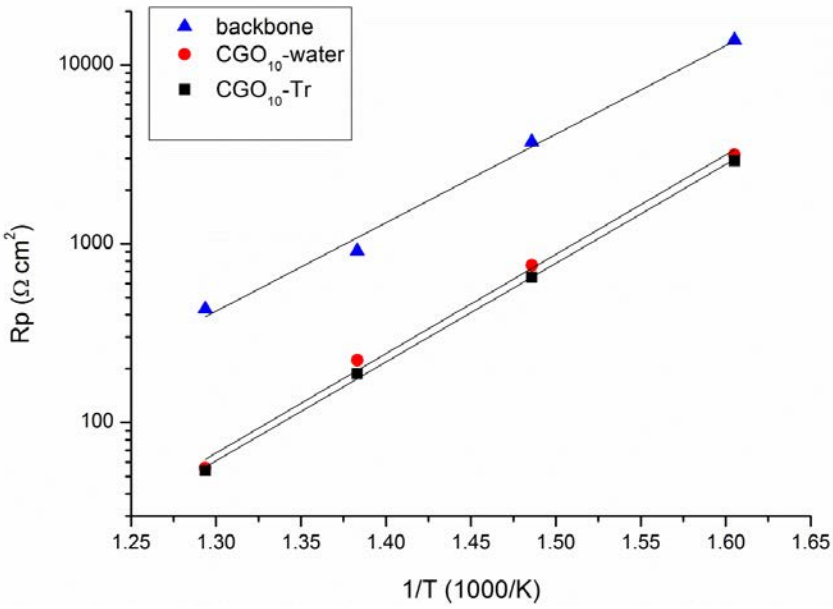


**Figure 9:** Arrhenius plot of polarization resistance (Rp) calculated from impedance spectra measured at + 4 V 1000 ppm propene + 10% $O_2$, 2L/h.

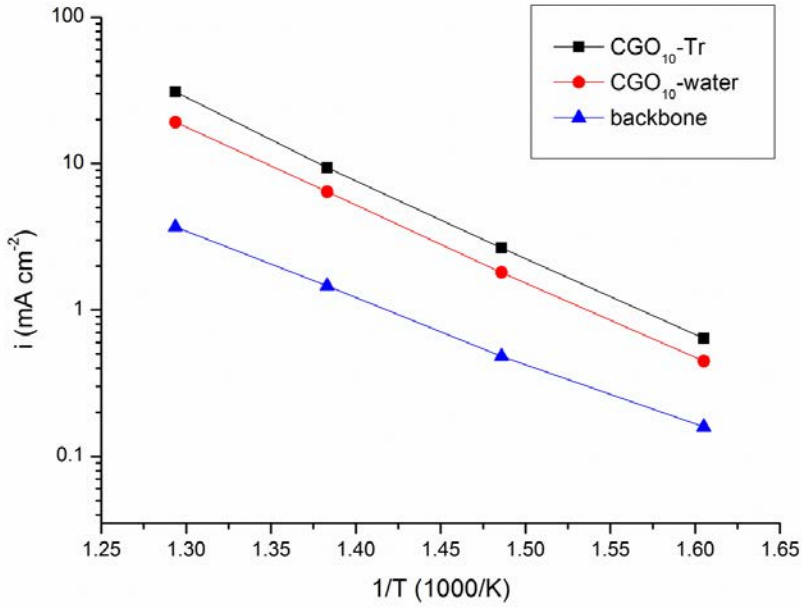


**Figure 10**: Arrhenius plot of current density at +4 V. Reaction mixture: 1000 ppm propene, 10% $O_2$, Ar to balance, 2 L/h.

Figures 11 and 12 show the impedance spectra for the backbone cell and $CGO_{10}$-Tr infiltrated cells recorded at different temperatures either at OCV or under polarization. At least two depressed arcs were visible. These spectra were modeled by using $R_\Omega$(R1Q1)(R2Q2)(R3Q3) and $R_\Omega$(R1Q1)(R2Q2)*(R3Q3)* as equivalent circuits at OCV and + 4 V, respectively. Here, $R_\Omega$ was the ohmic resistance of the electrode, R corresponds to the polarization resistance associated to one single arc and a Constant Phase Element (CPE) Q is used instead of capacitance C, because of non-ideal behavior [19]; the RC units in the equivalent circuit were then replaced by RQ elements. The impedance Z associated to the CPE is defined in Eq. 5 as:

$$Z = 1/(Y_0(j\omega)^{\alpha}) \qquad [5]$$

where $Y_o$ is the amplitude of the CPE and α is the depression value, which has a value between 0 and 1, where 1 correspond to an indeal capacitor C. (R1Q1) represents the high frequency (HF) arc and (R2Q2) and (R3Q3) represent medium (MF) and low frequency (LF) arc respectively.

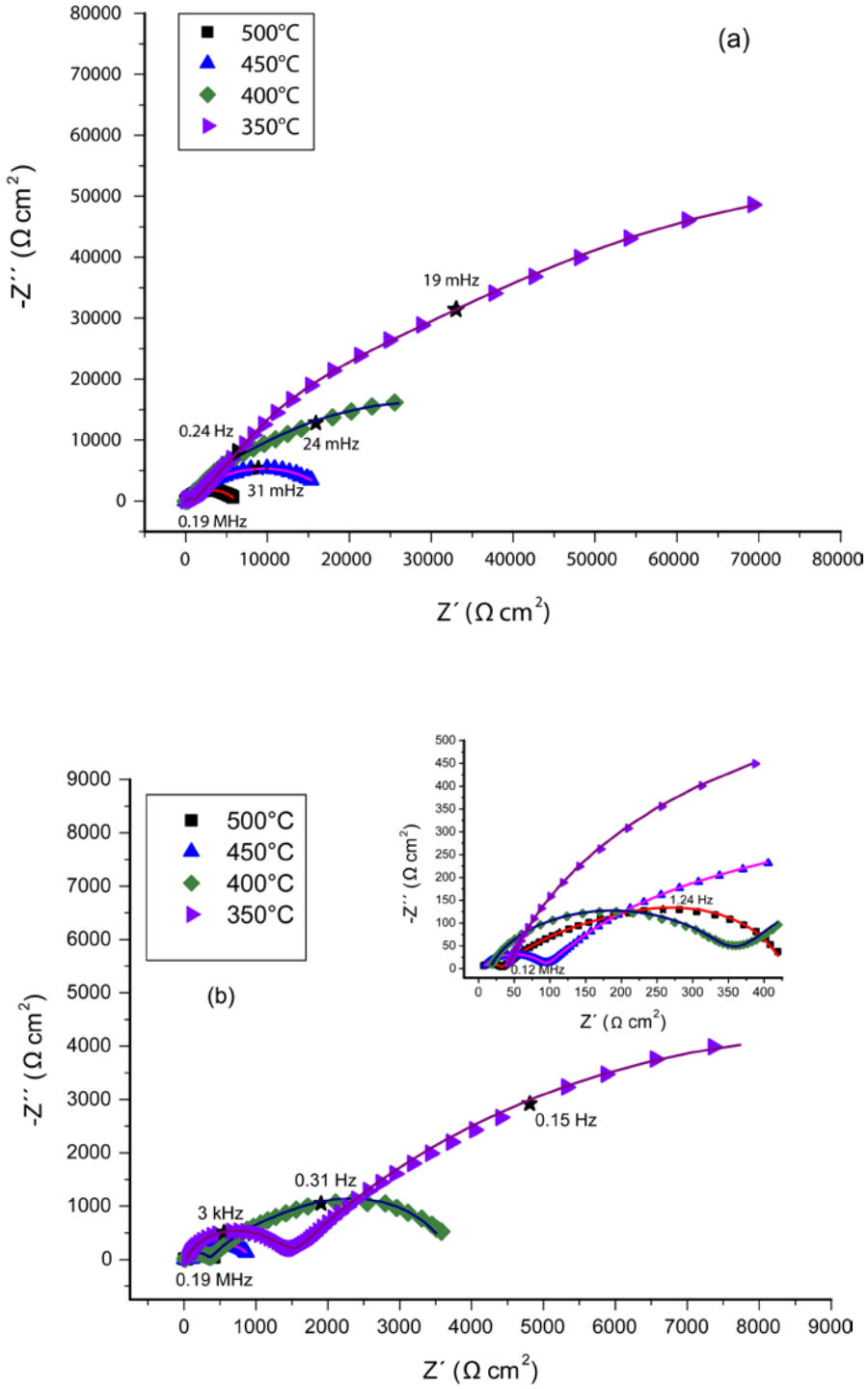


**Figure 11:** Impedance spectra (Nyquist plot) at different temperature for the backbone cell at a) open circuit voltage (OCV) and b) +4 V. Inset: impedance spectra plot at high frequencies. Reaction mixture: 1000 ppm propene, 10% O2, Ar to balance, 2L/h.

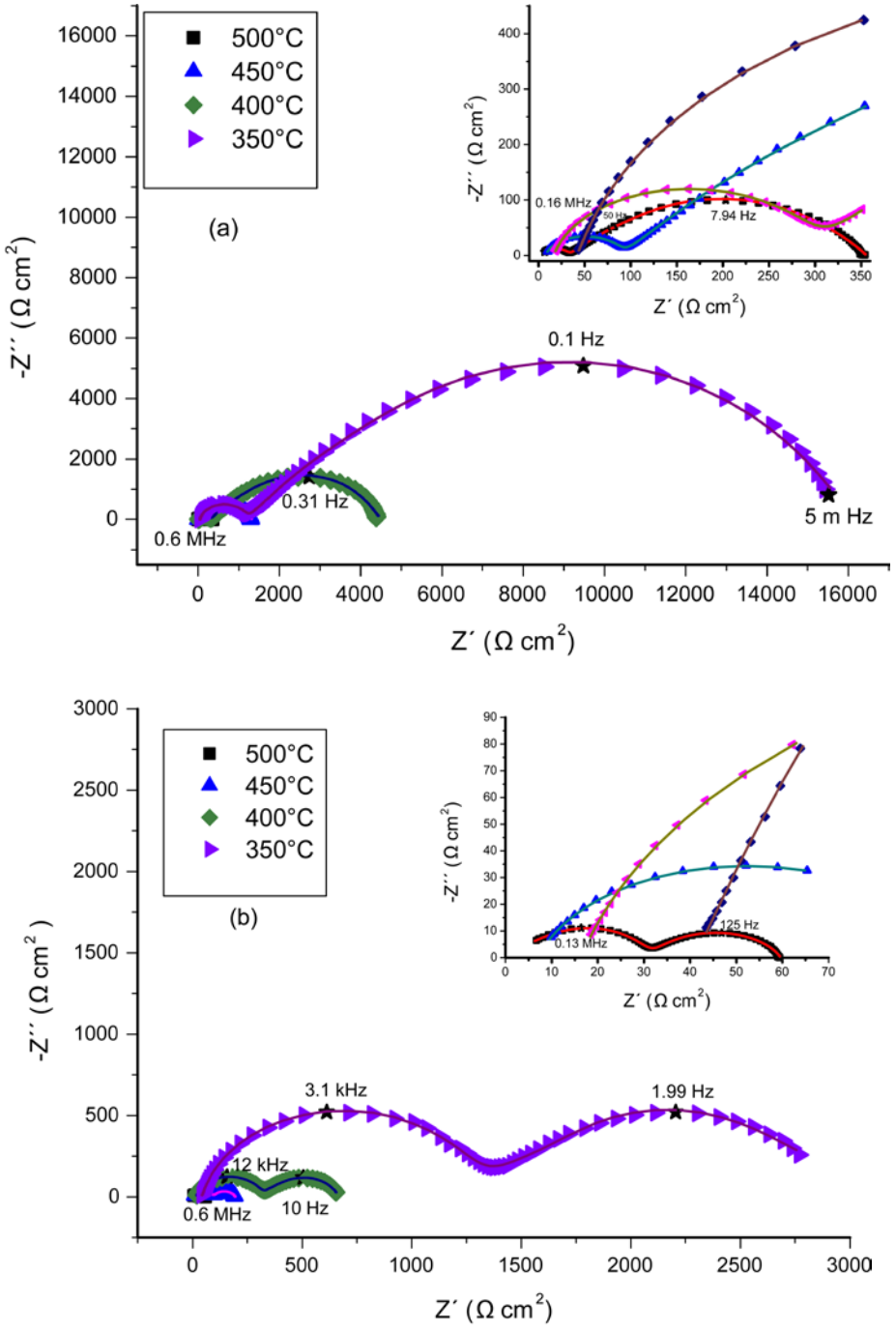


**Figure 12:** Impedance spectra (Nyquist plot) at different temperature for the $CGO_{10}$-Tr cell at a) open circuit voltage (OCV) and b) +4 V b). Inset: impedance spectra plot at high frequencies. Reaction mixture: 1000 ppm propene, 10% O2, Ar to balance, 2L/h.

From Figure 11 and 12 it can be observed that, due to $CGO_{10}$ infiltration, the polarization resistance has strongly decreased both at OCV and +4 V respect to the backbone cell. The inclined line, considered as a part of depressed semicircle visible for backbone cell,

was fully resolved for the $CGO_{10}$-Tr infiltrated cell either at OCV or at +4 V. This behavior was also observed by C. Borja et al. with Pd/CeO2 electrode interfaced with YSZ electrolyte, under oxygen and helium atmosphere [20]. The strong decrease of resistance was also associated for the second arc with a strong increase of maximum peak frequency, from 78 mHz of the backbone cell to 6.2 Hz of the $CGO_{10}$-Tr at 500°C OCV, showing an increased rate of electrode/chemical processes due to the $CGO_{10}$ infiltration.
Figure 13 shows the Arrhenius plot for the ohmic resistance $R_\Omega$; the activation energy for the ohmic resistance $R_\Omega$, 0.71 eV ± 0.02 eV, agreed very well with the activation energy for the electrical conduction of $CGO_{10}$ as reported by Mogensen at al. [21].

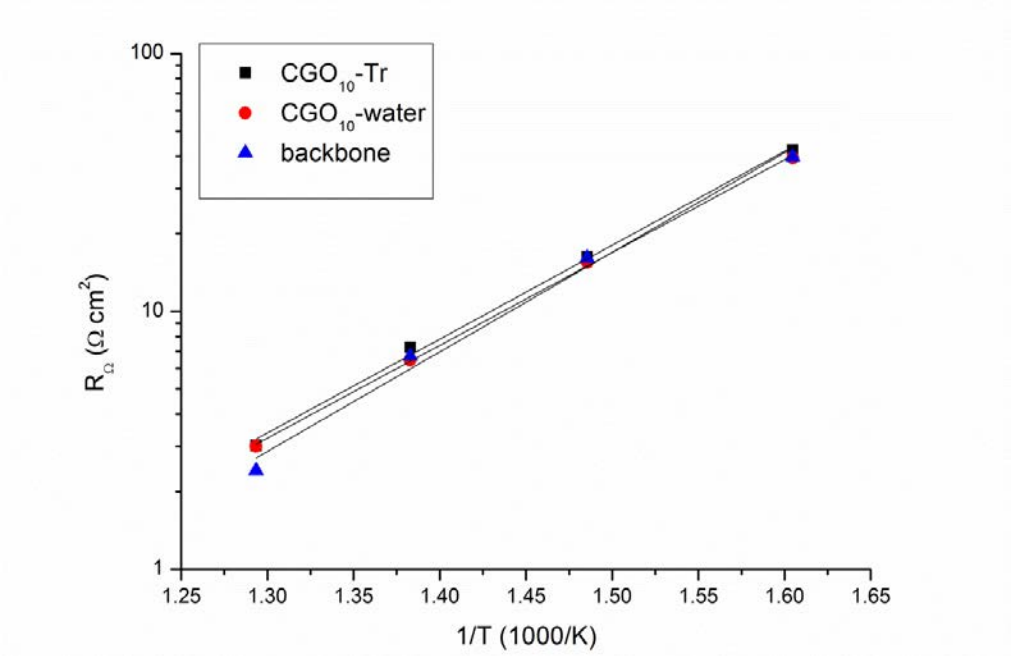


**Figure 13**: Arrhenius plot of ohmic resistance ($R_\Omega$) calculated from impedance spectra measured at OCV.

Figure 14 reports the Arrhenius plots for the resistance R1 both at OCV and under polarization as extracted from the spectra modeling for all the samples. The resistances R1 and the near equivalent capacitances associated to this arc were only slightly affected by polarization; the small change of resistance could be attributed to the modification of the cell microstructure upon polarization. $CGO_{10}$-water cell shows lower R1 values for all temperatures. This could be attributed to a different electrode bulk microstructure, although all the cells belong to the same production batch. The first semicircle of the spectra can be attributed to the grain boundaries conductivity, due to the low values of the capacitances (10^-8 F/cm^2), due to the independency from reaction atmosphere and an activation energy of 1.01 ± 0.04 eV.
The resistances and the near equivalent capacitances of the second semicircle (R2Q2) and (R3Q3) were strongly affected by polarization showing a strong decrease of

resistance due to the voltage application, then R2 and R3 can be associated to the electrode-electrolyte interface or to the electrode response.

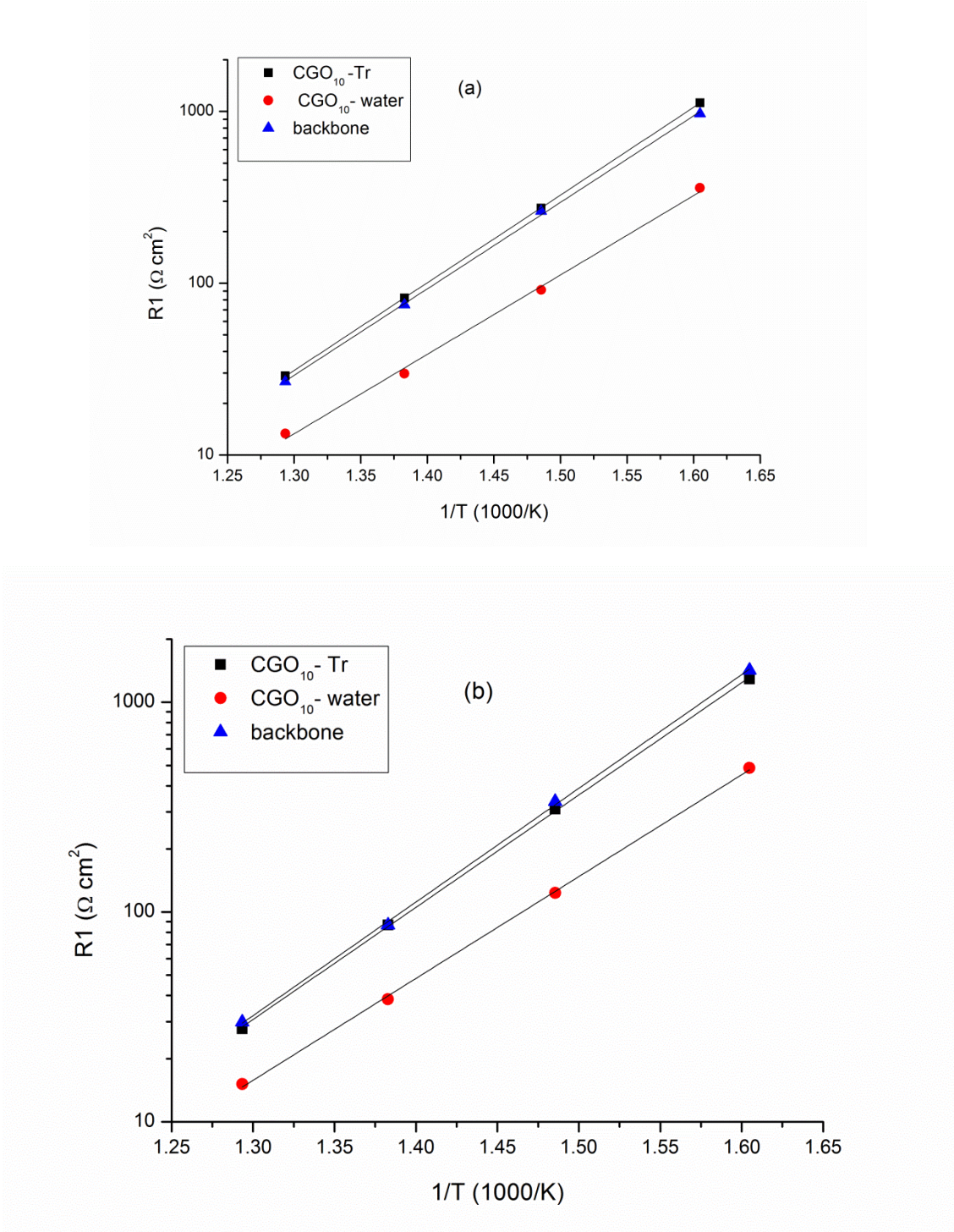


**Figure 14**: Arrhenius plot of resistances R1 of the first (R1Q1) model element at a) open circuit voltage (OCV) and b) at +4 V.

Since belonging to the electrode response, the resistances R2 and R3 were summed in the Arrhenius plot shown in Figure 15 both under OCV and +4 V, giving an almost

straight line for all the samples. The second semicircle with much higher capacitance (50-400 10^-4 F/cm^2) can be related to oxygen ion discharge reaction over the entire gas exposed electrode surface as suggested by Frantzis et al. [22]. The activation energy of this arc results to be 1.05 ± 0.08 eV, lower respect to the oxygen reduction reaction activation energy between 1.14 eV and 1.86 eV as reported by Co et al. [23] .

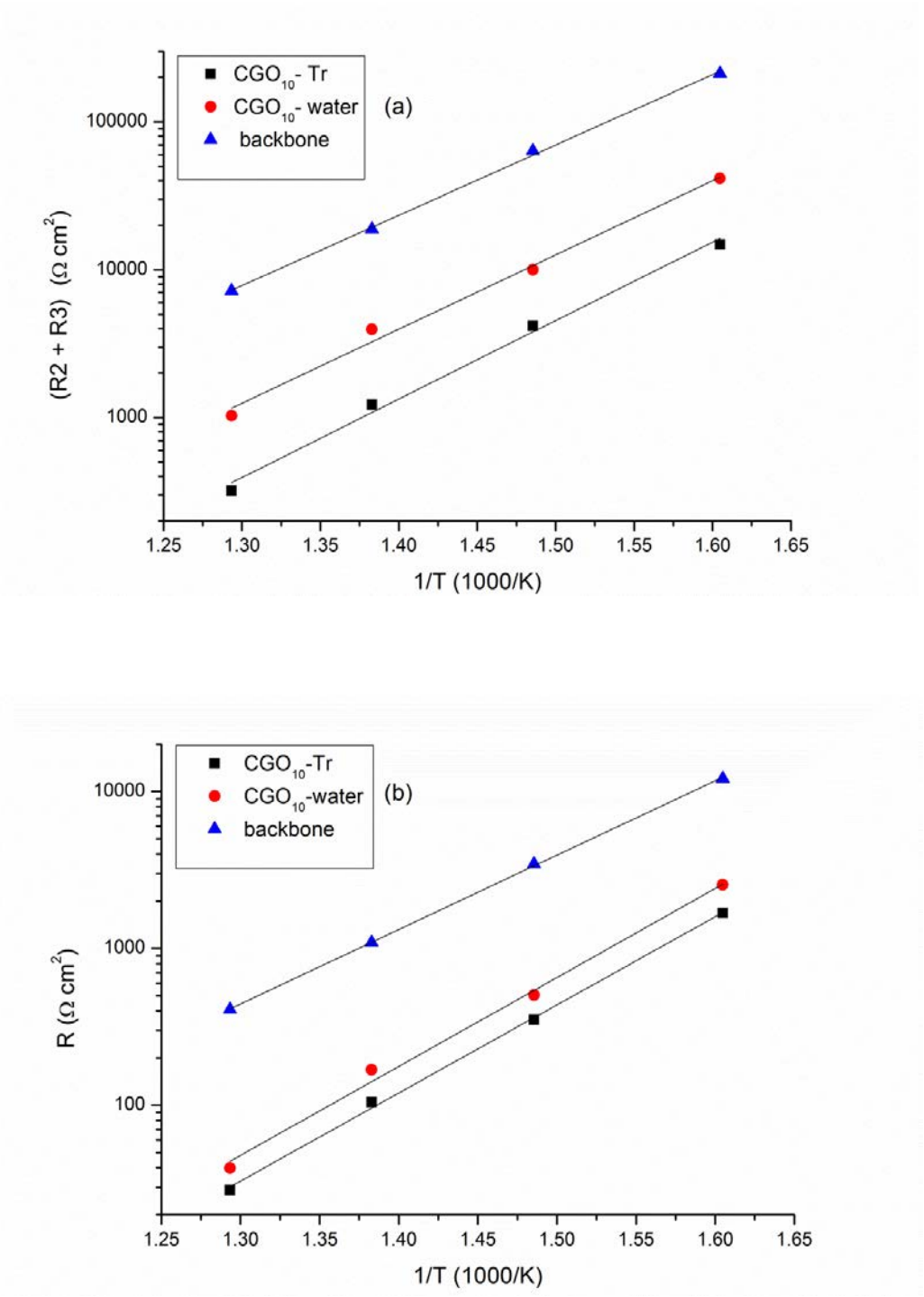


**Figure 15**: Arrhenius plot of resistances (R2+R3) of the second (R2Q2) and third (R2Q2) model element at a) open circuit voltage (OCV) and b) at +4 V.

The third element (R3Q3) used to simulate the data at OCV for all the samples disappeared for the infiltrated cells under anodic polarization but it is still present for the backbone cell. Due to the low frequency region of this third element, spreading from 6.23 Hz for $CGO_{10}$-Tr to 0.079 Hz for backbone cell at 500°C and OCV, this circuit element can be associated to a chemical reaction or surface diffusion process occurring at the electrode surface which resistance is strongly decreased by CGO infiltration. $CGO_{10}$ has a much higher oxygen exchange rate than LSM and the infiltration can extend the reaction site from electrode/electrolyte interface to the bulk electrode, decreasing enormously the resistances associated to oxygen exchange and propene oxidation processes.

## 4.5 Effect of $CGO_{10}$ infiltration loading on the porous reactor catalytic activity for propene oxidation

The backbone cell was infiltrated with $CGO_{10}$ precursor nitrate solution for 2 times (2A sample) and 4 times (4A sample); the heat treatment was repeated at every infiltration step at 400 °C for 2 h, as done for the cell infiltrated $CGO_{10}$-Tr (1A-sample) and previously illustrated in the experimental section. The loading of the infiltrated material was 5.5 % and 8.7% for 2A and 4A sample, respectively; the infiltration loading was calculated on the weight of the cell without infiltration (backbone).

The specific area measurements showed an increase of specific surface area with the number of the infiltrations to values of 4.2 $m^2/g$ and 7.1 $m^2/g$ for the 2A and 4A sample, respectively.

The intrinsic catalytic activity at OCV of the sample 2A and 4A together with 1A sample (as reported in Figure 4) is shown in Figure 16.

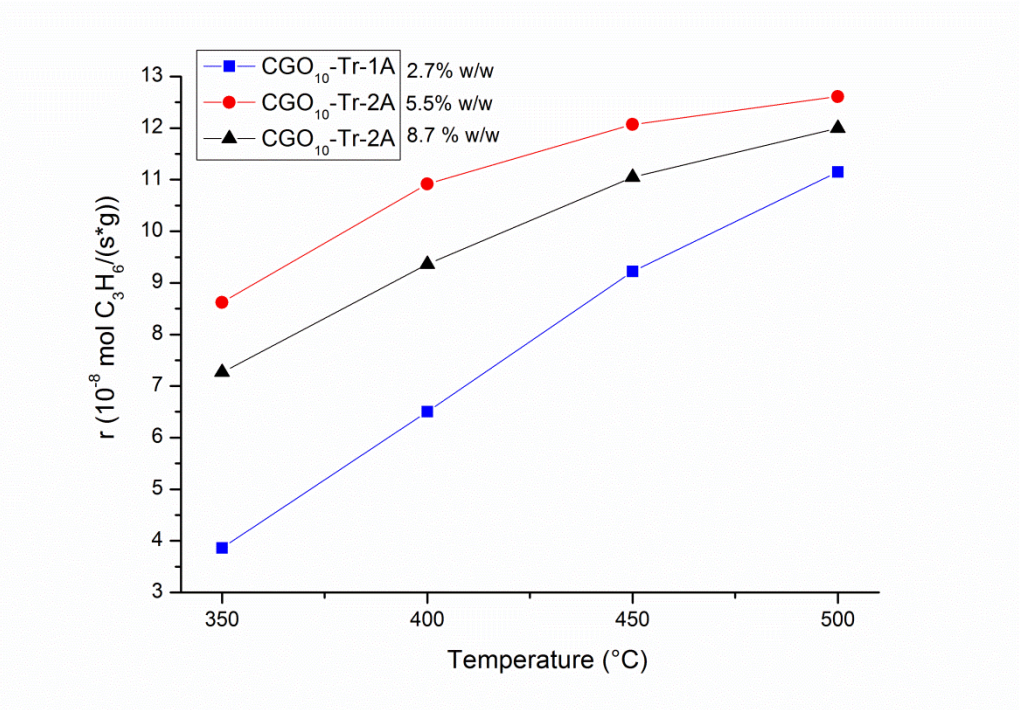


**Figure 16**: Intrinsic reaction rate as function of temperature for sample with different $CGO_{10}$ infiltration loading. Reaction mixture: 1000 ppm $C_3H_6$ +10% $O_2$, 2L/h, OCV.

The multiple infiltrations of $CGO_{10}$ increased the catalytic activity towards propene oxidation if compared to the sample 1A, particularly below 450 °C. At 500 °C the sample 2A and 4A reached 97.3 % and 97.1 % of propene conversion respectively with 98% of selectivity to $CO_2$. At 400° C the propene conversion was 82.3% and 75.9% for 2A and 4A sample, respectively. This result was expected and it was due to the higher number of active sites available for the propene oxidation.

It is important to observe that the catalytic activity of the sample 2A was higher compared to the sample 4A. This behavior could be explained by the partial blocking of the backbone pores caused by the high number of infiltrations. This was visible in the micrographs shown in Figure 17 for the samples 2A and 4A.

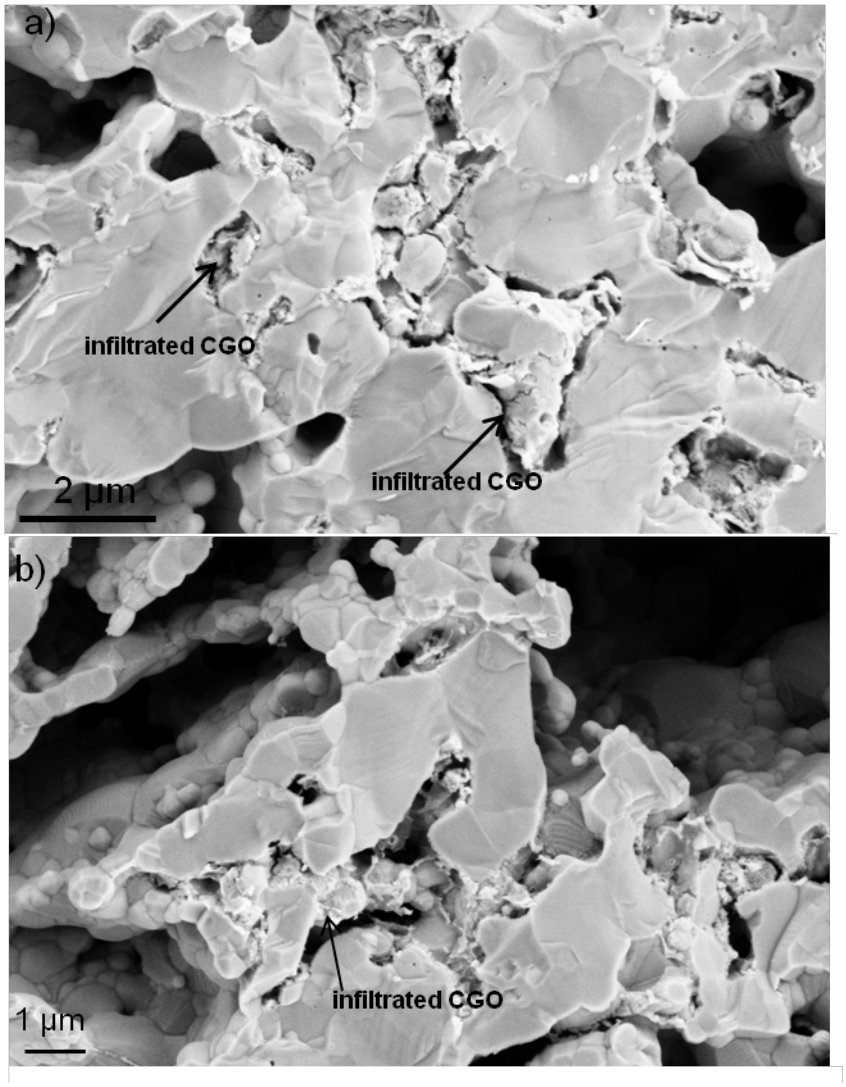


**Figure 17**: SEM micrographs of a) sample 4A and b) sample 2A

The small pores of the sample 4A were partially blocked if compared to the pores of the sample 2A; this could have limited the access of the reactive mixture into the reactor, decreasing the propene conversion.

As it was done with the 1A sample ($CGO_{10}$-Tr), the catalytic activity of the 2A and 4A samples was studied at OCV after the end of all chronoamperometry tests, in order to assess the stability of the reactor performance after multiple sequences of polarization. In this case the measurement of propene conversion was done not only at 500 °C but also at 400 °C.

As previously illustrated, the 1A sample did not show any significant change of catalytic activity after 30 h of polarization if compared to the backbone or to the $CGO_{10}$-water sample; the samples with multiple infiltrations of $CGO_{10}$ instead exhibited a decrease of propene conversion both at 500 °C and 400 °C if compared to the conversion measured before the chronoamperometry tests. The 2A sample showed a decrease of catalytic ac-

tivity of 2.3% and 1.4% at 400 °C and 500 °C, respectively. The 4A sample showed a decrease of 4.1% and 3.1% at the same temperatures.

The decrease of catalytic activity appeared to increase with the number of infiltrations. The beneficial effect of polarization on the catalytic activity, visible for the backbone and $CGO_{10}$-water samples and previously illustrated, was probably not enough to compensate the decrease of the propene conversion given by the instability of the multiple $CGO_{10}$ infiltrations. According to these results, the apparent stability of the sample 1A ($CGO_{10}$-Tr), as previously reported, could be due to the combined effect of the slight decrease of the infiltrated $CGO_{10}$ catalytic activity and the increase of catalytic activity of the backbone activated by long-term polarization, i.e. in the case of 1A sample the activity loss was compensated by the increase of the backbone catalytic activity after polarization.

In Figure 18 is shown the rate enhancement ratio (ρ) as function of $CGO_{10}$ loading in the backbone. The low ρ values of the sample 2A and 4A compared to the sample 1A could be attributed to the high conversion of propene of 60%-85% between temperatures of 350 °C and 400 °C. The high propene conversion established a strong external concentration gradient of the reactants limiting the effect of polarization on propene oxidation rate. This behavior could explain the higher ρ values shown by the sample 1A at 350 °C and 400 °C where the conversion were only 29% and 47%, respectively.

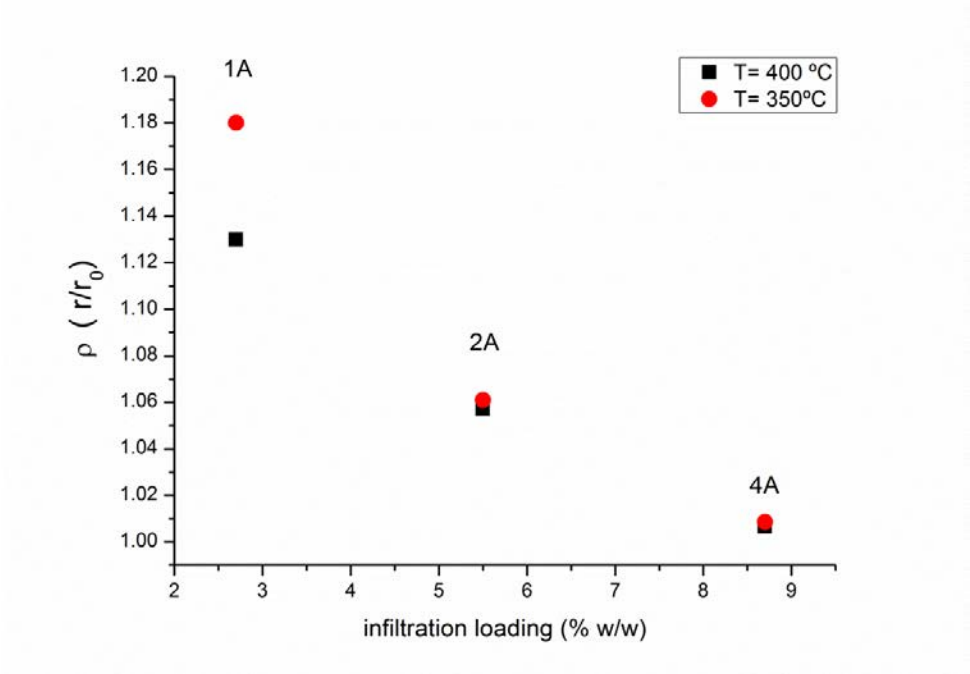


**Figure 18:** Rate enhancement ratio (ρ) as function of infiltration loading of $CGO_{10}$ at 400 °C and 500 °C. Reaction mixture: 1000 ppm propene, 10% $O_2$, Ar to balance 2 L/h

Figure 19 presents the polarization curve of the samples with different infiltration loading recorded at 400 °C with 1000 ppm propene and 10% oxygen at 2 L/h.

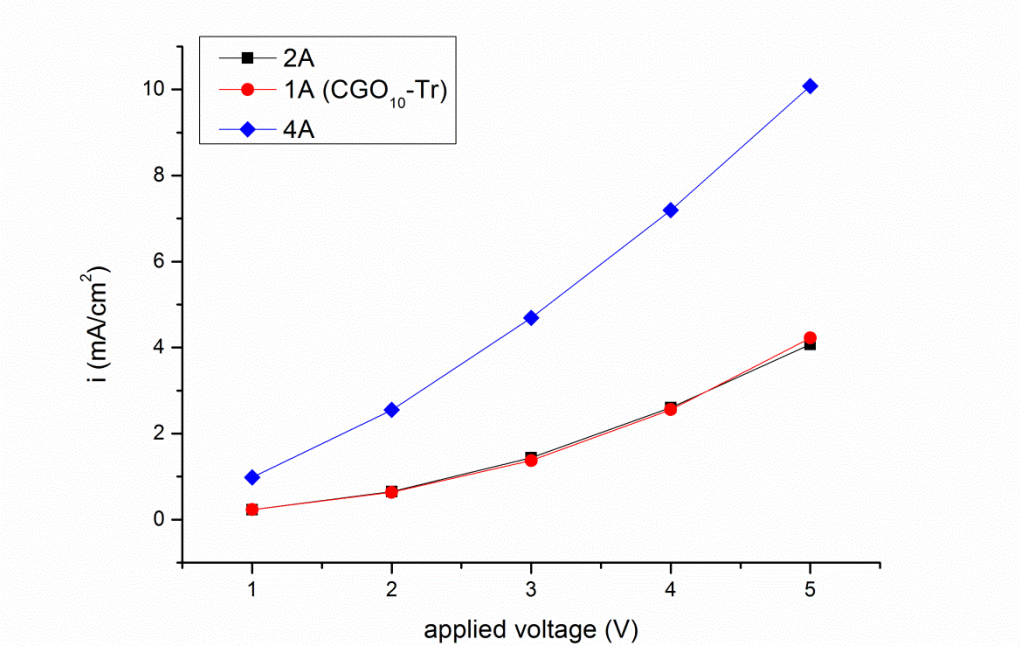


**Figure 19**: Polarization curve of the LSM/CGO sample with different $CGO_{10}$ infiltration loading recorded at 400 °C, 1000 ppm $C_3H_6$, 10% $O_2$ and 2 L/h.

The 1A and 2A samples exhibited similar polarization behavior while 4 times infiltration of $CGO_{10}$ was able to strongly increase the current density; this behavior could be ascribed to the reaching of the percolation threshold by the high loading of $CGO_{10}$ infiltration. The effect of 4 times infiltration on the polarization curve could confirm the blocking of the reactor pores visible in the SEM micrograph of Figure 17a: an alternative and easier pathway for the oxyge ions, compared to the pathway provided by the $CGO_{10}$ already present in the backbone composite, could be provided by the partial filling of the reactor pores and have caused the strong enhancement of current density.

A further study was carried on the sample 2A at 400 °C with the objective to comprehend the effects of flow and reactants concentrations on the propene conversion of the infiltrated backbone. Figure 20 illustrates the effect of gas flow on propene conversion and selectivity to $CO_2$.

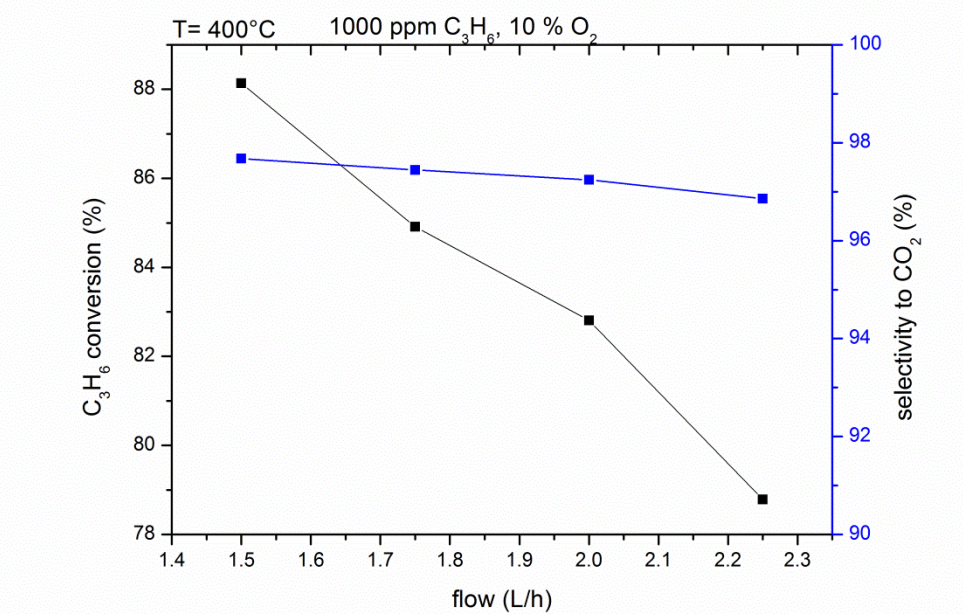


**Figure 20:** Effect of gas flow on propene conversion and selectivity to $CO_2$. Reaction mixture: 1000 ppm propene, 10% $O_2$, Ar to balance

An increase of flow induced a strong decrease of conversion while the selectivity to $CO_2$ was poorly affected. This behavior indicated the presence of external mass transfer limitations and could then explain the behavior of the rate enhancement ratio of Figure 18. Figure 21 shows the effect of oxygen concentration on the propene conversion.

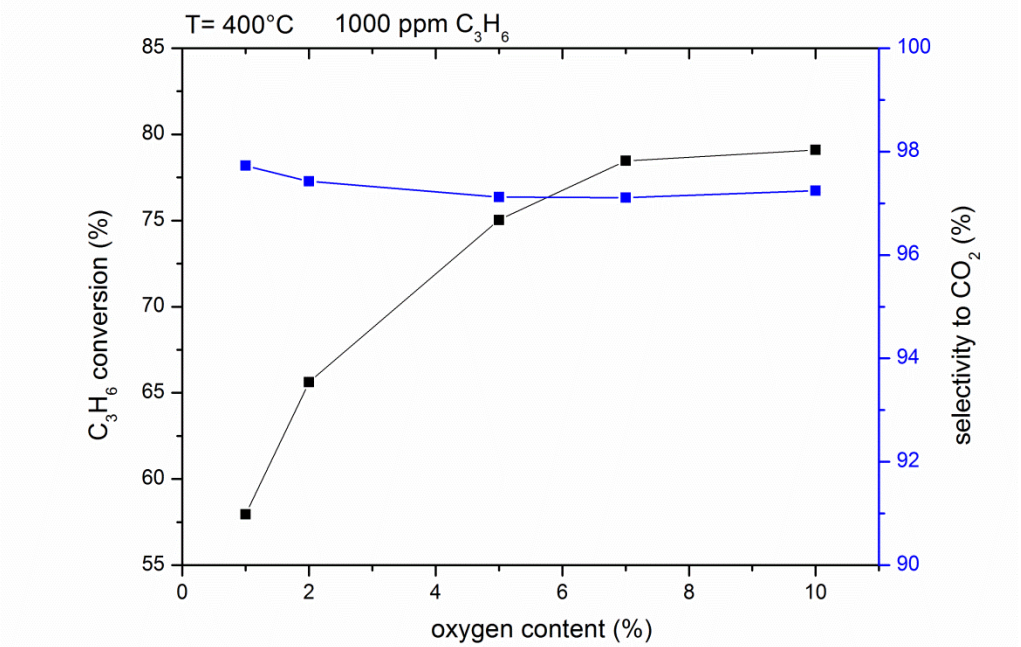


**Figure 21**: Effect of oxygen content on propene conversion and selectivity to $CO_2$. Reaction mixture: 1000 ppm propene, Ar to balance, 2 L/h

The selectivity to $CO_2$ was poorly affected by the change of oxygen content while the increase of oxygen concentration strongly increased the conversion up to 5% of oxygen and reached a plateau above 6% of oxygen. Similar behavior was observed by Vernoux et al. [18] and Kaloyannis et al. [24] for the oxidation of propene on Pt/YSZ.

The effect of propene concentration on propene conversion and selectivity of $CO_2$ is shown in Figure 22. The increase of propene concentration provoked a decrease of conversion; this behavior was in good agreement with the study of Kaloyannis et al. [24] on Pt/YSZ showing a decrease of reaction rate with the increase of propene concentration. The inhibition of the propene oxidation reaction on the surface was caused by the strong adsorption of propene on the catalyst surface. This specific reaction kinetic suggested a competitive adsorption mechanism of dissociatively chemisorbed oxygen and propene with stronger binding of propene than oxygen on the catalyst surface.

The selectivity to $CO_2$ decreased with an increase and it depended directly to the propene concentration.

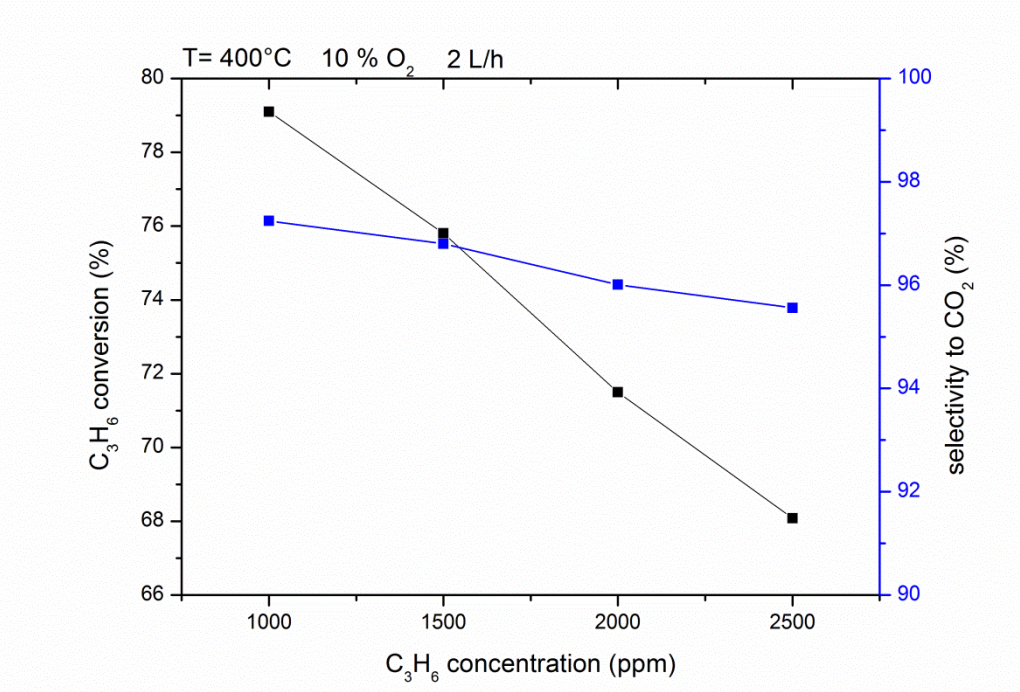


**Figure 22:** Effect of propene concentration conversion and selectivity to $CO_2$. Reaction mixture: 10% $O_2$, Ar to balance, 2 L/h

## 4.6 Conclusions

This work presented the possibility to deep oxidize propene with low cost materials, using a porous backbone structure made of $LSM_{15}$ and $CGO_{10}$ and used as a catalyst support for the infiltration of an hydrocarbons oxidation catalyst like the Gadolinium doped Ceria; the active catalyst infiltration procedure represented an easy and not time consuming method to increase the backbone activity for the oxidation of propene and the selectivity to $CO_2$ of the oxidation reaction both at open circuit voltage and under polarization. Although the infiltration procedure in this work was not optimized, the morphology and connectivity between $CGO_{10}$ infiltrated particles were observed to be fundamental for the reactor activity and susceptibility upon polarization towards propene oxidation. Particularly, the low calcination temperature of the $CGO_{10}$ precursors to form a continuos layer on the backbone surface was fundamental to obtain both good catalytic activity at open circuit voltage and high rate enhancement ratio values at low temperatures.

While the activation of the LSM/CGO electrode was expected due to the formation of oxygen vacancies on LSM surface, the massive increase of propene oxidation rate was totally unexpected and never reported before in literature. The formation of oxygen vacancies due to the prolonged polarization appeared to play a key role in the mechanism of propene oxidation.

The activation of the electrode and of the catalytic activity was clearly visible for the backbone and for $CGO_{10}$-water sample while no evident activation both for the electrochemical and catalytic performance was visible for $CGO_{10}$-Tr sample.

Multiple $CGO_{10}$ infiltrations, with low temperature calcination, showed a strong increase of catalytic activity measured at OCV; the prolonged polarization in this case induced a propene conversion decrease of maximum 4.1%.

The apparent stability of one time infiltrated sample ($CGO_{10}$-Tr) could be due to the increase of catalytic activity of the backbone able to counteract the performance decrease of the infiltrated $CGO_{10}$ material, although the measurement of the specific surface area of $CGO_{10}$-Tr infiltrated cell at the end of the test did not exhbit any significant change.

## References


1. T.V. Jonhson, SAE International 2011-01-0304
2. J. E. Hoffmann, *Journal of Metals ,* **40**, 40-44 (1988).
3. N. Yamazoe, Y. Teraoka, *Catalysis Today*, **8**, 175-199 (1990).
4. T. Seyama, *Catalysis Review. – Science and Engineering*, **34**, 281-300 (1992).
5. F.Gaillard, X. Li, M. Uray, P. Vernoux, *Cataysis Letters*, **96**, 177-183 (2004).
6. V.Roche, E. Siebert, M.C. Steil, J.P.Deloume, C. Roux, T. Pagnier, R. Revel, P. Vernoux, *Ionics*, **14**, 235-241 (2008).
7. P. Tsiakaras, C. Athanasiou, G. Marnellos, M. Stoukides, J.E ten Elshof, H.J.M Bouwmeester., *Applied Catalysis: A*, **169**, 249-261 (1998).
8. M. V., Twigg, *Applied Catalysis: B*, **70**, 2-15 (2007).
9. A.Trovarelli, *Catalysis Review. – Science and Engineering*, **38**, 439-520 (1996).
10. R.M.L. Werchmeister, K.K. Hansen, M. Mogensen *Material Research Bulletin, **45,** 1554 (2010).*
11. P. Blennow, K. H. Hansen, L. R. Wallenberg, M. Mogensen, *ECS Transactions.*, **13,** (26) 181-194 (2008).
12. P. Blennow, W. Chen, M. Lundberg, M. Menon, *Ceramic International* **35** (2009), 2959-2963.
13. A. Trovarelli, in *Catalysis by Ceria and Related Materials*, World Scientific Publishing Company, p. 424,1st edition (2002).
14. W. Wang, S.P. Jiang, *Journal of Solid State Electrochemistry* ,**8**, 914-922 (2004).
15. D. Ferri, L. Forni*, Applied Catalysis: B*, **16,** (1998) 119-126.
16. K.Chen, N. Ai, S.P. Jiang, *Journal of the Electrochemical Society,* **157**, P89-P94 (2010).
17. M. Stoukides, C.G. Vayenas, *Journal of Electrochemical Society,* **131**, 839-845 (1984).

18. P.Vernoux, F. Gaillard, L. Bultel, E. Siebert, M. Primet, *Journal of Catalysis*, **208**, 412-421 (2002).
19. M. E. Orazem, B. Tribollet, Electrochemical Impedance Spectroscopy, p. 233, John Wiley & Sons, (2008).
20. C. Borja-Jimenez,F. Dorado, A. de L. Cinsuegra , J.M.G. Vargas , J.L. Valverde , *Fuel Cells* ,**11**, 131-139 (2011).
21. M. Mogensen, N. M. Sammes, G. A. Tompsett, *Solid State Ionics* ,**129**, 63 (2000).
22. A. D. Frantzis, S. Bebelis, C.G. Vayenas, *Solid State Ionics* ,**136-137**, 863-872 (2000).
23. A. C. Co, S. J. Xia, V. I. Birss, , *Journal of Electrochemical Society,***152**, A570-A576 (2005).
24. A. Kaloyannis, C.G. Vayenas, *Journal of Catalysis*, **182**, 37-47 (1999).

# 5 THE EFFECT OF $CeO_2$ AND $Ce_{0.8}Pr_{0.2}O_{2-\delta}$ INFILTRATION ON THE $LSM_{15}/CGO_{10}$ ELECTROCHEMICAL REACTOR ACTIVITY IN THE ELECTROCHEMICAL OXIDATION OF PROPENE

## 5.1 Abstract

The effect of infiltrating on a $La_{0.85}Sr_{0.15}MnO_3/Ce_{0.9}Gd_{0.1}O_{1.95}$ 11-layer electrochemical reactor with $CeO_2$ and $Ce_{0.8}Pr_{0.2}O_{2-\delta}$ was studied in propene oxidation at open circuit voltage and under polarization as a function of reaction temperature. This work outlined the importance of catalytic and electrochemical properties of infiltrated material on the ability to increase propene conversion under polarization with good faradaic efficiency. Electrochemical impedance spectroscopy (EIS) was used to study the effect of infiltration material on electrode properties. The infiltration of a mixed ionic and electronic conductor (MIEC), like $Ce_{0.8}Pr_{0.2}O_{2-\delta}$, increased the electrode performance at low temperature but decreased the lifetime of the oxygen ion promoters on the catalyst/electrode surface, reducing the faradaic efficiency of the reaction. The infiltration of $CeO_2$ provided high propene conversion at open circuit and high effect of polarization associated with good faradaic efficiency, especially at low temperature.

## 5.2 Introduction

Air pollution from stationary and mobile sources has become one of most important environmental concerns of the last ten years. Stricter legislation on emission control has been adopted in the US, Europe and also emerging countries, like India and China [1]. Exhaust gases from spark and compression engines contribute to the degradation of air quality, especially in urban environments. Between these two, Diesel exhausts contain high levels of $NO_X$, volatile organic compounds (VOCs) and fine particulate matter (PM) contributing to respiratory problems and cardiovascular disease [2,3]. Supported metal catalysts, such as Pt and Pd, are usually employed both for catalytic combustion of hydrocarbons and NOx reduction [4]. They are very active at low temperature but suffer from high temperature sintering, poisoning from sulphur and their use is limited by high prices.

Alternative catalysts have thus been explored, such as hexaaluminates, single and doped transition metal oxides and perovskite [5].

Transition metal perovskites ($LaMO_3$) (M=Mn,Co) are possible alternative catalysts to noble metals in hydrocarbon combustion reactions due to the redox properties of the M cation, the presence of lattice defects and weakly bonded oxygen at the surface. They offer good thermal stability in oxygen and steam-rich atmospheres and low cost, but they currently have lower efficiencies [6,7]. For example, Spinicci et al. studied the activity of $LaMnO_3$ and $LaCoO_3$ towards combustion of VOCs and oxygen surface species mobility was identified as a requisite for high catalytic activity [8].

Catalyst activity can be enhanced by using Electrochemical Promotion of Catalysis (EPOC). EPOC is based on the control of catalyst work function by applying a potential or current to an electrocatalyst interfaced with a solid electrolyte. In 1981, Stoukides and Vayenas [9] demonstrated increased reaction rate and selectivity in ethylene catalytic oxidation on Ag. This phenomenon has also been studied using perovskite as a catalyst; Gaillard et al. demonstrated *in situ* control of activity and selectivity of $La_{0.8}Sr_{0.2}Co_{0.8}Fe_{0.2}O_3$ for deep oxidation of propene at 450 °C in air by EPOC [10]. Additionally, Roche et al. presented an electrochemical promotion effect for the deep oxidation of propane on lanthanum manganite [11]. Furthermore, Tsiakaras et al. studied the electrocatalytic behaviour of $La_{0.6}Sr_{0.4}Co_{0.8}Fe_{0.2}O_3$ perovskite deposited on yttria-stabilized zirconia (YSZ) during methane oxidation where oxygen was electrochemically supplied as $O^{2-}$ and found considerable changes in methane conversion and product selectivity [12]. Finally, Balomenou et al. developed a monolith electrochemical promoted reactor (MEPR) using Pt and Rh dispersed on a YSZ plate to measure the abatement of simulated and real automotive pollution and achieved electrochemical promotion in both situations [13].

The present work studied the possibility of using an 11-layer porous single chamber electrochemical reactor for the oxidation of propene, a major Diesel exhaust emission component [14], without precious metal. In this work, the whole reactor was thought of as a catalytic filter with a porous composite electrode interfaced with a porous electrolyte for Diesel exhaust after-treatment. Ceria is one of the best hydrocarbon oxidation catalysts known, and although ceria-based oxidation catalysts are normally coupled with a precious metal, alumina-supported ceria shows sufficient activity in the oxidation of unburned hydrocarbons in Diesel exhausts without the addition of precious metals [15]. In order to enhance the catalytic activity for a future full-scale application, the effect of $CeO_2$ and $Ce_{0.8}Pr_{0.2}O_{2-\delta}$ impregnation on reactor activity was therefore investigated. The influ-

ence of infiltrated material properties on the reactor performance was also investigated. To comply with these objectives, electrochemical impedance spectroscopy (EIS) was employed.

## 5.3 Experimental

### 5.3.1 Cell preparation

The 11-layer electrochemical reactor (backbone) was prepared by laminating layers of electrode and electrolyte made by tape casting for a total of 5 single cells. The electrolyte tape was made of $Ce_{0.9}Gd_{0.1}O_{1.95}$ purchased from Rhodia, while the electrode was made of a 35% weight $Ce_{0.9}Gd_{0.1}O_{1.95}$ ($CGO_{10}$) and 65% weight $La_{0.85}Sr_{0.15}MnO_3$ ($LSM_{15}$) composite (Haldor Topsoe). Slurries for tape casting were made from metal oxide powder, solvent, binder and graphite as pore former. The slurries were ball milled before tape casting. The cell was then sintered at 1250 °C for 2 h. The average diameter of the cells was 13 mm.

The cells were impregnated using a 1.5 M solution of 20 mol% $Pr(NO_3)_3$ + 80 mol% $Ce(NO_3)_3$ for $Ce_{0.8}Pr_{0.2}O_{2-\delta}$ ($CPO_{20}$) infiltration and with a 1.5 M solution of $Ce(NO_3)_3$ for $CeO_2$ infiltration with Triton X-100 as surfactant. Solutions were prepared with Millipore water, Triton X-100 (Sigma-Aldrich), Ce nitrate hexahydrate (Alfa Aesar) and Pr nitrate hydrate (Alfa Aesar). Infiltration was carried out in one step by applying vacuum to the cell after application of impregnation solution. After infiltration, the cell was calcined at 600 °C for 2 h. The weight of the cell was measured before infiltration and after calcination to estimate the infiltration loading. The $CeO_2$ and $CPO_{20}$ infiltrated cells weighted 0.172 g and 0.169 g, respectively.

The infiltration loading was equivalent to approximately 2.6-2.7% of the weight of the cell. Gold paste with 20% weight graphite was painted on both sides of the electrochemical reactor and used as the current collector. The cell weights were measured without the current collector and the cell areas were approximately 1.429 and 1.409 $cm^2$ for $CPO_{20}$ and $CeO_2$ infiltrated cells, respectively.

### 5.3.2 Reactor configuration

Figure 1 illustrates the reactor configuration. The sample was mounted in a tubular reactor between two alumina tubes with contact between the gold paste and the two Pt electrodes used as working and reference/counter electrodes under one atmosphere, as reported by Werchmeister et al. [16].

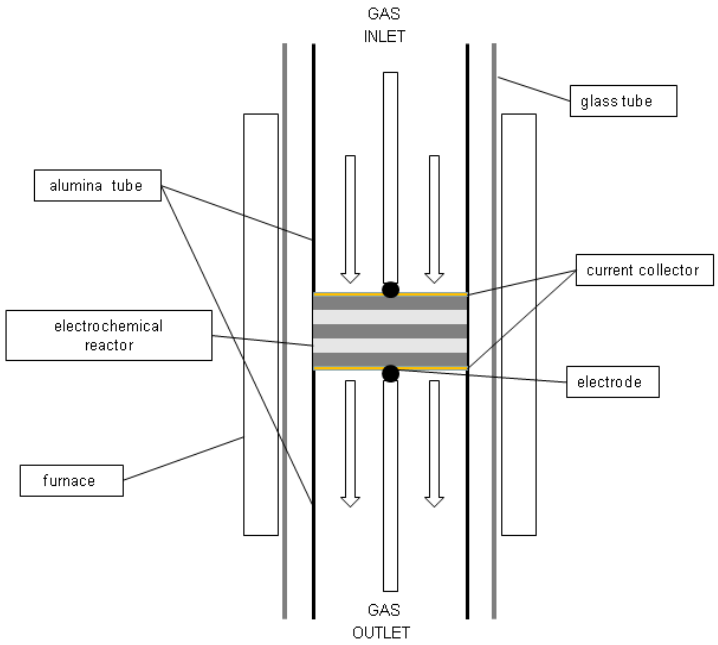


**Figure 1:** Scheme of the reactor configuration

The setup was placed inside a glass tube surrounded by a furnace. For the catalytic activity evaluation, a mixture of 10% $O_2$ (Air Liquide; 20% $O_2$ ± 2% Ar), 1000 ppm propene (Air Liquide; 1% ± 0.02 % propene in Ar) and Ar to balance was used with a total flow rate of 2 L $h^{-1}$ controlled by Brooks flow meters. Reactants and products were analysed by an on-line Agilent 6890 N gas chromatograph connected to the reactor and equipped with Hayesep N and Molsieve columns and a thermal conductivity detector. The reaction temperature was monitored by two thermocouples: one touching the cell and the other one placed 4 mm over the cell. The temperature range of the measurements was 300 °C - 500 °C.

## 5.4 Cell structural characterization

The 11-layer reactor morphology and infiltrated particle morphology were characterised with a Zeiss Supra-35 scanning electron microscopy (SEM). In addition, adsorption/desorption experiments (B.E.T.) using Krypton were conducted on the infiltrated samples to determine the specific surface area (SSA). The samples were measured in an Autosorp-1-MP before and after catalytic measurements where all the samples were de-gassed for 3 h under vacuum at 300 °C prior to adsorption. The BET specific surface areas were calculated from the adsorption isotherm keeping the values of the relative Krypton pressure ($p/p_0$) between 0.05 and 0.3 for all samples. Finally, X-ray diffraction (XRD) measurements were carried out with a STOE theta-theta diffractometer using Cu Kα (λ=1.540 Å) from 20° to 100° and with a 0.05 2$\theta$ step size.

### 5.4.1 Cell activity characterization

The polarisation effect on the cell is characterised by the rate enhancement ratio (ρ) defined by:

$$\rho = \frac{r}{r_o}$$

where $r_o$ is the catalytic rate (mol/s) at open circuit voltage (OCV) and $r$ is the catalytic rate (mol/s) under polarization

The faradaic efficiency was thus calculated as:

$$\Lambda = \frac{r - r_o}{\frac{I}{2F}}$$

where $I$ is the current measured under polarization and $F$ is Faraday´s constant.

### 5.4.2 Cell electrochemical characterization

A potentiostat (Gamry, reference 600 USA) was used to perform chronoamperometry tests and for recording impedance spectra. The open-circuit voltage of the cell was stabilised before every measurement. The impedance spectra were recorded at open-circuit voltage (OCV) and with an anodic bias of +4 V (+ 800 mV/cell) with respect to the open circuit voltage with an amplitude of 36 mV RMS over the frequency range 0.78 MHz to 5 mHz with 10 points/decade. The chronoamperometry tests were carried out for 2 h with anodic potentials from +1 V to 5 V with respect to the open-circuit voltage with 1 V steps followed by cathodic polarisation using the same procedure. The ohmic drop was not subtracted in the given potentials. The temperature range of these measurements was 300 °C - 500 °C.

The impedance spectra were analysed in ZSimpWin 3.21 software using Complex Non-Linear Square (CNLS) fitting. The inductance coming from the wiring was subtracted for every spectrum to perform the fitting. The spectra were validated using the Kramers-Kronig test for causality and time invariance.

An equivalent circuit was used containing a serial resistance, Rs, and a number of RQ or RG subcircuits. RQ is a resistance R in parallel with a Constant Phase Element (CPE). The impedance of a CPE is given by:

$$\frac{1}{Z} = Y = Y^{o}(j\omega)^{n}$$

where Z is the impedance, Y the admittance, $Y^0$ is the amplitude of the constant phase element admittance, j is the imaginary number and ω is the frequency.
The general impedance of the Gerischer element (G) is expressed by:

$$Z_G = \frac{1}{Y_o\sqrt{K_A + i\omega}}$$

where $Y^0$ is the admittance parameter and $K_A$ is the rate constant parameter.
The distribution of relaxation times (DRT) analysis was performed using in-house software based on Schichlein et al. [17]. The visual Hanning filter was used for data filtering and the filtering values was kept fixed for all analyses.

## 5.5 Result and Discussion

### 5.5.1 Catalyst characterization

Figures 2 and 3 show the micrographs of $CeO_2$ and $CPO_{20}$ infiltrated cells, respectively.

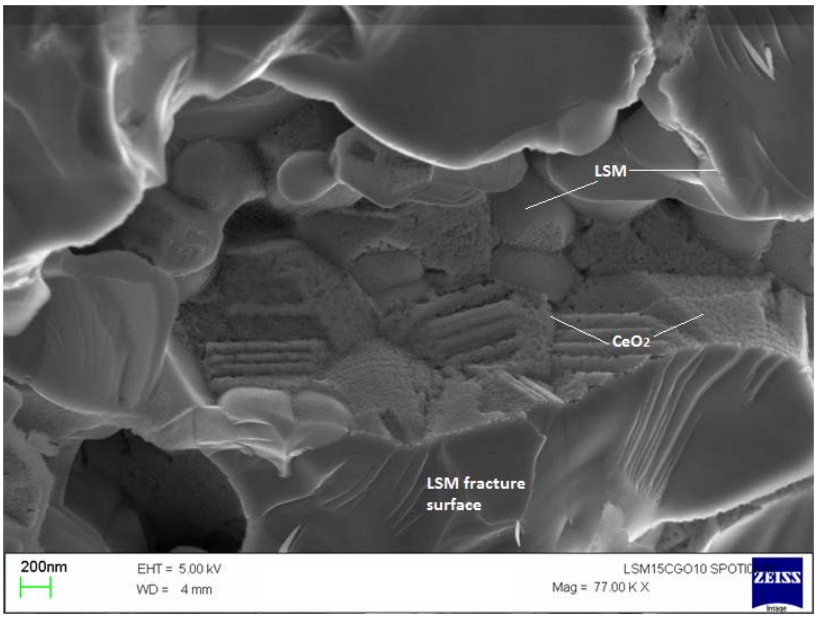


**Figure 2:** SEM micrograph of a $CeO_2$ infiltrated cell.

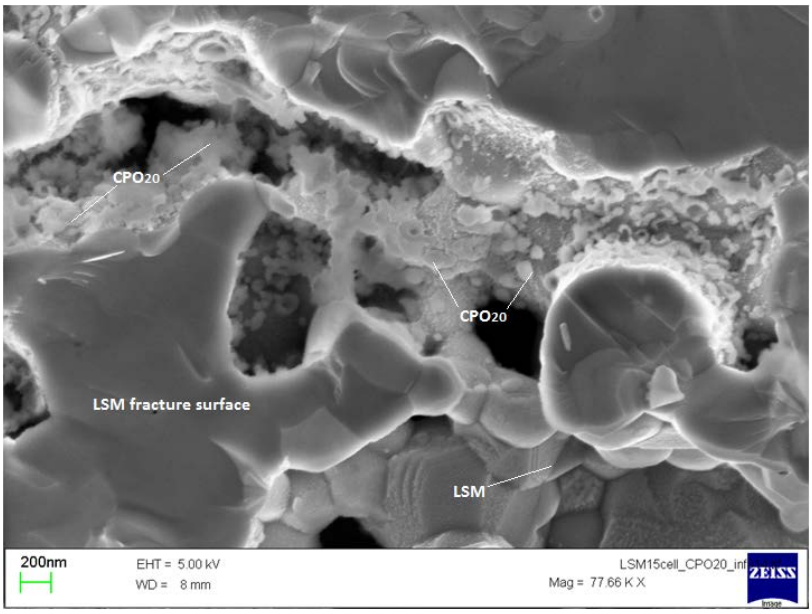


**Figure 3**: SEM micrograph of a $CPO_{20}$ infiltrated cell.

The good coverage of $CeO_2$ and $CPO_{20}$ particles on the $LSM_{15}$-$CGO_{10}$ surfaces was noticeable; the particles were arranged along the walls of the pores without blocking them.

The formation of solid solution between Ce and Pr was guaranteed by the exothermicity of Triton X-100 decomposition.

Moreover, the XRD recorded on $CPO_{20}$ powder and visible in Figure 4 displays nearly all of the characteristic reflections corresponding to the fluorite structure of $CeO_2$. No crystalline phases except the fluorite-type solid solution were detected, suggesting direct solid solution formation.

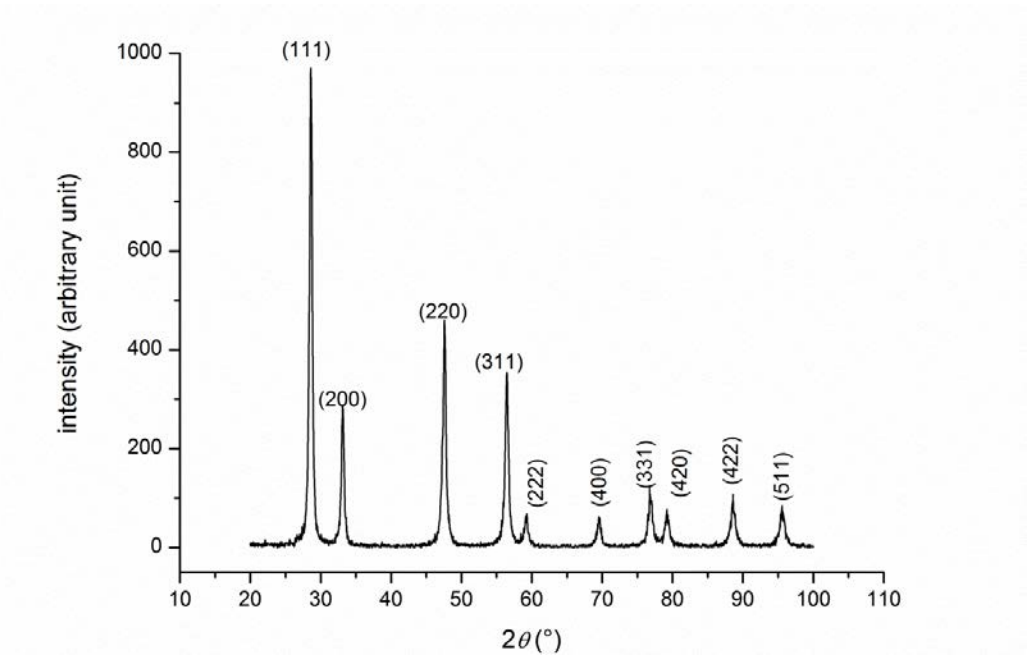


**Figure 4:** XRD powder pattern of $CPO_{20}$ powder.

The $CPO_{20}$ particles showed different agglomeration behaviour with respect to $CeO_2$, one that has already been reported by Kharton et al. [18], where a $Ce_{0.8}Gd_{0.18}Pr_{0.02}O_{2-\delta}$ composite showed segregated Pr and Gd enriched particles along the grain boundaries. Co-doping with Pr increased the tendency for phase segregation along the grain boundaries of $Ce(Gd)O_{2-\delta}$. Also in this case, the introduction of $Pr^{+4}$ ions could have changed the nucleation properties of $CeO_2$ on the $LSM_{15}/CGO_{10}$ composite backbone, giving rise to a diffusion of Pr ions into $LSM_{15}$ and $CGO_{10}$. However, the formation of perovskite phases like $PrMnO_3$ could not be excluded.

$CeO_2$ was found to have a specific area of 2.43 $m^2/g$. $CeO_2$ area is higher than the one of $CPO_{20}$ which is equal to 1.64 $m^2/g$. This is due to the different particle morphologies. From the SEM micrographs it was possible to observe that the distribution of $CeO_2$ particles was more uniform and the adhesion of $CeO_2$ on the backbone surface was more optimal than $CPO_{20}$. Additionally, the infiltration procedure was able to increase the specific area of the backbone cell by at least one order of magnitude [19].

### 5.5.2 Catalyst activity tests

Figure 5 shows the intrinsic catalytic reaction rate towards propene oxidation measured at open circuit voltage (OCV).

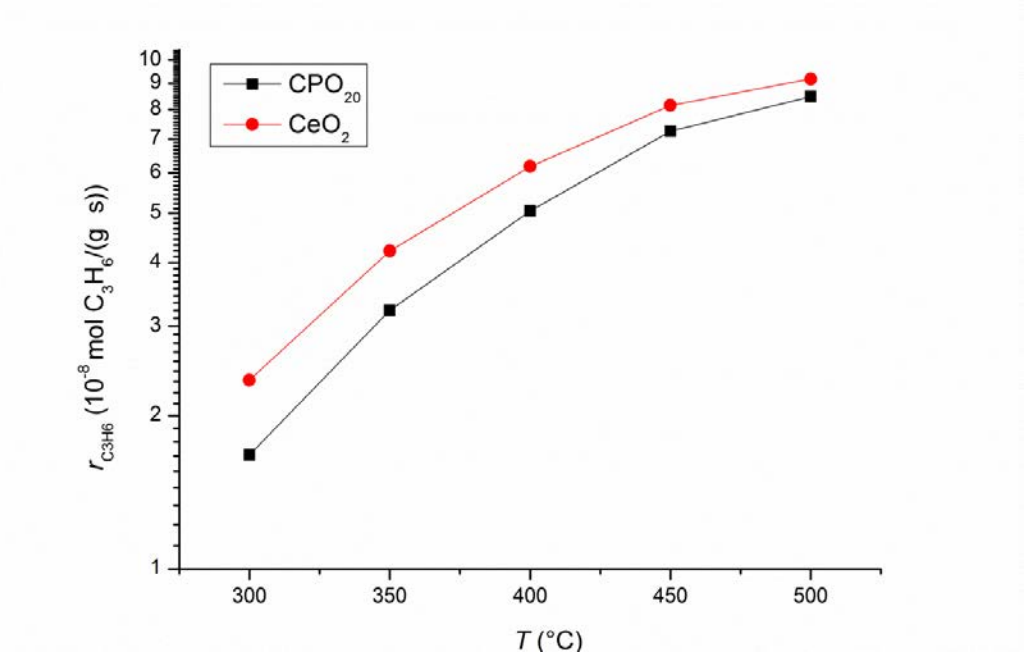


**Figure 5**: Reaction rate for propene oxidation as a function of temperature in 1000 ppm $C_3H_6$ and 10% $O_2$ at 2 L/h.

The $CeO_2$ infiltrated cell showed higher reaction rates with respect to the $CPO_{20}$ infiltrated cell at all temperatures; the conversions of propene at 400 ºC for $CeO_2$ and $CPO_{20}$ infiltrated cells were 46.8% and 37.7%, while at 300 ºC they were 17.8% and 13.5%, respectively. The better activity of $CeO_2$ at low temperature could be attributed only partially to the larger specific surface area. The selectivity towards $CO_2$ was almost 100% at all temperatures for $CeO_2$, but only 91-92% for the $CPO_{20}$ infiltrated cell. Reddy et al. using XPS reported an enrichment of Pr in the surface region up to 44%, higher than that nominal content of 20% [26]. A partial surface segregation of Pr forming $Pr_6O_{11}$ could be the reason for the lower activity of $CPO_{20}$. $Pr_6O_{11}$ is recognised as a good catalyst for methane and CO oxidation due to its high redox potential, but the catalytic activity of praseodymia seems to be limited by the difficult reoxidation of $Pr_2O_3$ [20]. $Pr_6O_{11}$ could have some activity for propene oxidation, but it could be relatively inactive compared to ceria due to the high stability of reduced $Pr_2O_3$. The lower selectivity to $CO_2$ observed for $CPO_{20}$ with CO formation suggested that oxygen from $Pr_6O_{11}$ was not utilised in the same way as from ceria under the reaction conditions. Zhao et al. observed a decrease in reaction rate for n-butane oxidation with the incorporation of $Pr^{+4}$ into ceria. This decrease in reaction rate was anyway lower than the reaction rate decrease observed for ceria doped with

Sm, Gd, Nb and Ta [15]. As observed by Zhao et al. for the oxidation of n-butane over ceria and Samaria-doped ceria (SDC), the common assumption that doping ceria will increase its activity is not always correct [21]. If we compare the reaction rate of the backbone (3.88 $10^{-8}$ mol $C_3H_6/(s\times g)$) at 400 ºC as reported in [19], infiltration resulted in a substantial increase in reaction rate. The extraction of apparent activation energy was outside the scope of this analysis, and observing a slope change in the reaction rate curves due to possible diffusion limitations of reactants already between 350 ºC and 400 ºC, is difficult.

During the application of anodic polarization, being this reactor symmetric, one side worked as anode and the other side as a cathode. At the cathodic side molecular oxygen was reduced to lattice oxygen, which was then pumped by this anodic voltage through the oxygen vacancies of $CGO_{10}$ to the surface of $LSM_{15}$. The pumped oxygen lattice on the anodic side can react directly with adsorbed propene to form $CO_2$ and $H_20$ or recombined to molecular oxygen through oxygen evolution reaction. Figure 6 shows the effect of polarisation at +4 V on the infiltrated cells at different reaction temperatures, expressed as rate enhancement ratio.

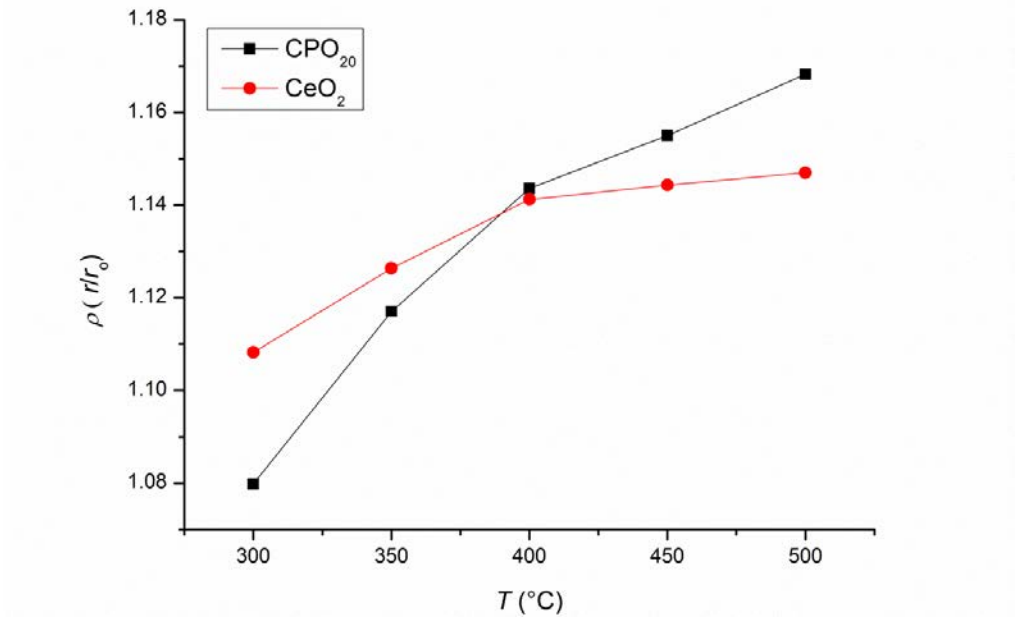


**Figure 6**: Rate enhancement ratios of $CeO_2$ and $CPO_{20}$ infiltrated cells as a function of temperature.

It was possible to observe that the polarization effect was higher at low temperature for $CeO_2$ than for $CPO_{20}$, but it became more prominent on $CPO_{20}$ with increasing temperature. The $CeO_2$ infiltrated cell reaction enhancement curve strongly flattened at temperatures higher than 400 °C possibly due to limiting reactant diffusion limitations inside the electrode pores; this phenomenon might limit the effect of polarization on propene conversion.

The rate enhancement ratio behaviour could be attributed to two types of regimes. Ceria has very low electronic and ionic conductivity, the latter being only 3% of the total conductivity [22]. At low temperature (300-400 ºC), some of the oxygen ions thus have the opportunity and time to backspillover from $CGO_{10}$ on the deposited ceria surfaces and act as electronegative promoters of propene oxidation without recombine to form molecular oxygen. The increased propene reaction rate on $CeO_2$ at low temperatures could also be due to the contribution of a polarisation-induced double layer established between the $O^{2-}$ back-spill on ceria surfaces and the $O_2$ adsorbed from the gas phase.

On the contrary, $CPO_{20}$ has much higher electronic and ionic conductivity, behaving as a mixed ionic electronic conductor; the mixed conductivity was able to strongly expand the TPB area. This characteristic hindered the possible back-spill of oxygen ions to the $CPO_{20}$ surfaces because the kinetics of promoter consumption, in the case of $CPO_{20}$, might be fast due to the high reactivity of the promoter at the three phase boundaries, as suggested by Roche et al. [11]. The $O^{-2}$ recombination and following oxygen evolution, although the latter contributes to the total current, did not produce any increase in propene conversion. Figure 7 shows the behaviour of faradaic efficiency for $CeO_2$ and $CPO_{20}$. It is possible to observe that the two samples showed similar efficiency at high temperature (450-500 ºC). Below this temperature range $CPO_{20}$ exhibited a quasi-flat faradaic efficiency with decreasing temperature; $CeO_2$ instead showed a sharp increase with decreasing temperature. The explanation is given in the electrochemical characterization section.

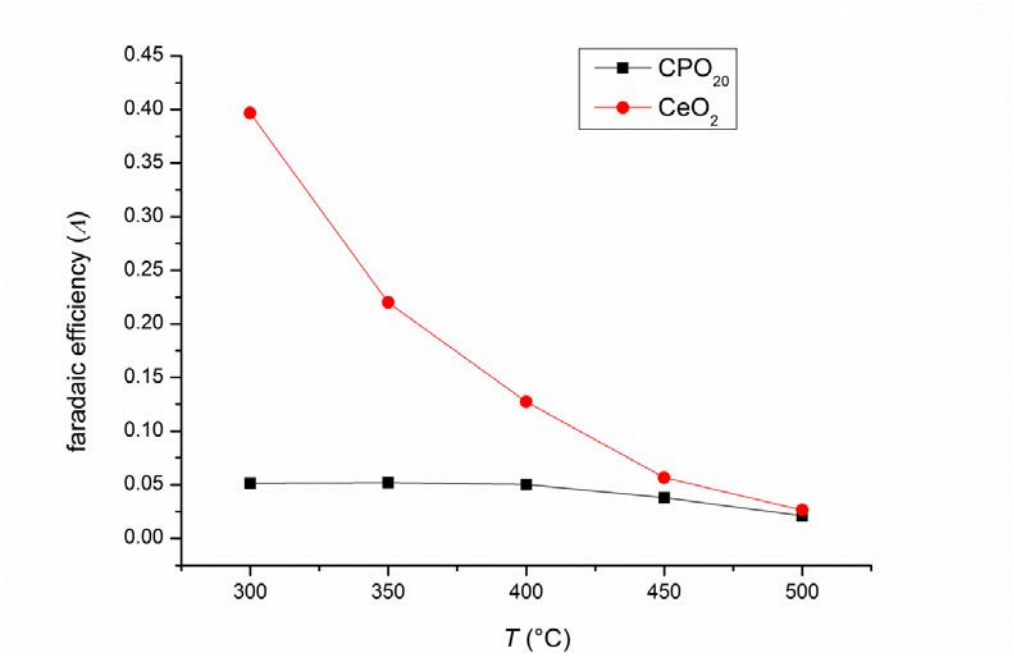


**Figure 7**: Faradaic efficiency of $CeO_2$ and $CPO_{20}$ infiltrated cells versus temperature.

### 5.5.3 Electrochemical characterization

Figures 8 and 9 show the Arrhenius plots of polarization resistance ($R_p$) at OCV and under polarisation for $CPO_{20}$ and $CeO_2$ extracted from impedance spectra.

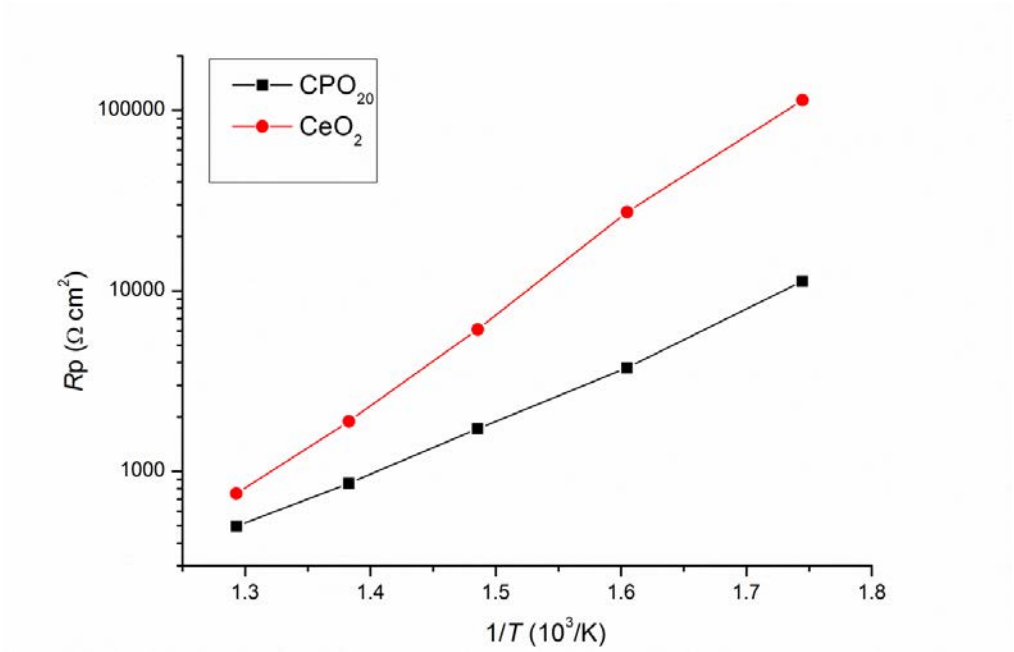


**Figure 8** : Arrhenius plots of polarisation resistance ($R_p$) for $CeO_2$ and $CPO_{20}$ infiltrated cells recorded at OCV with 1000 ppm $C_3H_6$, 10% O2, 2L/h.

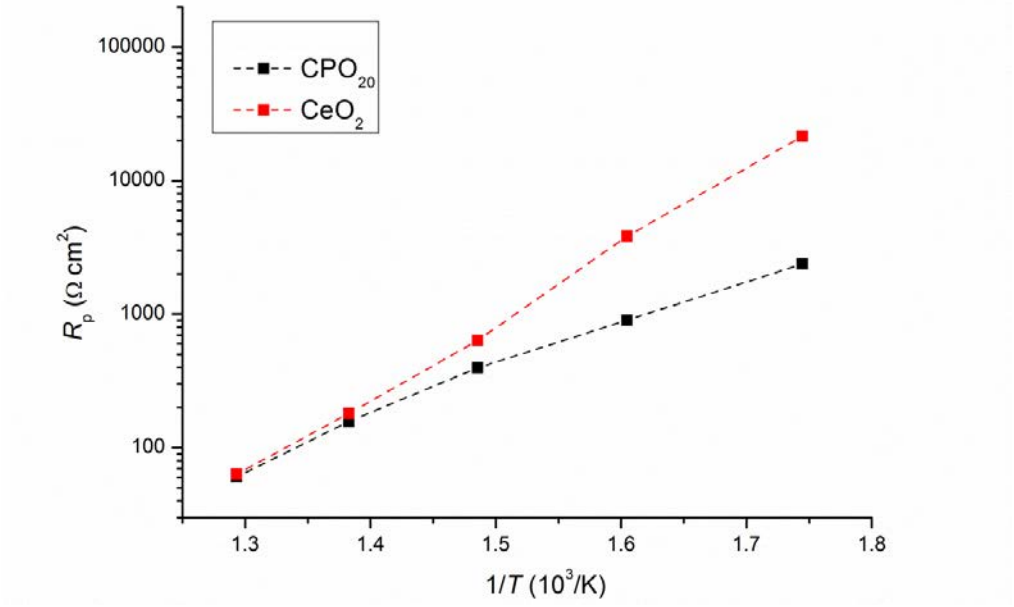


**Figure 9:** Arrhenius plots of polarization resistance ($R_p$) for $CeO_2$ and $CPO_{20}$ infiltrated cells at +4 V with 1000 ppm $C_3H_6$, 10% O2, 2L/h.

$CPO_{20}$ infiltration gave a better electrode performance, showing lower polarisation resistance at lower temperatures compared to $CeO_2$. This could be attributed to the mixed ionic-electronic conduction behaviour of $CPO_{20}$. $CPO_{20}$ infiltration was also able to expand the TPB area and decrease the resistance associated with electrochemical reactions occurring on the surface. The activation energy of the $R_p$ for $CPO_{20}$ was 0.59 ± 0.03 eV, much lower than the activation energy of the $CeO_2$ infiltrated cell (0.97 ± 0.04 eV). This meant that the electrode performance for $CPO_{20}$ was less susceptible to temperature decreases than for $CeO_2$. The activation energy of $CeO_2$ was close to the value of the backbone cell at OCV (0.93 ± 0.04 eV) reported in previous study [19]. The infiltration of $CeO_2$ was thus able to decrease the polarization resistance of the backbone without changing the reaction mechanism. Typical EPOC behaviour could be visible in this case where a catalyst with high catalytic performance, like $CeO_2/LSM_{15}$, is coupled with an electrode with low exchange current at low temperature.

Figure 9 illustrates the Arrhenius plot of the polarization resistance measured at +4 V.

At high temperatures (450-500 ºC) the decrease of $R_p$ for $CeO_2$ upon anodic polarization was found to be very high, reaching resistance values similar to those obtained for $CPO_{20}$. Presumably the polarization response of the backbone became predominant on the infiltrated material polarization response. For this reason, at these temperatures, the faradaic efficiencies for both cells exhibited similar low values. At temperatures below 450 ºC, the effect of anodic polarization on $CeO_2$ polarization resistance drastically decreased; high $R_p$ coupled with good enhancement ratio ($\rho$) value caused the sharp increase of efficiency observed for $CeO_2$ in Figure 7. For $CPO_{20}$, however, the effect of polarization decreased with much lower activation energy: low $R_p$ coupled with low enhancement ratio ($\rho$) caused the flattening of the efficiency observed for $CPO_{20}$. The activation energy value extrapolated at high temperature for $CPO_{20}$ curve was 0.82 ± 0.03 eV. The activation energy extracted for temperatures between 400 ºC and 300 ºC was 0.61 ± 0.01 eV instead; presumably the effect of mixed conductivity on $R_p$ became predominant in this temperature range causing the slope change. The activation energy of polarization resistance ($R_p$) measured under polarization of +4 V for $CeO_2$ was 1.13 ± 0.05 eV; both the infiltrated exhibited an increase of activation energy under anodic voltage. This change of activation energy could be due to a modification of reaction mechanism establishing under polarization.

In order to obtain high faradaic efficiency it is necessary to reduce the speed of $O^{2-}$ recombination to molecular oxygen and so to increase the promoter lifetime. In the case of $CPO_{20}$ the kinetic of promoter consumption was very high (low $R_p$) also at low temperature if compared to $CeO_2$; this was the cause of low faradaic efficiency.

Figures 10 and 11 show the impedance spectra of $CeO_2$ and $CPO_{20}$ infiltrated cells recorded at OCV and +4 V at 450 °C together with the Bode plot of the imaginary part of the recorded spectra.

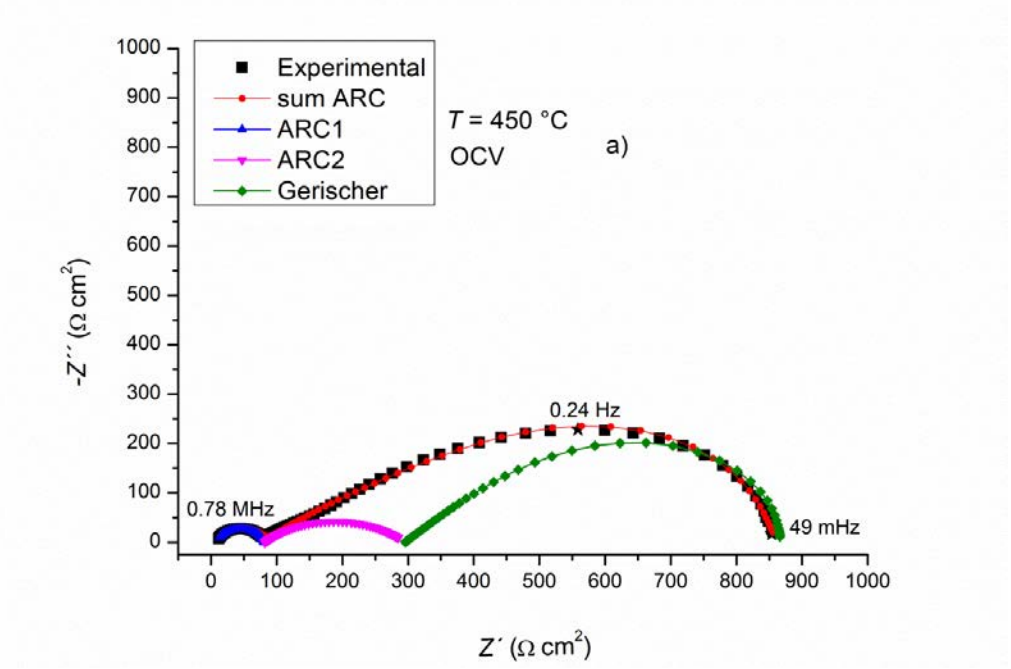


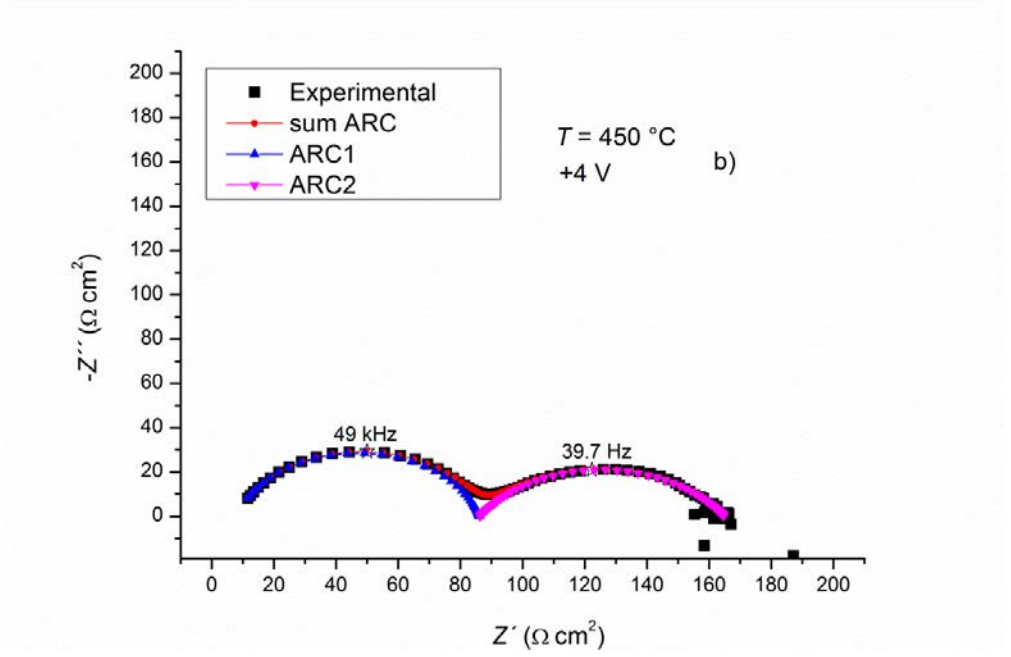

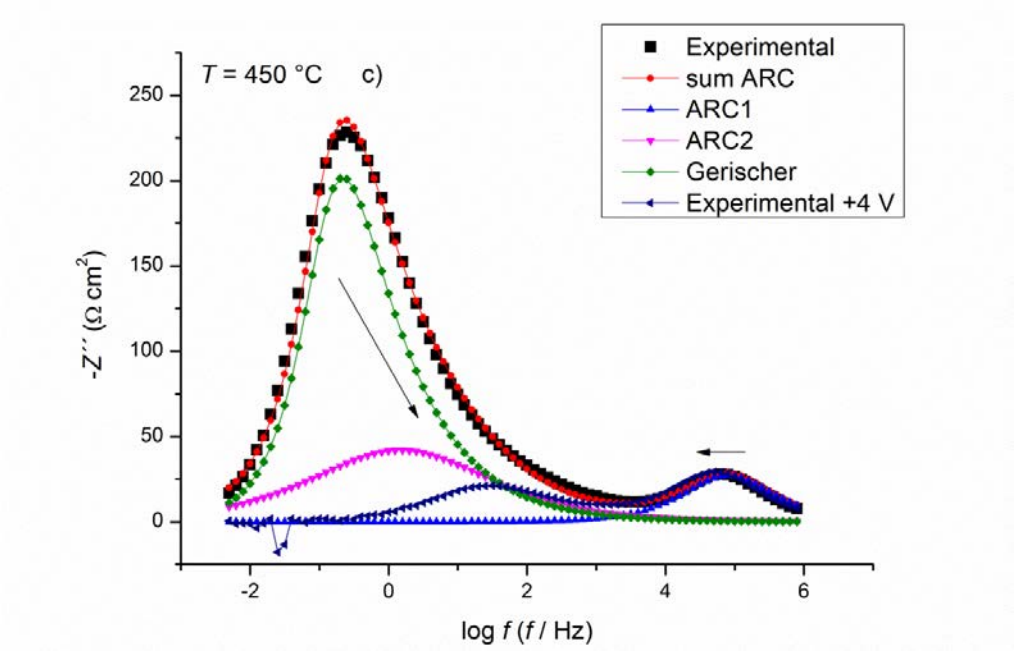


**Figure 4**: Nyquist plots of impedance spectra of a $CPO_{20}$ infiltrated cell recorded at a) OCV, b) +4 V and c) Bode plot of impedance spectra at 450 °C and OCV with 10% $O_2$ and 1000 ppm $C_3H_6$ at 2 L/h.

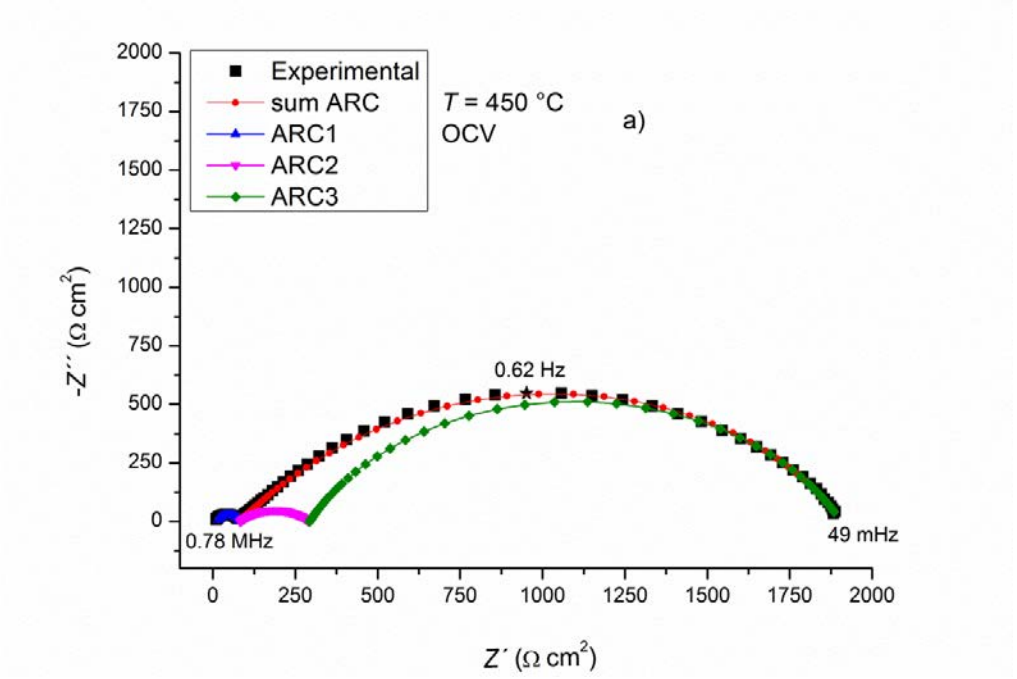

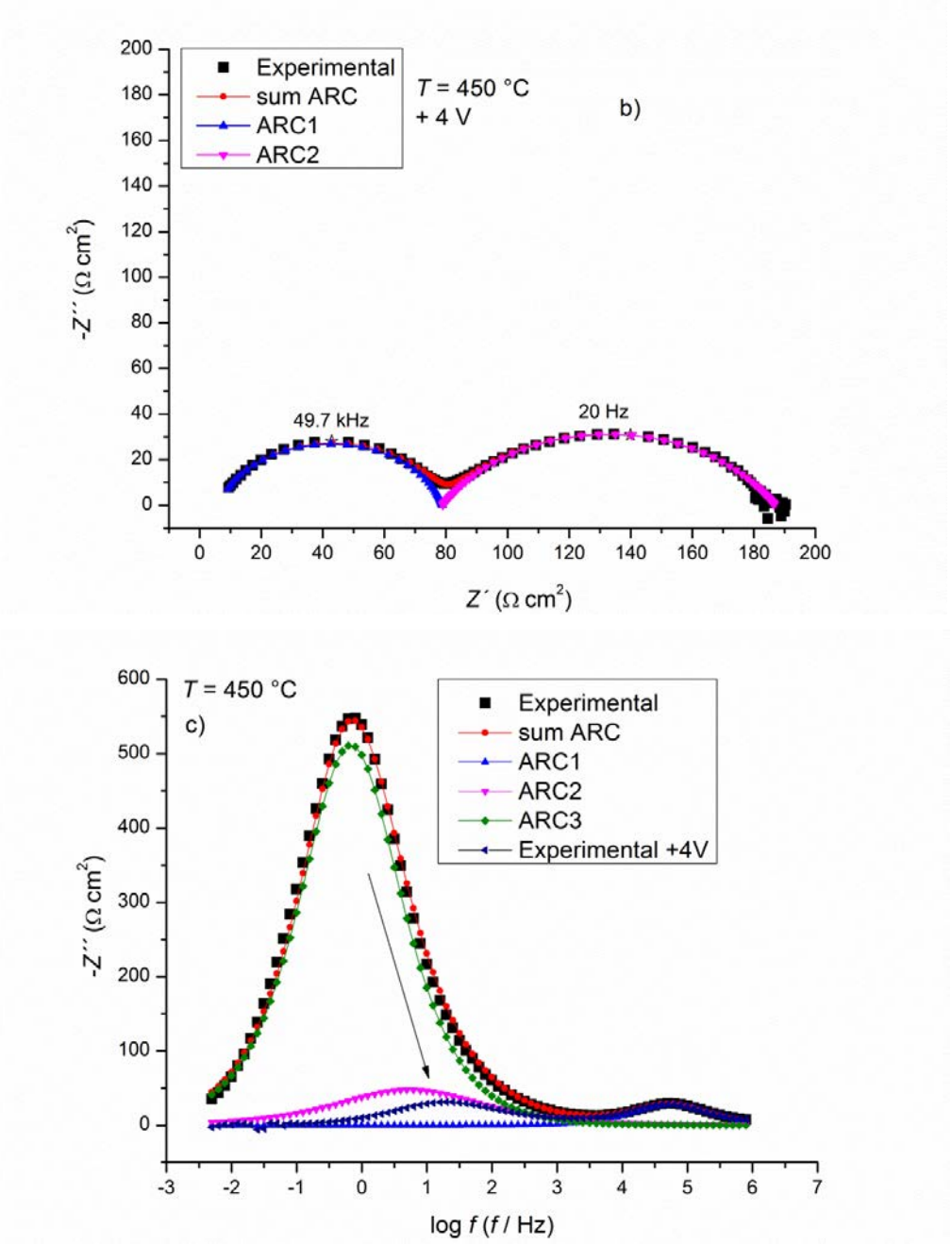


**Figure 11**: Nyquist plots of impedance spectra of a $CeO_2$ infiltrated cell recorded at a) OCV, b) +4 V and c) Bode plot of the impedance spectra as a function of frequency at 450 °C and OCV with 10% $O_2$ and 1000 ppm $C_3H_6$ at 2 L/h.

At least two depressed arcs were visible in these plots. The polarization to +4 V (0.8 mV/cell) strongly affected the impedance responses; a strong decrease in resistance was visible for the peak at low frequency for both infiltrated cells, as was an increase in characteristic peak frequency. Additionally, the impedance spectra under polarisation clearly displayed only two well defined depressed arcs where the impedance contribution at medium frequency either disappeared or merged with the impedance response at low frequency. Moreover, the inclined line visible at medium frequency completely disap-

peared when polarisation was applied. The impedance contribution at high frequencies (Figures 10c and 11c) was differently affected by polarization depending on the infiltration material. This impedance contribution at this temperature was likely due to oxygen ion transport from the electrolyte to the $LSM_{15}$ electrode. The peak for the $CeO_2$ infiltrated cell was not affected by polarisation and the imaginary part of the spectra recorded under polarisation completely overlapped with the spectra recorded at OCV. On the contrary, the high frequency peak of the $CPO_{20}$ infiltrated cell showed a small increase in resistance when polarised at +4 V associated with a peak frequency decrease. This meant that, in the case of $CPO_{20}$, it was possible to observe a charge transfer contribution even at these high frequencies; the overlapping between oxygen ion transport and electrode reactions could be due to the mixed conductivity of $CPO_{20}$.

The distribution of relaxation times (DRT) analysis visible in Figure 12 associated to the impedance spectra in oxygen and propene at 450 °C for $CeO_2$ and $CPO_{20}$ showed three main peaks at high, medium and low frequencies.

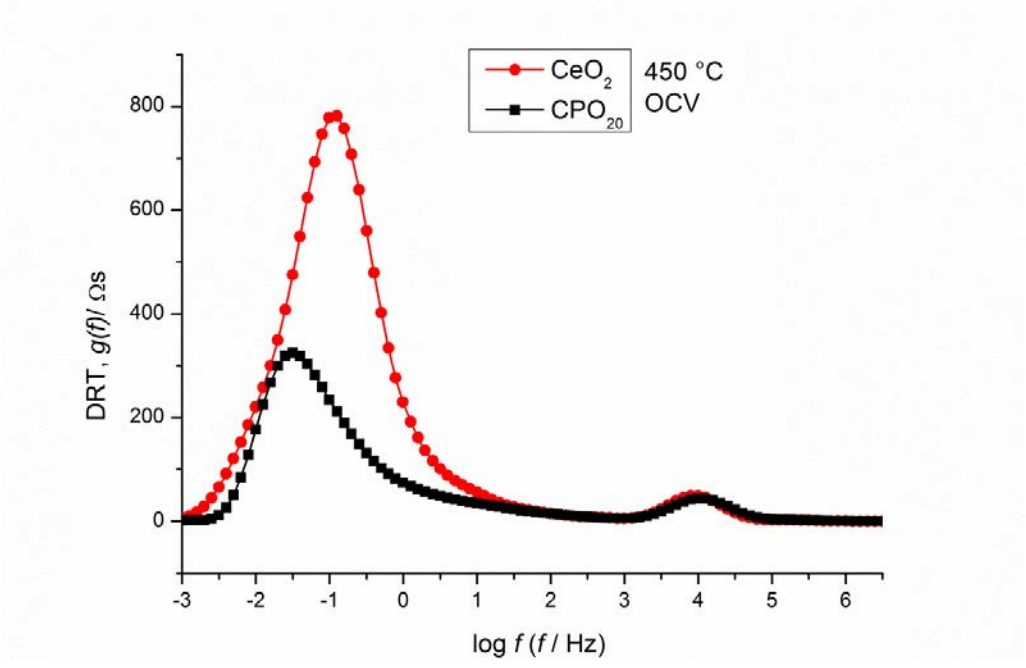


**Figure 12**: Distribution of relaxation times (DRT) for $CeO_2$ and $CPO_{20}$ spectra recorded at 450 °C and OCV with 10% $O_2$ and 1000 ppm $C_3H_6$ at 2 L/h.

The peak at medium frequency was not well resolved and appeared as a shoulder overlapping the main peak at lower frequencies. The peak at high frequency (10.4 kHz) appeared at the same frequency and had similar resistance for both of the infiltration materials, so it was likely independent of infiltration material at high temperatures and at OCV. However, this effect could be attributed only to the backbone. The reconstruction of $CeO_2$ impedance spectra through DRT analysis was only possible using three RQ ele-

ments, confirming the presence of a process at medium frequency. The DRT analysis for the $CPO_{20}$ infiltrated cell showed behaviour typical of a Gerischer element at low frequency, as reported by Endler et al. with a single cell using a LSCF cathode [23]. The mixed ionic electronic behaviour of $LSM_{15}$ usually visible at high cathodic polarization or low partial pressure of oxygen, associated to superficial oxygen vacancy formation, was enhanced by $CPO_{20}$ infiltration. The Gerischer behaviour reflected that the overall oxygen reduction reaction on the mixed conducting $CPO_{20}$ layers proceeded under the conditions where diffusion of oxygen vacancies in the electrode and diffusion of adsorbed oxygen species on electrode surface are kinetically coupled with the electrode exchange reaction between oxygen vacancies and gaseous oxygen (charge transfer reaction) at the electrode/gas interface [24].

Figure 13 and 14 exhibit the DRT analysis of the influence of reaction atmosphere at 500 °C on impedance spectra for the $CPO_{20}$ and $CeO_2$ infiltrated cell, respectively. From Figures 13 and 14, the relaxation at high frequency and the shoulder at medium frequency were not dependent on reaction atmosphere; these peaks could then be associated to oxygen ion transport in the electrolyte and across the electrolyte-electrode interface at TPB.

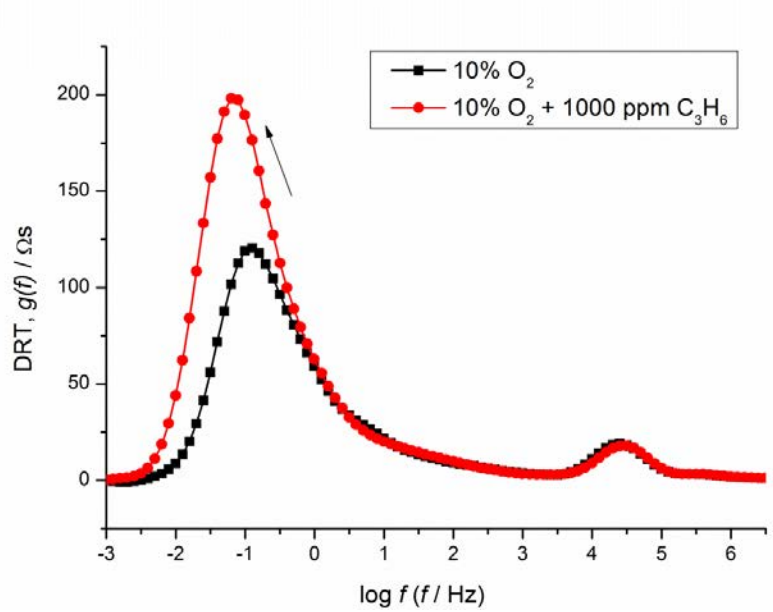


**Figure 13**: Distribution of relaxation times (DRT) in the $CPO_{20}$ spectra recorded at 500 °C and OCV with 10% $O_2$ and 10% $O_2$ + 1000 ppm $C_3H_6$ at 2 L/h.

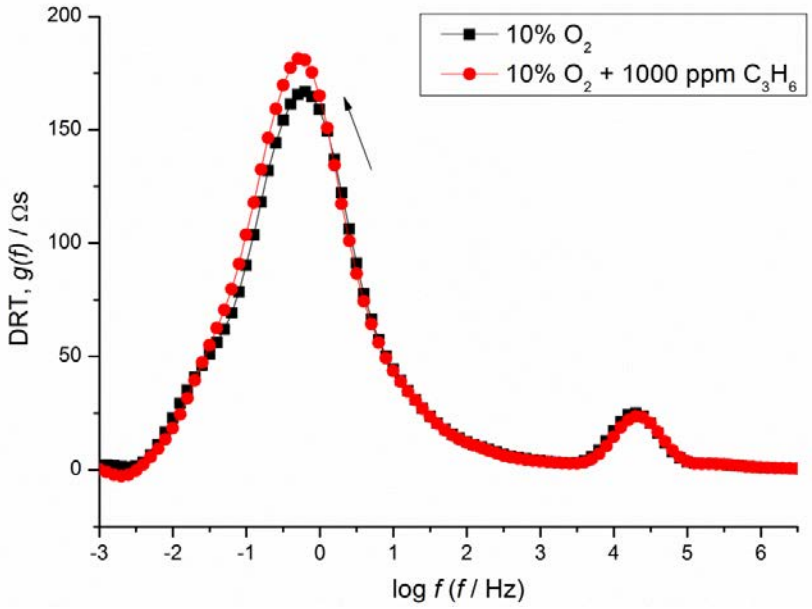


**Figure 14**: Distribution of relaxation times (DRT) in the $CeO_2$ spectra recorded at 500 °C and OCV with 10% $O_2$ and 10% $O_2$ + 1000 ppm $C_3H_6$ at 2 L/h.

The relaxation at low frequency exhibited an increase in resistance associated to a frequency decrease when propene was introduced into the reactor. This behaviour could be due to oxygen dissociation and transport on the $LSM_{15}$ surface. These suprafacial processes on the electrode were coupled with electrochemical process, as verified by the effect of polarization on resistance in the low frequency arc (Figure 10c and 11c). Propene adsorption on $LSM_{15}$ and $CGO_{10}$ surfaces decreased the rate and interfered with the oxygen exchange reaction on the electrode surface, increasing the resistance of the low frequency peak.

This behaviour was exhibited by the $CeO_2$ infiltrated cell (Figure 14), as relaxation at high frequency was not affected by the reaction atmosphere. The relaxation at low frequency increased resistance and moved to slightly lower frequencies with the introduction of propene. In the case of $CeO_2$, this effect was less pronounced than for the $CPO_{20}$ cell (Figure 13). Zheng Y. et al. studied the effect of oxygen vacancies on the oxygen reduction reaction (ORR) on $La_{0.8}Sr_{0.2}MnO_3$ [25]. After a 3 hours cathodic polarization at 800 °C, the size of polarization resistance on impedance spectra reduced significantly because of the *in-situ* generation of oxygen vacancies. The size of low frequency arc increased slightly with the variation of methane partial pressure at constant oxygen partial pressure. These changes were more significant than those before the cathodic polarization but still lower than those generated by oxygen partial pressure change. This experiment demonstrated that oxygen and methane began to have a competitive adsorption on *in-situ* generated oxygen vacancies created by cathodic polarization.

$CeO_2$ and $CPO_{20}$ are well known oxygen buffers with high oxygen storage/release capacity (OSC) due to the high mobility of lattice defects, like oxygen vacancies. Reddy et al. showed that a ceria-praseodymia system exhibited five times higher OSC than a pure ceria sample [26]. The high OSC of ceria-praseodymia was due to the increased presence of oxygen vacancies respect to $CeO_2$ and cooperative $Ce^{4+}/Ce^{3+}$ and $Pr^{4+}/Pr^{3+}$ redox couples. For this characteristic the influence of the adsorption of propene on impedance spectra was more pronounced on $CPO_{20}$ than on $CeO_2$; this effect was clearly visible on DRT spectra reported in Figure 13.
Thus the efficiency towards oxygen storage capacity was a measurement of sensitivity of the electrode to the reaction atmosphere change.

### 5.5.4 Spectra deconvolution: $CPO_{20}$ infiltrated cell

The spectra were modelled using R(RQ)(RQ)(RQ) and R(RQ)(RQ)G as equivalent circuits at OCV for $CeO_2$ and $CPO_{20}$ [19]. In this case, the Gerischer element (G) was used to account for the mixed ionic and electronic behaviour of $CPO_{20}$.
The simulation of the $CPO_{20}$ infiltrated cell was made using two models. The first model with two CPE elements and one Gerischer element was used at temperatures between 500 °C and 400 °C. The second model with three CPE elements was used at temperatures below 400 °C. As reported by Fagg et al. [27], at temperatures close to 350 °C the total conductivity in air for a $Ce_{0.8}Pr_{0.2}O_{2-\delta}$ system showed decreased activation energy as the conductivity became predominantly electronic through the reoxidation of $Pr^{3+}$ to $Pr^{4+}$ with decreasing of oxygen vacancies. The evaluation of the model was based on fitting residuals, accepting the lowest residual as the most reliable fitting. The choice of model was thus based on reaction temperature and was able to take into account the change in ionic conductivity of $CPO_{20}$. The high frequency process observed in the spectra (ARC1) had activation energy of 0.78 ± 0.06 eV. The arc closed completely at high frequency when the temperature reached 300 °C. The near equivalent capacitance lay between $2.04 \times 10^{-8}$ F/cm$^2$ and $2.8 \times 10^{-8}$ F/cm$^2$ and was independent of temperature between 500 °C and 350 °C. The independence from temperature and gas phase shift (Figure 13) attributed this arc to the migration of oxygen ions from the electrolyte to the $LSM_{15}/CGO_{10}$ electrode
At 300 °C an increase in the capacitance to $7.5 \times 10^{-8}$ F/cm$^2$ was observed. This behaviour could have been due to the overlap of the electrolyte grain boundaries response with the oxygen ion migration. This was not clearly visible in the DRT analysis likely due to the time constants overlap, but it was confirmed by the full closing of the arc at 300 °C.

The extraction of the activation energy for this high frequency process was performed using the resistance values obtained at temperatures above 300 °C. The high frequency arc (ARC 1) was slighlty influenced by polarisation at +4 V, an increase in arc resistance for temperatures below 500 °C and a small increase in activation energy (0.86 ± 0.1 eV) were observed. At the same time the near equivalent capacitance increased to 3.2-4.1 × $10^{-8}$ F/cm$^2$.

The process belonging to the medium frequency region (ARC 2) had an activation energy of 0.58 ± 0.1 eV and a near equivalent capacitance that increased with temperature from 2.2 × $10^{-4}$ F/cm$^2$ at 300 °C to 5 × $10^{-4}$ F/cm$^2$ at 500 °C. This arc showed a slight dependence on reaction atmosphere and due to the increase of capacitance with the temperature, this arc could be correlated to the adsorption, diffusion or charge transfer at or near the three-phase boundary (i.e., increasing temperature will increase the TPB zone and thereby increase the associated capacitance). This part of the spectrum was fitted with a CPE element having n-values between 0.45 and 0.53 depending on the temperature. The slope of this arc, the ratio of $-Z''$ and $Z'$, calculated from the Nyquist plot increased with increasing temperature from 0.25 to 0.5. The distorted shape of the medium frequency arc was explained by the porous structure of the electrode. For an electrode-process described by an R-CPE parallel circuit, the impedance response in a porous electrode will be approximated by the square root of the impedance of the R-CPE element [28]:

$$Z_{R-CPE,porous} = \sqrt{Z_{R-CPE}}$$

In Figure 10b, the application of +4 V was able to strongly affect ARC 2 and ARC 3, reducing them to a single process/arc. In this case it was possible to observe from the Nyquist plot in Figure 10b two well separated arcs over the entire spectra. The low frequency arc was associated to a two orders of magnitude increase in peak characteristic frequency and to a near equivalent capacitance of 4.9-9.4 $10^{-5}$ F/cm$^2$, but the dependence on temperature was not clear. The capacitance increased with decreasing temperature until 400 °C, and then decreased again at 350 °C and 300 °C. The polarisation decreased capacitance by one order of magnitude with respect to OCV. The second arc clearly lost its characteristic slope during polarisation. In this case, the n-value of the CPE used was between 0.59 and 0.64. The new arc formed under polarization had an activation energy of 0.59 ± 0.07 eV, similar to the value obtained at OCV. We could therefore argue that the polarisation only affected the third arc. ARC 3 was modelled using two different elements. At temperatures of 350 °C and 300 °C, an RQ element was

used to simulate this arc. The spectra for both temperatures did not close at lower frequencies, complicating the fitting. This arc was strongly influenced by reaction atmosphere, had an activation energy of 0.79 ± 0.06 eV and a near equivalent capacitance of 2.6-2.8 × $10^{-3}$ F/$cm^{2.}$ At temperatures between 400 °C and 500 °C, an RG element was used to simulate the spectra. Such an impedance response has been argued to arise in both mixed electronic and ionic conductors, such as $LaSrCoO_3$, and in LSM/YSZ when cathodically polarised. This characteristic was not visible on $CeO_2$ infiltrated cell spectra, so it was possible that this behaviour was a result of $CPO_{20}$ infiltration where oxygen ion diffusion through $CPO_{20}$ was coupled with oxygen ion discharge at the extended TPB.

In mixed ionic electronic conductor cathodes, oxygen ion diffusion is argued to occur primarily along bulk paths, giving high capacitance values near 1 F/$cm^2$ [29]. In this study, the capacitance was found to be 1.1×$10^{-3}$ F/$cm^2$ at 500 °C and increased to 3.5×$10^{-3}$ F/$cm^2$ at 400 °C. These values were far from values found by Adler [29] (1 F/$cm^2$). A value of 100 µF was also found by Hjalmarsson et al. using $LaCoNiO_3$-CeGdO and attributed to oxygen transport confined to the electrode surface rather than the bulk [30]. Oxygen ion diffusion could follow two different paths: along the electrode surface ($LSM_{15}$) or along bulk paths ($CPO_{20}$). The activation of the resistance, $R_G$, associated to a Gerischer element was found to be 0.44 ± 0.05 eV.

### 5.5.5 Spectra deconvolution: $CeO_2$ infiltrated cell

The spectra of the $CeO_2$ infiltrated cell were modelled using 3 CPE elements in series with a resistance R(RQ)(RQ)(RQ) for all temperatures. The spectra at 350 °C and 300 °C recorded at OCV also did not close at low frequencies. The first process at high frequencies visible in DRT analysis of Figure 12 was associated to the first arc (ARC 1). The activation energy of this arc was 1.14 ± 0.15 eV at OCV and was surprisingly higher than the value obtained for the $CPO_{20}$ cell. The difference in ARC 1 resistance between $CeO_2$ and $CPO_{20}$ cells is mainly visible for temperatures between 400 °C and 300 °C and not for higher temperatures. This behaviour is confirmed by DRT analysis of Figure 12, Figure 13 and 14 where the two cells show a similar resistance for the relaxation contribution at high frequency.

The application of +4 V polarisation had no effect on the resistance of this arc with an observed activation energy of 1.13 ± 0.08 eV. It was thus possible to infer that also this part of the spectra could be influenced by the infiltration material especially at medium-low temperature and could contain overlapping processes. This overlap would compli-

cate separation of two close relaxation times belonging to the infiltrated material and the backbone.

As verified for $CPO_{20}$, the near equivalent capacitance of this arc was almost unaffected by temperature both at OCV and at +4 V (values between 4.5 and 4.7 × $10^{-8}$ F/$cm^2$). At 300 °C, where the first arc was fully closed on the high frequency side, the capacitance dropped to 2.9 × $10^{-8}$ F/$cm^2$. At this temperature it was possible to measure the electrolyte grain boundaries contribution to conductivity. Additionally, this arc was not affected by reaction atmosphere. Analysing its characteristics, this arc was attributed to the migration of oxygen ions from the electrolyte to the $LSM_{15}/CGO_{10}$ electrode.

As observed for $CPO_{20}$, the polarization effect for the $CeO_2$ infiltrated cell was also visible on the second/third arc (ARC 2-ARC 3) and associated to a strong decrease in resistance and increased peak frequency (Figure 11c and 11b). This part of the spectrum was modelled with two RQ at OCV. For ARC 2 (Figure 11a), n-values used for the fitting ranged from 0.49 to 0.68 and the activation energy was 0.79 ± 0.03 eV. The near equivalent capacitance increased from 1.3 to 2.1 × $10^{-4}$ F/$cm^2$ with increasing temperature. In addition, this arc was also affected by the infiltration material. The two modelled arcs visible at OCV merged into one when the cell was polarized at +4 V (Figure 11b). The activation energy measured at +4 V was 1.11 ± 0.06 eV with only one arc observable at this voltage, and contrary to $CPO_{20}$, this activation energy likely belonged to a different process. The near equivalent capacitance increased from 5.2 × $10^{-5}$ F/$cm^2$ at 300 °C to 8 × $10^{-5}$ F/$cm^2$ at 500 °C. The polarization, as observed for $CPO_{20}$, was able to decrease the capacitance by one order of magnitude. The temperature dependence, the polarisation effect and the insensitivity to atmosphere (Figure 14) assigned this arc to the charge transfer near or at the TPB.

The third arc (ARC 3) was only modelled and visible at OCV. This arc was affected by reaction atmosphere, as shown in the DRT analysis of Figure 14, and by temperature with an activation energy of 0.98 ± 0.04 eV. The near equivalent capacitance strongly increased with temperature from 8.6 × $10^{-5}$ F/$cm^2$ at 300 °C to 5.7 × $10^{-4}$ F/$cm^2$ at 500 °C. This process was thus related to the adsorption and dissociation of oxygen, as well as electrode reaction, on the catalyst/electrode surface.

For both infiltrated material, ARC 1 was attributed to oxygen ion transport between the electrolyte and LSM and to grain boundary conductivity; these processes were not faradaic. The strong resistance decrease upon polarization of ARC 2 and ARC 3 indicated that medium and high frequency part of the spectra contained a charge transfer contribution following the Butler-Volmer equation. This behaviour did not exclude the possibility that chemical/physical processes could contribute to the total resistance; these

processes, if associated to an electrochemical process, can exhibit the general Butler-Volmer behaviour [31]. According to C.J. Borja, [32] ARC 2 could be tentatively attributed to the charge transfer reaction taking place at the three phase boundaries:

$$O^{2-} \rightarrow O_{(TPB)} + 2e^{-}$$

The oxygen formed at TPB could undergo different reactions: it could recombine to form molecular oxygen, react with adsorbed propene giving rise to an increase of reaction rate or migrate over the entire gas-exposed catalyst electrode surface establishing an effective double layer able to increase the reaction rate above the faradaic limit (EPOC).

The ARC 3 was the most affected by introduction of propene in the gas mixture as also reported by Butlel with Pt/YSZ system [33]. Propene was strongly adsorbed on electrode surface; it is possible to argue that the introduction of propene could interfere with a process involving biatomic oxygen or dissociated oxygen on the surface. Kaloyannis et al. [34] reported a competitive adsorption mechanism of dissociative chemisorbed oxygen and propylene during electrochemical promotion studies with stronger binding of propylene than oxygen on the Pt catalyst surface. As illustrated before, the sensitivity to propene introduction was dependent on infiltrated material and especially on its oxygen vacancies mobility.

Upon applying positive potential the increase in catalyst work function is obtained primarily by the increase in the coverage of the backspillover oxide ions $O^{\delta-}$; the effects should be to enhance the reactivity of surface oxygen species coming from the gas phase and changing the adsorption strength of the adsorbates like oxygen and propene. The effect of polarization on impedance spectra in this work was visible at medium and low frequency associated to one order of magnitude decrease of both resistance and capacitance; the impedance spectra recorded under polarization did not show any new semicircle with high capacitance (> 200 μF/cm$^2$) as reported by Vayenas et al. [35] and attributed to backspillover oxygen semicircle. In this work EPOC behavior was not visible, probably due to the fast reaction of oxygen ions with another oxygen or with propene; the short lifetime of the oxygen ions hindered the possibility to the effective double layer formation between the catalyst and the gas phase. Kambolis et al. [36] did not observe EPOC in propane oxidation on LSCF/GDC electrode but it was observed on Pt infiltrated LSCF/GDC electrode, especially at low temperature (267 °C). The impregnation of Pt had two effects: increase the reaction rate towards propane oxidation at OCV and also the electrode polarization resistance ($R_p$) measured at OCV. These two combined effects gave rise to EPOC behavior.

## 5.6 Conclusions

The catalytic activity of a $CeO_2$ infiltrated cell in propene oxidation was shown to be superior to a $CPO_{20}$ system. The performance in terms of polarization effect on propene oxidation was strongly influenced by electrochemical and electrical properties of the infiltrated material. $CeO_2$ infiltrated cell exhibited high electrode resistance if compared to $CPO_{20}$. The activity of $CeO_2$ in propene oxidation was highly influenced by polarization, especially at low temperatures, and displayed good faradaic efficiency. The low electrode resistance of $CPO_{20,}$ instead, was detrimental to obtain good faradaic efficiency at low temperature, likely due to the short lifetime of oxygen ion promoters given by mixed conductivity of $CPO_{20}$.

Impedance spectra exhibited three main features belonging to oxygen ion migration/grain boundary conductivity, charge transfer reaction of oxygen ion and $O_2$ adsorption/dissociation on the electrode surface. The spectra recorded under anodic polarization showed a strong decrease of resistance and capacitance at medium-low frequency range while the contribution at high frequency was unaffected.

The introduction of propene in the reaction atmosphere affected the low frequency contribution on impedance spectra; $CPO_{20}$ was affected on a major extent, probably due to the higher oxygen vacancies mobility compared to $CeO_2$. EPOC behaviour was not visible for both the infiltrated cells; the backspillover of oxygen ions was hindered by the high reactivity of the oxygen promoter at the TPB.

## References


1. A. Wiartalla, L. Ruhkamp, Y. Rosefort, B. Maassen, B. Sliwinsky, T. Schornbus, T. Laible (2011) *SAE International* 2011-01-2097.
2. A. Miller Kristin, *The New England Journal of Medicine*, **356**, 447-458 (2007).
3. G. Oberdoster, *Inhalation Toxicology* ,**16**,437–445 (2004).
4. T.V. Jonhson, *SAE International* 2011-01-0304, (2011).
5. T.V. Choudhary, S. Banerjee, V. R. Choudhary , *Applied Catalysis A: General*, **234**,1-23. (2002).
6. N. Yamazoe, Y. Teraoka, *Catalysis Today,* **8**, 175-199 (1990).
7. T. Seyama, *Catalysis Review Science and Engineering*, **34**, 281-300 (1992).
8. R. Spinicci, M. Faticanti, P. Marini, S. De Rossi, P. Porta, *Journal of Molecular Catalysis,* **197**, 147-155 (2003).
9. M. Stoukides, C. G. Vayenas, *Journal of Catalysis* **70**, 137-146 (1981).
10. F. Gaillard, X. Li, M. Uray, P. Vernoux *Catalysis Letters*, **96**, 177-183 (2004).
11. V. Roche, E. Siebert, M.C. Steil, J.P. Deloume, C. Roux, T. Pagnier, R. Revel, P. Vernoux, *Ionics,* **14**, 235-241 (2008).
12. P. Tsiakaras, C. Athanasiu, G. Marnellos, M. Stoukides, J.E. ten Elshof, H.J.M. Bouwmeester, *Applied Catalysis A: General,* **169**, 249-261 (1998).
13. S.P. Balomenou, D. Tsiplakides, C.G. Vayenas, S. Poulston, V. Houel, P. Collier, A.G. Konstandopoulos, C. Agrafiotis *Topics in Catalysis*, **44**, 481-486 (2007).
14. M.V. Twigg, *Applied Catalysis B: Environmental*, **70**, 2-15 (2007).
15. S. Zhao, R.J. Gorte, *Applied Catalysis A: General*, **248**, 9-18 (2003).
16. R.M.L. Werchmeister, K.K. Hansen, M. Mogensen, *Material Research Bulletin,* **45**, 1554-1561 (2010).
17. H. Schichlein, A.C. Muller, M. Voigts, A. Krugel, E. Ivers-Tiffée, *Journal of Applied Electrochemistry*, **32**, 875-882 (2002).

18. V.V. Kharton, A.P. Viskup , F.M. Figueiredo, E.N. Naumovich, A.L. Shaulo, F.M.B. Marques, *Materials Letters*, **53**,160-164 (2002).
19. D. Ippolito, K.B. Andersen, K.K Hansen, *Journal of the Electrochemical Society*, **159**, P1-P8 (2012).
20. E.S. Putna, J.M. Vohs, R.J Gorte., G.W. Graham, *Catalysis Letters,* **54**, 17-21(1998).
21. S. Zhao, J. Gorte , *Applied Catalysis A: General*, **277**,129-136 (2004).
22. M. Mogensen, N.M. Sammes, G.A. Tompsett, *Solid State Ionics,* **129**, 63-94 (2000).
23. C. Endler, A. Leonide, A. Weber, F. Tietz, E. Ivers-Tiffée, *Journal of the Electrochemical Society*,**157**, B292-B298 (2010).
24. B.A. Boukamp, M. Verbraeken, D.H.A. Blank, P. Holtappels, *Solid State Ionics,* **157**, 29-33 (2003).
25. Y. Zheng, R. Ran, S.Z. Qiao, Z. Shao, *International Journal of Hydrogen Energy*, **37**, 4328:4338 (2012).
26. B.M. Reddy, G. Thrimurthulu, L. Katta, Y. Yamada, S.E. Park *Journal of Physical Chemistry C* , **113**, 15882-15890 (2009).
27. D.P. Fagg, D. Perez-Coll, P. Nunez, J.R. Frade, A.L. Shaula, A.A. Yaremchenko, V.V. Kharton, *Solid State Ionics*, **180**, 896-899 (2009).
28. E. Barsoukov, J.R. Macdonald, *Impedance Spectroscopy: Theory, Experiment and Applications*, 1st edn. Wiley (2005).
29. S.B. Adler *Solid State Ionics,* **111**, 125-134 (1998).
30. P. Hjalmarsson , M. Mogensen Journal of Power Sources, **196**, 7237-7244 (2011).
31. J.D. Kim, G.D. Kim, J.W. Moon, Park Y., *Solid State Ionics*, **143**, 379-389 (2001).
32. Borja C.J., Dorado F., de L.Consuegra A, .Vargas J.M.G., Valverde J.L., *Fuel Cells,* **11**, 131:139 (2011).
33. L. Bultel, M. Henault, C. Roux, C. Siebert, B. Beguin, F. Gaillard, M. Primet, P. Vernoux *Ionics* , **8**,136:141 (2002).
34. A. Kaloyannis, C.G. Vayeans, *Journal of Catalysis,* **182**, 37-47 (1999).

35. Frantzis A.D., Bebelis S., Vayenas C.G., *Solid State Ionics,* **136**, 137:863-872 (2000).

36. A. Kambolis, L. Lizzaraga, M.N. Tsampas, L. Burel, M. Rieu, J.P. Viricelle, P. Vernoux, *Electrochemistry Communications* ,**19**, 5-8 (2012).

# 6 ELECTROCHEMICAL OXIDATION OF PROPENE WITH A $LSF_{15}/CGO_{10}$ ELECTROCHEMICAL REACTOR

## 6.1 Abstract

A porous electrochemical reactor, made of $La_{0.85}Sr_{0.15}FeO_3$ as electrode and $Ce_{0.9}Gd_{0.1}O_{1.95}$ as electrolyte, was studied for the electrochemical oxidation of propene over a wide range of temperatures.

$Ce_{0.9}Gd_{0.1}O_{1.95}$ was used as infiltration material to enhance the effect of polarization on propene conversion, especially at low temperature. The influence of infiltrated material calcinations temperature on the reactor electrochemical behavior has been evaluated by using electrochemical impedance spectroscopy.

The results suggested that the $Ce_{0.9}Gd_{0.1}O_{1.95}$ morphology played a crucial role to suppress the competing oxygen evolution reaction and promote the oxidation of propene under polarization, with high faradaic efficiencies.

## 6.2 Introduction

Volatile Organic Compounds (VOCs) are recognized as major contributors to air pollution, leading to the formation of ozone in urban and regional areas [1]. VOCs can be generated by stationary sources of industrial processes like painting, manufacturing of organic compounds, dry cleaning, etc. and mobile sources such automobile exhausts. Catalytic oxidation of VOCs is a process of great interest since it operates at reduced temperature (200 °C-500 °C) if compared to the thermal incineration (700 °C-1100 °C) [2]. The commercial catalysts for VOCs oxidation are: supported noble metals [3], metals oxides [4,5,6,7,8] and a mixture of noble metals and metal oxides [9]. Noble metals possess higher catalytic activity than metal oxides but their use is limited by high cost and scarcity.

Transition metal oxides like perovskites have been widely investigated for hydrocarbons oxidation. Perovskite possess high thermal stability, good mobility of lattice defects and large amount of non-stochiometric oxygen: these properties make them a valid alternative to noble metals for hydrocarbons oxidation [10,11].

Solid electrolyte can be used to electrochemically promote the catalytic reaction rate of the electrode/catalyst in an electrochemical membrane reactor (EMR). Ions can be pumped to the catalyst surface modifying the reaction rate and product selectivity [12].

Different authors explored the possibility to modify the catalytic rate of VOCs oxidation. For example Li et al. studied the oxidation of toluene on Ag deposited on oxygen ion conductor like Yttria-stabilized zirconia (YSZ) [13]. Roche et al. studied the propane deep oxidation using $La_{0.7}Sr_{0.3}MnO_3$ deposited on YSZ[14]. Gaillard et al. used $La_{0.8}Sr_{0.2}Co_{0.8}Fe_{0.2}O_3$ on YSZ for the oxidation of propene at 450° C in air excess [15].

The application of this concept for automotive exhausts purification was explored by Balomenou et al. in a monolith electrochemical plate reactor for simultaneous hydrocarbons oxidation and NO reduction, using Pt and Rh as electro-catalyst dispersed on YSZ plate, both into a simulated and real Diesel exhausts environment [16].

In this study a porous cell reactor, made of $La_{0.85}Sr_{0.15}FeO_3$ (LSF) as electrode and $Ce_{0.9}Gd_{0.1}O_{1.95}$ (CGO) as electrolyte, has been studied in the oxidation of propene, a major component of Diesel exhausts [17]. LSF has been chosen as electrode thanks to both high electronic conductivity ($10^2$ S/cm at 400 °C) and to the ionic conductivity ($0.6 \times 10^{-5}$ S/cm at 500°C) provided by Sr doping [18]. The CGO has been used as electrolyte thanks to its superior ionic conductivity at low temperatures ($10^{-4}$ S/cm at 500°C) if compared to YSZ [19].

The infiltration of active material has been widely applied for the improvement of cathode and anode performances [20,21,22,23]. In the case of cathode material like $La_{1-x}Sr_xFeO_3$ or $La_{1-x}Sr_xMnO_{3\pm\delta}$, the primary goal for infiltrating catalytically active component was to increase the $O_2$ dissociation rate on the electrode surface, while adding ionic or mixed conductor could extend the three phase boundary (TPB). As observed by Bidrawn et al., discrepancies exist in literature in the assessment of the determining property responsible for the electrode performance increase. Bidrawn et al. concluded that differences in the electrode morphology could be the main reason for the disagreement found in literature [24].

In this work the effect of $Ce_{0.9}Gd_{0.1}O_{1.95}$ infiltration on the catalytic and electrochemical performance of porous reactor was studied. The objective was to better understand the influence of infiltrated material morphology on the electrocalytic behavior of the porous reactor.

Three different samples were tested with respect to propene conversion in the temperature range 250 °C-500 °C. The samples was characterized by use of electrochemical impedance spectroscopy (EIS) and subjected to polarization while the gas composition was monitored by a gas chromatograph (GC).

The three samples differed from each other: one was not infiltrated (backbone-BB), the second (CGO-LT) and the third one (CGO-HT) were infiltrated with CGO and calcined at 400 °C and 850 °C for 2 hours, respectively.

## 6.3 Experimental

### 6.3.1 Fabrication of porous reactor

The reactor used in this study was ceramic made of 11 alternating layers of electrode and electrolyte. The electrolyte tape was made of $Ce_{0.9}Gd_{0.1}O_{1.95}$ (CGO) purchased from Rhodia, while the electrode was made of a 35% weight $Ce_{0.9}Gd_{0.1}O_{1.95}$ and 65% weight $La_{0.85}Sr_{0.15}FeO_3$ (LSF) purchased from American Elements. For the fabrication of the electrode, LSF and CGO were mixed with binder, dispersant and graphite as pore former; the slurries were ball milled before tape casting. The CGO electrolyte was produced following the same procedure of the electrode. Six electrodes and five electrolyte green tapes were laminated together alternatively. Round cells were stamped with a diameter of 18 mm. The cells were then sintered at 1250 °C for 2 h. The sintering was able to burn the graphite and generate the desired porosity. Detailed description can be found in [25]. The average diameter of the cells after sintering was 14.5 mm. Before the test was carried on, gold paste with 20% weight graphite was painted on both sides of the electrochemical reactor and used as porous current collector. Figure 1 shows an image of the porous reactor with the gold current collector on top.

### 6.3.2 Impregnation

The reactors were impregnated using a 1.35 M aqueous solution of 10 mol% $Gd(NO_3)_3$ + 90 mol% $Ce(NO_3)_3$ with 10% weight of Triton X-100 as surfactant with respect to the water. Solutions were prepared with Millipore water, Triton X-100 (Sigma-Aldrich), Gd nitrate hexahydrate (Alfa Aesar) and Ce nitrate hydrate (Alfa Aesar). Infiltration was carried out in one step by applying vacuum to the sample after application of impregnation solution. After infiltration, the infiltrated samples were calcined at 400 °C and at 850 °C for 2 and denominated CGO-LT and CGO-HT, respectively. The weight of the cell was measured before infiltration and after calcination to estimate the loading of the infiltrated material. The weights of the sample after CGO calcination were 0.205 g and 0.257 g for CGO-LT and CGO-HT, respectively and 0.1973 g for the backbone. The CGO infiltration loading was equivalent to approximately 3-3.1% of the weight of the cell for both infiltrated samples. The area of the samples was 1.697 $cm^2$ for BB, 1.664 $cm^2$ for CGO-LT and 1.648 $cm^2$ for CGO-HT.

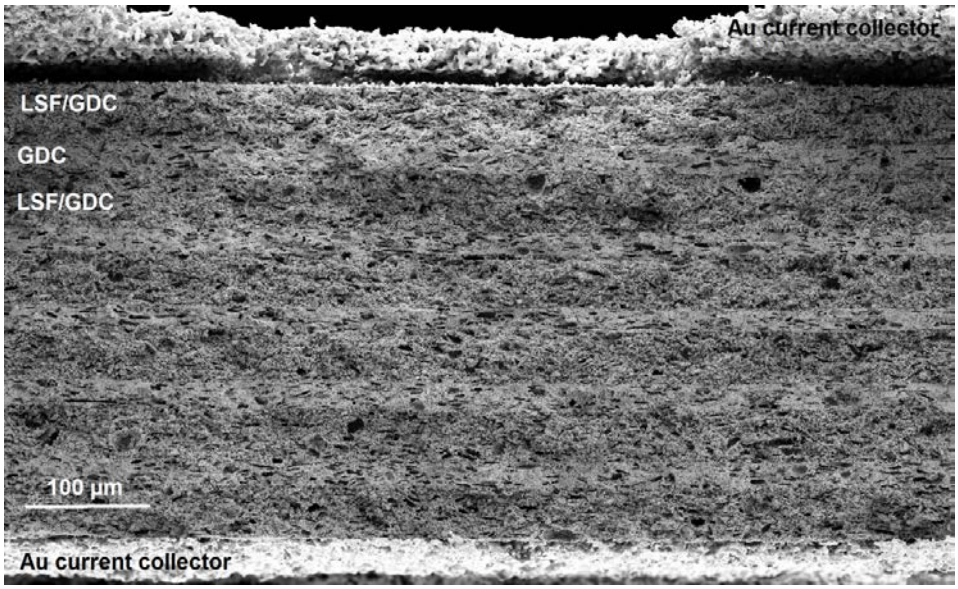


**Figure 1**: Cross-section SEM micrograph of 11-layers porous reactor

### 6.3.3 Test setup

The sample was mounted in a tubular reactor between two alumina tubes with contact between the gold paste and the two Pt electrodes used as working and reference/counter electrodes under one atmosphere, as reported by Werchmeister et al. [26]. The sample and the alumina tubes were surrounded by a quartz tube and mounted vertically in a furnace. Figure 2 illustrates the setup configuration.

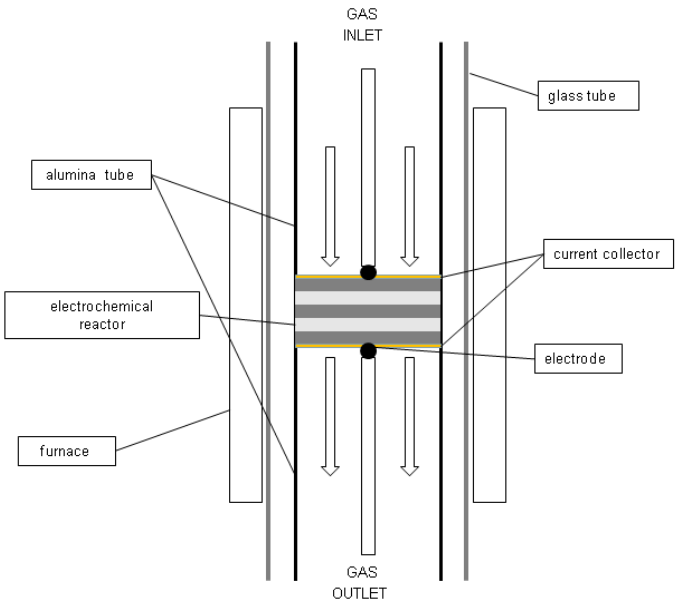


**Figure 2**: Schematic diagram of measurement setup

### 6.3.4 Electrochemical measurements

A potentiostat (Gamry, reference 600 USA) was used to perform chronoamperometry tests and for recording impedance spectra. The open-circuit voltage of the cell was stabilized before every measurement. The impedance spectra were recorded at open-circuit voltage (OCV) with root mean square amplitude of 36 mV over the frequency range 0.78 MHz to 5 mHz with 10 points/decade with a reaction atmosphere composed of 1000 ppm propene ($C_3H_6$), 10% $O_2$ at 2 L/h, unless otherwise stated.
The chronoamperometry tests were carried out for 2 h with anodic potentials of +4 V with respect to the open-circuit voltage. The impedance spectra were recorded before and right after the chronoamperometry test. The reactor temperature was increased to 500 °C and kept at this temperature for 2 h to remove possible contaminants. The electrochemical tests were started at 500 °C and then repeated, decreasing the reactor temperature with 50 °C step down to 250 °C. After this, the temperature was increased again at 500°C to evaluate the reactor performance after prolonged polarization.
The impedance spectra were analyzed with ElChemea Analytical software using Complex Non-Linear Square (CNLS) fitting. The inductance coming from the wiring was subtracted for every spectrum to perform the fitting. The spectra were validated using the Kramers-Kronig test for causality, linearity and time invariance.

### 6.3.5 Catalytic activity measurements

For the catalytic activity evaluation of the samples, a mixture of 10% $O_2$ (Air Liquide; 20% $O_2$ ± 2% Ar), 1000 ppm propene ($C_3H_6$) (Air Liquide; 1% ± 0.02% propene in Ar) and Ar to balance was used with a total flow rate of 2 L $h^{-1}$ controlled by Brooks flow meters. The $C_3H_6$, CO and $CO_2$ concentrations in the outlet stream were monitored by an on-line Agilent 6890 N gas chromatograph, equipped with Hayesep N and Molsieve columns and a thermal conductivity detector.
The magnitude of the effect of polarisation on the propene oxidation rate was evaluated by two commonly used parameters.
First, the rate enhancement ratio (ρ) defined by:

$$\rho = \frac{r}{r_o}$$

and the apparent faradaic efficiency (Λ):

$$\Lambda = \frac{r - r_o}{\frac{I}{nF}}$$

where $r_o$ is the catalytic rate at open circuit voltage (OCV) and $r$ is the catalytic rate measured under polarization. $I$ is the current recorded with +4 V polarization, $n$ the number of exchanged electrons during the electrode reaction, ($n$ = 2 in this case) and $F$ is the Faraday constant.

### 6.3.6 Scanning electron microscopy

The structure and morphology of the porous reactor and infiltrated material were examined in a Zeiss Supra 35 electron microscopy equipped with a field emission gun. SEM images were recorded in two ways. The reactor was broken and inserted into the microscope to check the infiltration material morphology. The second way involved the mounting of the cell in epoxy resin, polished and carbon coated with the objective to inspect the overall structure of the reactor layers.

## 6.4 Results and Discussion

### 6.4.1 Structural characterization

Figure 3 shows the micrographs of not infiltrated and infiltrated cells. It is possible to observe that the calcinations at low temperature (400 °C) favored the formation of a thin CGO layer on LSF/CGO composite particles, while the calcinations at 850 °C induced the formation of not interconnected nano-sized particles of 18-20 nm.

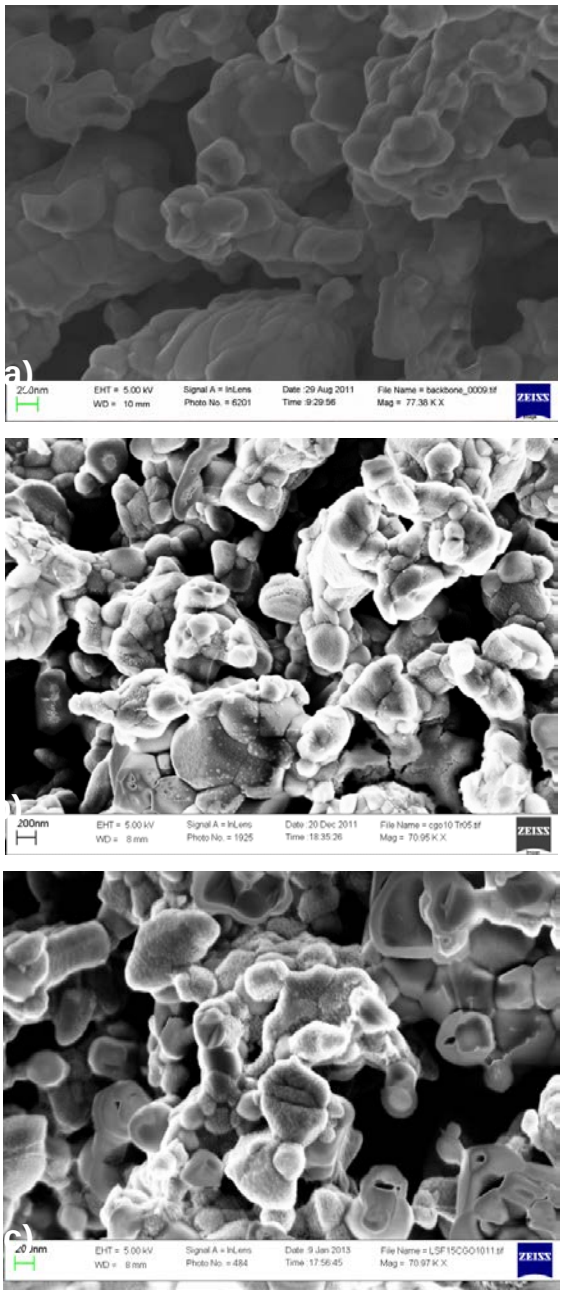


**Figure 3**: SEM micrographs of : a) backbone, b) CGO-LT and c) CGO-HT cells

The high calcination temperature of CGO provoked the shrinkage of the layer formed at lower temperature into nanoparticles. The specific surface area for backbone, CGO-HT and CGO-LT were 0.93 $m^2/g$, 1.27 $m^2/g$ and 4.4 $m^2/g$, respectively; the BET analysis confirmed that the increase of calcination temperature produced a decrease of specific surface area. Since the backbone composite (LSF/CGO) was already sintered at 1250 °C, the decrease of surface area was attributed to the sintering of the infiltrated material. An increase of average grain size and specific surface area was observed also by Blennow et al. [21] with CGO infiltrated $SrTiO_3$ anodes upon increase of calcination temperature from 350 °C to 650 °C in air.

### 6.4.2 Catalytic and electrocatalytic activity

Figure 4 shows the reaction rate for propene oxidation at different temperatures for the backbone and for the CGO infiltrated cells measured at OCV. CGO-LT exhibited the highest catalytic activity. The propene conversion reached by CGO-LT and CGO-HT was 59% and 46 % at 400 °C, respectively; the backbone reached 21% at the same temperature. It was clear that the infiltration of CGO was able to strongly increase the cell catalytic activity particularly starting from 300 °C. The performance decrease of the CGO-HT compared to CGO-LT sample was mainly due to a reduced catalyst specific surface area induced by higher calcinations temperature.

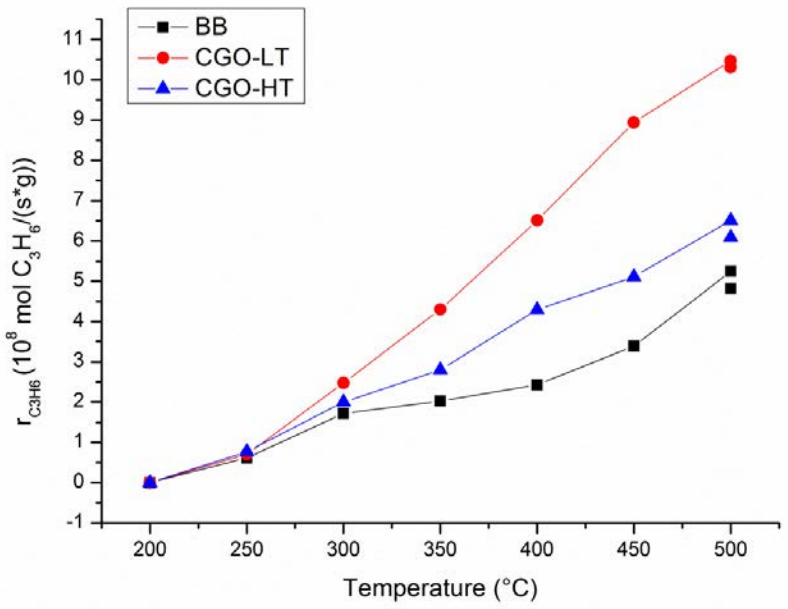


**Figure 4:** Reaction rate for propene oxidation as a function of temperature in 1000 ppm $C_3H_6$ and 10% $O_2$ at 2 L/h, OCV

The selectivity to $CO_2$ for CGO-LT was 100% at all temperatures; the backbone and CGO-HT instead did not exhibit full selectivity to $CO_2$ but only 93%-96% between 500 °C and 350 °C, producing CO as co-product. Since BB and CGO-HT cell exhibited similar selectivity to $CO_2$, it possible to attribute to the specific morphology of CGO in CGO-LT the capability to suppress the CO formation, through the higher coverage of LSF reactive sites given by the continuos layer.

The backbone made of LSF/CGO in this work showed lower reaction rate if compared to the backbone made of LSM/CGO studied our group [27], $3.88\times10^{-8}$ against $2.43\times10^{-8}$ mol $C_3H_6$/g×s at 400 °C for LSM and LSF, respectively. The amount of CGO in the electrode composite was the same for both the cell so it could be possible to ascribe this difference to the different catalytic properties of LSF. To our knowledge no studies were carried on $La_{1-x}Sr_xFeO_3$ catalytic properties for propene catalytic oxidation, although Kremenic et al.[28] reported lowest propene oxidation activity for $LaFeO_3$ in the series $LaMO_3$ with M=Cr, Mn, Fe, Co, Ni, with $LaMnO_3$ and $LaCoO_3$ showing the highest catalytic activity. The low $O_2$ adsorption on $LaFeO_3$, fundamental for the suprafacial oxidation mechanism, was addressed as the cause for the low activity. Morooka et al. [29] studied the correlation between M-O metal oxide bond heat of formation ($\Delta H_o$) and propene oxidation activity: Fe (as $Fe_2O_3$) exhibited lower catalytic activity if compared to $MnO_2$ or $Co_3O_4$ due to the higher heat of formation of its oxide, correlated to the easiness of the oxide to be reduced.

As it is possible to observe in Figure 4, the reaction rate measured at OCV at 500 °C, during post test measurements showed a decrease of propene conversion of 8%, 6% and 1.5% for the backbone, CGO-HT and CGO-LT, respectively. The CGO was able to partially mitigate the electrode/catalyst degradation and this protection effect was stronger for CGO-LT cell. The LSF/CGO backbone exhibited an opposite behavior compared to LSM/CGO backbone cell reported by our group [27]: the post test measurements for LSM showed an increase of catalytic activity coupled with an enhancement of electrode performance (higher current density).

Figure 5 illustrates the current density measured at +4 V as a function of reactor temperature. The infiltration of CGO increased the electrode performance starting at temperatures of 350°-400 °C while no clear effect was visible at reduced temperatures; particularly, the CGO-LT cell exhibited the highest current densities values between 400°C and 500°C. As suggested by Jiang [30] et al., the CGO infiltration could have enhanced the adsorption and dissociation of $O_2$ and created an effective ionic diffusion pathway along CGO film to the TPB. This beneficial effect seemed dependent also on the morphology of the infiltrated CGO since CGO-HT showed lower current densities

compared to CGO-LT; a thin layer of CGO could have been able to create the continuous ionic pathway for the oxygen ions to reach the TPB, improving the electrode performance under polarization. If the beneficial effect of CGO infiltration is providing an high ionic conductivity pathway to oxygen ions, at reduced temperatures (250 °C-350° C), the infiltrated CGO beneficial effect was supposed to disappear due to its low ionic conductivity and the backbone porous reactor was driving the electrochemical performance under polarization. This behavior could explain the similar current densities values exhibited by all the samples between 250 °C and 300 °C.

As it was observed for propene conversion, the current density measured at 500 °C during post test measurements exhibited a decrease of 14%, 8.7% and 11.4% for the BB, CGO-LT and CGO-HT, respectively. Also in this case the CGO infiltrated counteracted the electrode degradation; CGO-LT exhibited the highest beneficial effect against electrode/catalyst degradation. Blennow et al. [20] studied the effect of Ni:CGO co-infiltration on Nb-doped $SrTiO_3$ (STN):FeCr composite conductivity as a function of oxygen partial pressure. The sample was subjected to a redox cycle changing the oxygen partial pressure from $10^{-27}$ to 1 atm and backward. The recovery of conductivity was higher for the non-infiltrated composite anode compared to the anode with Ni:CGO infiltration. They suggested that CGO could have changed the reduction kinetic of STN making STN reduction energetically more difficult. The LSM behaved differently from LSF: LSM usually activates upon cathodic polarization. This effect has been widely reported in literature [31,32,33] and attributed to the oxygen vacancies formation on LSM surface, able to enhance oxygen dissociation and oxygen species surface diffusion of to the TPBs

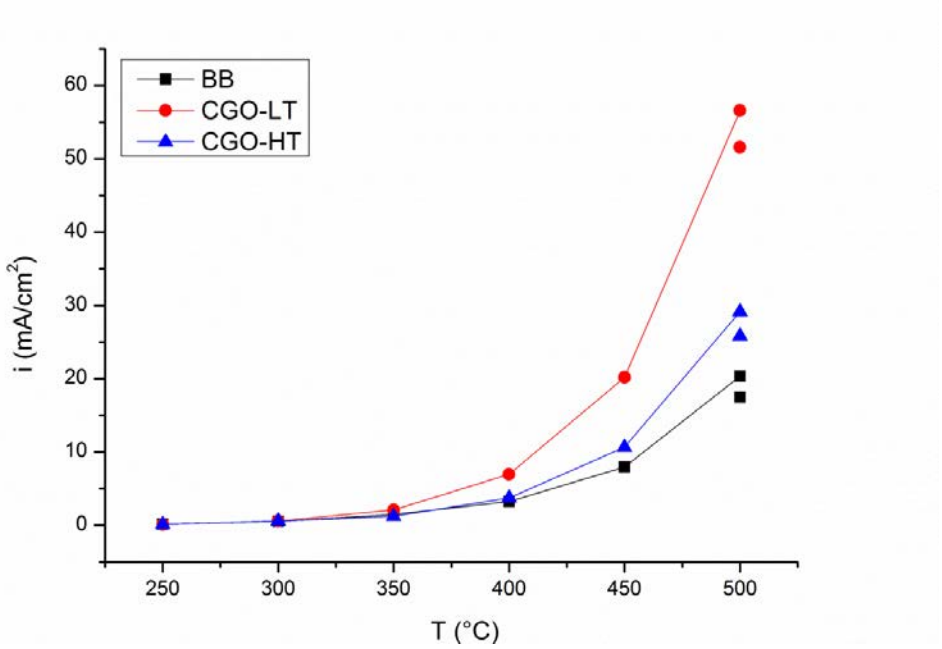


**Figure 5:** Current densities measured at +4V as a function of reaction temperature recorded in 1000 ppm $C_3H_6$, 10% $O_2$, 2L/h

The application of +4 V (0.8 V/cell) at 500 °C in 10% $O_2$ was equivalent to an oxygen partial pressure of $1.36 \times 10^{-22}$ atm, according to the Nernst equation, on the part of the cell polarized cathodically, being this reactor symmetric. As reported by Mizusaki [34], the concentration of oxygen vacancies in $LaSrFeO_3$ depends only on $Sr^{2+}$ doping level at oxygen partial pressure below $10^{-5}$ atm; the charge neutrality is obtained by first reduction of $Fe^{4+}$ to $Fe^{3+}$ and in the next step oxygen desorption takes place by reduction of $Fe^{3+}$ to $Fe^{2+}$. As reported by Poulsen [35], the formation of oxygen vacancies in the LSM instead is massive upon reduction of oxygen partial pressure, causing an increase of electrode performance. Mizusaki reported that the reduction of Fe in LSF was accompanied by a decrease in p-type conductivity [36]; this could be the cause for the electrode degradation. The LSM electronic conductivity instead was reported to be stable also for low $O_2$ partial pressures thanks to large oxygen excess non-stoichiometry, as reported by Mizusaki in the LSM conductivity measurements at 1273 K [37]. In this work, the CGO, especially if nano-sized, could have provided oxygen ions ($O^{2-}$) and suppress the reduction of $Fe^{4+}$ to $Fe^{3+}/Fe^{2+}$ and the consequent decrease of conductivity.

Figure 6 shows the micrographs of fresh and tested backbone cell; no clear structural or morphological differences were visible between the two micrographs and cracks in the electrode structure were absent. It is possible to infer that structural modification were not the cause of the decrease of electrode performance.

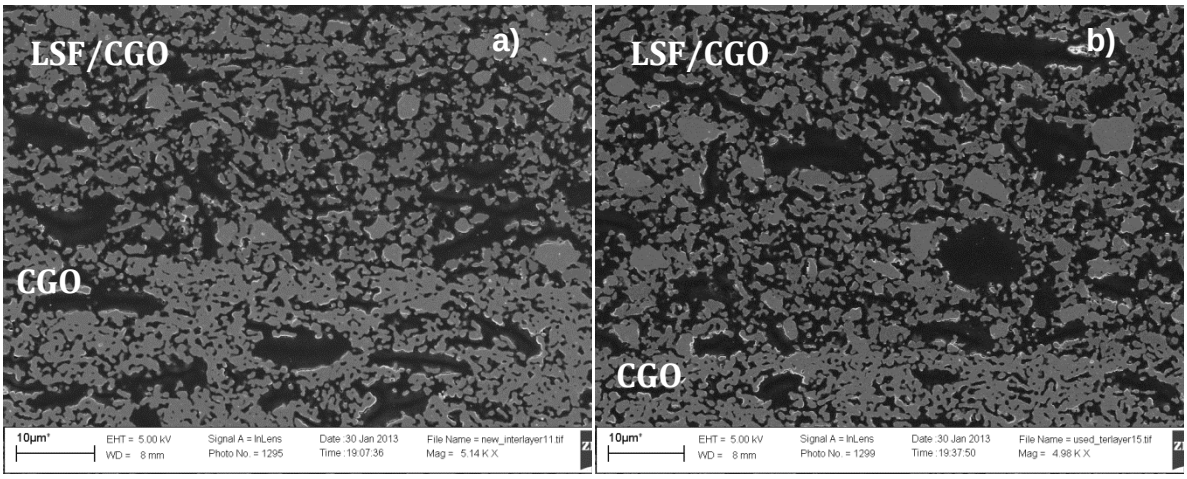


**Figure 6**: SEM micrograph of a) fresh b) tested BB cells embedded in epoxy

Figure 7 illustrated the Arrhenius plot of the ohmic resistance ($R_s$) of the system (bulk electrolyte + contact), extracted from the impedance spectra recorded with 1000 ppm propene and 10% $O_2$ at OCV as high frequency intercept of Z´ at $\omega \rightarrow \infty$, after the inductance of the wires was removed.

The activation energy of $R_s$ agreed well with value reported by Mogensen [38] for $Ce_{0.9}Gd_{0.1}O_{1.95}$.

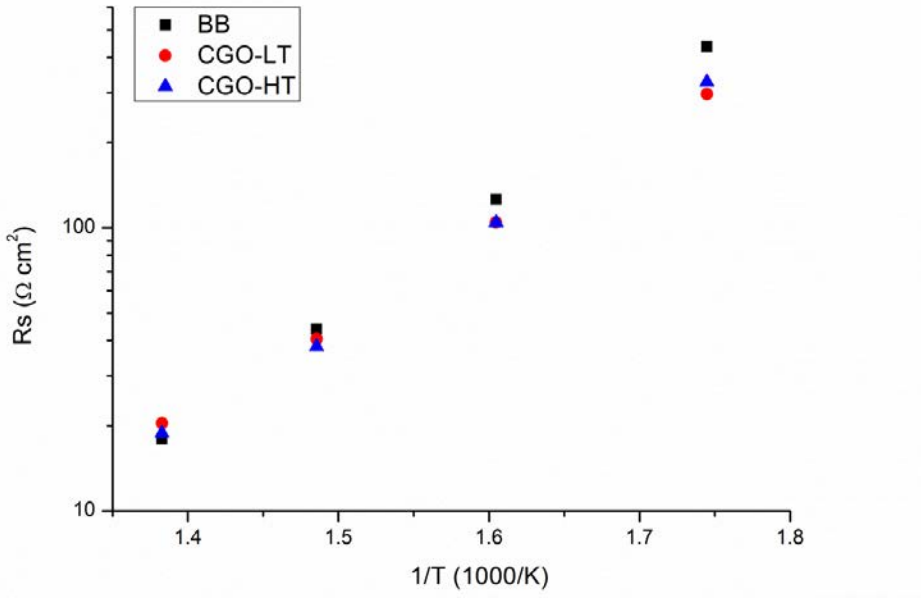


**Figure 7**: Arrhenius plot of ohmic resistance ($R_s$) for BB, CGO-LT and CGO-HT

It is possible to observe a discrepancy between the resistance values of the BB cell and those belonging to CGO-LT and CGO-HT; the discrepancy appeared as an increase of Rs, especially for BB cell for temperature below 400 °C. Since the test was started at

500 °C and the temperature was decreased by 50 °C down to 250 °C. A decrease of conductivity of the perovskite phase would be expected to increase the ohmic losses. This phenomenon was less severe for the samples infiltrated with CGO, confirming the protective behavior of the CGO infiltrated against electrode degradation.

Figure 8 exhibits the rate enhancement ratio (ρ) curve together with the faradaic efficiency as a function of reaction temperature, measured upon application of +4 V.

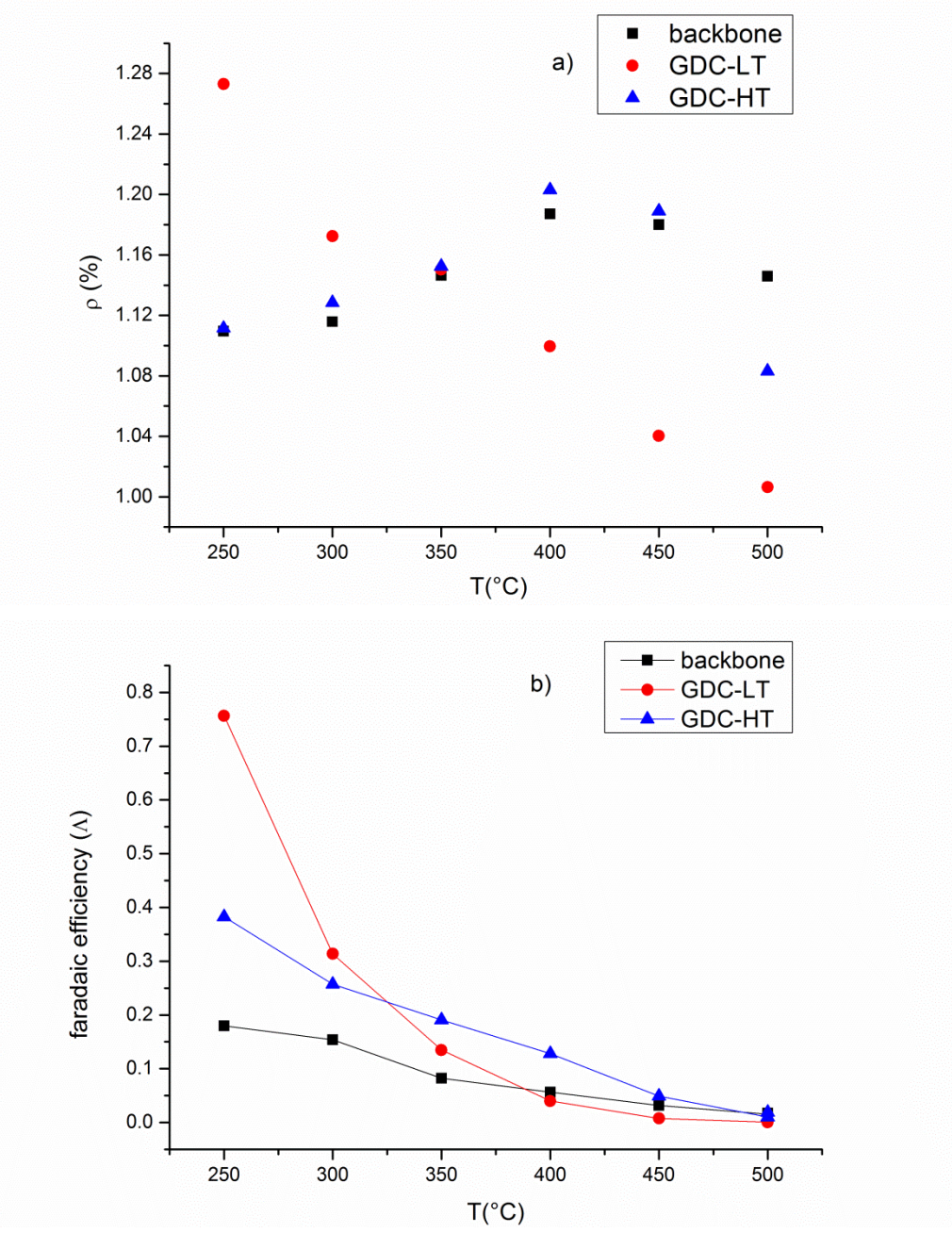


**Figure 8 5**: Rate enhancement ratio a) and current efficiency b) curves as function of reaction temperature

The ρ curve was affected by different variables depending on electrode performance and propene conversion. The backbone and CGO-HT cells exhibited a ρ trend with a

maximum at 400 °C followed by decrease of ρ at lower temperatures. The CGO-LT cell instead, exhibited a constants increase of ρ with decreasing temperature.

At temperatures above 400 °C the current density increased exponentially for all the samples, exhibiting high speed of oxygen evolution reaction on the electrode working as anode, according to the reaction:

$$O_O^X \rightarrow O_{ads,TPB} + V_o^{\bullet\bullet} + 2e^-$$

where $V_o^{\bullet\bullet}$ is an oxygen vacancies and $O_o^x$ is lattice oxygen.

This caused the ρ to decrease with increasing temperature. The lifetime of oxygen ions (reactants) was strongly reduced by the increase of electrode performance with temperature increase. The selectivity of $O^{2-}$ towards propene electrooxidation decreased due to the high speed of oxygen ions consumption by the oxygen evolution reaction. Moreover both the CGO infiltrated cells were affected by diffusion limitations caused by high propene conversion, especially at temperatures of 450 °C and 500 °C. For example, the CGO-LT cell exhibited high electrode performance from 400 °C coupled with very high propene conversion: 81% and 95% at 450 °C and 500 °C, respectively. These two coupled effects were deleterious to obtain high ρ values.

As it is possible to observe in Figure 8a, between 250 °C and 350 °C, the tested cells showed opposite behavior. The ρ of CGO-HT and of the backbone cell decreased upon temperature decrease while, for the CGO-LT cell, it increased with temperature decrease following the trend visible at higher temperatures. Since all the cells had similar electrode performance/current density at +4 V at 250 °C and 300 °C, the different behavior could be ascribed to the different infiltrated material morphology. Since the ρ behavior of CGO-HT was similar to the backbone, except for temperature above 450 °C where diffusion limitations could be present. It is possible to infer that the high temperature calcination of infiltrated CGO increased the catalytic activity while did not affect the rate enhancement ratio. The formation of a thin layer of CGO, at low calcinations temperature for CGO-HT, could have isolated some electron conducting LSF particles and partially destroying the TPBs. The spillover of oxygen ions on CGO surface and the following reaction with propene in this case could be slightly favored at the expense of the oxygen evolution reaction.

In the Figure 8b the values of faradaic efficiencies were reported as a function of reaction temperature. The current efficiency is a measure of the amount of oxygen ions (mol O/s) pumped through the electrolyte and reacting with propene to form the oxidation products: $H_2O$, $CO_2$ and CO. The current density values include the contribution from the

oxygen evolution reaction and propene electrooxidation. The gas analysis measurement permits to measure the difference between the propene oxidation rate under polarization (r) and the rate at OCV ($r_0$) and estimate the selectivity between the propene electrooxidation and the oxygen evolution reaction.

It is possible to notice that all three samples exhibited low current efficiencies at high temperature (500 °C-400 °C), due to the high speed of oxygen evolution reaction and due to the effect of diffusion limitations (the latter for CGO-LT and CGO-HT). In particular the CGO-LT cell showed the lowest current efficiencies in this range of temperatures. The current efficiency increased with temperature decrease with different rates between the samples. For the backbone and CGO-HT cells the increase was almost linear with temperature and it reached 1.18 and 1.30 at 250 °C, respectively. This behavior meant that the infiltration of CGO followed by high temperature calcinations was only partially able to suppress the oxygen evolution reaction if compared to the backbone. The CGO-LT showed instead a strong rise of current efficiency with temperature decrease, demonstrating that in this case the formation of a thin layer of CGO was able to suppress to a higher extent the oxygen evolution.

### 6.4.3 Effect of CGO infiltration on impedance spectra

Representative examples of impedance spectra recorded at 450 °C with 1000 ppm propene and 10% $O_2$ are shown in Figure 9 together with their deconvolution. Comparison between the BB and the infiltrated cells data indicated that the shape of spectra depended somewhat on the infiltration of CGO and on the CGO calcination temperature.

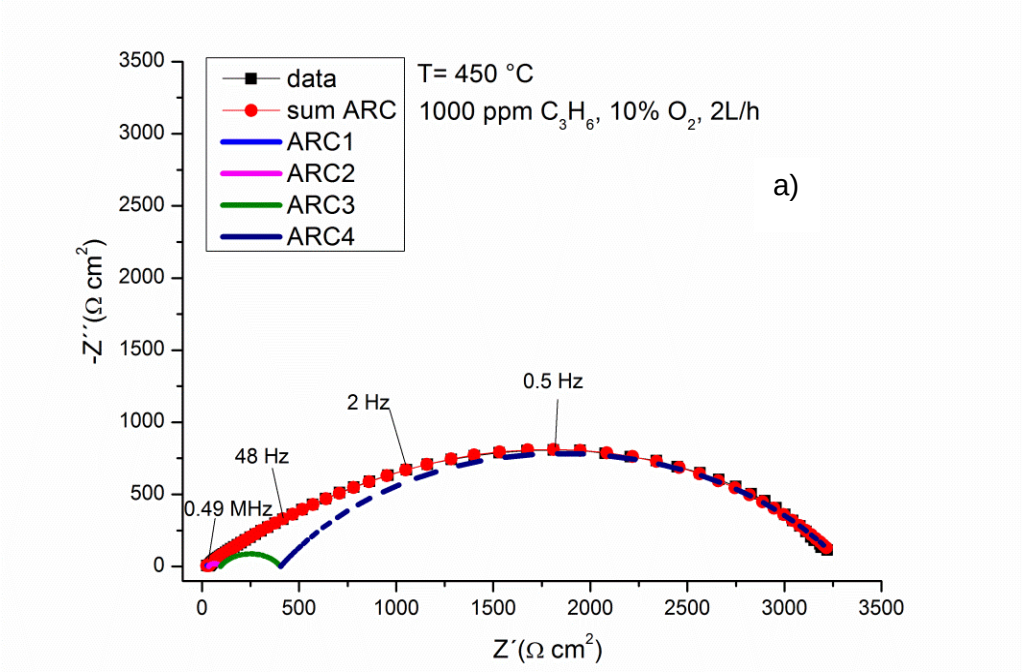
data
sum ARC
ARC1
ARC2
ARC3
ARC4
T= 450 °C
1000 ppm C3H6, 10% O2, 2L/h
a)
0.5 Hz
2 Hz
48 Hz
0.49 MHz
-Z´´(Ω cm2)
Z´(Ω cm2)
0
500
1000
1500
2000
2500
3000
3500

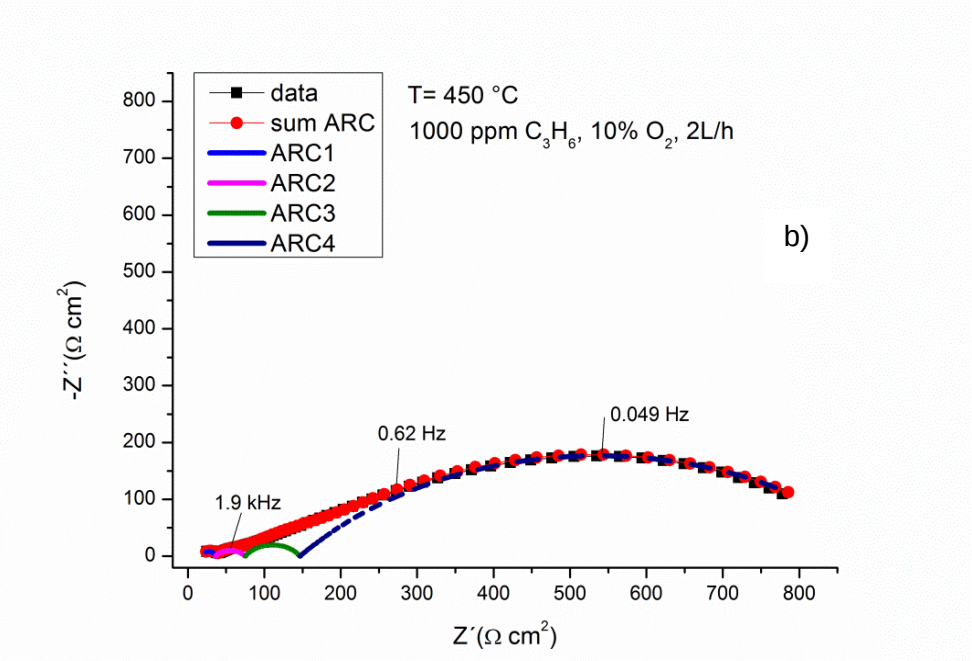
data
sum ARC
ARC1
ARC2
ARC3
ARC4
T= 450 °C
1000 ppm C3H6, 10% O2, 2L/h
b)
0.049 Hz
0.62 Hz
1.9 kHz
-Z´´(Ω cm2)
Z´(Ω cm2)
0
100
200
300
400
500
600
700
800

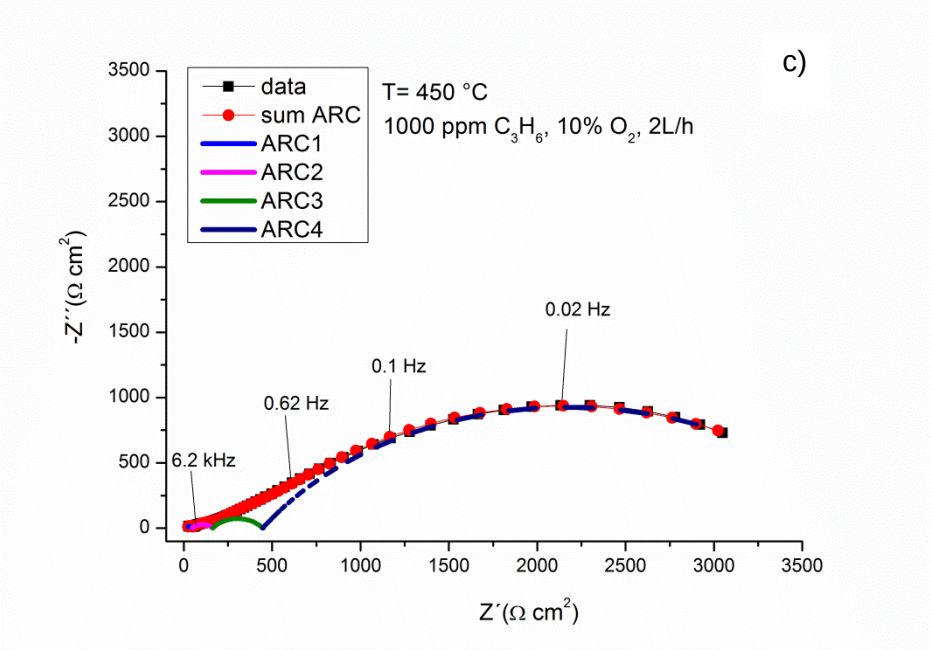


**Figure 9**: Nyquist plots of the impedance spectra for a) CGO-LT, b) BB and c) CGO-HT cells recorded at 450 °C, 10% $O_2$ and 1000 ppm $C_3H_6$, OCV.

The ohmic resistance ($R_s$) adjusted phase angle (δ) vs log f (Figure 10 below) highlighted that the BB and CGO-HT cells were affected by similar electrochemical/chemical processes while CGO-LT presented a large frequency region (10-800 Hz) of kinetically mixed process characterized by δ>30°.

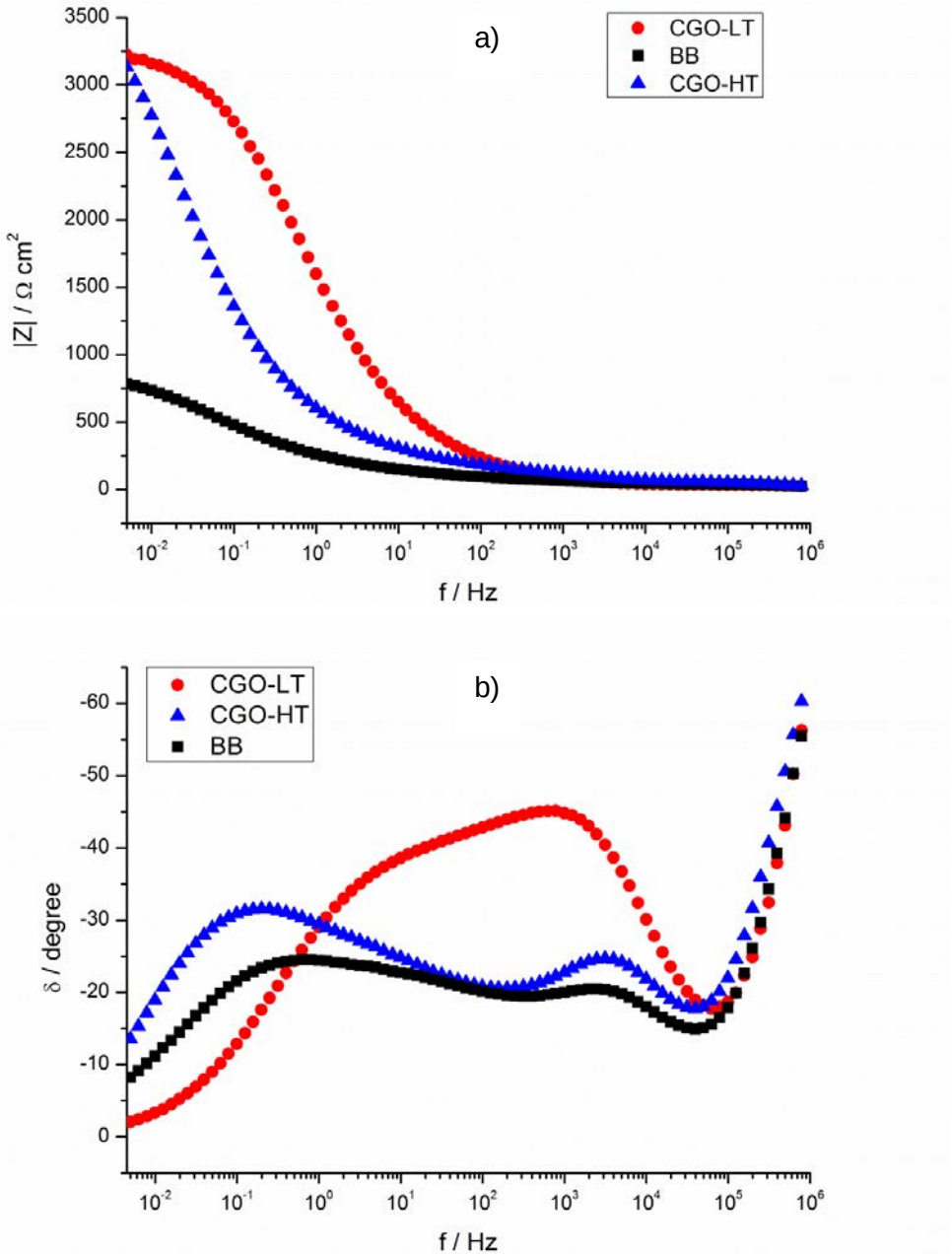


**Figure10**: Bode plot of the impedance spectra: a) magnitude and b) phase angle for CGO-LT, BB and CGO-HT cells recorded at 450 °C, 10% $O_2$ and 1000 ppm $C_3H_6$, OCV.

According to the impedance data, the polarization resistance ($R_p$) has been obtained as difference between the ohmic resistance $R_s$ at Z´ if $\omega \rightarrow \infty$ and Z´ if $\omega \rightarrow 0$. Figure 11 reports the Arrhenius plot of the polarization resistance ($R_p$) extrapolated from the impedance spectra recorded with in the presence of 1000 ppm propene and 10% $O_2$ at OCV between 500 °C and 350 °C.

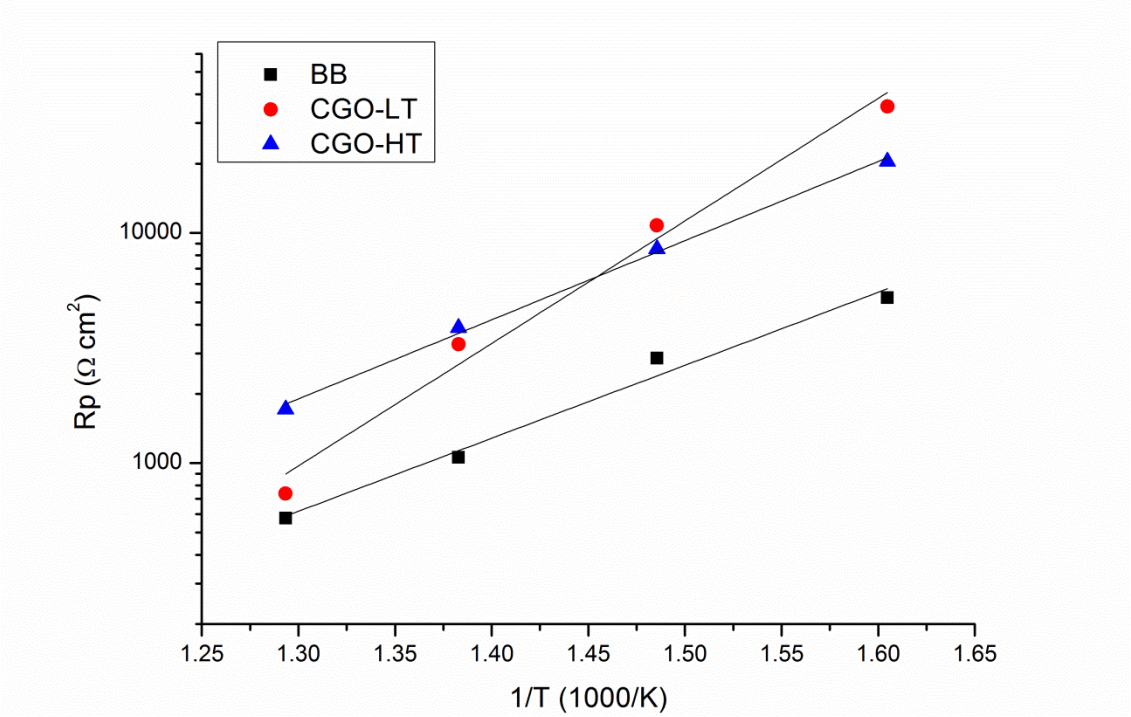


**Figure11:** Arrhenius plot of polarization resistance (Rp) for BB, CGO-LT, and CGO-HT.

The $R_p$, measured at OCV, increased with the infiltration of CGO in the backbone. CGO-HT cell had similar activation energy of BB cell, while CGO-HT exhibited higher activation. The comparison between the current density values of Figure 5 with the Rp behavior of Figure 11 revealed that the Rp was strongly influenced by the applied voltage; particularly for CGO-LT and CGO-HT cells.

The $R_p$ dependence on temperature further confirmed that CGO calcination temperature and morphology strongly affected the electrode behavior. At 500 °C the CGO-LT sample exhibited close $R_p$ value if compared to the BB cell. The formation of a thin CGO layer, at low temperature, could have been helpful to maintain good electrode performance due to the good ionic conductivity of CGO at 500 °C. The strong decrease of ionic conductivity of CGO with high activation energy (0.69 eV) [19] if compared to the LSF electronic conductivity (0.17 eV) [18], could be the cause of the drastic $R_p$ increase with temperature; i.e., the CGO conductivity is the dominating factor influencing the electrode performance. The CGO layer, covering the LSF particles, acted as an insulating layer reducing the electrode performance by decreasing the length of the three phase boundaries (TPB). This effect was stronger for the CGO-LT than for CGO-HT due to the different infiltrated CGO morphology characteristics.

The equivalent circuit, shown in Figure 12, has been chosen for the theoretical analysis of the different electrode processes. $CPE_i$ and $R_i$ are the constant phase element and

charge transfer resistance, respectively. The CPE impedance is $Z_{CPE} = A^{-1}(j\omega)^{-1}$ , where A is a CPE coefficient and α is a fractional exponent.

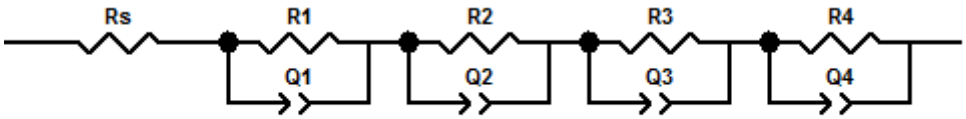


**Figure 12**: Equivalent circuit used for data analysis

Although all the samples have been tested at temperatures as low as 250 °C, the impedance data fitting has been performed on the spectra recorded between 500 °C and 350 °C where the electrode contribution to the impedance spectrum was evident; below 350 °C the main impedance contribution was given by CGO grain boundaries oxygen ions conductivity.

The process located at the highest frequency and fitted by subcircuit ($R_1Q_1$) had activation energy of 1 eV for all the tested cells. The value of activation energy was extrapolated between 450 °C and 350 °C because the relaxation frequency of this contribution at 500 °C was above the upper frequency limit (0.78 MHz) of the measurements. The capacitance value laid between 1.3 and 1.8 × $10^{-8}$ F/$cm^2$ and it was not affected by temperature. The introduction of propene in the reactive system or the change in oxygen partial pressure did not affect the resistance of this arc. Due to these characteristics, this arc could be attributed to the grain boundaries conductivity of CGO electrolyte.

The processes located at medium and medium-low frequencies were fitted by subcircuit ($R_2Q_2$) and ($R_3Q_3$). Figure 13 shows the Arrhenius plot of the resistances $R_2$ and $R_3$. The $R_2$ temperature dependence was similar for BB and CGO-HT cells with activation energy of 0.5 eV and 0.45 eV, respectively. The $R_2$ for CGO-LT cell instead was much more affected by temperature, showing activation energy of 1.03 eV.

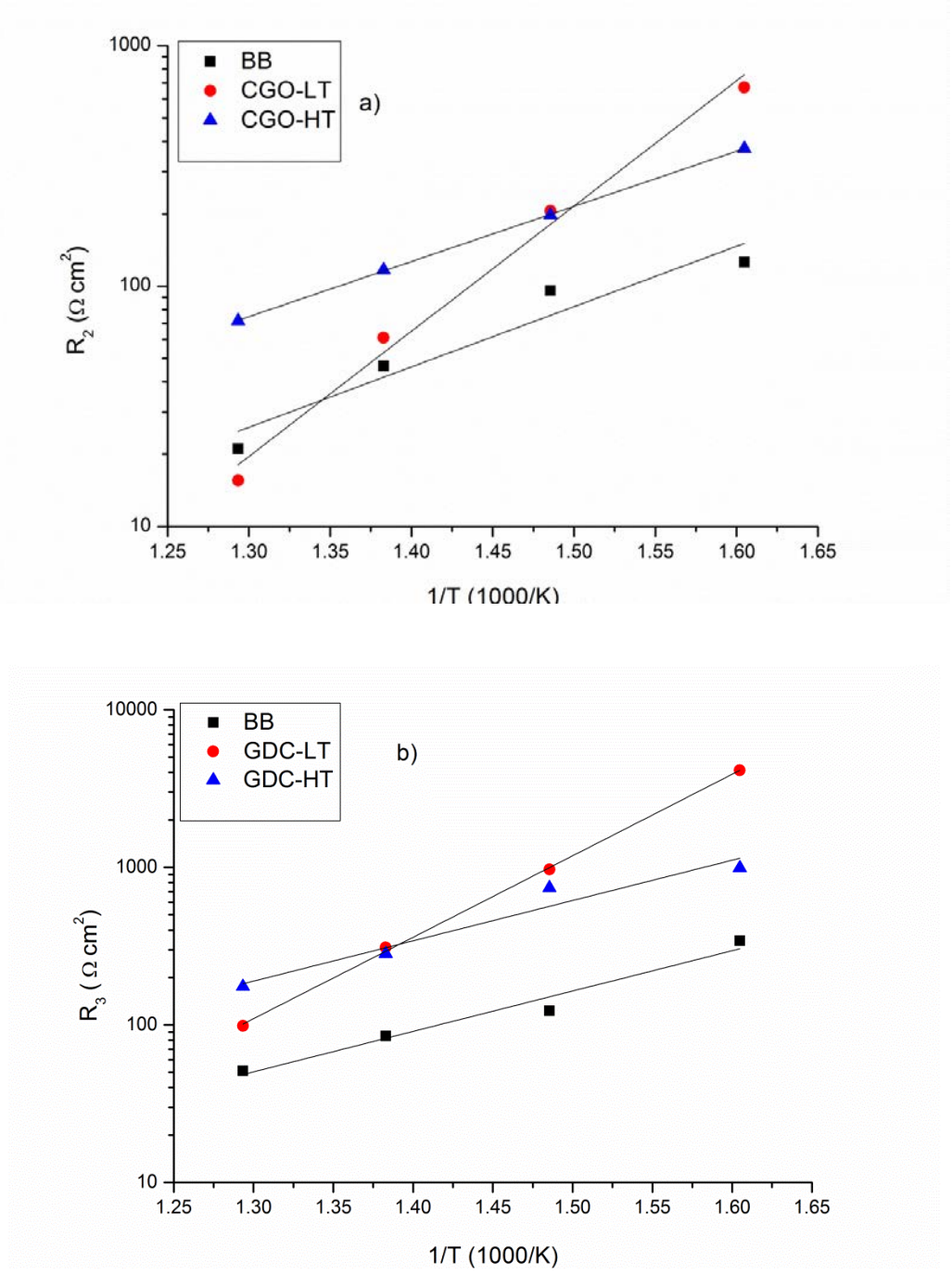


**Figure 13:** Arrhenius plots of a) $R_2$ and b) $R_3$ for BB, CGO-LT, and CGO-HT

Table I gives the typical impedance fitting impedance parameters of the subcircuit ($R_2Q_2$) for the impedance spectra recorded at 450 °C and 350 °C with 10% $O_2$ and 1000 ppm of propene.

| | BB | | | CGO-LT | | | CGO-HT | | |
|---|---|---|---|---|---|---|---|---|---|
| | Q2, $S\ cm^{-2}\ s^n$ | n | R2×Q2, $s^n$ | Q2, $S\ cm^{-2}\ s^n$ | n | R2×Q2, $s^n$ | Q2, $S\ cm^{-2}\ s^n$ | n | R2×Q2, $s^n$ |
| 450 °C | $9.03\times10^{-5}$ | 0.6 | $4.2\times10^{-3}$ | $6.47\times10^{-5}$ | 0.74 | $3.95\times10^{-3}$ | $5.93\times10^{-5}$ | 0.58 | $6.93\times10^{-3}$ |
| 350 °C | $4.46\times10^{-5}$ | 0.67 | $5.63\times10^{-3}$ | $5.14\times10^{-5}$ | 0.71 | $3.45\times10^{-2}$ | $1.51\times10^{-5}$ | 0.64 | $5.63\times10^{-3}$ |

**Table I**: fitted impedance parameters from the equivalent circuit for the subcircuit (R1Q1)

Because the peak frequency is equal to the inverse of resistance times the capacity, it is possible to observe that the summit frequency for BB and CGO-HT cell was stable with temperature, which resulted in a capacitance dependent on temperature. On the opposite for CGO-LT, the increase of temperature induced one order of magnitude decrease of frequency, resulting in a weaker dependence of the capacitance on temperature. Jiang et al. [23] found similar capacitance values ($10^{-6}$ F/cm$^2$) for a LSM electrode impregnated with CGO, and attributed this process to the charge transfer reaction at TPB. The characteristic time of this process for CGO-LT at 350 °C was very high if compared to BB and CGO-HT cells.

As shown in Figure 13b, the resistance $R_3$ exhibited activation energy similar to $R_2$ both for BB and CGO-HT (0.51 eV) and for CGO-LT (1.02 eV). Table II illustrates the typical fitting parameters associated with the subcircuit ($R_3Q_3$) for the impedance spectra recorded at 450 °C and 350 °C with the presence of propene.

| | BB | | | CGO-LT | | | CGO-HT | | |
|---|---|---|---|---|---|---|---|---|---|
| | Q3, $S\ cm^{-2}\ s^n$ | n | R3×Q3, $s^n$ | Q3, $S\ cm^{-2}\ s^n$ | n | R3×Q3, $s^n$ | Q3, $S\ cm^{-2}\ s^n$ | n | R3×Q3, $s^n$ |
| 450 °C | $7.27\times10^{-4}$ | 0.64 | $6.18\times10^{-2}$ | $1.80\times10^{-4}$ | 0.65 | $5.56\times10^{-2}$ | $5.49\times10^{-4}$ | 0.61 | $1.55\times10^{-1}$ |
| 350 °C | $8.63\times10^{-4}$ | 0.5 | $2.95\times10^{-1}$ | $1.15\times10^{-4}$ | 0.63 | $4.76\times10^{-1}$ | $6.42\times10^{-4}$ | 0.5 | $6.37\times10^{-1}$ |

**Table II**:fitted impedance parameters from the equivalent circuit for the subcircuit (R2Q2)

In this case, the strong increase in frequency demonstrated the weak dependence of the capacitance on temperature for all the samples. Chen et al. [33] and Kim et al. [39] reported similar values of capacitance for LSM/YSZ composite cathode, and associated this process with the incorporation of oxygen ion transfer from the TPB to the CGO lattice.
Figure 14 illustrates the Arrhenius plot for the resistance associated with the low frequency subcircuit ($R_4Q_4$).

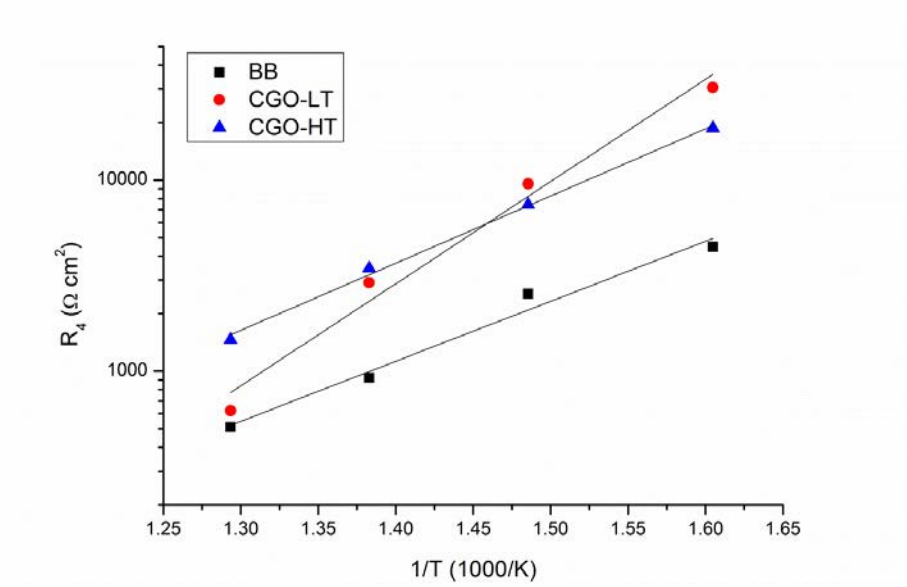


**Figure 14**: Arrhenius plot of $R_4$ for BB, CGO-LT, and CGO-HT

The process at low frequency associated with $R_4$ was responsible for about 85-90% of the entire polarization resistance ($R_p$); $R_4$ represented the dominant process of the electrode. Also in this case, the activation energy showed close values between BB and CGO-HT of 0.63 eV and 0.7 eV, respectively.
The resistance of CGO-LT cell was strongly dependent on temperature with activation energy of 1.1 eV. The CGO infiltration had detrimental effect on the resistance of this process, as previously observed for $R_2$ and $R_3$, although the CGO-LT low frequency resistance exhibited similar values if compared to the BB cell.
Table III illustrates the fitting parameters associated with the subcircuit ($R_4Q_4$).

| | BB | | | CGO-LT | | | CGO-HT | | |
|---|---|---|---|---|---|---|---|---|---|
| | Q4, S $cm^{-2}$ $s^n$ | n | R4×Q4, $s^n$ | Q4, S $cm^{-2}$ $s^n$ | n | R4×Q4, $s^n$ | Q4, S $cm^{-2}$ $s^n$ | n | R4×Q4, $s^n$ |
| 450 °C | $1.95\times10^{-3}$ | 0.54 | 1.5 | $1.72\times10^{-4}$ | 0.63 | 0.5 | $1.09\times10^{-3}$ | 0.62 | 3.76 |
| 350 °C | $2.53\times10^{-3}$ | 0.54 | 7.7 | $1.29\times10^{-4}$ | 0.58 | 3.93 | $1.2\times10^{-3}$ | 0.62 | 22.4 |

**Table III**: fitted impedance parameters from the equivalent circuit for the subcircuit (R4Q4)

It is possible to observe from Table III how the strong increase of characteristic frequency with temperature demonstrated the weak dependence of capacitance on temperature. The characteristic frequency of this process for CGO-LT was higher at both temperatures if compared to BB and CGO-HT samples. The closure of the low frequency arc (ARC4) for CGO-LT, visible on the Nyquist plots of Figure a, demonstrated the high speed of this process on this cell.

Figure 15 shows the Nyquist plots of the impedance spectra of CGO-LT cell, recorded respectively with 10% $O_2$ and 10% $O_2$ with 1000 ppm of propene at 500 °C. The purpose was to illustrate the effect of the change of the reaction atmosphere on the impedance response.

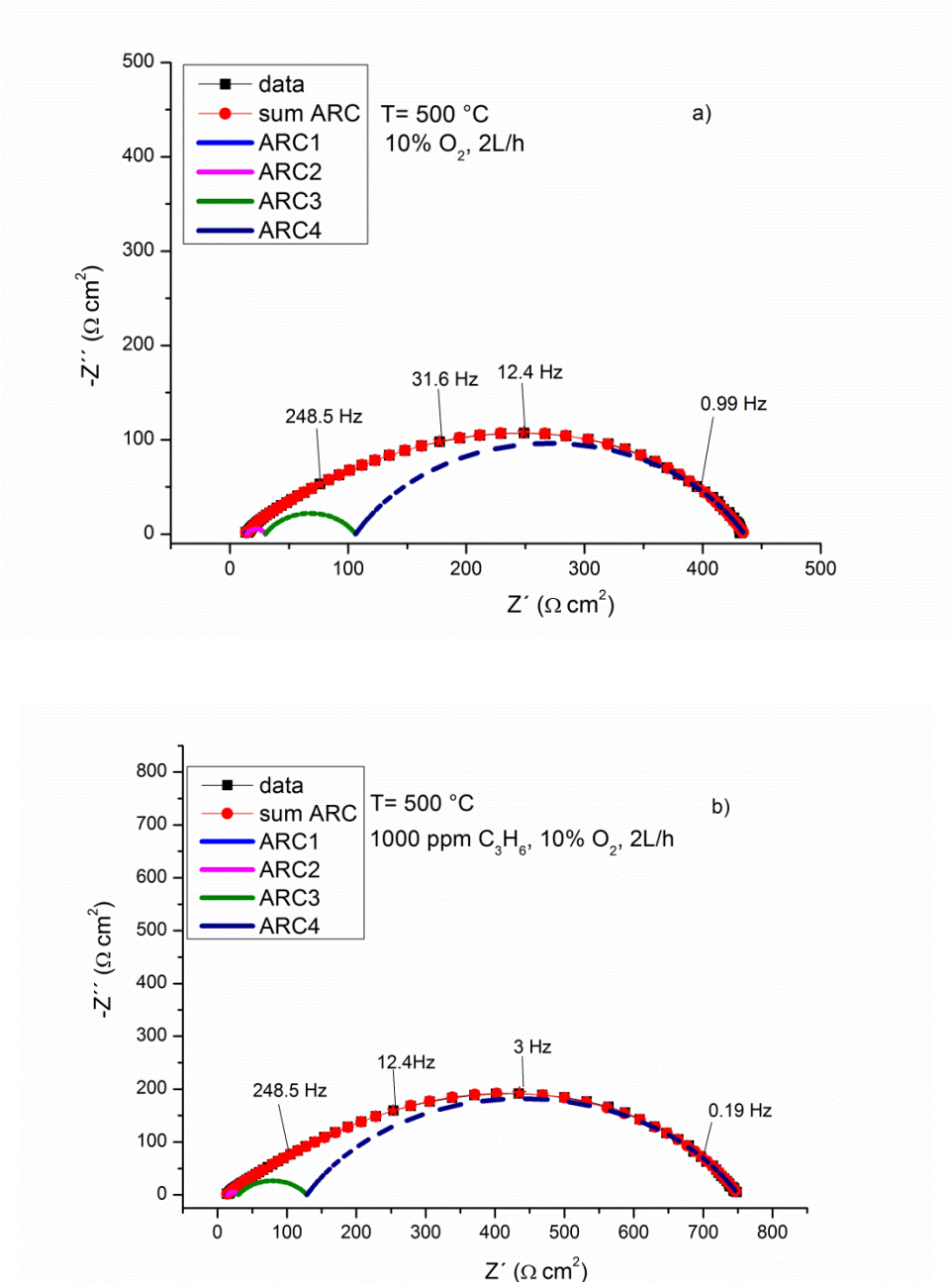


**Figure 15**: Nyquist plots of the impedance spectra of the CGO-LT cell recorded at 500 °C: a) 10% $O_2$ , b) 10% $O_2$ and 1000 ppm $C_3H_6$, 2 L/h OCV.

The introduction of propene caused a strong increase of resistance associated with the low frequency process ($R_4$), while the processes located at medium and medium-low frequencies were only slightly affected by propene introduction. The resistance $R_4$ increased from 430 Ω $cm^2$ to 740 Ω $cm^2$. The pseudo-capacitance (Q4) of this process increased together with the resistance. The introduction of propene decreased the characteristic peak frequency of one order of magnitude. This effect was already

observed by Ippolito et al. [40] on LSM/CGO electrode. The strong adsorption of propene on the electrode is strongly competing with adsorption and the dissociation of oxygen on the electrode surface. Due to its characteristics this process could be associated to the dissociation and surface diffusion of oxygen on the electrode.

## 6.5 Conclusions

In this study, the effect of the calcination temperature of the infiltrated material on the electrochemical oxidation of propene has been evaluated. The effect of morphology has been correlated with the electrochemical properties of the reactor by using of electrochemical impedance spectroscopy.

The infiltration of CGO increased the catalytic activity of the reactor starting from 350 °C. The degradation of the electrode has been partially mitigated by the infiltrated CGO.

The different morphologies of infiltrated CGO, obtained by different calcination temperatures, played a fundamental role. The formation of a thin and continuous layer of CGO, obtained with low temperature calcination, suppressed the competing reaction of oxygen evolution on the electrode and favored the reaction of propene oxidation with the oxygen ions supplied to the electrode through the electrolyte.

On the contrary, the formation of nanoparticles at high calcination temperature only partially suppressed the oxygen evolution reaction, resembling the performance of the non infiltrated cell. This behavior was confirmed by the analysis of the impedance spectra.

## References

1. R. Atkinson, *Atmospheric Environment*, **34**, 2063–2101 (2000)

2. W. B. Li, J. X. Wang, and H. Gong, *Catalysis Today*, **148**, 81–87 (2009)

3. P. Madcot, A. Fakche, B. Kellah, and G. Mabdonb, *Science*, **3**, 283–294 (1994).

4. R. Spinicci, A. Tofanari, and M. Faticanti, *Journal of Molecular Catalysis*, **176**, 247–252 (2001).

5. M. Baldi, E. Finocchio, and F. Milella, *Applied Catalysis B: Environmental*, **16**, 43–51 (1998)

6. V. Blasin-Aubé, J. Belkouch, and L. Monceaux, *Applied Catalysis B: …*, **43**, 175–186 (2003).

7. S. Irusta, M. Pina, M. Menendez, and J. SantamarÄ±a, *Journal of Catalysis*, **412**, 400–412 (1998)

8. L. F. Liotta et al., *Applied Catalysis A: General*, **347**, 81–88 (2008)

9. S. Scirè, S. Minicò, C. Crisafulli, C. Satriano, and A. Pistone, *Applied Catalysis B: Environmental*, **40**, 43–49 (2003).

10. N. Yamazoe and Y. Teraoka, *Catalysis Today*, **8**, 175–199 (1990).

11. T. Seiyama, *Catalysis Reviews*, **34**, 281–300 (1992).

12. G. Marnellos and M. Stoukides, *Solid State Ionics*, **175**, 597–603 (2004)

13. N. Li and F. Gaillard, *Applied Catalysis B: Environmental*, **88**, 152–159 (2009)

14. V. Roche et al., *Ionics*, **14**, 235–241 (2008)

15. F. Gaillard, X. Li, M. Uray, and P. Vernoux, *Catalysis Letters*, **96**, 177–183 (2004).

16. S. P. Balomenou et al., *Topics in Catalysis*, **44**, 481–486 (2007).

17. M. Twigg, *Applied Catalysis B: Environmental*, **70**, 2–15 (2007).

18. Y. Ren, R. Küngas, R. J. Gorte, and C. Deng, *Solid State Ionics*, **212**, 47–54 (2012)

19. B. C. H. Steele, *Solid State Ionics*, **129**, 95–110 (2000).

20. P. Blennow et al., *Fuel Cells*, in press (2013)

21. P. Blennow and K. Hansen, *ECS …*, **13**, 181–194 (2008)

22. T. Z. Sholklapper, C. Lu, C. P. Jacobson, S. J. Visco, and L. C. De Jonghe, *Electrochemical and Solid-State Letters*, **9**, A376 (2006)

23. S. P. Jiang, X. J. Chen, S. H. Chan, and J. T. Kwok, *Journal of The Electrochemical Society*, **153**, A850 (2006)

24. F. Bidrawn, G. Kim, N. Aramrueang, J. M. Vohs, and R. J. Gorte, *Journal of Power Sources*, **195**, 720–728 (2010)

25. K. B. Andersen, F. B. Nygaard, Z. He, M. Menon, and K. K. Hansen, *Ceramics International*, **37**, 903–911 (2011)

26. R. M. L. Werchmeister, K. K. Hansen, and M. Mogensen, *Materials Research Bulletin*, **45**, 1554–1561 (2010)

27. D. Ippolito, K. B. Andersen, and K. K. Hansen, *Journal of The Electrochemical Society*, **159**, P57 (2012)

28. G. Kremenic and J. Nieto, *J. Chem. Soc., Faraday …*, **81**, 939–949 (1985)

29. Y. Morooka and a Ozaki, *Journal of Catalysis*, **5**, 116–124 (1966)

30. S. P. Jiang and W. Wang, *Journal of The Electrochemical Society*, **152**, A1398 (2005)

31. X. J. Chen, S. H. Chan, and K. a. Khor, *Electrochemical and Solid-State Letters*, **7**, A144 (2004)

32. W. Wang and S. Jiang, *Solid State Ionics*, **177**, 1361–1369 (2006)

33. X. Chen, *Solid State Ionics*, **167**, 379–387 (2004)

34. J. Mizusaki, M. Yoshihiro, S. Yamauchi, and K. Fueki, *Journal of Solid State Chemistry*, **58**, 257–266 (1985).

35. F. Poulsen, *Solid State Ionics*, **129**, 145–162 (2000)

36. J. Mizusaki, *Solid State Ionics*, **52**, 79–91 (1992)

37. J. Mizusaki et al., *Solid State Ionics*, **132**, 167–180 (2000).

38. M. Mogensen, N. M. Sammes, and G. A. Tompsett, *Solid State Ionics*, **129**, 63–94 (2000).

39. J. Kim, G. Kim, J. Moon, and Y. Park, *Solid State Ionics*, **143**, 379–389 (2001).

40. D. Ippolito and K. K. Hansen, *Journal of Solid State Electrochemistry* (2012) , **17**, 895-908 (2012)

# 7 IMPEDANCE SPECTROSCOPY AND CATALYTIC ACTIVITY CHARACTERIZATION OF A HIGHLY POROUS $LSM_{15}/CGO_{10}$ ELECTROCHEMICAL REACTOR FOR THE OXIDATION OF PROPENE

## 7.1 Abstract

This study aims to characterize the electrochemical and catalytic behaviour of a $La_{0.85}Sr_{0.15}MnO_3/Ce_{0.9}Gd_{0.1}O_{1.95}$ electrochemical porous reactor for propene oxidation under lean conditions. Electrochemical impedance spectroscopy was used to study the effect of propene introduction on the reactive system. Propene competed with the adsorption and dissociation of oxygen on the electrode surface, inducing a strong increase in electrode resistance, mainly located in the low-frequency region of the impedance spectrum. The application of anodic polarization strongly increased propene conversion, although the current efficiency remained low. Prolonged polarization enhanced reactor catalytic activity and electrode performance due to the formation of oxygen vacancies on the electrode surface.

## 7.2 Introduction

The reduction of air pollution has become an international concern over the last ten years because of increases in emissions from mobile and stationary sources. Among these sources, volatile organic compounds (VOCs) represent a serious environmental problem, together with NOx, SOx and particulate matter, which lead to the formation of ozone in urban and regional areas [1].

Catalytic oxidation is an efficient method to destroy VOCs at temperatures (200-500 °C) lower than those required for thermal incineration (700-1100 °C). Practical applications require deep oxidation of VOCs at low concentrations. Supported metal catalysts such as Pt and Pd are usually employed due to their high activity at low temperature, but their use is limited by cost.

Transition-metal perovskite ($LaMO_3$) (M=Mn,Co) is a potential alternative to noble metals for catalytic oxidation of hydrocarbons [2,3] due to its large amount of non-stoichiometric oxygen and a high concentration of lattice defects, in some cases with mixed ionic and

electronic conductivity properties [4]. Perovskites possess good thermal stability, although preserving a high surface area while obtaining the perovskite structure is a challenge.
Electrochemical membrane reactors (EMR) have been widely studied for different chemical reactions of industrial interest [5]. As demonstrated by Stoukides and Vayenas in ethylene catalytic oxidation on silver using an $O^{2-}$ conductor, the catalytic rate can be modified by electrochemistry when $O_2$ is co-fed with the reactant [6]. The increase in reaction rate was found to be considerably higher than the rate of oxygen ion supply to the electrode; a single ion can activate the reaction of more than one gaseous adsorbed species, giving rise to a phenomenon known as electrochemical promotion of catalysis (EPOC). Most work on this topic has been conducted on metal catalysts such as Pt, Pd, Ru and Ag, but this phenomenon has also been studied on perovskites that simultaneously act as a catalyst and an electrode. Roche studied the effect of doped lanthanum strontium manganite for deep propane oxidation and showed an electrochemical promotion effect [7]. Gaillard demonstrated *in situ* control of activity and selectivity on $La_{0.8}Sr_{0.2}Co_{0.8}Fe_{0.2}O_3$ for deep oxidation of propene at 450 °C in 2% $O_2$ [8].

The aim of this work was to study the electrochemical and catalytic behavior of porous electrochemical reactor under lean conditions for the oxidation of propene, a major VOC component of Diesel engine exhausts [9], without precious metals. The entire reactor was thought as a highly porous catalytic filter for a possible application in a Diesel exhausts purification system. An additional objective was to better understand the electrochemical properties of the $La_{0.85}Sr_{0.15}MnO_3/Ce_{0.9}Gd_{0.1}O_{1.95}$ composite at temperatures below those normally used for solid oxide fuel cell operation and in the presence of a hydrocarbon. Electrochemical impedance spectroscopy (EIS) was employed to meet these objectives.

## 7.3 Experimental

### 7.3.1 Fabrication of the porous reactor

The reactor used in this study was ceramic made of 11 alternating layers of electrode and electrolyte. The electrolyte tape was made of $Ce_{0.9}Gd_{0.1}O_{1.95}$ (CGO) purchased from Rhodia, while the electrode was made of a 35% weight $Ce_{0.9}Gd_{0.1}O_{1.95}$ and 65% weight $La_{0.85}Sr_{0.15}MnO_3$ (LSM) purchased from Haldor Topsoe. For the electrode fabrication slurries for tape casting were made mixing LSM and CGO, solvent, binder, graphite and poly methyl methacrylate (PMMA) as pore formers. The CGO electrolyte was fabricated following the same procedure of the electrode. The slurries were ball-milled before tape

casting. Six electrodes and five electrolytes green tapes were laminated alternatively to obtain 5 stacked single cells. The reactor behaves as a symmetric cell.

Round cells were stamped out from the tapes with 18 mm diameter. The cells were then sintered at 1250 °C for 2 h. The desired porosity was obtained by burning the pore formers during the sintering. The final reactor had a final area of 1.36 $cm^2$, thickness of 210 µm and weight of 0.128 g, measured without the gold current collector. Before the test was carried on, gold paste with 20% weight carbon was painted on both sides of the electrochemical reactor and used as porous current collector. An image of the 11 layers reactor is shown in Figure 1.

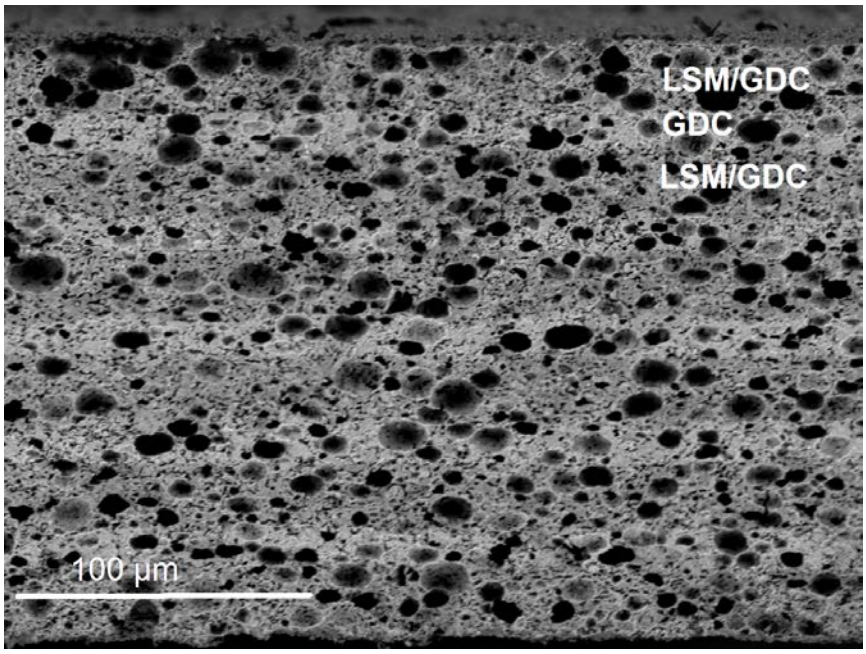


**Figure 1**: Cross-section micrograph of the electrochemical reactor.

### 7.3.2 Test setup

The sample was mounted in a tubular reactor between two alumina tubes with contact between the gold paste and the two Pt electrodes used as working and reference/counter electrodes under one atmosphere, as previously reported by our group [10]. The sample and the alumina tubes were surrounded by a quartz tube and mounted vertically in a furnace. The reaction temperature was monitored by two thermocouples: one touching the cell and the other one placed 4 mm over the cell. Figure 2 illustrates the setup configuration.

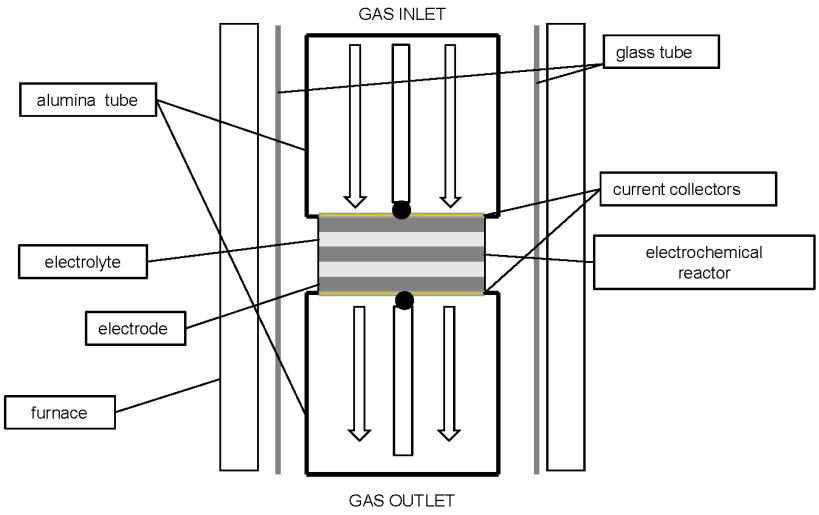


**Figure 2**: Scheme of the setup configuration

### 7.3.3 Electrochemical characterization

A potentiostat (Gamry, reference 600 USA) was used to perform chronoamperometry tests and for recording impedance spectra. The open-circuit voltage of the cell was stabilised before every measurement. The impedance spectra were recorded at open-circuit voltage (ocv) and with an anodic bias of +4 V using root mean square amplitude of 36 mV over the frequency range 0.78 MHz to 5 mHz with 10 points/decade. The temperature range of impedance measurements was 350 °C - 500 °C.

The chronoamperometry tests, coupled with gas analysis, were carried out for 2 h with anodic potentials from +1 V to +5 V (with respect to the open-circuit voltage) using 1 V steps. After the chronoamperometry tests the reactor was left at ocv for 5 h, and the cell was polarized for 5 h at +4 V to measure the effect of prolonged polarization on propene conversion. After 5 h polarization the chronoamperometry tests were repeated from +1 V to +5V with 1 V step, as described previously. The ohmic drop was not subtracted from the given potentials. The recording of the impedance spectra with different reaction atmospheres at 500 °C and 400 °C was performed before the chronoamperometry tests to avoid that electrode modifications induced by polarization could affect the measurements.

The impedance spectra were analysed with ZSimpWin 3.21 software using Complex Non-Linear Square (CNLS) fitting. The inductance from the wiring was subtracted for every spectrum before to perform the fitting. The spectra were validated using the Kramers-Kronig test for causality and time invariance.

The distribution of relaxation times (DRT) analysis was performed using in-house software based on Schichlein et al. [11]. A visual Hanning filter was used for data filtering, and the filtering values were fixed for all analyses.

An analysis of differences in impedance spectra (ADIS), based on Jensen´s work [12], was used to separate the different contributions affecting the impedance spectrum upon changes in reaction parameters.

$\Delta Z'(f_n)$ is defined as:

$$\Delta Z'(f_n)=\{[\Delta Z'(f_{n+1})- \Delta Z'(f_{n-1})]_{\varphi} - [\Delta Z'(f_{n+1})- \Delta Z'(f_{n-1})]_{\varphi^*}\}/[\ln(f_{n+1})-\ln(_{fn-1})]$$

where $\Delta Z'(f_{n+1})$ is the real part of Z at $n$+1 measurement frequency and $[\Delta Z'(f_{n+1})- \Delta Z'(f_{n-1})]$ is the difference between $\Delta Z'(f_{n+1})$ and $\Delta Z'(f_{n-1})$, measured under the specific operating condition φ;φ* represents the reference operating condition.

### 7.3.4 Catalytic activity measurements

For the catalytic activity evaluation of the reactor, a mixture of 10% $O_2$ (Air Liquide; 20% $O_2$ ± 2% Ar), 1000 ppm propene (Air Liquide; 1% ± 0.02% propene in Ar) and Ar (to balance) was used, with a total flow rate of 2 L $h^{-1}$ that was controlled by Brooks flow meters. The $C_3H_6$, CO and $CO_2$ concentrations in the outlet stream were monitored by an on-line Agilent 6890 N gas chromatograph, equipped with Hayesep N and Molsieve columns and a thermal conductivity detector. $CO_2$, CO and $H_2O$ were the only detected products in the outlet gas.

The magnitude of the effect of polarisation on the propene oxidation rate was evaluated by two commonly used parameters as suggested by Vayenas [13].

First, the rate enhancement ratio ($\rho$) defined by:

$$\rho = r / r_o$$

and the apparent faradaic efficiency ($\Lambda$):

$$\Lambda=(r-r_o) / (I/nF)$$

where $r_o$ is the catalytic rate (mol O/s) at open circuit voltage (ocv) and $r$ is the catalytic rate (mol O/s) measured under polarization. $I$ is the current recorded under polarization,

n the number of exchanged electrons during the electrode reaction, (n=2 in this case) and F is the Faraday constant.

### 7.3.5 Structural characterization

The structure and morphology of the reactor was evaluated in a Hitachi TM 1000 tab-letop microscope. The porosity of the electrochemical reactor was measured by mercury intrusion porosimetry using Micrometrics Autopore IV.

## 7.4 Results and discussion

### 7.4.1 Reactor structure characterization

Figure 1 shows a cross-section micrograph of the electrochemical reactor.
In the micrograph, the adhesion between the laminated layers after sintering was good; no cracks induced by the different sintering behavior of LSM and CGO were visible. The reactor porosity was 48 %, as indicated by mercury intrusion measurements. The distribution of pores was homogeneous along the entire reactor cross-section; this means that the pore formers (carbon and PMMA) did not agglomerate in the slurries before tape casting resulting in a pore formers uniform dispersion in the green tape before sintering.
Figure 3 illustrates the pore size distribution of the electrochemical reactor obtained from mercury intrusion measurements.

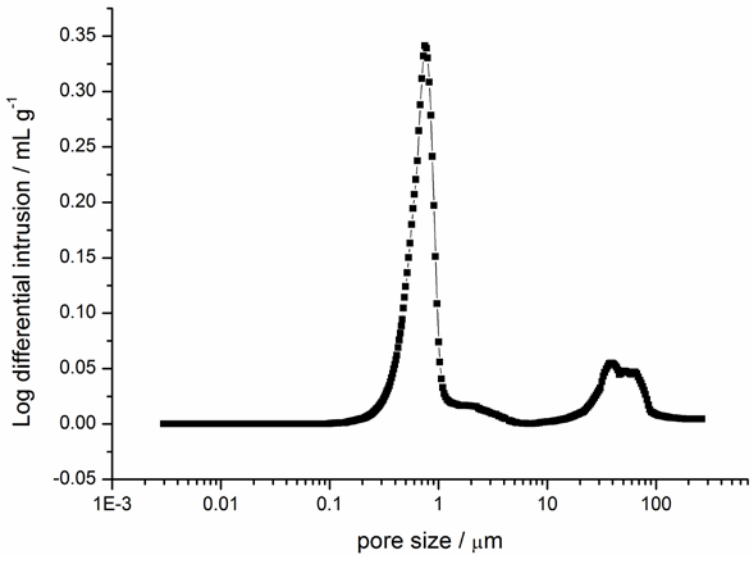


**Figure 3**: Logarithmic Differential Intrusion as a function of pore size of the reactor obtained from mercury intrusion measurements.

The main contribution to porosity was derived from pores measuring 0.5 µm to 4.5 µm, which accounted for 80 % of the total porosity; the remaining portion was derived from pores measuring 20 to 100 µm. The PMMA, used to form the pores, was responsible for the large round pores visible in Figure 1; the PMMA pore former permitted an increase in cell porosity while high mechanical strength of the reactor was maintained. The use of PMMA could have had beneficial effects by reducing the gas pressure drop along the reactor and facilitating access of the reactive mixture to the electrolyte/electrode contact area.

### 7.4.2 Electrochemical characterisation

*Effect of reaction atmosphere variation*

Figures 4A and 4B show the analysis of differences in impedance spectra (ADIS) as a function of oxygen partial pressure ($pO_2$) at 500 °C and 400 °C, respectively; the impedance spectrum recorded in 2% $O_2$ was used as reference. The figures include also the Nyquist plots of the impedance spectra used for ADIS and recorded at both temperatures.

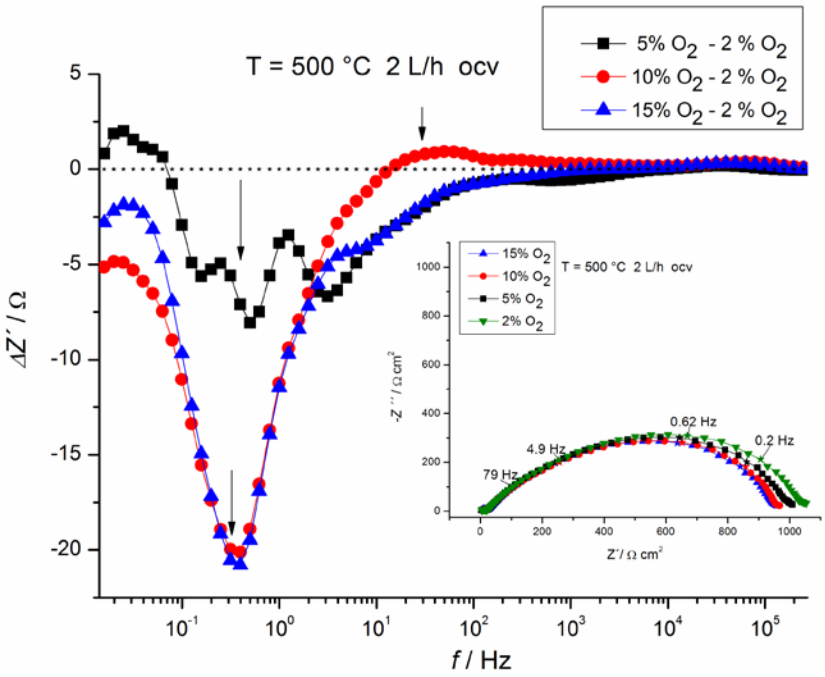


**Figure 4A**. ADIS of spectra recorded at 500 °C, ocv and 2 L/h under different $pO_2$: 2% $O_2$ as reference. Inset: Nyquist plots of the impedance spectra recorded under different $pO_2$, OCV and 2 L/h.

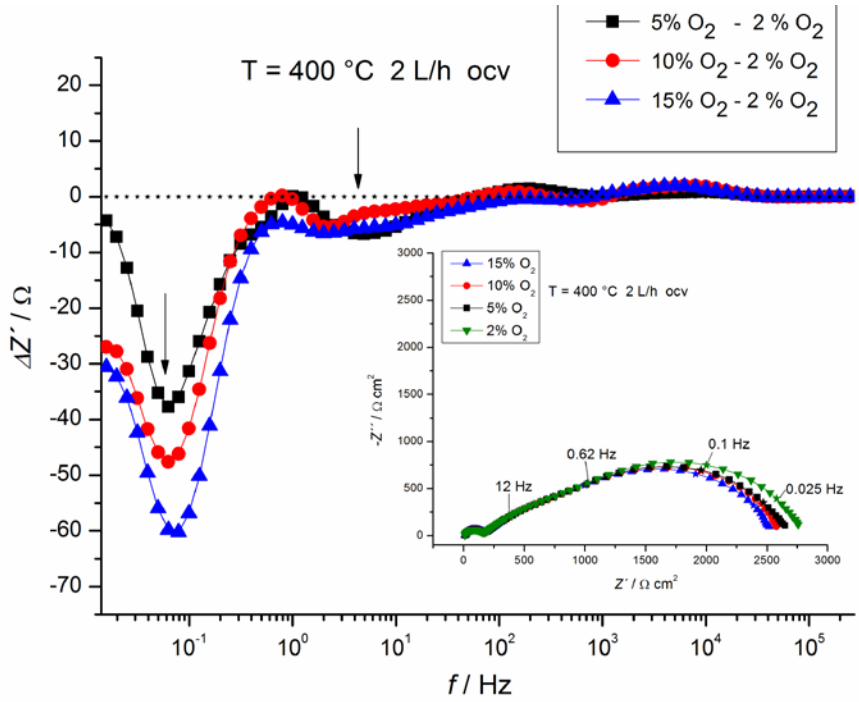


**Figure 4B**; ADIS of spectra recorded at 400 °C, ocv and 2 L/h under different $pO_2$: 2% $O_2$ as reference. Inset: Nyquist plots of the impedance spectra recorded under $pO_2$, OCV and 2 L/h.

Three main frequency regions can be identified: high frequency (100 Hz-1 MHz), medium frequency (1Hz-100 Hz) and low frequency (5 mHz-1 Hz). The first region was not affected by changes in oxygen concentration. The medium-frequency region exhibited a small resistance decrease that did not exceed 5 Ω; this small resistance change was independent of oxygen concentration. The oscillation visible for ADIS of 5% $O_2$-2% $O_2$ was generated by the calculation of ΔZ´ since no noise was detectable in the impedance spectra, as reported by the Nyquist plots in Figure 4A. Even with a 100 °C change in temperature, the characteristic frequency of the contribution at medium frequency was not significantly altered, as compared to the process observed at lower frequency. The low-frequency region was the most affected by the oxygen concentration change, showing a decrease in resistance with increased oxygen partial pressure. The change was centred at 0.4-0.5 Hz at 500°C and around 0.06 Hz at 400 °C, with a ten-fold decrease in the characteristic time/speed. The maximum ΔZ´ reached at 500 °C was lower than at 400 °C; clearly, the low-frequency process was affected by both gas composition and temperature.

According to the impedance data, the polarization resistance ($R_p$) has been obtained as difference between the ohmic resistance ($R_s$) at Z´ if $\omega \rightarrow \infty$ and Z´ if $\omega \rightarrow 0$. Figure 5 shows the $R_p$ of the cell as a function of $pO_2$ at 500 °C and 400 °C. The curves exhibited similar dependence on $pO_2$ at both temperatures: 0.039 and 0.04 at 500 °C and 400 °C, respectively. These values were closed to those reported by Jiang et al. on LSM/YSZ at

500 °C [14]. Although the difference between the two values was small, the ADIS reported in Figure 4 was able to identify the part of the spectra affected by resistance change and the effect of temperature on the electrode $R_p$ with $pO_2$ variation.

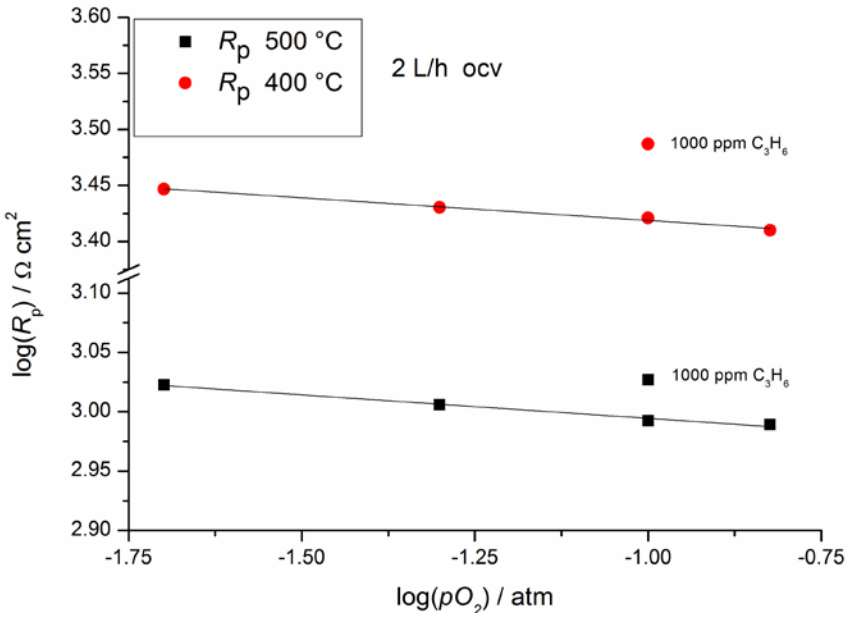


**Figure 5**: $pO_2$ dependence of $R_p$ at 500°C and 400°C, OCV and 2L/h

Figures 6A and 6B show the ADIS as a function of propene concentration in the presence of 10% $O_2$ at 2 L/h, recorded at 500 °C and 400 °C, respectively; 750 ppm $C_3H_6$ with 10% $O_2$ spectrum was used as reference. The figures report also the differences between the spectrum recorded with $C_3H_6$ and 10% $O_2$ and only with 10% $O_2$. Nyquist plots of the impedance spectra used for the ADIS were inserted in the figures. The high-frequency contribution showed a slight decrease in resistance at both temperatures, likely caused by a slight increase in electrode temperature resulting from propene oxidation although neither a decrease of ohmic resistance ($R_s$) nor a reactor temperature increase were measured. The medium-frequency response was not affected by propene introduction at 500 °C but exhibited an increase of resistance at 400 °C.

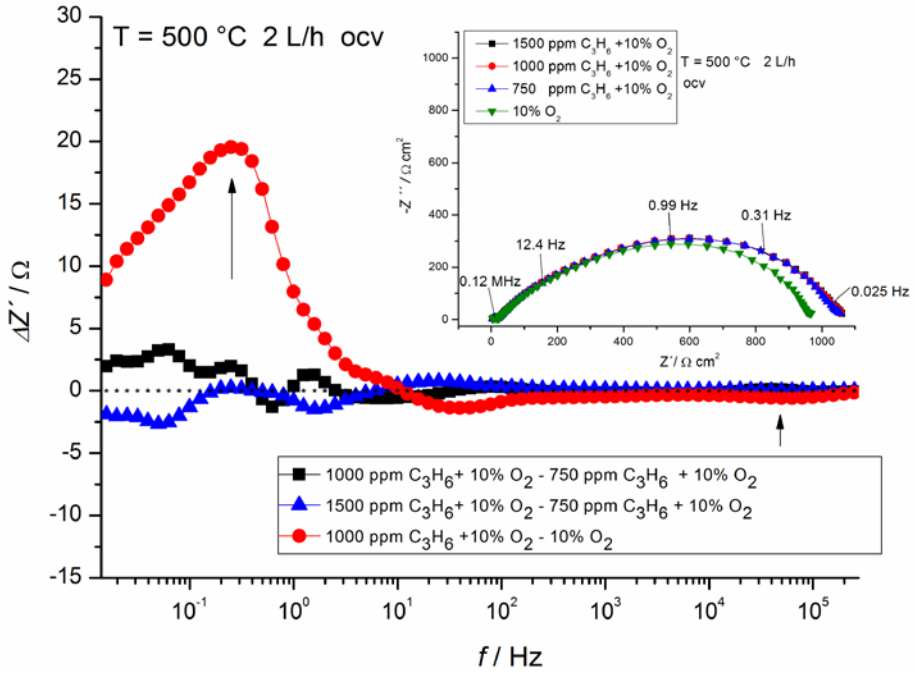


**Figure 6A**: ADIS of spectra recorded at 500 °C, ocv and 2 L/h under different $C_3H_6$ concentrations: 750 ppm $C_3H_6$ + 10% $O_2$ as reference. Inset: Nyquist plots of the impedance spectra recorded at ocv and 2 L/h.

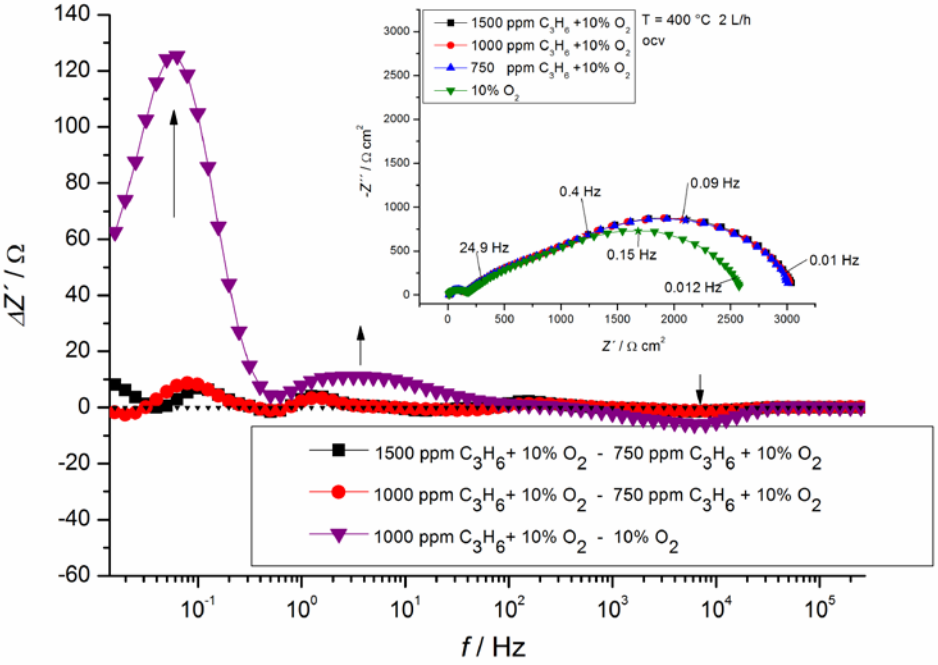


**Figure 6B:** ADIS of spectra recorded at 400 °C, ocv and 2 L/h under different $C_3H_6$ concentrations: 750 ppm $C_3H_6$ + 10% $O_2$ as reference. Inset: Nyquist plots of the impedance spectra recorded at ocv and 2 L/h.

The introduction of 1000 ppm of propene in the reactor induced an increase in resistance in the low-frequency region, with peaks centred at 0.2 Hz and 0.05 Hz for 500 °C and 400 °C, respectively. Additionally, in the case of propene introduction, the effect on the

electrode was stronger at 400 °C than at 500 °C, as shown by the $R_p$ values in presence of 1000 ppm propene together with $O_2$ reported in Figure 5. While the increase of resistance at 500 °C was comparable with maximum change of $pO_2$ (15% $O_2$ to 2% $O_2$), at 400 °C the introduction of propene induced a twofold increase of resistance if compared with the change of resistance due to the $pO_2$ change from 15% to 2%. At both temperatures, the impedance spectra were not influenced by the propene concentration change when propene was already present in the reaction atmosphere, i.e. no difference was visible between the spectra recorded with 1000 ppm /1500 ppm and 750 ppm of $C_3H_6$ in the presence of 10% $O_2$. This behaviour is clearly shown by the ADIS of Figures 6A and 6B, where ΔZ´ oscillates on the zero-line between -2.5 Ω and 2.5 Ω.

Distribution of relaxation times (DRT) analysis was performed on spectra at 500 °C and 400 °C, both in the presence of oxygen and oxygen with propene at ocv. The results are shown in Figures 7A and 7B. Three different relaxation peaks belonging to three different processes were evident. At 500 °C, the process at the medium frequency (3-100 Hz) was not well-resolved and was difficult to separate from the contribution at the lower frequency. At 400 °C, however, the medium-frequency process became clearly visible. The DRT analysis provided further information about the system with respect to ADIS, taking into account the change in imaginary impedance of the spectra.

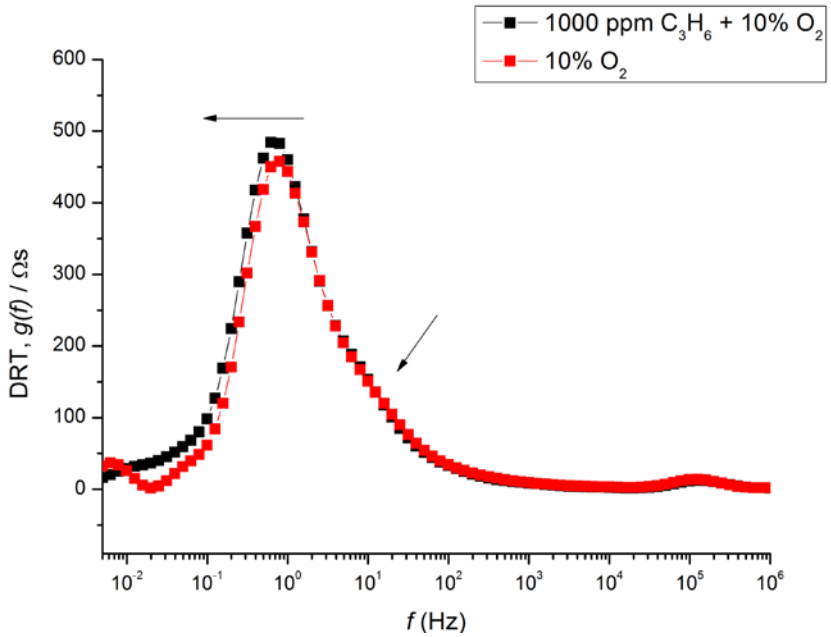


**Figure 7A**: Distribution of relation times (DRT) recorded at 500 °C and OCV with 10% $O_2$ and 1000 ppm $C_3H_6$ 10% at 2 L/h.

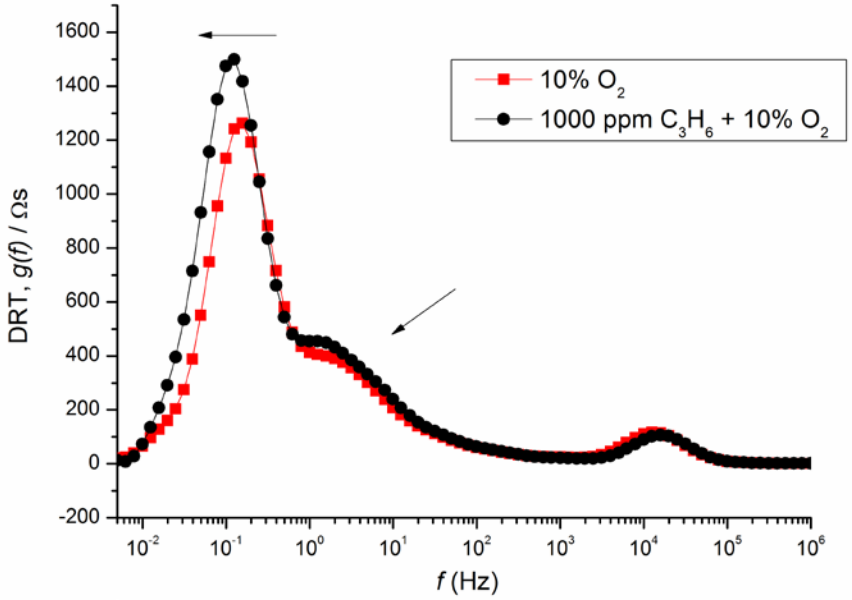


**Figure 7B**: Distribution of relation times (DRT) recorded at 400 °C and OCV with 10% $O_2$ and 1000 ppm $C_3H_6$ 10% at 2 L/h.

The introduction of propene not only was able to increase the resistance of the third contribution at low frequency but also caused a clear shift of the peak towards lower frequencies; as observed for resistance, the frequency shift was temperature-dependent: it increased with a temperature decrease. Propene slightly affected the medium-frequency portion of the spectra at 400 °C; this behavior was not visible at 500 °C. The effect of propene on impedance spectra laid in the same frequency decade as the change in oxygen concentration, as confirmed by Figures 6A and 6B. The DRT analysis of the effect of oxygen variation (not shown) showed an increase in resistance upon a decrease in oxygen concentration without any frequency shift.

According to the ADIS results, the low frequency part of the spectra was the most affected by gas composition variation. Moreover the variation of resistance, induced by a change of reaction atmosphere, increased with decreasing temperature. The temperature programmed desorption study of Caillol et al. [15] demonstrated that the adsorption of $O_2$ on $La_{0.8}Sr_{0.2}MnO_3$ increased with increase of temperature starting from 200 °C; this behavior showed the existence of an activated oxygen adsorption process. Fierro et al. [16] reported similar behavior for $LaMnO_3$, exhibiting active oxygen adsorption between 77 °C and 252 °C. The explanation of the dependence of low frequency process resistance from variation of temperature and oxygen was not straightforward. Multiple oxygen species exist on LSM surface, like $O_2^-$ and $O_2^{2-}$, at different temperatures, as reported by Caillol [15]. The concentration of this species on the electrode surface could be influenced

by the increase of electronic conductivity of LSM with temperature and resulting ionization of the adsorbed oxygen. The situation was complicated by the presence of CGO in the composite; the molecular oxygen could also interact with the oxygen vacancies present on CGO surface.

Also the introduction of propene had a stronger effect on impedance spectra if compared to the variation of the oxygen partial pressure. This behavior could be ascribed to the adsorption of propene on the electrode surface, as reported by Tascon et al. in their study of $LaMnO_3$ [17]. Cortes Corberan [18] reported that the fraction of irreversibly adsorbed propene on $PrCoO_3$ was significantly depressed by oxygen preadsorption. Those results suggest that both oxygen and propene adsorb on the same active site. Because the increase in electrode resistance appeared at frequencies close to the frequencies affected by the oxygen variation, it is possible that the introduction of propene interferes with the process involving diatomic oxygen or dissociated oxygen on the surface, likely causing the increase of resistance visible in the impedance spectra. Vernoux et al. studied the oxygen activity on Pt/YSZ as function of temperature in presence of oxygen and propene in the reaction atmosphere, using Solid Electrolyte Potentiometry (SEP) measurements. The oxygen activity increased with propene conversion and it reached its highest value when propene conversion was maximal [19]. This behavior could explain the increased effect of propene introduction in the system at 400 °C compared to 500 °C since the propene conversion is expected to be higher at 500 °C than 400 °C, as it will be shown later in the text.

The electrode response exhibited no dependence on propene concentration when propene was already present in the reaction atmosphere, as illustrated in Figures 6A and 6B. As studied by Kaloyannis et al. [20], the reaction kinetics between propene and oxygen on a Pt/YSZ electrocatalyst, showed a sharp maximum with respect to propene pressure at temperatures between 400 °C and 460 °C: the rate was zero order in propene, above the concentration maximum. The described kinetics suggested a competitive adsorption mechanism between oxygen and propene. Propene has π-electrons in its structure being an unsaturated hydrocarbon; this characteristic makes it an electron-donor, strongly adsorbing on catalyst surface. The strong adsorption of propene could easily saturate the electrode surface and make the electrode insensitive to propene concentration variation.

*Effect of ±15 °C temperature variation*

A further study was performed at 400 °C. The temperature ranged from values that were 15 °C higher to values that were 15 °C lower than the reference temperature of 400 °C. This test was performed using both 10% oxygen and 10% oxygen with 1000-ppm propene. The small temperature variation permitted the study of the system in a quasi-steady state.

Figure 8A illustrates the ADIS conducted on impedance spectra recorded at a temperature difference of 15 °C, using the spectrum in 10% oxygen at a fixed temperature as a reference. The Nyquist plot of the impedance spectra recorded with 15° C are shown in Figure 8B.

The analysis confirms the presence of three contributions, each affected to a different extent by changes in temperature and atmosphere.

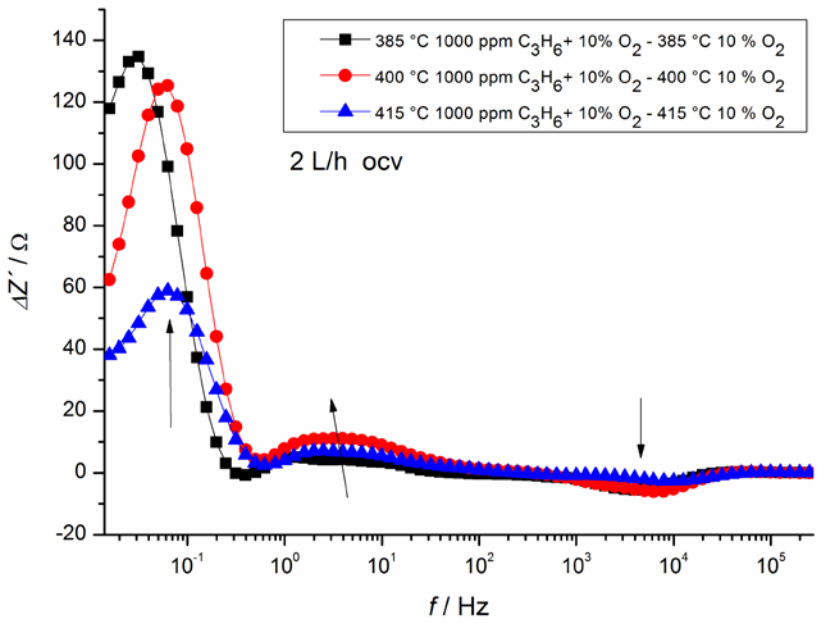


**Figure 8A:** ADIS of spectra recorded at 415 °C, 400 °C and 385 °C, 2 L/h in 10% $O_2$ and 10% $O_2$ and 1000 ppm $C_3H_6$, ocv and 2 L/h: 10 % $O_2$ used as reference at each temperature

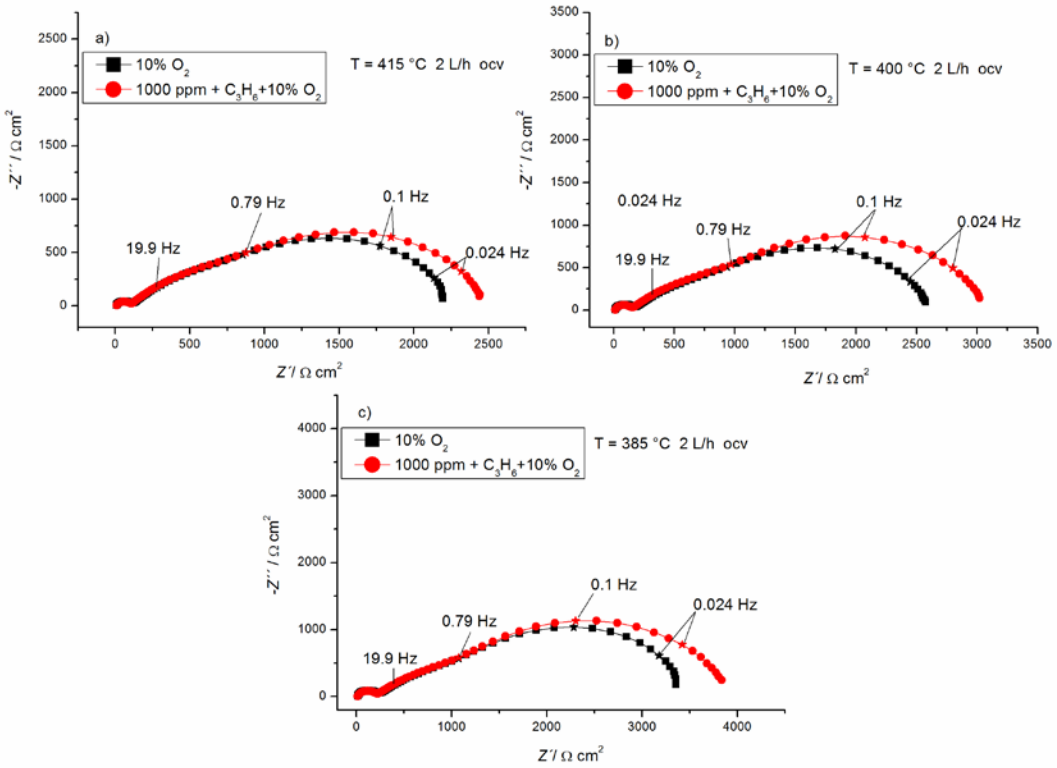


**Figure 8B:** Nyquist plot of the impedance spectra recorded at a) 415°C b) 400° C and b) 385 °C with 10% $O_2$ and 1000 ppm $C_3H_6$, 2L/h and at ocv.

At high frequencies ($10^3$-$10^5$ Hz), the introduction of propene caused a decrease of resistance; this behaviour could be due to the local increase in temperature associated with catalytic propene oxidation, as illustrated in Figure 6B, but also in this case neither decrease of $R_s$ nor reactor temperature increase were detectable.

At medium frequencies ($10^1$-$10^2$ Hz), the analysis showed a slight increase in resistance with the introduction of propene, but without a specific temperature-dependent pattern. The low-frequency ($10^{-2}$-1 Hz) portion was the most affected by propene introduction; the $\Delta Z'$ rose with decreasing temperature and, consequently, the frequency associated with this contribution increased with an increase in temperature. The 15 °C temperature change confirmed that the process at low frequency was thermally activated and strongly dependent on the composition and on the nature of the gases composing the reaction atmosphere.

*Effect of electrode polarisation*

Figures 9A and 9B show the impedance spectra recorded at 500 °C and 400 °C with 10% $O_2$ and 1000 ppm propene, together with Bode plots of real and imaginary impedance.

The polarization considerably reduced the resistance of the medium- and low- frequency processes, causing an order of magnitude increase in the characteristic frequencies at both temperatures. The effect of polarization on the process located at high frequency was negligible compared to the effect visible on medium and low frequency part of the spectra.

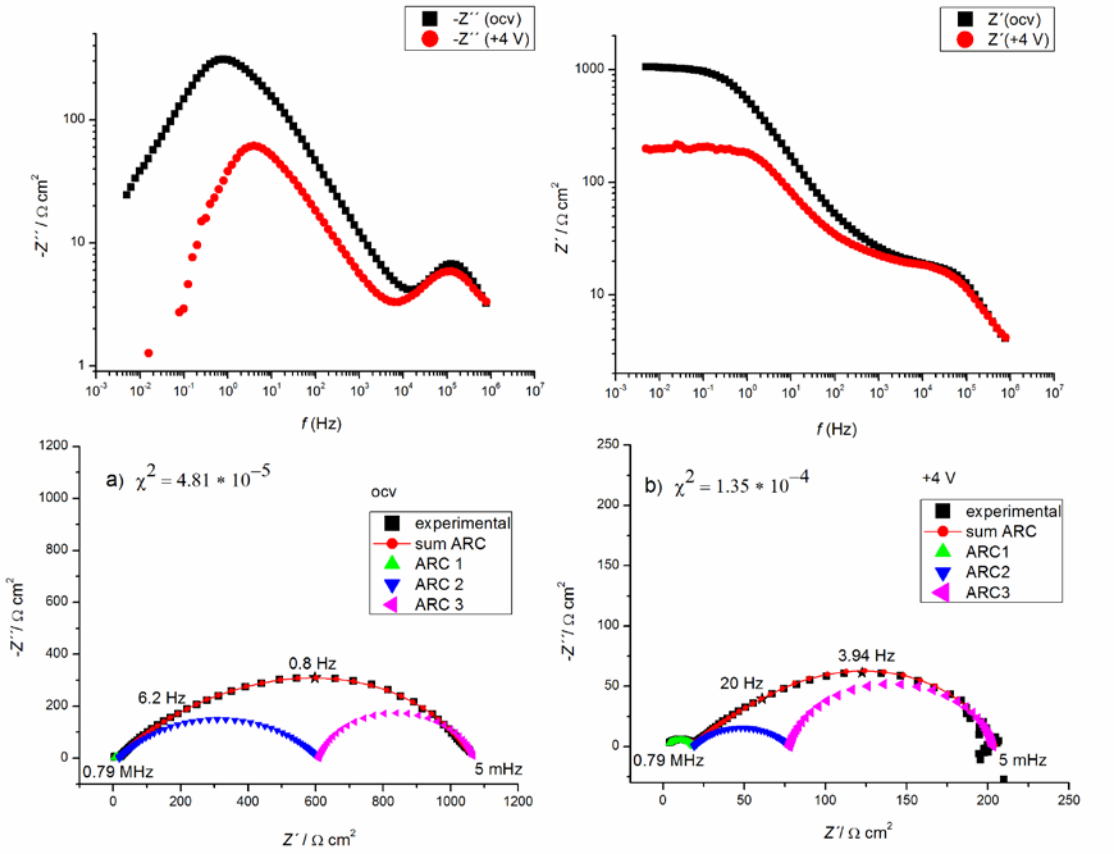


**Figure 9A**: Nyquist and Bode plots of spectra recorded at 500 °C, a) at ocv and b) with +4 V bias with 1000 ppm $C_3H_6$ + 10% $O_2$, 2 L/h**.** Inset: circuit model used for the impedance spectra fitting

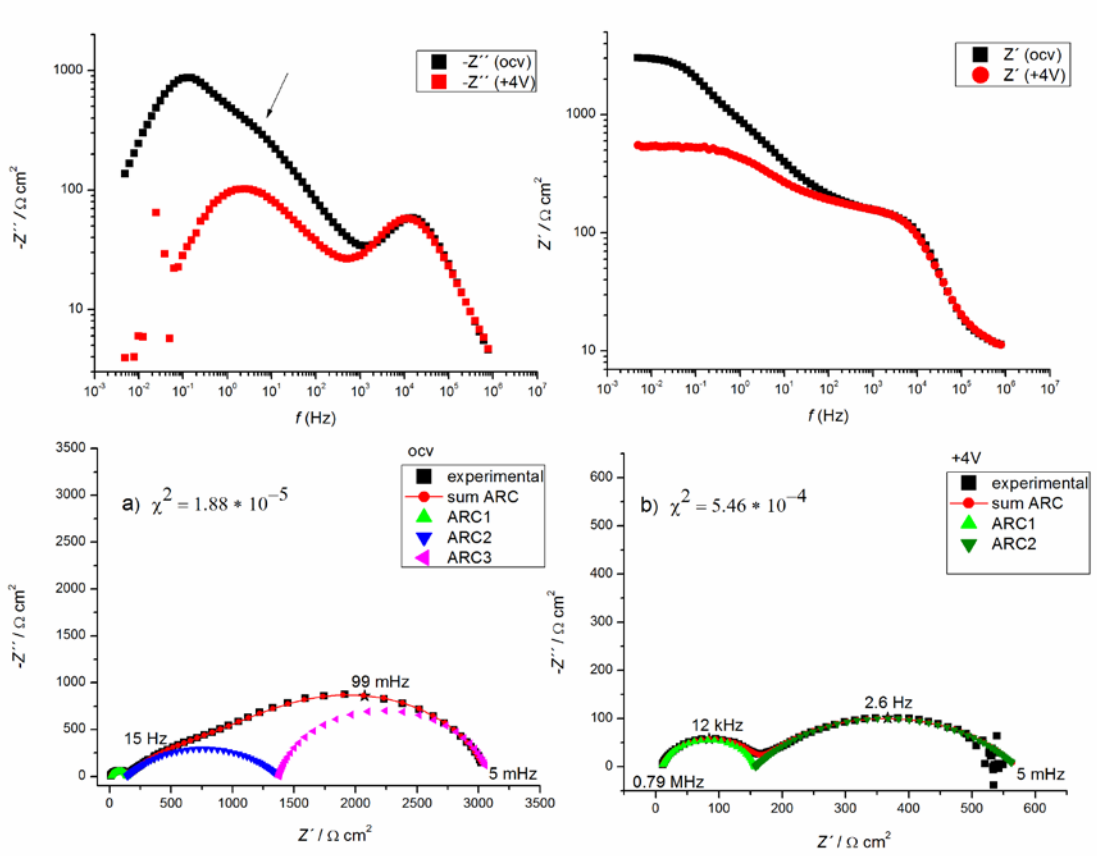


**Figure 9B**: Nyquist and Bode plots of spectra recorded at 400 °C, a) at ocv and b) with +4 V bias with 1000 ppm $C_3H_6$ + 10% $O_2$. Inset: circuit model used for the impedance spectra fitting

The decrease in resistance affected the low-frequency portion of the spectra to a major extent compared with the medium frequency. The shape of the Bode plot of the imaginary impedance in the case of 500 °C remained unchanged with polarization; the shoulder at medium frequencies that was visible at 400 °C completely disappeared with polarization, likely due to complete merging with the contribution at lower frequencies.

Figure 10 illustrates the Arrhenius plot of the polarization resistance ($R_p$) for the spectra recorded at ocv and +4 V. The application of +4 V led to an order of magnitude decrease in polarization resistance. The $R_p$ activation energy extracted at +4 V was 0.43 eV ± 0.02 eV; it was slightly lower than the activation energy measured at ocv (0.52 eV ± 0.02 eV). This behaviour could be due to a change in the reaction mechanism upon polarisation, involving only the processes visible at medium and low frequencies.

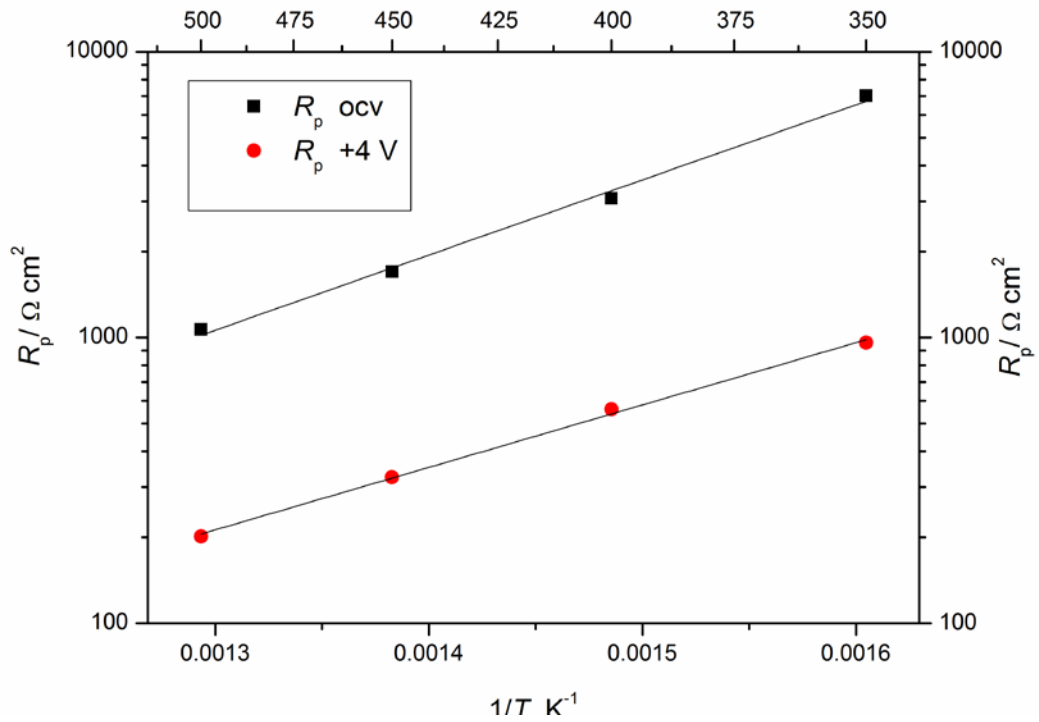


**Figure 10**: Arrhenius plot of polarisation resistance ($R_p$) at ocv and under polarization (+4V) of the spectra recorded with 1000 ppm $C_3H_6$, 10% $O_2$, 2 L/h

The reactor was polarized continuously for 5 h at +4 V in order to characterize the effect of prolonged polarization on the impedance response; an impedance spectrum was recorded before and after 5 h of anodic polarization. A decrease in $R_p$ was observed after polarisation; the decrease in both the imaginary and the real impedance affected the entire frequency range, but at high frequencies, only the spectra recorded at 500 °C and 450 °C exhibited an impedance change. The $R_s$ value of the spectra recorded at ocv after 5 h of polarization did not change. The electronic conductivity in the CGO is caused by the reduction of $Ce^{4+}$ to $Ce^{3+}$ at low $pO_2$ and high temperatures with the formation of electronic defects [21,22]. The reduction of CGO induced by polarization would have changed the ohmic resistance; the stable behavior of $R_s$ confirmed the stability of CGO with prolonged polarization.

Improvement of the LSM electrode with cathodic polarisation has been widely reported in the literature and it is associated with the formation of oxygen vacancies on the LSM surface, which enhances the surface diffusion of O intermediates to the TPB [23]. Being this reactor symmetric, one side functioned as an anode and the other side functioned as a cathode during the application of anodic polarisation. Electrode performance was enhanced on the cathodically polarised side by the incorporation of segregated/inhibiting SrO into the LSM lattice and the subsequent reduction of Mn ions, as proposed by Wang [24].

$$V'_{La,LSM} + SrO + 3Mn^{\bullet}_{Mn,LSM} + e^- \rightarrow O^x_{O,LSM} + Sr'_{La,LSM} + 3Mn^x_{Mn,LSM} \quad \text{Eq. 1}$$

where $V'_{La,LSM}$ are the cation vacancies on the LSM lattice sites, $O^x_{O,LSM}$ are the $O^{2-}$ ions in the LSM lattice sites, $Sr'_{La,LSM}$ represents a Sr ion introduced into a La lattice site in the LSM; and $Mn^{\bullet}_{Mn,LSM}$ and $Mn^x_{Mn,LSM}$ are $Mn^{4+}$ and $Mn^{3+}$ in LSM, respectively.
Further cathodic polarisation will result in oxygen vacancy formation according to:

$$O^x_{O,LSM} + 2Mn^x_{Mn,LSM} + V^{\bullet\bullet}_{O,CGO} + 2e^- \rightarrow O^x_{O,CGO} + 2Mn'_{Mn,LSM} + V^{\bullet\bullet}_{O,LSM} \quad \text{Eq. 2.}$$

where $V^{\bullet\bullet}_{O,CGO}$ and $V^{\bullet\bullet}_{O,LSM}$ are oxygen vacancies of CGO and formed on the LSM surface respectively, and $Mn'_{Mn,LSM}$ are $Mn^{2+}$ ions.
The electrode performance on the anodic side of the reactor was decreased by the consumption of oxygen vacancies and the re-segregation of SrO layers, as shown in the backwards reaction of Eqs. 1 and 2.
The real decrease in $R_p$ was partially hindered by the anodically polarised side of the reactor but showed that the beneficial effect of cathodic polarization was stronger than that of anodic polarization, especially at high temperatures. The re-segregation of SrO and the formation of cation vacancies on the LSM are highly energetic and relatively slow compared to the formation of oxygen vacancies; this difference could explain the general electrode improvement, although one side of the cell was anodically polarised.

*Fitting of the impedance data*

In agreement with previous literature on LSM/YSZ [25,26,27], the equivalent circuit in Figure 11 has been chosen for fitting the calculated with experimental impedance spectra. The $R_s$ is the ohmic resistance of the system (bulk electrolyte + contact), extracted from the impedance spectra as high frequency intercept of Z´ at $\omega \rightarrow \infty$, after the inductance of the wires was removed. $CPE_i$ and $R_i$ are the constant phase element and charge transfer resistance, respectively.

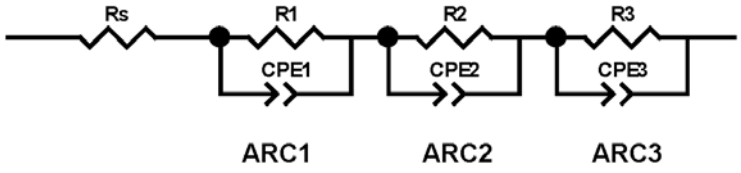


**Figure 11**: Circuit model used for fitting of the impedance spectra

The impedance of the CPE is given by:

$$1/Z=Y=Y^0(j\omega)^n$$

where $Z$ is the impedance, $Y$ the admittance, $Y^0$ is the amplitude of the constant phase element admittance, $j$ is the imaginary number and $\omega$ is the frequency. The near equivalent capacitance ($F/cm^2$) was calculated using the formula:

$$C_{eq}=(Y^0\times R)^{(1/n)}/R$$

In the Figure 9 is shown an example of the impedance spectra recorded at 500 °C and 400 °C at OCV and under polarization together with the corresponding circuit model and deconvolution arcs. For the spectra recorded at 500 °C, strong overlap existed between contributions at medium and low frequencies, while the process at high frequency was clearly separated. The existence of a process at medium frequency was confirmed by the DRT analysis at 400 °C reported in Figure 7B where an impedance contribution appeared at medium frequencies.

A fourth (RQ) element was added to the equivalent circuit but $X^2$ did not decrease of one order of magnitude to consider it as a valid improvement of impedance spectra fitting, according to the suggestion given in [28].

The spectra recorded under polarization of +4 V exhibited noise for frequencies below 0.3 Hz and 0.06 Hz at 500 °C and 400 °C, respectively. This behaviour was probably induced by a modification of LSM with the formation of oxygen vacancies during the measurement; only the low frequency part of the spectra, where long time is needed to measure the different impedance data, was affected by noise. The fitting of the spectra recorded under polarization was carried out although the residual errors obtained from Kramers-Kronig test showed high values at low frequency. The distribution of the data in the Nyquist plots of the impedance spectra recorded at +4 V, visible in Figures 9A and 9B, was not random but the semicircle clearly closed at low frequency. The increase of one order of magnitude of the $\chi^2$ values for the fitting of the spectra recorded under polarization was due to the low frequency noise.

*High-frequency arc*

The first contribution to the impedance spectrum (ARC1) was independent from oxygen partial pressure, suggesting that neither atomic oxygen nor molecular oxygen were

involved in this step. The application of +4 V bias during the spectra recording had no effects on arc resistance if compared to medium and low frequencies arcs. The independence from polarization excluded that the first contribution was a charge transfer process or a physical/chemical process preceding or following a charge transfer step. The impedance modelling showed that near equivalent capacitance was independent on temperature with values of $7.2\text{-}8\times10^{-8}$ F/cm$^2$. The high-frequency arc was affected by long-term polarisation only at high temperatures, as described previously; the polarisation caused a small decrease in capacitance. This behaviour was reported by Chen [29] in the study of the effect of cathodic treatment time on LSM/YSZ electrode at 850 °C. In Chen´s study, the decrease in capacitance supported the conclusion that the contact region between the LSM electrode and the YSZ electrolyte was reduced under cathodic current treatment.

The activation energy of 0.92 eV ± 0.03 eV was similar to the value reported by Perez-Coll [30] for the grain boundary conductivity of CGO. The activation energy extracted from spectra under polarization was 0.91 eV ± 0.04 eV, showing that this contribution was not influenced by the applied bias.

According to Steele [31], the grain boundary effect for clean CGO cannot be detected above 500 °C. However, the grain boundary contribution dominates the total conductivity up to 1000 °C for impure CGO samples. Nyquist plots of impedance spectra recorded at 150°C under 10% oxygen exhibited two semicircles. The high frequency semicircle belongs to the CGO bulk conductivity, with an equivalent capacitance of $4.52\times10^{-10}$ F/cm$^2$ and a summit peak frequency of 145 kHz. The low-frequency peak could be ascribed to the contribution of the pure grain boundaries, with an equivalent capacitance of $2.5\times10^{-7}$ F/cm$^2$ and a summit peak frequency of 160 Hz.

Activation energy of 1 eV for oxygen ions transfer from $La_{0.85}Sr_{0.15}MnO_3$ electrode to YSZ electrolyte was reported by Jørgensen et al. [32]; also this process did not exhibit any dependency from oxygen concentration and polarization.

Although some characteristics of this arc were similar to the process of oxygen ion transfer from LSM to GDC, especially at higher temperatures, this contribution was assigned to the response of $O^{2-}$ transport through CGO grain boundaries thanks to the activation energy value similar to that reported by Perez-Coll [30] and to the low capacitance values.

### 7.4.3 Medium and low frequency arcs

The strong decrease of resistance and increased peak frequency with polarization visible at medium and low frequency (ARC2 and ARC3) in the Bode plots of Figures 9, indicated that this part of the spectra contains a charge transfer contribution following the But-

ler-Volmer relation. Physical/chemical processes like adsorption and dissociation of oxygen on the electrode surface and oxygen surface diffusion could not be ruled out; these processes, if coupled with a charge transfer reaction, can also exhibit the general Butler-Volmer relation [26,29].

The strong overlapping of the (R2Q2) and (R3Q3) semicircles was the cause of the high correlation values between R2 and R3, particularly at high temperature. The presence of a medium frequency process was confirmed by the DRT analysis in Figure 7B and by the ADIS with 15 °C change of reaction temperature in Figure 8A.

The two modelled arcs merged into one when +4 V was applied to the cell at 400 °C and 350 °C; so it was no longer possible to use the circuit model shown in Figure 11 but only two circuit elements were used instead.

Due to the strong correlation of these two processes and the strong effect of polarization, the resistances $R_2$ and $R_3$ were merged together in the Arrhenius plot of Figure 12.

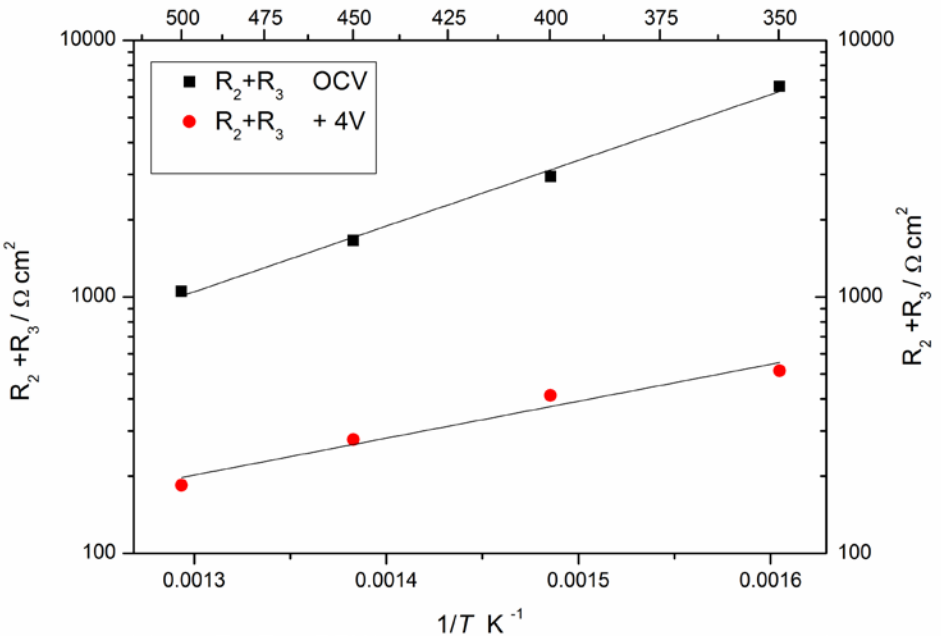


**Figure 12**: Arrhenius plot of ($R_2$ + $R_3$) as extracted from modelling of the spectra recorded with 1000 ppm $C_3H_6$, 10% $O_2$, 2 L/h

The activation energy extracted at ocv was 0.51 eV ± 0.04 eV while at +4 V was 0.29 eV ± 0.07 eV. The activation energy of $R_2$+$R_3$ at ocv was very close to the activation energy found for the $R_p$ at ocv, as reported previously; this was in agreement with the fact that $R_2$ and $R_3$ together were responsible of more than 90% of the total polarization resistance.

The reduced activation energy measured at +4 V could be to a change of reaction mechanism. The relative influence of anodic and cathodic reactions was unknown due to the symmetric configuration of the reactor.

At ocv the process at medium frequency exhibited slight dependence on reaction atmosphere change if compared to the process at low frequency. The near equivalent capacitance of ARC2 laid between 1.1 and 1.4 × $10^{-4}$ F/cm$^2$ and did not exhibit a clear trend with temperature. This part of the spectrum was simulated with n-values between 0.6 and 0.5 decreasing with temperature. The capacitance values extracted at +4 V for 500° C and 450 °C were similar to the values obtained at ocv.

It was not possible to unambiguously associate this arc to a specific process due to the arc behavior inconsistency.

The process at low frequency (ARC3) was characterized by dependency on oxygen content and particularly by the introduction of propene in the reaction environment; the effect of $pO_2$ and propene introduction into the system on resistance was stronger with decreasing temperature. This thermally activated behavior ruled out the possibility that this process could be associated to gas diffusion due to the independence of gas diffusion on temperature [33].

The near-equivalent capacitance increased with temperature from 8.45 × $10^{-4}$ F/cm$^2$ at 350 °C to 1.8 × $10^{-3}$ F/cm$^2$ at 500 °C; increasing temperature increased the TPB zone and thereby increased the associated capacitance. The application of +4 V strongly reduced the resistance of this arc, and the capacitance decreased of one order of magnitude to 3.5 × $10^{-4}$ and 3.2 × $10^{-4}$ F/cm$^2$ for 500 °C and 450 °C, respectively; only at these two temperatures it was still possible to separate ARC3 from ARC2 in the spectra recorded under polarization.

The propene introduction into the reactive system was able to increase the $R_p$ of the entire spectra of a higher extent compared to the $pO_2$ change; the increase of $R_p$ as mainly caused by this low frequency process as proved by the ADIS and DRT analysis. The competition of propene and oxygen for the adsorption on the same reaction site could be the cause for the $R_p$ increase.

Due to its characteristics, this arc could be associated to the adsorption of oxygen and following dissociation on the electrode surface; the propene could interfere with this mechanism due to the formation of strong bonding between propene and the electrode surface, as previously illustrated.

The decrease of resistance of ARC3, visible in the spectra recorded under polarization, was explained by its association with an electrochemical step; this will make the process dependent on polarization or current application to the electrode.

### 7.4.4 Catalytic activity characterization

The catalytic activity and the effect of polarization on propene conversion were studied in detail at two reaction temperatures and at different applied voltages.

Figure 13 shows the effect of polarization on propene conversion.

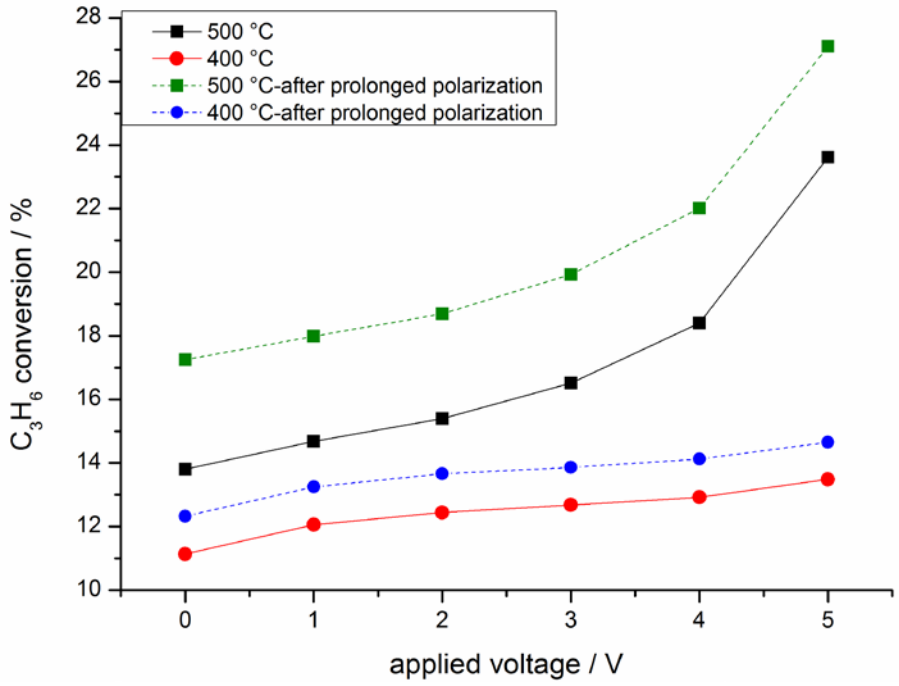


**Figure 13**: Propene conversion versus applied voltage with 1000 ppm $C_3H_6$, 10% $O_2$ and 2 L/h at 500 °C and 400 °C.

At 500 °C, a strong increase in conversion was evident, particularly above 2 V and following the current density behavior. Propene conversion reached 23.6 % at +5 V. The selectivity for $CO_2$ increased with increasing voltage from 86% to approximately 91% at +5 V. The dependence of $CO_2$ selectivity on voltage could be explained by the direct electrooxidation of the carbonaceous species formed on the catalyst surface and carried out by the highly active lattice oxygen pumped onto the electrode. At 400 °C the propene conversion reached 13.5 % at +5 V, and $CO_2$ selectivity was 100% in the whole voltage range.

The catalytic and polarization tests were repeated at both temperatures after 5 h of anodic polarization at +4 V, as described in the experimental part, in order to study the effect of prolonged polarization on catalytic performances.

The prolonged polarization strongly affected the conversion of propene: the conversion was measured at ocv after 5 h of polarization and it increased from 13.8 % to 17.2 % at

500 °C and from 11.1 % to 13.2 % at 400 °C. This behavior was previously observed by Ippolito et al. [34].

on the LSM/ CGO composite. The reduction of the LSM electrode, from $Mn^{3+}$ to $Mn^{2+}$, can occur with the concomitant generation of oxygen vacancies. This phenomenon not only will enhance the surface diffusion of oxygen species at the TPB enhancing the electrode performance, but also will increase the adsorption of propene on *in situ* generated oxygen vacancies, as proposed by Zheng [35] in the case of methane oxidation over $La_{0.8}Sr_{0.2}MnO_3$.

The increase of propene conversion, measured at ocv after 5 h of anodic polarization was applied, could be caused by oxygen vacancies formation during polarization on the cathodically polarized portion of the electrode. The oxygen vacancies could be involved in the formation of highly reactive anionic oxygen species ($O^-_{2,ads}$) as proposed by the study of Labaky [36] on oxygen ion conductor $Y_2O_3$-$ZrO_2$ catalyst for oxidation of propene. The oxidation of propene could take place through Mars-Van Krevelen mechanism where gaseous oxygen is reduced to form lattice oxygen by oxygen vacancies, while propene is oxidized by lattice oxygen.

Figures 14 and 15 illustrate the rate enhancement ratio ($\rho$) and faradaic efficiency ($\Lambda$), respectively, as a function of the applied voltage.

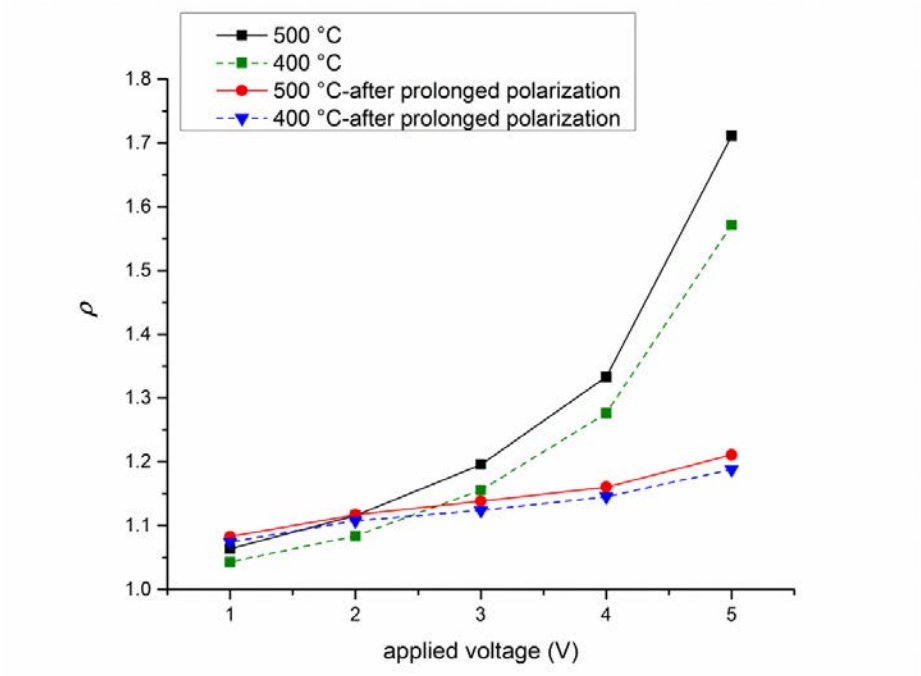


**Figure 14**: Rate enhancement ratio ($\rho$) versus applied voltage with 1000 ppm $C_3H_6$, 10% $O_2$ and 2 L/h at 500 °C and 400 °C.

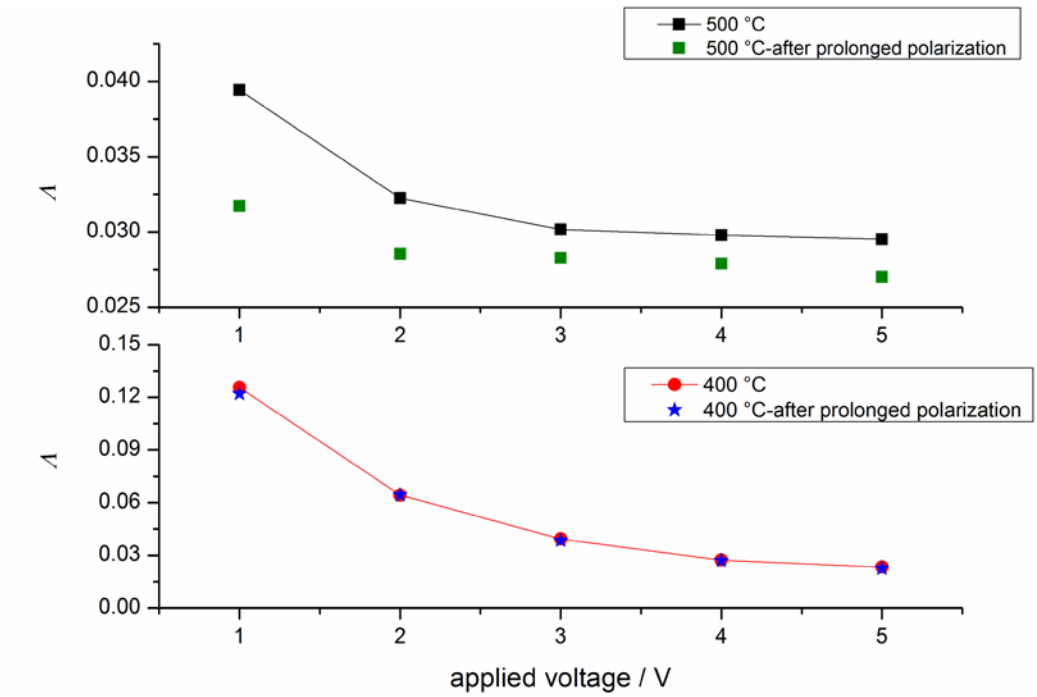


**Figure 15**: Faradaic efficiency ($\Lambda$) versus applied voltage at 500 °C and 400 °C.

The effect of polarization on propene conversion ($\rho$) was less pronounced at 400 °C than at 500 °C due to the strong increase in electrode resistance associated with oxygen reduction and $O^{2-}$ oxidation reactions, coupled with the decrease in CGO ionic conductivity. The effect of polarization was similar at low voltages for both temperatures, and the region at low polarization was associated with the highest faradaic efficiency values. This behavior was in agreement with the work of Li [37] on Ag and with the work of Roche on LSM [7]. At low voltage, the surface coverage of $O^{2-}$ and the speed of oxygen ion recombination into molecular oxygen are low, increasing the probability that oxygen ions will react directly with propene. The competing molecular oxygen formation reaction became faster with temperature and voltage, causing the sharp decrease in faradaic efficiency.

Prolonged polarization affected both the enhancement ratio and the faradaic efficiency, as illustrated in Figures 14 and 15. The improvement of propene conversion upon 5 h of polarization was coupled with the increase of electrode activity, which was confirmed by the increased current density. The increase in electrode performance (current density) was more pronounced at 500 °C compared to 400 °C; the current density increase was very low at 400 °C, but it was still measurable.

The improvement of propene conversion measured at OCV ($r_o$), after the reactor was polarized for 5 h, was not followed by a concomitant increase in the effect of polarization on propene conversion ($r$), likely causing the sharp decrease in the rate enhancement ratio ($\rho$) and the faradaic efficiency, as shown in Figures 14 and 15. The electrode performance increase, after 5h polarization, caused an increase in the speed of the competing

reaction of oxygen ion recombination at TPB to form molecular oxygen, causing a sharp decrease in faradaic efficiency (Figure 15), especially at 500 °C.

It is necessary to increase the oxygen-ion promoter lifetime to increase the possibility that propene will react directly with oxygen ions or monatomic oxygen at the surface. This means that the speed of the competing oxygen evolution reaction, occuring under anodic polarization, should be strongly decreased: the electrode should exhibit high polarization resistance for this reaction. The prolonged polarization had a double effect: it increased the propene conversion and selectivity measured at OCV and it strongly enhanced the electrode performance through the formation of oxygen vacancies. The latter effect became detrimental to obtain high current efficiencies but could eventually recover the electro-catalyst performance from the effect of sintering or long-term use.

## 7.5 Conclusions

The studied electrochemical reactor was characterised using electrochemical impedance spectroscopy that probed the behaviour of the LSM/CGO composite at low temperatures in the presence of propene.

The introduction of propene mainly affected the low-frequency region of the impedance spectra, increasing its resistance. The increase of resistance with propene introduction in the reactive system was stronger than the resistance change induced by oxygen partial pressure variation and it increased with decrease in reactor temperature. The impedance spectra were also insensitive to propene concentration change when oxygen was present in the reactive system. The propene, due to its high adsorption strength on the electrode surface derived from its unsaturated bonds, interfered with the adsorption and dissociation of oxygen at the electrode active sites, causing the increase of polarization resistance.

The ADIS and DRT analysis, carried out on the impedance spectra, exhibited at least three contributions to the polarization resistance. The CGO grain-boundary response was detectable at high frequencies and it was not affected by polarization and reaction atmosphere. The contributions at low and medium frequencies exhibited a strong decrease in resistance with +4 V polarization. While the low frequency process was associated with the adsorption and dissociation of oxygen on the electrode surface, the contribution at medium frequency was difficult to associate to any electrochemical/physical process due to the inconsistency of its behaviour with oxygen and propene concentration change.

The conversion of propene was strongly increased by polarization, although the faradaic efficiency remained low even at low temperatures and voltages. Prolonged polarization increased the catalytic activity and electrode performance due to the formation of polarization-induced oxygen vacancies. The electrode improvement, induced by the 5 h anodic polarization, had a detrimental effect on both the enhancement ratio and the faradaic efficiency, due to the increased speed of the competing oxygen evolution reaction at the electrode surface.

## References


1. R. Atkinson*, Atmospheric Environment*, **34**, 2063-2101(2000).
2. N. Yamazoe, Y. Teraoka, *Catalysis Today*, **8**, 175-199 (1990).
3. T. Seyama, *Catalysis Review-Science and Engineering* ,**34**, 281-300 (1992).
4. P.J. Gellings, Bouwmeesteer H.J.M, Catalysis Today, **58**, 1-53 (2000).
5. G. Marnellos, M. Stoukides, Solid State Ionics, 175, 597-603 (2004).
6. M. Stoukides, C. G. Vayenas, *Journal of Catalysis*, **70**, 137-146 (1981).
7. V. Roche, E. Siebert, M.C. Steil, J.P. Deloume, C. Roux, T. Pagnier, R. Revel, P. Vernoux, *Ionics*, **14**, 235-241 (2008).
8. F. Gaillard, X. Li, M. Uray, P. Vernoux, *Catalysis Letters* , **96**,177-183 (2004).
9. M. V. Twigg, *Applied Catalysis B: Environmental*, **70**, 2-15 (2007).
10. D. Ippolito, K.K. Hansen, Journal of Solid State Electrochemistry, **17**, 895-908 (2012).
11. H. Schichlein, A.C. Muller, M. Voigts, A. Krugel, E. Ivers-Tiffée, *Journal of Applied Electrochemistry*, **32**, 875-882 (2002).
12. S. H. Jensen, A. Hauch. P.V. Hendriksen, M. Mogensen, *Journal of the Electrochemical Society*, **156**, B757-B764 (2009).
13. C.G. Vayenas, S. Bebelis, C. Pliangos, S. Brosda, D. Tsiplakides, *Electrochemical Activation of Catalysis: Promotion, Electrochemical promotion and Metal-Support Intreactions*, Kluwer Academic/Plenum Publishers, New York, 2001.
14. Y. Jiang, S Wang, Y. Zhang, J Yan, W Li, *Solid State Ionics*, **110**, 111-119 (1998).
15. N Caillol, M. Pijolat, E. Siebert, *Applied Surface Science*, **253**, 4641 (2007).
16. J.L.G. Fierro, J. M. D. Tascon, L. Gonzalez Tejuca, *Journal of Catalysis*, **89**, 209 (1984).
17. J.M.D. Tascon, *Journal of Colloid and Interface Science*, **102**, 373-379 (1984).
18. V. Cortes Corberan, *Journal of Colloid and Interface Science,* **129**, 270-277 (1989).

19. P. Vernoux, F. Gaillard, L. Bultel, E. Siebert, M Primet, *Journal of Catalysis,* **208**, 412-421 (2002).
20. A. Kaloyannis, C.G. Vayeans, *Journal of Catalysis*, **182**, 37-47 (1999).
21. H. Yahiro, K. Eguchi, H. Arai, *Solid State Ionics,* **36**, 71-75 (1989).
22. T. Kudo, H. Obayashi, *Journal of the Electrochemical Society*, **123**, 415-421 (1976).
23. X.J. Chen, *Solid State Ionics*, **167**, 379-387 (2004).
24. W. Wang, J. S. Ping, *Solid State Ionics*, **177**, 1361-1369 (2006).
25. J. Wang, Y. Zhang, T Liang, C Deng, J. Xu, *Journal of Power Sources*, **209**, 415-420 (2012).
26. J.D. Kim et al., *Solid State Ionics,* **143**, 379-389 (2001).
27. S. P. Jiang, W. Wang, *Journal of the Electrochemical Society*, **152**, A1398-A1408 (2005).
28. E. Barsoukov, J.R. Macdonald, *Impedance Spectroscopy: Theory, Experiment and Applications*, 2nd ed., Wiley Interscience, Hiboken, New Jersey, 2005.
29. X.J. Chen, K.A. Khor, S.H. Chan, *Journal of Power Sources,* **123**, 17-25 (2003).
30. D.Perez-Coll, G.C. Mather, *Solid State Ionics,* **181,** 20-26 (2010).
31. B.C.H.Steele, *Solid State Ionics*, **129**, 95-100 (2000).
32. M.J. Jørgensen, M. Mogensen, *Journal of Electrochemical Society*, **148**, (2001) A433-A442.
33. S. Primdhal, M. Mogensen, *Journal of the Electrochemical Society,* **146**, 2827-2833 (1999).
34. D.Ippolito, K.B. Andersen, K.K. Hansen, *Journal of the Electrochemical Society,* **159**, P1-P8 (2012).
35. Y. Zheng, R. Ran, S.Z.Qiao, Z. Shao, Study On Oxygen Activation and Methane Oxidation over $La_{0.8}Sr_{0.2}MnO_3$ Electrode In Single Chamber Solid Oxide Fuel Cell Via An Electrochemical Approach, *International Journal of Hydrogen Energy* , **37**, 4328:4338 (2012).

36. M. Labaki, S. Siffert, J.-F. Lamonier, E A. Zhilinskaya, *Applied Catalysis B: Environmental*, **43**, 261-271 (2003).

37. N.Li, F. Gaillard, Catalytic Combustion of Toluene over Electrochemically Promoted Ag Catalyst, *Applied Catalysis B: Environmental*, **88**, 152-159 (2009).

# 8 EFFECT OF $Co_3O_4$ AND $CeO_2$ INFILTRATION ON THE ACTIVITY OF A $LSM_{15}/CGO_{10}$ HIGHLY POROUS ELECTROCHEMICAL REACTOR FOR PROPENE OXIDATION

## 8.1 Abstract

The objective of this work was to study the effect of $Co_3O_4$ and $Co_3O_4/CeO_2$ infiltration of a $La_{0.85}Sr_{0.15}MnO_3/Ce_{0.9}Gd_{0.1}O_{1.95}$ electrochemical porous reactor on the catalytic activity and selectivity to $CO_2$ for propene oxidation at open circuit voltage and under polarization. The effect of the infiltration of $Co_3O_4$ and $Co_3O_4/CeO_2$ on the electrochemical properties of the reactor was also investigated by electrochemical impedance spectroscopy (EIS).

The cells infiltrated with $Co_3O_4$ and $Co_3O_4/CeO_2$ exhibited high catalytic activity for propene oxidation; the high conversion of propene limited the effect of polarization on the propene oxidation rate, exhibiting a maximum around 300 °C.

The infiltration of $Co_3O_4$ did not improve the electrode performance compared to the non-infiltrated reactor while the co-infiltration of $CeO_2$ and $Co_3O_4$ was able to strongly decrease the polarization resistance of the porous reactor. The beneficial effect of $CeO_2$ on the electrode activity was attributed to the increased concentration of stable oxygen species on the electrode surface.

## 8.2 Introduction

Among transition metal oxides, perovskites, zirconia based catalysts, manganese and cobalt oxides, have been claimed for their effectiveness in VOCs oxidation [1] . $Co_3O_4$ was found as one of the most active catalyst for propene oxidation after Pt, Pd and Cu due to its low oxide heat of formation corresponding to $Co_3O_4$ easiness to be reduced, as reported by Morooka et al. [2]; this property becomes important when the Mars Van-Krevelen redox cycle is predominat over 400 ºC.

Jhaveri et al. [3] studied propene oxidation on perovskite and mixed oxides; $CeO_2$-$Co_3O_4$ and $CuCo_2O_4$ were found to be the most active towards propene oxidation. More recently Liotta et al. [4] showed the high activity of Ce/Co (1:1 molar ratio) and $Co_3O_4$ for propene oxidation; the higher activity of $Co_3O_4$ and Co/Ce (1:1) with respect to the remaining

Co/Ce mixture samples was attributed to their higher mobility of lattice oxygen reacting with propene to form $CO_2$. The coupling of $Co_3O_4$ with $CeO_2$ favored the dispersion of $Co_3O_4$ crystallites and increased the surface area. Wirwalsky et al. [5] impregnated $CeO_2$ support with 5% weight of $Co_3O_4$; this catalyst presented the highest propene oxidation activity if compared with $Co_3O_4$ impregnated on $Al_2O_3$ and $TiO_2$. Temperature programmed reduction experiments showed that ceria, at the vicinity of cobalt species, was reduced at much lower temperature and in higher quantity.

The infiltration of $Co_3O_4$ or $Co_3O_4/CeO_2$ mixture into LSM/YSZ or LSM/CGO composite electrodes is poorly explored in literature and it appeared to be some disagreement on to the effect of $Co_3O_4$ and $Co_3O_4/CeO_2$ on the electrode performance. Imanishi et al. [6] reported an improvement of oxygen reduction reaction activity of LSM/YSZ cathode infiltrated with $Co_3O_4$ and $Co_3O_4/CeO_2$ and tested at 800 ºC for 100 h; the particle aggregation was suppressed by $CeO_2$ introduction. On the contrary Huang et al. [7] observed that the impregnation of CoOx on LSM/YSZ had negligible effect on both the I-V curve and the impedance spectrum. They suggested that the enhanced performance upon addition of Co in previous studies was due to the formation of $La_{1-x}Sr_xCoO_3$ perovskite phase with much higher ionic conductivity compared to the barely LSM.

## 8.3 Experimental

The reactor used in this study was ceramic made of 11 alternating layers of electrode and electrolyte. The electrolyte tape was made of $Ce_{0.9}Gd_{0.1}O_{1.95}$ (CGO) purchased from Rhodia, while the electrode was made of a 35% weight $Ce_{0.9}Gd_{0.1}O_{1.95}$ and 65% weight $La_{0.85}Sr_{0.15}MnO_3$ (LSM) purchased from Haldor Topsoe. For the electrode fabrication slurries for tape casting were made mixing LSM and CGO, solvent, binder, graphite and poly methyl methacrylate (PMMA) as pore formers. The CGO electrolyte was fabricated following the same procedure of the electrode. The slurries were ball-milled before tape casting. Six electrodes and five electrolytes green tapes were laminated alternatively to obtain 5 stacked single cells. The reactor behaves as a symmetric cell.

Round cells were stamped out from the tapes with 18 mm diameter. The cells were then sintered at 1250 °C for 2 h. The desired porosity was obtained by burning the pore formers during the sintering.

The porous reactor was used as a backbone for the infiltration of a 1.5 M equimolar solution of $Co(NO_3)_3$ and $Ce(NO_3)_3$ to obtain $Co_3O_4/CeO_2$ (Co/Ce 1:1) into the backbone and with a 1.5 M solution of $Ce(NO_3)_3$ to obtain $CeO_2$. Solutions were prepared with Millipore

water, Triton X-100 (Sigma-Aldrich), Ce nitrate hexahydrate (Alfa Aesar) and Co nitrate hexahydrate (Alfa Aesar). Infiltration was carried out in one step by applying vacuum to the cell after application of impregnation solution. After infiltration, both the infiltrated cells were calcined at 600 °C for 2 h. The weight of the cell was measured before infiltration and after calcination to estimate the infiltration loading. The infiltration loading was equivalent to approximately 2.0-2.1% of the weight of the cell. The cells were denominated $Co_3O_4$ and Co/Ce, respectively. The weight of the cell after infiltration was 0.133 g and 0.131 g for $Co_3O_4$ and Co/Ce, respectively.

Gold paste with 20% weight graphite was painted on both sides of the electrochemical reactor and used as the current collector. The cell weights were measured without the current collector and the cell areas were approximately 1.358 and 1.432 $cm^2$ for $Co_3O_4$ and Co/Ce infiltrated cells, respectively.

The sample was mounted in a tubular reactor between two alumina tubes with contact between the gold paste and the two Pt electrodes used as working and reference/counter electrodes under one atmosphere, as reported by Werchmeister et al. The sample and the alumina tubes were surrounded by a quartz tube and mounted vertically in a furnace.

For the catalytic activity evaluation of the reactor, a mixture of 10% $O_2$ (Air Liquide; 20% $O_2$ ± 2% Ar), 1000 ppm propene (Air Liquide; 1% ± 0.02% propene in Ar) and Ar (to balance) was used, with a total flow rate of 2 L $h^{-1}$ that was controlled by Brooks flow meters. The catalytic activity was measured from 150 °C to 500 °C with 50 °C increase in temperature. Temperature programmed oxidation (TPO) test was performed with a heating rate of 60 °C/h starting from 25 °C to 500 °C with 1000 ppm $C_3H_6$ and 10% oxygen at 2 L/h both at OCV and with a polarization of +4 V.

Reactants and products were analysed by an on-line Agilent 490 Micro chromatograph connected to the reactor and equipped with Porapak Q and Molsieve 5X columns and two thermal conductivity detectors.

A potentiostat (Gamry, reference 600 USA) was used to perform chronoamperometry tests and for recording impedance spectra. The open-circuit voltage of the cell was stabilized before every measurement. The impedance spectra were recorded at open-circuit voltage (OCV) bot in 10% $O_2$ and 1000 ppm propene ($C_3H_6$) + 10% $O_2$ at 2 L/h with root mean square amplitude of 36 mV over the frequency range 0.78 MHz to 5 mHz with 10 points/decade.

The distribution of relaxation times (DRT) analysis was performed using in-house software based on Schichlein et al.[21]. A visual Hanning filter was used for data filtering, and the filtering values were fixed for all analyses. The analysis of differences in impedance

spectra (ADIS) [22] was used to evaluate the effect of propene introduction on impedance response.

The chronoamperometry tests were carried out for 2 h with anodic potentials of +4 V (+ 800 mV/cell) with respect to the open-circuit voltage. The ohmic drop was not subtracted in the given potentials.

The magnitude of the effect of polarisation on the propene oxidation rate was evaluated by two parameters:

first, the rate enhancement ratio ($\rho$) defined by:

$$\rho = r / r_o$$

and the apparent faradaic efficiency ($\Lambda$):

$$\Lambda=(r-r_o) / (I/nF)$$

where $r_o$ is the catalytic rate (mol O/s) at open circuit voltage (ocv) and $r$ is the catalytic rate (mol O/s) measured under polarization. $I$ is the current recorded under polarization, n the number of exchanged electrons during the electrode reaction, (n=2 in this case) and F is the Faraday constant.

The structure and morphology of infiltrated material were examined in a Zeiss Supra 35 electron microscopy equipped with a field emission gun.

## 8.4 Results and Discussion

### 8.4.1 Structure Characterization

Figures 1 and 2 show the SEM micrographs of the backbone cell infiltrated with $Co_3O_4$ and Co/Ce, respectively. It is possible to observe that the distribution of the infiltrated material is uniform on the pore walls for both cells; some of the electrode surfaces were not reached by infiltrated material probably due to the presence of closed porosity. The analysis of SEM micrographs did not show any clear differences in the agglomeration behavior or arrangement of the $Co_3O_4$ and $Co_3O_4/CeO_2$ infiltrated material on the backbone surfaces; it is worth to highlight that the simple addition of Pr ions into the infiltration solution (Chapter 5) deeply influenced the morphology of the $Ce_{0.8}Pr_{0.2}O_2$ compared to $CeO_2$, although both the material were calcined at the same temperature, like in this case. The morphology of the infiltrated material appeared to be driven not only from the calcination temperature but also from the ions interactions with the backbone surface and from the microstructure of the backbone. Liotta et al. [4] showed that the addition of $Co_3O_4$ to $CeO_2$ decreased the particle size of both ceria and cobalt oxide. In this study the SEM micrographs showed that the infiltrated material is well distributed along the backbone and reached the inner layer of the porous cell structure through use of vacuum during the infiltration procedure.

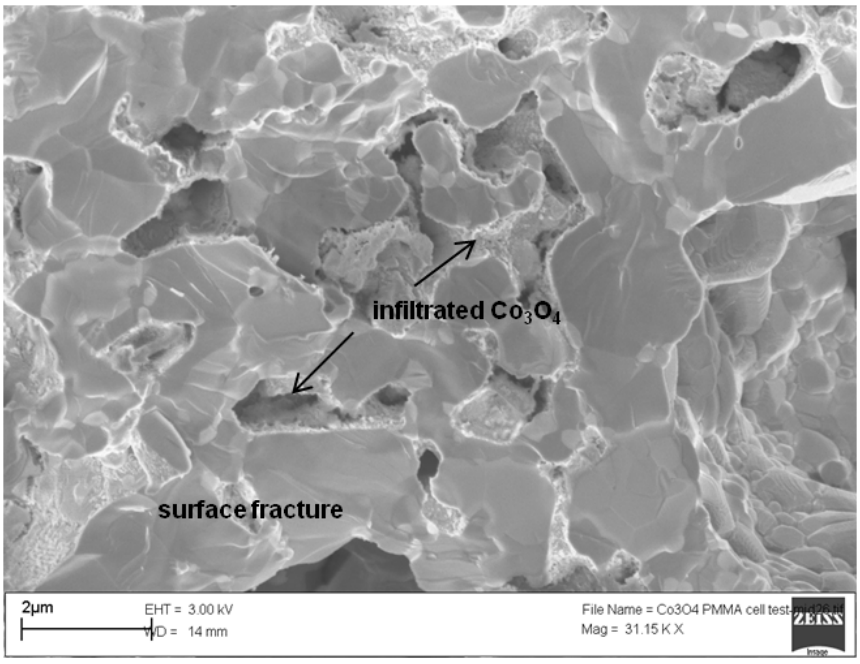


**Figure 1**: cross section SEM micrograph of $Co_3O_4$ infiltrated backbone cell (inner layer)

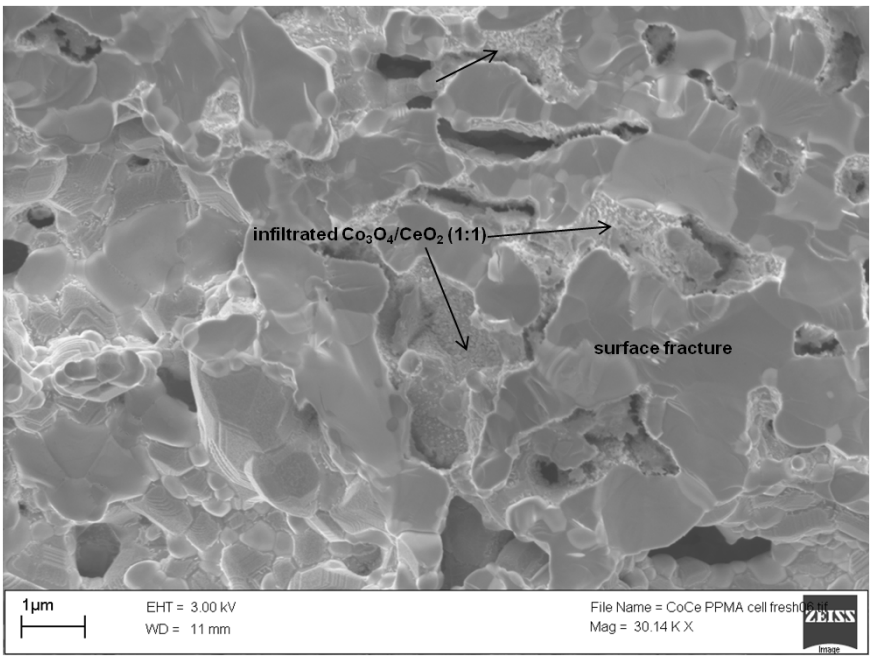


**Figure 2**: cross section SEM micrograph of Co/Ce (1:1) infiltrated backbone cell (inner layer).

### 8.4.2 Catalytic activity characterization

Figure 3 shows the propene conversion data for the cell infiltrated with $Co_3O_4$ and with Co/Ce mixture measured from 250 ºC to 500 ºC. It is possible to observe that propene conversion was above 90% already at 400 ºC. The selectivity to $CO_2$ was 100% at all temperatures confirming that $Co_3O_4$ and $CeO_2$ exhibit very good activity for CO oxidation, as reported by Yao et al. [8]. Previous results on LSM/CGO electrochemical reactor cell without infiltration (backbone-Chapter 7.4.4) showed only 14% conversion of propene and 86% selectivity to $CO_2$ at 500 °C, with carbon formation. In this case a carbon mass balance was carried during each run. It was found that the $C_3H_6$, $CO_2$, in the exit stream accounted for almost all the inlet $C_3H_6$. A maximum of 5 % of the inlet $C_3H_6$ could not be accounted for by the carbon mass balance. Typically, the discrepancy decreased with increase in temperature and may be due to slow adsorption of $CO_2$ on the catalyst surface which is reduced at higher temperatures. The addition of $CeO_2$ to $Co_3O_4$ increased the catalytic activity especially at low temperatures (250-300 °C). Co/Ce exhibited a reaction rate of $8.26 \times 10^{-8}$ mol $C_3H_6/(g \times s)$ against $7.48 \times 10^{-8}$ mol $C_3H_6/(g \times s)$ shown by the Co3O4 infiltrated cell, measured at 300 °C.

The conversion measurement was repeated at 300 °C and 400 °C and no change was observed for the conversion values at these two temperatures, confirming the good stability of both infiltrated materials. It should be noted that tests were carried out well below the limit of thermal stability (700-750 °C) of $Co_3O_4$ [8].

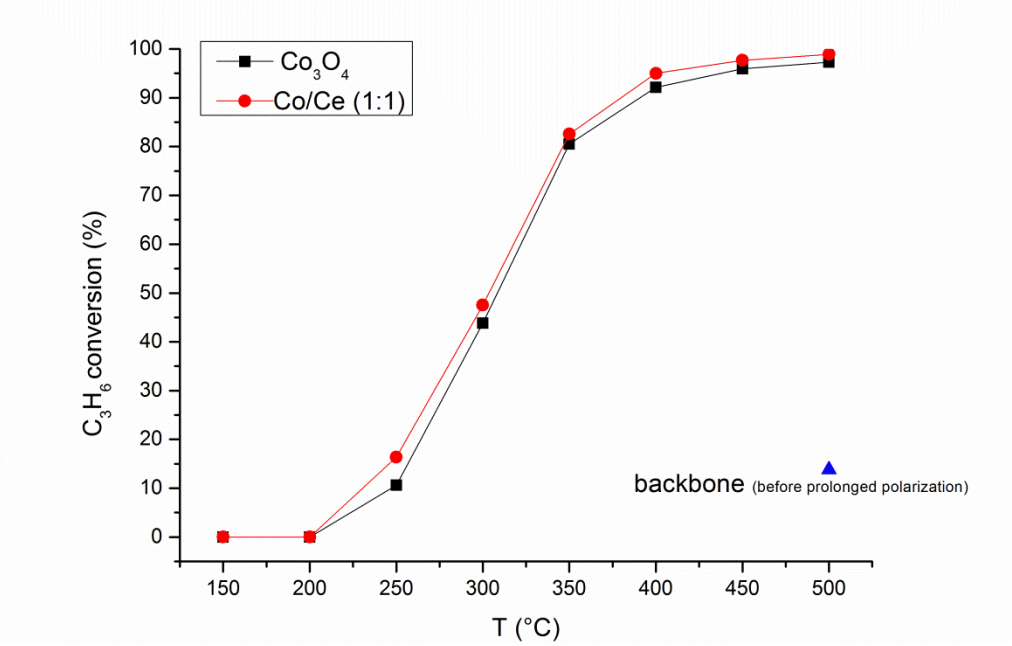


**Figure 3**: $C_3H_6$ conversion (%) as function of reaction temperature at OCV. Reaction mixture: 1000 ppm $C_3H_6$ + 10%$O_2$, 2 L/h Ar to balance.

Figure 4 shows the effect of +4 V (+0.8 mV/cell) polarization on propene oxidation rate expressed as rate enhancement ratio (ρ) at different reaction temperatures. It is possible to observe that the effect of polarization on the propene oxidation rate exhibited a behavior with a maximum at 300 °C and was strongly limited at temperatures above 300 °C where the ρ values were similar for both infiltrated cells. The faradaic efficiencies (Λ) at 300 °C were respectively 0.48 and 0.36 for $Co_3O_4$ and Co/Ce samples and fell below 0.015 at 400 °C for both cells.

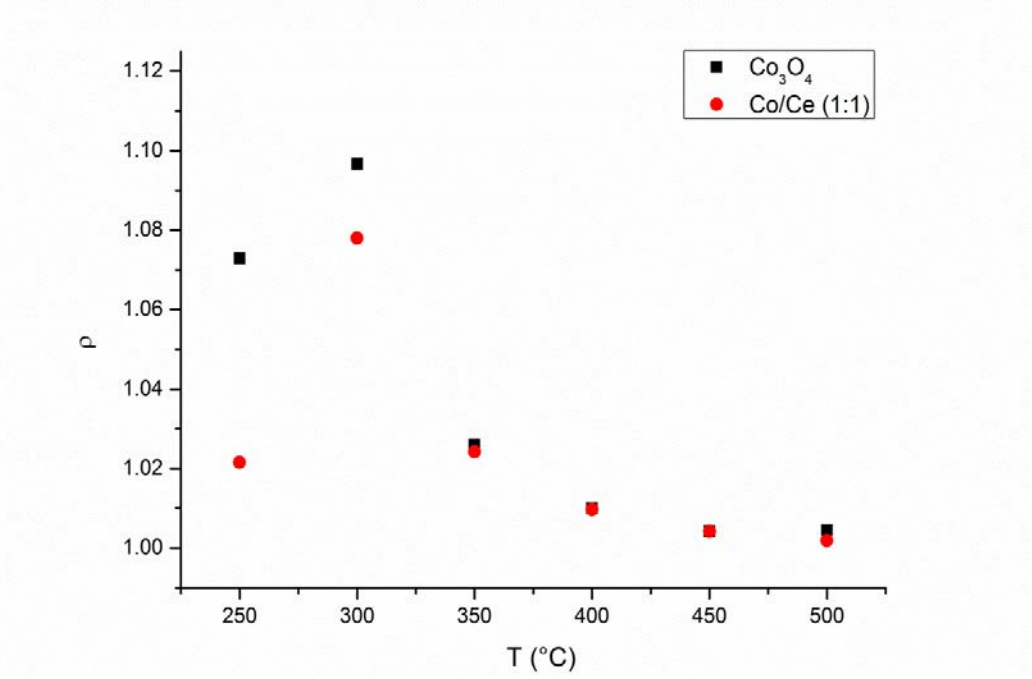


**Figure 4**: Rate enhancement ratio (ρ) versus temperature measured with +4 V bias, 1000 ppm $C_3H_6$ +10% $O_2$, 2L/h

A further study was conducted on $Co_3O_4$ infiltrated cell. Temperature Programmed Oxidation (TPO) was carried on at OCV first and then with the application of +4 V from room temperature to 500 °C in order to better characterize the effect of polarization on propene conversion as a function of temperature. The ratio between the reaction rate at fixed temperature for the oxidation of propene measured at +4 V ($r$) and that measured at OCV ($r_0$) permitted to calculate ρ as function of the reaction temperature. Figure 5 illustrates the ρ behavior as function of reaction temperature for the $Co_3O_4$ infiltrated cell. It was possible to observe that the effect of polarization on propene conversion started to increase at around 250 °C, it reached a maximum at 320 °C and then it decreased with further temperature increase, confirming the behavior of ρ observed in Figure 4.

The polarization effect on propene conversion was affected by different factors. The reactants mass transfer limitations caused by high propene conversion rate and the high electrode performance (low $R_p$) limited the polarization effect on the oxidation rate at temperatures above 320 °C, likely causing the decreasing of ρ.

The high conversion rate of propene given by the good catalytic activity of $Co_3O_4$ established a mass transfer regime that limited the access of reactants to the electrode surface; in fact, already at 300 °C, the $Co_3O_4$ exhibited a propene conversion close to 50% that appeared to be a critical limit to obtain high ρ values. Moreover the high electrode performance (low $R_p$) (see the electrochemical characterization section, Figure 7) at high temperatures enhanced the reaction of oxygen recombination to gaseous

oxygen, decreasing the possibility that the oxygen pumped through the electrolyte to the electrode surface could directly react with the adsorbed propene. These two combined effects caused the sharp decrease of ρ above 320 °C. On the opposite, at low temperatures (150-250 °C), almost no effect of polarization on propene oxidation rate was visible due to the low amount of pumped oxygens available for the direct propene electrooxidation.

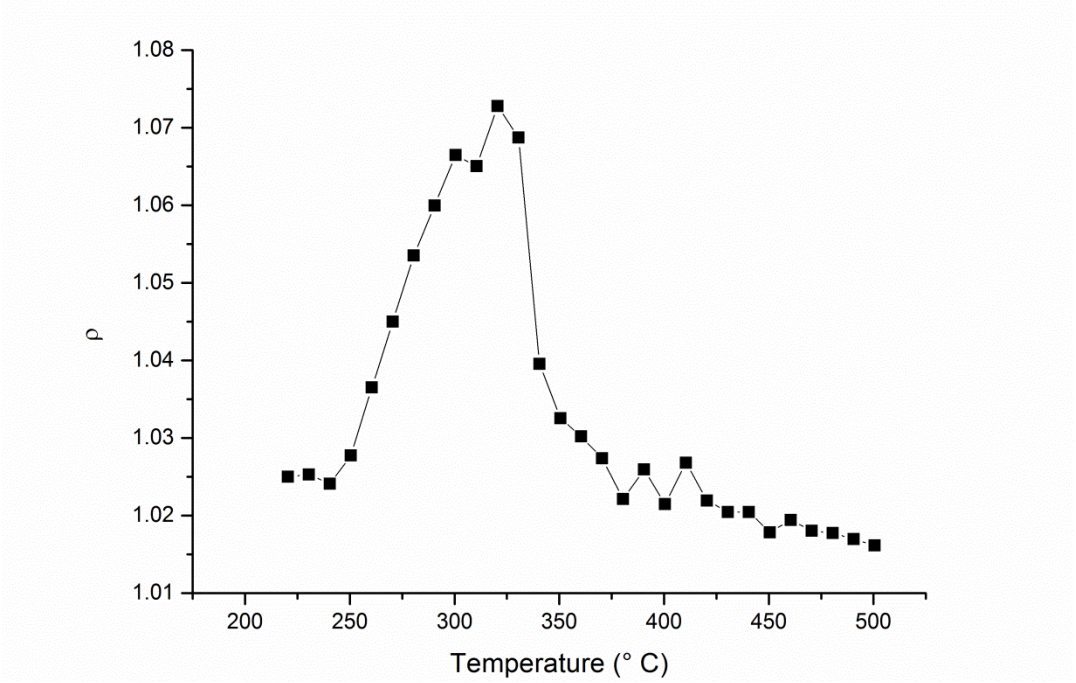


**Figure 5**: Rate enhancement ratio (ρ) versus temperature recorded at +4 V during TPO measurement for $Co_3O_4$ cell with 1000 ppm $C_3H_6$+10% $O_2$, 2L/h

The long-term polarization activated the LSM/CGO backbone cell, as described in Chapter 7. The backbone cell activation was measurable by an increase of both current density and propene conversion; this behavior was attributed to the oxygen vacancies formation on LSM electrode surface induced by polarization. In this study the infiltrated cells did not exhibit any propene conversion improvement after +4 V was applied for 5 hours; the stability and very high catalytic activity of $Co_3O_4$ and $CeO_2$ could have hidden the improvement of LSM catalytic activity induced by the polarization.

### 8.4.3 Electrochemical characterization

Figure 6 shows the Nyquist plot of the impedance spectra for the backbone and infiltrated cells recorded under 10% $O_2$, OCV and 500 °C.

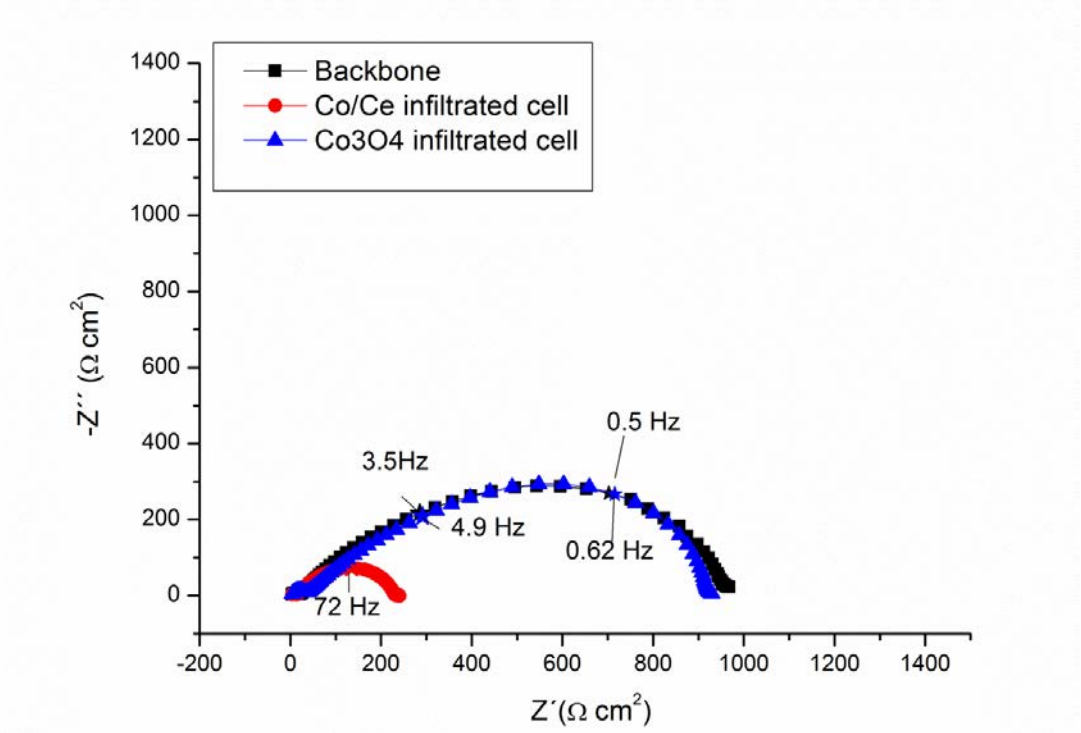


**Figure 6**: Nyquist plot of the impedance spectra for the backbone and infiltrated cells recorded at OCV with 10% $O_2$, 2 L/h, 500 °C

It possible to observe that $Co_3O_4$ addition had negligible effect on electrode performance; it showed similar impedance behavior if compared with the backbone cell. This is in agreement with the study of Huang et al. [7] on infiltration of LSM-YSZ composite. The improvement of electrode performance observed by Imanishi et al. [6] with infiltration of $Co_3O_4/CeO_2$ could be due to the formation of a $LaCoO_3$ phase with excess of $La_2O_3$. Samson et al. [9] reported that the infiltration of $LaSrCoO_3$ and $LaCoO_3$ on CGO backbone had similar effect on electrode performance: very small differences were observed between $R_p$ values of $LaSrCo_3$ and $LaCoO_3$, although their electronic conductivities at 600 °C in air differ of one order of magnitude.

On the opposite, in this work the co-infiltration of $CeO_2$ together with $Co_3O_4$ strongly improved the electrode performance of the backbone; the $R_p$ measured in 10% $O_2$ decreased from 950 Ω $cm^2$ to 240 Ω $cm^2$ at 500 °C, as shown in Figure 6. The electrode improvement with Co/Ce co-infltration was confirmed also with the presence of 1000 ppm $C_3H_6$ and 10% $O_2$ in the reaction atmosphere, as shown in the Arrhenius plot of $R_p$ in Figure 7. The activation energies extracted from the impedance spectra recorded at OCV with propene present in the reactive mixture were 0.76 eV ± 0.09 eV and 0.66 eV ± 0.1 eV for $Co_3O_4$ and Ce/Co, respectively.

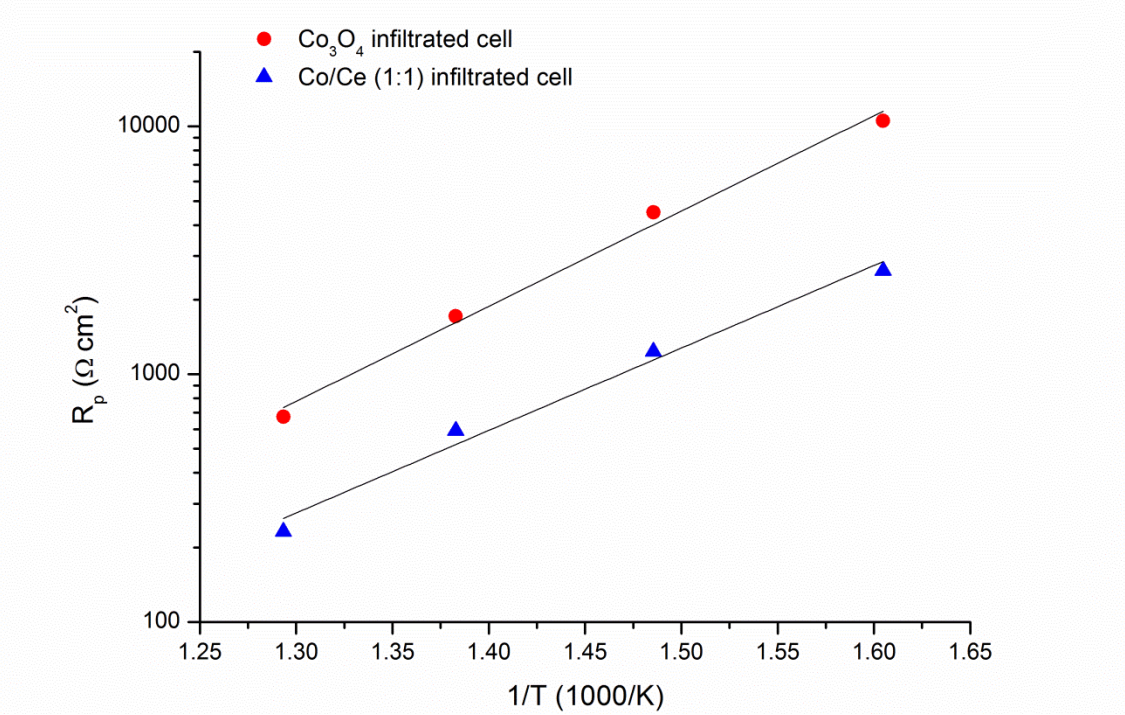


**Figure 7**: Arrhenius plot of polarization resistance ($R_p$) for $Co_3O_4$ and Ce/Co infiltrated cell extracted from impedance spectra recorded at OCV, 2L/h, 1000 ppm $C_3H_6$ and 10% $O_2$.

This behavior has been already observed by our group in a previous work on infiltration of $CeO_2$ on LSM/CGO electrode [10]. It is possible to deduce that $CeO_2$ was the main reason for the electrode improvement. The electronic conductivity of bulk materials varies in this order: $LaSrMnO_3$ > $Co_3O_4$ > $CeO_2$ with values of 2.1, 0.012 and $10^{-6}$ S/cm at 500 °C and 1 atm $O_2$, respectively [11, 12, 13]. The electrode performance increase upon ceria infiltration cannot be attributed to the electronic conductivity. Kungas et al. [14] suggested that the oxygen surface exchange and not the ionic conductivity could be the rate limiting step for composite cathode like $LaSrFeO_3$-YSZ. $LaSrMnO_3$, if compared to $LaSrFeO_3$ has very low ionic conductivity at high oxygen partial pressure [11,15]; the LSM electrode used in this work electrode was also affected by low oxygen ion diffusion rate trough the electrode.

The adsorption of oxygen on $CeO_2$ occurs with the formation of super oxide species ($O_2^-$); the concentration of these surface species is increased by $Zr^{4+}$ incorporation in the ceria structure. The high oxygen storage capacity (OSC) of $CeO_2$ and in particular of $Ce_{1-x}Zr_xO_{2-x/2}$ varies with the population of $O_2^-$, as reported by Descorme et al. [16]. DRIFT study carried on by Caillol et al. [17] identified $O_2^-$ and $O_2^{2-}$ as species on LSM surface both under helium and oxygen atmosphere at 600 °C. Recent works of Lee [18] and Piskunov [19] on oxygen adsorption on $LaBO_3$ (B=Mn,Fe,Co,Ni) and $LaSrMnO_3$, using DFT calculations, have predicted that the stable surface species at low temperature are $O_2^-$

and $O_2^{2-}$ species. The good electrode performance of $CeO_2/Co_3O_4$ infiltrated cell could be due to the high concentration and stability of these oxygen species on the electrode surface. Further tests will be needed to confirm this hypothesis.

Figure 8 and Figure 9 show the effect of propene introduction into the reactive system at 400 °C on $Co_3O_4$ and Co/Ce infiltrated cell, respectively.

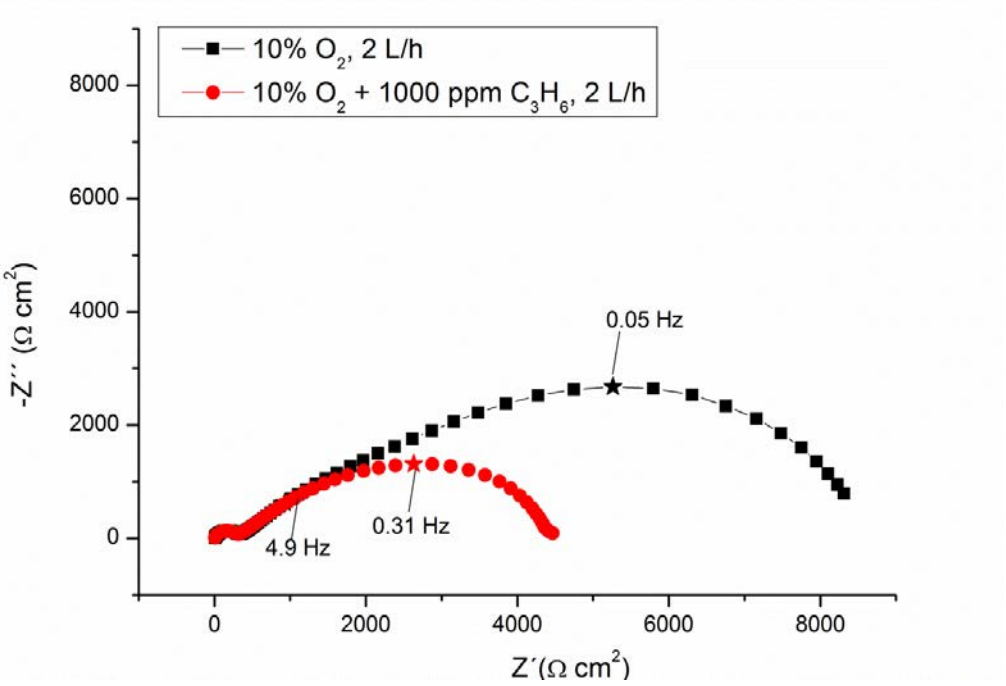


**Figure 8**: Nyquist plot of impedance spectra of $Co_3O_4$ infiltrated cells recorded at OCV with 10% $O_2$ and 10% O2 + 1000 ppm $C_3H_6$, 2 L/h, 400 °C

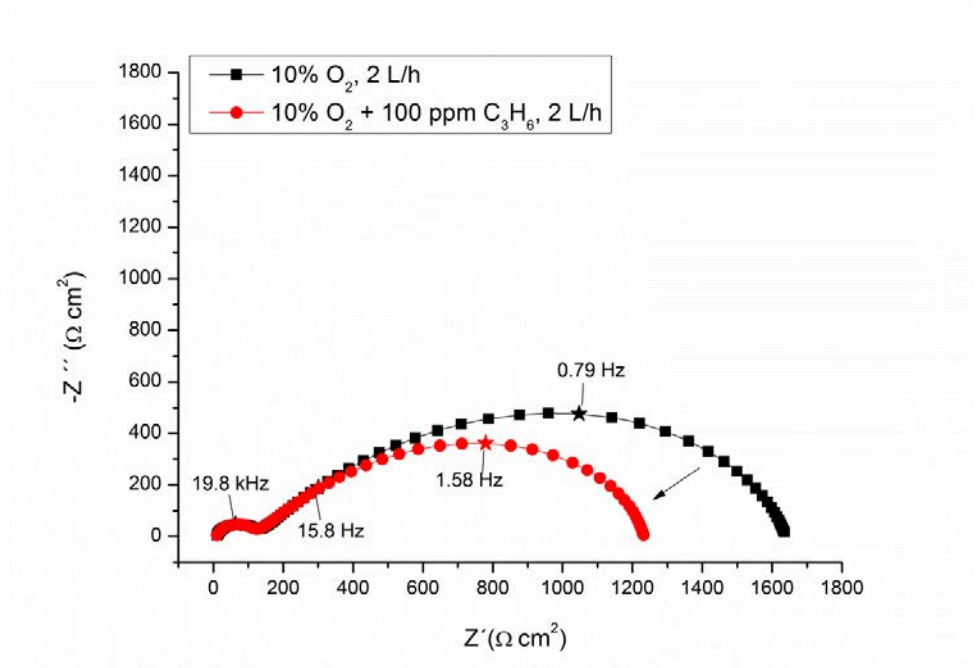


**Figure 9**: Nyquist plot of impedance spectra of Co/Ce (1:1) infiltrated cells recorded at OCV with 10% $O_2$ and 10% $O_2$ + 1000 ppm $C_3H_6$, 2 L/h, 400 °C

The propene introduction provoked a strong decrease of resistance together with a characteristic peak frequency increase at medium and low frequency. This behavior was never observed before in our studies where usually the propene introduction into the reactive system caused an increase of resistance associated to peak frequency decrease, as illustrated in Chapter 7. This phenomenon has previously been was attributed to the strong adsorption of propene competing with oxygen adsorption and dissociation on the electrode surface, likely causing the resistance increase. In this study local hot spots due to the exothermic propene oxidation reaction were not excluded although neither serial resistance ($R_s$) nor the resistance R1 associated to the grain boundaries were observed upon propene introduction into the reactive system. Moreover a resistance increase at low frequency was measured in our previous work with $CPO_{20}$ and $CeO_2$ infiltration [10] even in the presence of relatively high propene conversion rate.

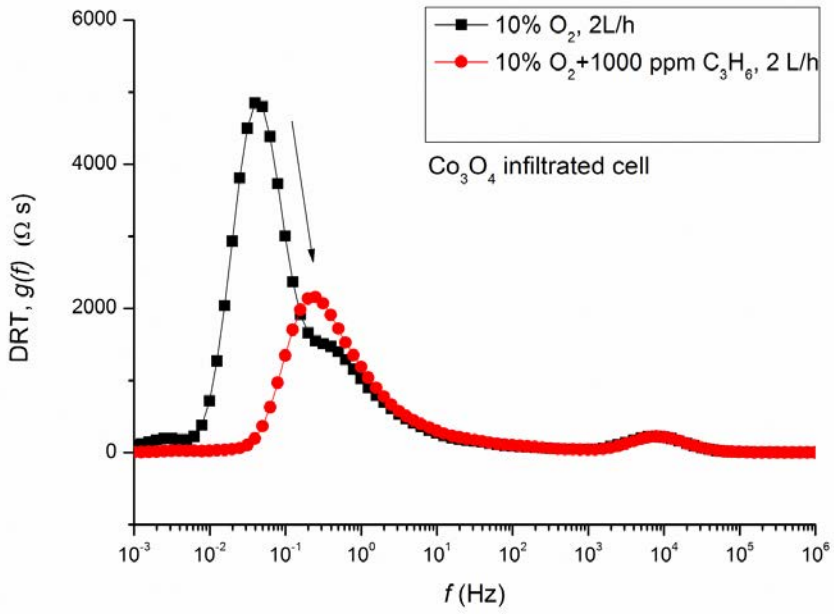


**Figure 10**: Distribution of relaxation time (DRT) analysis of $Co_3O_4$ infiltrated cell under 10% $O_2$ and 10% $O_2$ + 1000 ppm $C_3H_6$, 2 L/h, OCV at 400 °C

Figures 10 and 11 illustrate the DRT analysis of the effect of propene introduction on $Co_3O_4$ and Co/Ce infiltrated cells, respectively. DRT analysis on $Co_3O_4$ infiltrated cell showed three clear contributions under 10% oxygen atmosphere at 0.8 kHz, 0.45 Hz and 0.04 Hz, with similar characteristics to those observed for the backbone cell (Figure 7B, Chapter 7). The propene introduction reduced the resistance and merged the two contributions at low and medium frequency. The same behavior was observed for Co/Ce

(1:1) infiltrated cell upon introduction of propene shown in Figure 11, although in this case the contribution at medium frequency in both atmospheres was difficult to separate from the low frequency contribution and the effect of propene on the resistance was less extended.

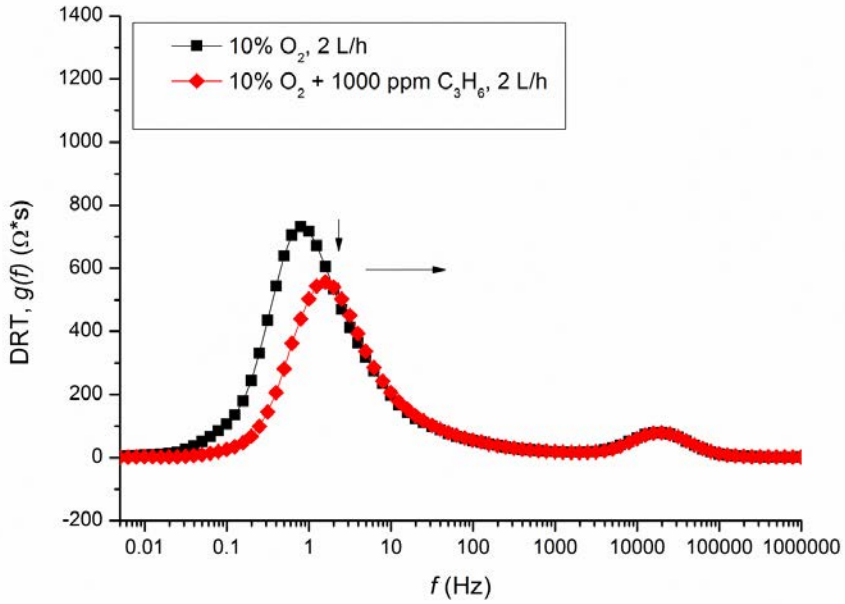


**Figure 11**: Distribution of relaxation time (DRT) analysis of Co/Ce (1:1) infiltrated cell under 10% $O_2$ and 10% $O_2$ + 1000 ppm $C_3H_6$, 2 L/h, OCV at 400 °C

Further study was conducted on $Co_3O_4$ cell in order to study the effect of propene concentration on impedance response. Figure 12 illustrates the ADIS analysis as a function of propene concentration using 750 ppm $C_3H_6$ with 10% oxygen as reference.

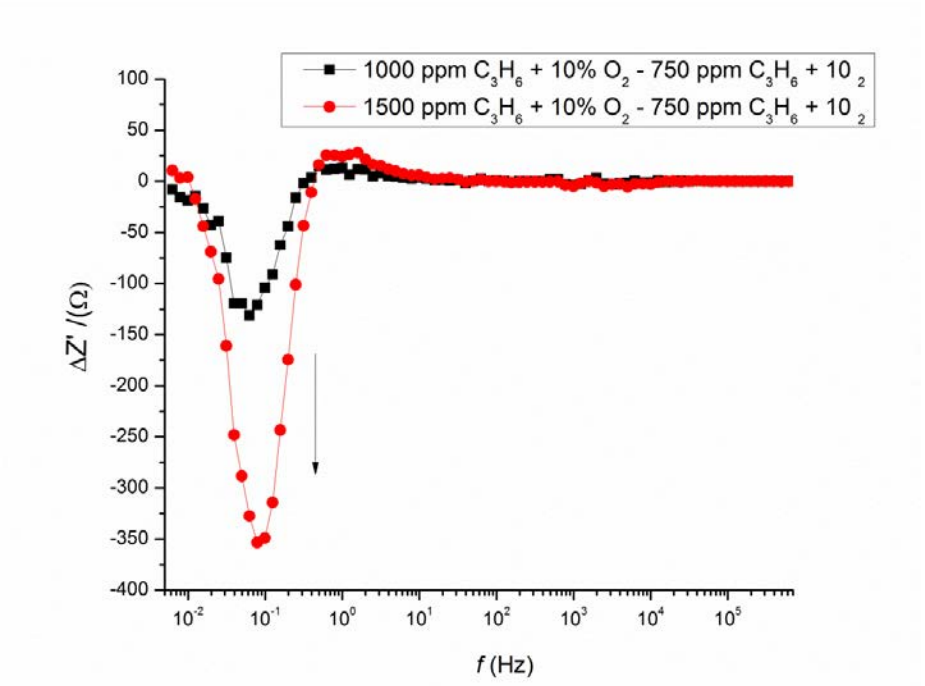


**Figure 12**: ADIS of $Co_3O_4$ infiltrated cell under different concentration of propene in the reactive system at 400 °C, OCV, 2 L/h.

The propene concentration increase caused a resistance decrease with a peak frequency located at about 0.08 Hz. As it is possible to observe in Figure 6B-chapter 7, the backbone cell impedance response instead was almost insensitive to propene concentration variation in presence of oxygen.

The low frequency contribution visible in the impedance spectra could be directly caused by the heterogeneous chemical reaction of propene oxidation catalyzed by $Co_3O_4$. Werchmeister et al. [20] found similar behavior on $La_{0.85}Sr_{0.15}MnO_3/Ce_{0.9}Pr_{0.1}O_2$ symmetric cell in the study of electrochemical $NO_x$ reduction. In their work the introduction of NO and $O_2$ in the reaction environment caused a decrease of polarization resistance, particularly at 500 °C and 400 °C. The cause of $R_p$ decrease was due to the disappearing of low frequency arc when $O_2$ was present with NO. The authors attributed the low frequency to the formation of $NO_2$ catalyzed by the $La_{0.85}Sr_{0.15}MnO_3$ in the presence of oxygen.

## 8.5 Conclusions

High propene conversion and full selectivity to $CO_2$ was reached by infiltration of $Co_3O_4$ and $Co_3O_4/CeO_2$ into porous cell stack. Although the cells exhibited similar catalytic activity, $CO_3O_4$ showed the highest rate enhancement ratio. The effect of polarization on propene conversion for the $Co_3O_4$ infiltrated cell exhibited a sharp maximum around 300 °C and then decreased with increasing reaction temperature. The temperature region

around 300 °C appeared to be optimal to avoid strong reactants mass transfer limitations inhibiting the effect of polarization on propene oxidation rate and the coverage of the electrode surface by the oxygen ions, pumped through the electrolyte, was enough to promote the direct electrooxidation of propene.

$Co_3O_4/CeO_2$ co-infiltration strongly increased the electrode performance while the $Co_3O_4$ infiltration did not affect the polarization resistance measured in 10% $O_2$ if compared to the backbone cell.

The introduction of propene into reactive system induced a strong decrease of electrode resistance mainly located at low frequency while medium and high frequency remained unaffected. The low frequency contribution decrease with increasing propene concentration and it was directly assigned to the propene oxidation catalytic reaction on $CO_3O_4$ surface.

## References

1. W. B. Li, J. X. Wang, and H. Gong, *Catalysis Today*, **148**, 81–87 (2009)

2. Y. Morooka and a Ozaki, *Journal of Catalysis*, **5**, 116–124 (1966)

3. N. C. Jhaveri, L. S. Caretto, and K. Nobe, *Industrial & Engineering Chemistry Product Research and Development*, **14**, 142–146 (1975)

4. L. F. Liotta et al., *Applied Catalysis A: General*, **347**, 81–88 (2008)

5. F. Wyrwalski, J.-M. Giraudon, and J.-F. Lamonier, *Catalysis Letters*, **137**, 141–149 (2010)

6. N. Imanishi et al., *Fuel Cells*, **9**, 215–221 (2009)

7. Y. Huang, J. M. Vohs, and R. J. Gorte, *Journal of The Electrochemical Society*, **153**, A951 (2006)

8. Y. U. Yao, *Journal of Catalysis*, **33**, 108–122 (1974).

9. A. J. Samson, M. Søgaard, and N. Bonanos, *Electrochemical and Solid-State Letters*, **15**, B54 (2012)

10. D. Ippolito and K. K. Hansen, *Journal of Solid State Electrochemistry*, **17**, 895–908 (2013)

11. J. Mizusaki et al., *Solid State Ionics*, **132**, 167–180 (2000).

12. A. Trovarelli, *Catalysis by Ceria and Related Materials*, Imperial College Press, (2002), p. 408–410.

13. *The Landolt-Bornstein Database*, Springer Materials.

14. R. Küngas, F. Bidrawn, E. Mahmoud, J. M. Vohs, and R. J. Gorte, *Solid State Ionics*, **225**, 146–150 (2012)

15. J. Mizusaki, M. Yoshihiro, S. Yamauchi, and K. Fueki, *Journal of Solid State Chemistry*, **58**, 257–266 (1985).

16. C. Descorme, *Journal of Catalysis*, **196**, 167–173 (2000)

17. N. Caillol, M. Pijolat, and E. Siebert, *Applied Surface Science*, **253**, 4641–4648 (2007)

18. Y.-L. Lee, J. Kleis, J. Rossmeisl, and D. Morgan, *Physical Review B*, **80**, 224101 (2009)

19. S. Piskunov, J. Timo;, and S. Echard, *Physical Review B*, **83**, 2–4 (2011).

20. R. M. L. Werchmeister, K. K. Hansen, and M. Mogensen, *Journal of The Electrochemical Society*, **157**, P35 (2010)

21. H. Schichlein, A.C. Muller, M. Voigts, A. Krugel, E. Ivers-Tiffée, *Journal of Applied Electrochemistry*, **32**, 875-882 (2002).

22. S. H. Jensen, A. Hauch. P.V. Hendriksen, M. Mogensen, *Journal of the Electrochemical Society*, **156**, B757-B764 (2009).

# 9 OVERALL DISCUSSION, CONCLUSIONS AND OUTLOOK

In this chapter the findings from the experimental analysis will be discussed with the objective to provide a complete picture of the factors affecting the catalytic activity and efficiency of the electrochemical reactor under study for the oxidation of propene.

## 9.1 Overall Discussion

The objective of this project was to study the possibility to deep oxidize propene in a porous electrochemical reactor for the purification of Diesel exhausts and comprehend the effect of active materials infiltration on the catalytic activity and efficiency of the reactor.

### 9.1.1 The behavior of LSM/CGO and LSF/CGO backbone in the electrochemical oxidation of propene

In this project two different electrodes have been produced and tested: $La_{0.85}Sr_{0.15}MnO_3$ and $La_{0.85}Sr_{0.15}FeO_3$, using $Ce_{0.9}Gd_{0.1}O_{1.95}$ as electrolyte. These two different reactors have been used as backbone for the infiltration of different active materials.
During the catalytic activity test without infiltration, both the reactors have shown conversion of propene at OCV of 3.88 * $10^{-8}$ mol/s*g for LSM/CGO and 2.43 * $10^{-8}$ mol/s*g for LSF/GDC, measured at 400 °C; these values correspond to a propene conversion of 26.4% and 21.1% for LSM/CGO and LSF/CGO, respectively.
The disadvantage of the use of the solely backbone as reactor for the oxidation of propene was the unwanted formation of CO as reaction co-product with selectivity to $CO_2$ as low as 86%-90% at the highest tested temperature together with low conversion of propene.
The LSM/CGO reactor exhibited the highest values in terms of effect of polarization on propene oxidation rate (ρ) and faradaic efficiency (Λ), particularly at the beginning of the activity characterization test when the electrode was fresh.
The two reactors exhibited remarkable differences both in the electrode performance in terms of polarization resistance ($R_p$) and in the effect of prolonged polarization on the catalytic activity and current density.

The LSF/CGO backbone showed one order of magnitude lower $R_p$ compared to LSM/CGO in the temperature range of 350 °C-500 °C together with a reduced activation of 0.63 eV if compared to LSM/CGO with 0.93 eV. The lower $R_p$ values of LSF/CGO backbone could be probably attributed to the higher ionic conductivity of LSF if compared to LSM and to the microstructural differences of the two electrodes that appeared to play a crucial role in the electrode behavior.

The prolonged polarization had a deleterious effect on LSF/CGO backbone decreasing its catalytic activity, measured at OCV, of about 14% at 500 °C; this phenomenon was coupled to a decrease of current density and increase of ohmic resistance with increasing test time.

On the opposite side, the LSM/CGO backbone, subjected to prolonged polarization, exhibited an increase of current density together with a substantial enhancement of catalytic activity of 58%, measured at 500 °C and OCV. While the activation of the LSM/CGO electrode was expected due to the formation of oxygen vacancies on LSM surface, the massive increase of propene oxidation rate was totally unexpected and never reported before in literature for perovskites or simply confused with a permanent EPOC effect. The formation of oxygen vacancies due to the prolonged polarization appeared to play a key role in the mechanism of propene oxidation.

If the increase of propene conversion, due to prolonged polarization, could be favorable from a classic catalytic point of view to contrast the catalyst activity degradation with time in a real Diesel exhausts after treatment application, the improvement of electrode performance turned out to be deleterious to obtain high current efficiencies; this was demonstrated by the decrease of Λ for LSM/CGO backbone subjected to 30 h of prolonged polarization.

### 9.1.2 The effect of active material infiltration into LSM/CGO and LSF/CGO backbone on catalytic and electrochemical activity

The infiltration of $Ce_{0.9}Gd_{0.1}O_{1.95}$ (CGO) was carried on both LSM/CGO and LSF/CGO backbones. In both backbones the infiltration of CGO was able to considerably increase the propene conversion at OCV, particularly for temperatures above 300 °C, and to increase the reaction selectivity to $CO_2$, thanks to the good catalytic activity of $CeO_2$ as catalyst for deep hydrocarbons oxidation.

Multiple infiltrations of CGO into LSM/CGO backbone increased the conversion of propene at OCV; the infiltration with a loading of 8.7% weight of CGO caused the partial blocking of reactor pores, preventing the access of the reactants into the inner layers of

the reactor and causing a decrease of propene conversion compared to the backbone with lower CGO loading.

An instability problem of the infiltrated material upon prolonged polarization was encountered with increasing the number of infiltrations, causing a decrease of propene conversion at OCV.

The infiltration of CGO has a different effect on the electrochemical behavior of the two different backbones; the one step CGO infiltration reduced the $R_p$ from 49 kΩ $cm^2$ to 4.3 kΩ $cm^2$ for LSM/CGO measured at 400 °C and OCV, while the CGO infiltration on LSF/CGO induced an increase of $R_p$ from 2.8 kΩ to 10.7 kΩ measured at 400 °C and OCV. Moreover the infiltration of CGO into LSF/CGO preserved the electrode from the degradation, affecting both the catalytic activity and the electrode performance.

As reported in literature, the beneficial effect of CGO infiltration on the LSM-based electrode could be due to an increase of the speed of oxygen adsorption and dissociation on the electrode surface; if this was the case, the same electrode improvement should be visible also for LSF/CGO backbone. It is worth to highlight that the infiltration of CGO with low temperature heat treatment on LSM/CGO did not significantly changed the activation energy of $R_p$ measured at OCV if compared to the infiltration of CGO on LSF/CGO using the same heat treatment.

The result of the study of the effect of infiltrated CGO heat treatment temperature indicated that the morphology of the infiltrated material determines the electrochemical characteristics of the electrode and the magnitude of the effect of polarization on propene conversion.

The heat treatment at low temperature (400 °C-2 h) of the infiltrated CGO precursors permitted to obtain the highest rate enhancement ratio and faradaic efficiencies at reduced temperatures, both for LSM/GDC and LSF/GDC. A continuous layer of infiltrated active material, obtained with a low temperature heat treatment, could increase the lifetime of the backspillover $O^{\delta-}$ ions promoters on the electrode surface, consequently enhancing the effect of polarization on propene conversion. This mechanism appeared more clearly from the tests carried on LSF/CGO backbone infiltrated with CGO where the change of catalytic activity after prolonged polarization was reduced if compared to LSM/GDC electrode, making easier the phenomenological characterization.

The infiltration of active material like CGO helped also to comprehend the role of the propene conversion on the rate enhancement ratio behavior. Particularly, the ρ was limited for conversion of propene above 50%-55% due to the external diffusion limitations of the reactants; it was difficult to obtain high ρ values under external mass transfer regime,

the effect of polarization on propene conversion was strongly limited by the availability of the reactants at the electrode/catalyst surface.

The infiltration of $CeO_2$ and $Ce_{0.8}Pr_{0.2}O_{2-\delta}$ ($CPO_{20}$) on LSM/GDC backbone helped to clarify the role of the electrical properties of the infiltrated material on the rate enhancement ratio and faradaic efficiency of the whole reactor.
Both the infiltrated materials were able to decrease the $R_p$ of the LSM/CGO backbone measured at OCV; particularly at high temperatures (450 °C and 500 °C) $CeO_2$ and $CPO_{20}$ exhibited close $R_p$ values, both at OCV and +4 V. This was surprising in the case of $CeO_2$ infiltration since $CeO_2$ has very low total conductivity at high oxygen partial pressure if compared to a mixed ionic and electronic conductor like $CPO_{20}$. This phenomenon needs to be further investigated.
The activation energy of the $R_p$ measured at OCV for the $CeO_2$ infiltrated cell showed close values to the activation energy of the LSM/CGO backbone and of the CGO infiltrated cell; on the contrary the CPO exhibited much lower activation energy of 0.59 eV, resulting to be much less affected by temperature. The low electrode polarization resistance shown by $CPO_{20}$ infiltrated backbone could be attributed to its mixed conductivity transport property.
Between 300 °C and 400 °C, where the conversion of propene was limited between 13.5% and 46%, the LSM/CGO backbone infiltrated with $CeO_2$ exhibited both higher ρ and Λ values compared to $CPO_{20}$. The low electrode polarization resistance of $CPO_{20}$ was detrimental to obtain high faradaic efficiency at low temperatures, likely due to the short lifetime of oxygen ion promoters given by mixed conductivity of $CPO_{20}$ that favoured the competing reaction of oxygen evolution.

### 9.1.3 The new LSM/CGO backbone with high porosity

A backbone based on LSM/GDC composite but with increased porosity was produced with the objective to decrease the pressure drop along the reactor and avoid the clogging of the pores by particulate matter present in the real Diesel engine exhausts.
The use of an additional pore former like the PMMA to the graphite was able to increase the porosity to 48% introducing a dual pores distribution with pores between 0.5 µm and 4.5 µm and between 20 µm and 100 µm.
The change of microstructure remarkably improved the electrochemical performance; decreasing the $R_p$ respect to the backbone fabricated using only graphite as pore former

and approaching both the polarization resistances and activation energy of the $CPO_{20}$ infiltrated LSM/CGO backbone produced only with graphite as pore former.

The strong electrode improvement of the new backbone could probably be attributed to the increase of the three phase boundary (TPB) for the electrochemical reaction, due the increased ease of the access of the reactants to the inner part of the reactor. The catalytic activity for propene oxidation of the new backbone produced using also PMMA decreased if compared to the catalytic activity of the backbone produced only with graphite, although the same relative amount of LSM and CGO was used for the reactor production. A change of the reactant fluid dynamic into the reactor with the introduction of new pores distribution could be a possible cause.

The low conversion of propene permitted to study in more detail the effect of polarization on propene oxidation rate reducing the effect of the reactants diffusion limitation. Moreover the low polarization resistance and the closing of the impedance spectra at low frequency permitted to study in more detail the effect of propene introduction on the impedance spectra.

The initial polarization test at 500 °C and 400 °C exhibited remarkable increase of propene conversion with ρ values up to 1.7 at 500 °C and 1.55 at 400 °C, upon the application of +5 V. After the prolonged polarization at +4 V for 5 h, it was possible to observe an increase of propene conversion measured at OCV of 24.6 % at 500 °C and 18.9 % at 400 °C. The beneficial effect of the polarization for the propene conversion at OCV had, instead, a detrimental effect on both the rate enhancement ratio and on the faradaic efficiency.

The electrode activation by polarization, detected also with higher magnitude on the LSM/CGO backbone made with only graphite, increased the speed of the competing oxygen evolution reaction decreasing the selectivity towards the electrochemical oxidation of propene.

The detailed ADIS and DRT analysis carried on the impedance spectra helped to explain the cause of the $R_p$ increase with propene introduction into the reactive system. The propene, due to its high adsorption strength on the electrode surface, derived from its unsaturated bonds, interfered with the adsorption and dissociation of oxygen at the electrode active sites (oxygen vacancies), causing the increase of polarization resistance.

The infiltration of $Co_3O_4$ and $Co_3O_4/CeO_2$ into LSM/CGO backbone strongly increased the propene conversion reaching 80% already at 350 °C and with 100 % of selectivity to $CO_2$ at all temperatures.

A temperature programmed oxidation (TPO) analysis in presence of propene and oxygen was carried on $Co_3O_4$ infiltrated backbone, both at OCV and under a polarization of

+4 V. The comparison of the two TPOs permitted to calculate the rate enhancement ratio at different reaction temperatures; it was possible to observe a behavior of ρ with a maximum around 320 °C where the conversion of propene was slightly below 50%. This temperature was the optimum between the non structural factors influencing the rate enhancement ratio: the CGO ionic conductivity and the minimum electrode surface coverage of the electrochemically pumped oxygen ions at low temperature, the mass transfer limitation of the reactants to the reaction zone and the electrode polarization resistance for the competing oxygen evolution reaction.

## 9.2 Conclusions

This Ph.D. project demonstrated that the electrochemical oxidation of propene was possible through the use of an electrochemical reactor for the electrochemical purification of Diesel exhausts.

This project helped to better understand how the effect of polarization on propene conversion was a complex function of multiple variables: the microstructure of the backbone, the polarization resistance of the electrodes, both at OCV and under polarization, the electrical and morphological properties of the infiltrated material and the specific reaction conditions like the propene conversion. A continuous layer of the infiltrated material, the low conversion of propene to avoid mass transfer limitations of the reactants and the high polarization resistance of the electrodes at low temperature, appeared to be crucial to obtain high faradaic efficiencies.

The LSM/GDC backbone exhibited both higher catalytic activity and higher faradaic efficiency for the electro-oxidation of propene if compared to LSF/GDC backbone. Although the catalytic activity could be easily enhanced by the infiltration of an active material like CGO, stability problems arose for the LSF/CGO backbone under prolonged anodic polarization.

Although the microstructure is generally known to be a key factor in determining the electrochemical behaviour of an electrode, the decrease of polarization resistance and catalytic activity, obtained by the use of PMMA as pore former together with the graphite, was still surprising and raised further the importance of controlling the reactor microstructure to obtain the desired performance both in terms of catalytic and electrode activity.

The infiltration of CGO treated at low temperature to form a continuous layer on the LSM/CGO backbone was the best compromise to obtain high propene conversion at OCV together high rate enhancement ratio and faradaic efficiency values at low temperatures (300-350 °C). Although some stability problems affected the performance of

multiple infiltrated CGO on LSM/CGO backbone, the strong activation of LSM upon prolonged polarization was able to partially counteract the instability of the infiltrated CGO.

## 9.3 Outlook

In the next future it will be fundamental to focus on the study of the effect of the co-existence of NOx, propene and oxygen in the reaction atmosphere on the electrochemical reactor activity for the simultaneous reduction of NOx and oxidation of propene through voltage application. It will be important to clearly evaluate the extent of the homogenous reactions between NOx, propene and oxygen together with the heterogeneous reactions involving these gas species, together with the catalyst forming the backbone composite.

Since the infiltration of NOx-storage compound like BaO on LSM/CGO has been proven to be effective in the electrochemical reduction of NOx in presence of oxygen; it is fundamental to infiltrate BaO together with CGO with the objective to match the NOx storage property of BaO with the ability of gadolinium doped ceria to get high conversion of propene at OCV and high faradaic efficiency at low temperature.

A test on real Diesel engine exhausts of the best performing infiltrated backbone, for both reactions found during laboratory scale test, would be beneficial to comprehend the effect of particulate matter, high content of $H_2O$, $CO_2$ and prolonged polarization on the reactor activity and stability.

An alternative use of this porous electrochemical reactor, for the only catalytic oxidation of hydrocarbons and electrochemical oxidation of particulate matter at reduced temperatures in competition with the Diesel particulate filters, should be taken into consideration.